Small Angle Scattering Studies of Self Assembly

in Lipid Mixtures

by

Divya Singh

A dissertation submitted to The Johns Hopkins University in conformity with the

requirements for the degree of Doctor of Philosophy.

Baltimore, Maryland

April, 2008

Abstract

Systems consisting of mixtures of a long and a short-tail lipid, commonly referred to as 'biclles', have recently shown promise in membrane protein crystallization and have been used for some time as an alignable media for use in NMR based protein structure determination. However, the phase behavior of these lipid mixtures remains poorly understood. This dissertation reports small angle scattering studies to gain an understanding of the structure and composition, as well as the mechanism of structural transformation by systematically tailoring those mixtures. A detailed understanding of the phase behavior is essential to adapting them for specific applications.

In DMPC/DHPC (or C14/C6) mixtures at temperatures ~10-15°C below the melting transition temperature T_m of the long tail lipid C14, small angle neutron scattering (SANS) experiments with mixtures of hydrogenated and deuterated lipids give direct evidence of the segregated discoidal morphology, while use of standard mixed surfactant theories account to first order for the size of the discs.The deviation of their dilution induced growth from the fully segregated models, an evidence

of net mixing of the long lipid into the short lipid rim, is confirmed by contrast enhanced SANS. Previously ignored and unaccounted for, such a mixing behavior is essential for the energetics of a self-assembled mixture of two lipids with vastly different spontaneous curvatures. When the low temperature study is extended to other phospholipid-detergent mixtures, universality of the discoidal phase is observed, highlighting the role of the rigid, gel state long lipid and the edge tension reducing properties of the short lipids in the self-assembly. As a step further, when the size of the smaller lipid species is increased to consist of eight carbon tails, (C14/C8 mixture), elongated tablet like aggregates with flat, non circular cross-section are the predominant structures, as shown by complimentary SANS and SAXS (small angle X-ray scattering) techniques. Similar structures are also observed in C14/C6 mixtures at temperatures near and above the T_m of C14 lipids. Chain-melting at higher temperatures in C14/C6 mixtures and mixing of the two lipids due to decreasing chain length difference (or hydrophobic mismatch) in C14/C8 are found to be equivalent effects, affecting the interfacial and bulk properties of the aggregates, and leading to preferential growth in one-dimension.

.

Advisor(s): Dr. Paul Butler and Dr. Lionel Porcar

Readers(s): Prof. Robert Leheny and Prof. Daniel Reich

Acknowledgements

This dissertation would not have been possible without the help and support of numerous people at JHU and at NIST, who have been with me in my Phd journey, that almost ended up becoming the second 'marathon' of my life. I cannot possibly thank everyone enough.

Foremost, I thank Prof. Bob Leheny, for mentoring and encouraging me to do things, that brought me to JHU in the first place. The adventurous journey I undertook, would not have been possible without his constant support. While the big part of getting here with a thesis, would not have been happened, had I not met Dr. Paul Butler in the corner office, next to his office at the NIST Center for Neutron Research (NCNR). If not for his willingness to have me work with him on this project, I wouldn't have been able to take this small step into research. Finally, Dr. Lionel Porcar has been the one, from whom I have learnt the art and science of experimentation; that a successful experiment lies not only in planning well, but also in thinking through every small step you do. As advisors, both Lionel and Paul have taught me the value of working in teams. While their excitement with good science was infectious, their high standards, I can only hope to match some day.

At JHU, I value the interactions I had with emeritus Professor Susan Domokos, and Professors Bertrand Garcia-Moreno, Kalina Hristova and Scott Kuo during the early stages of my studies. I would like to thank all the faculty members who agreed to serve on my committees. The excellent staff in the Physics and Astronomy department, made the daily working of life possible. I could call it my home away from home. To each and every member of staff, my heartful thanks.

A number of people at NIST have provided useful insights, thoughtful discussions and much needed support, over the course of this project. Prof. David Worcester (visiting from Missouri) has been my source for everything lipids. His enthusiasm for the smallest nuances of lipid phase behavior, made me see the beauty of my research project. Dr. Steve Kline has been valuable help in every modeling or analysis question I ever had. Dr. Ursula Perez-Salas (now at Argonne) was always fun to work with in the lab. I wish we could have worked together more. Dr. Dan Neumann always checked up on me and the progress of this work. I thank him for his generosity in having me share NIST resources. Dr. Susan Krueger was always there to take care of the logistics of my stay. The excellent support staff members make it the welcoming place for everyone.

And could I even imagine life without all the friends I made while in Gaithersburg and Baltimore? Life in JHU would not have been the same without the AID family, myself and a few friends nurtured for several years, and which shaped my thinking over these years. My roommates, Anubha and Anshu, few friends from IIT days, Shivani, Shakti and Parul

and all the friends in the department, I couldn't have survived without you all. At NIST, my officemates, Sang, Danny and Elena and staff scientists, William and Larry were always there to brainstorm. I will cherish the time spent at NCNR, in the company of so many scientists, leaders in their respective fields. Many runners among them, helped me in my running pursuits towards the end of my stay.

That brings me to the 'marathon' aspect of this work. When I completed the Marine Corps marathon the in October 2007, working on the thesis was like this huge mountain ahead of me. The lessons from that marathon training however, could not have come at a better time. I knew the slow and steady work done so far, had to culminate in a sprint in the end. Or atleast that is the sign of a good training, in the words of my coaches Nick and Jay. Thank you Marathon Charity Partners, for your wonderful work and many thanks to my fellow runners for making it such a memorable experience. My thesis work, like the 'marathon' itself, would not be a finish without the camaraderie and encouragement of fellow runners/students. This finish, affirms my continued work to bring smile to the poorest face I can remember.

Finally, without the unconditional love and support of my family, particularly my parents, I would not be who I am today. Papa, you remain the biggest inspiration of my life. Mamma, nothing in the world can match your devotion. The completion of this project owes much to the love and care I have received over the past few years from Bala Krishnamoorthy, my confidant, inspiration for work and everything else in life. Words cannot possibly convey my gratitude, hopefully a lifetime of love will.

To my Mother Shanti Singh and
my Grandmothers, Muneshwari Devi and Angrahita Devi
Whose struggles and dedication, my life has benefitted from.

I want to know how God created the world. I'm not interested in this or that phenomenon, in the spectrum of this or that element. I want to know his thou-ghts, the rest are details.

From E. Salaman, 'A Talk With Einstein', The Listener 54 (1955),

pp. 370-371

Contents

List of Figures

List of Tables

Chapter 1

Introduction And Objectives

Self-assembly, the spontaneous organization of small components into more complex macromolecules without any physical bonds, is ubiquitous in both nature and industry. In synthetic assemblies, liquid crystals and porous nano composites are important examples. In nature, the lipid bilayer is one of the most important self-assembled systems [2]. Lipid bilayer structures are the building blocks of cell membranes and form compartments within the cell. Aided by specific membrane proteins inserted in the bilayer, they are responsible for complex transport and signalling functions across the membrane[3]. Several commercial and scientific applications of lipid bilayers to form drug containing vesicles [4] have found potential applications in improving human health (Maxfield and Tabas's article in [3]). This has made an understanding of self-assembly processes in simpler bio-mimetic membrane systems and molecular self-assembly in general, a subject of intense experimental, theoretical and computational efforts in recent years. This thesis, will focus on understanding the self-assembly in a bio-mimetic system consisting of mixtures of lipids, that has applications in very important problem in biological research involving the understanding of membrane protein structures (Bowie's article in [3]).

In addition to their biological significance, bio-mimetic membranes have attracted

the attention of physicists since the pioneering work of Helfrich [5]. Model lipid bilayers represent a quasi-two-dimensional systems [6, 7] exhibiting rich phase behavior as a function of many extensive variables. Their remarkable material properties like flexibility and stability ([8] and references there in) have made them popular among soft-matter scientists ([7, 9], [10] and references there in). While model membranes composed of a single lipid have been the subject of intense study [11, 12], two component lipid membranes offer additional complexities [13, 14, 15]. The great success Physics has enjoyed from mapping complex problems into simple, solvable models can be expected to explain the remarkable self-assembly process in such systems.

Importance of Membrane Proteins and Challenges in Understanding their Structures

Biological membranes are highly selective permeability barriers composed of phospholipids and membrane proteins known to be arranged in a two-dimensional fluid mosaic model [[6], Engelman's article in [3]]. A cartoon of such a bilayer membrane is shown in Fig.1.1. In the absence of membrane proteins, cells could not participate in biological processes involving transport across membranes, charge separation and energy converting mechanisms. However, despite their obvious importance, high resolution (4Å or less) structures have been determined for only 88 unique membrane proteins: nine in the past couple of years [16]. This is a small number, especially if compared to structures of their water-soluble counterparts which number about 30000 ([17] and Protein Data Bank (www.pdb.org)). Membrane protein structure determination thus remains one of today's great scientific challenges [3, 18]. One step further in the same direction is the interest in understanding the interaction between membrane proteins and the cell membranes and how they influence the structure and function of each other.

Several membrane protein structures have been determined by X-ray crystallography [18], but the difficulty in purification and crystallization of membrane proteins are a
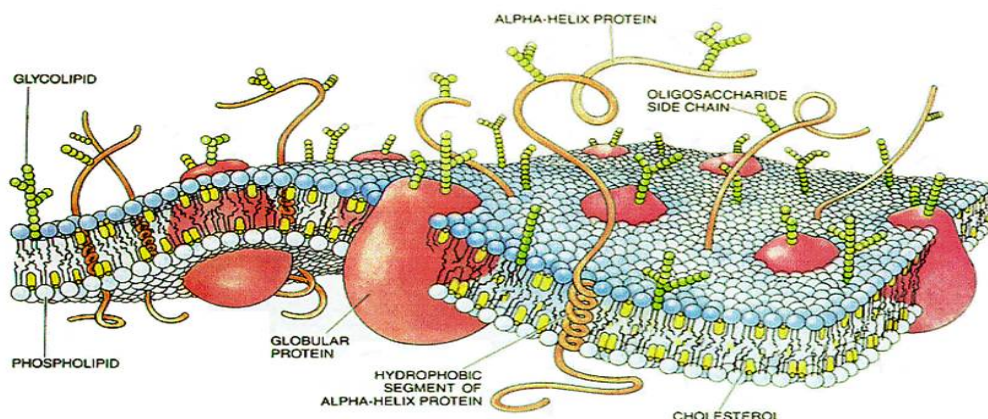
Figure 1.1: Cartoon of a bilayer membrane composed of phospholipids and membrane proteins (public image from NIST web page).

limitation of this technique [3, 17, 18]. The difficulty with membrane proteins, to great extent arises from the amphiphillic (both hydrophobic and hydrophillic character) character of these proteins, which is critical to their function within membranes. The lack of membrane protein structural data slows the development of those biotechnologies that would benefit from a more detailed understanding - for instance, drug therapies targeting the protein's specific chemical functionality. It is reasonable to expect that knowledge of the underlying phase behavior of the lipid assemblies that can incorporate membrane proteins is integral to understanding the molecular basis of different crystallization strategies, and thus their full exploitation.

Amphiphillic Hosts

To overcome issues due to the amphiphillic character of membrane proteins, different strategies have been proposed. They involve removing the protein from its native environment using an amphiphillic molecule as well as reconstituting it into a similar host. Evidently, a good model system has to match the packing requirements of the membrane protein. A list of several such hosts studied in the literature is included in Fig.1.2. Barring the cubic phase, the smaller assemblies, based on phospholipids and detergents have been found to be

3

useful in nuclear magnetic resonance (NMR) based structure elucidation techniques ([19], comprehensive review in [20]) without the need for crystallization.
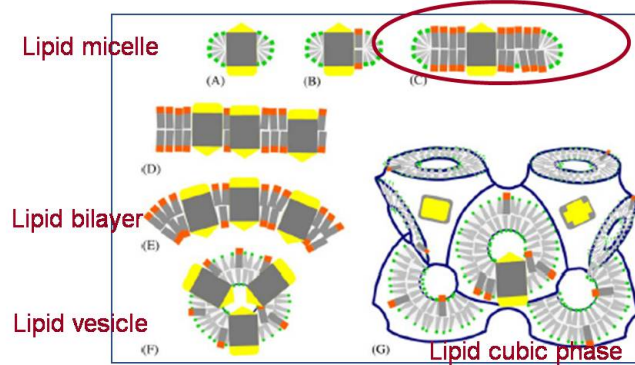
Figure 1.2: Various strategies for studying reconstituted membrane proteins (adapted from [21]).

The simplest model system is micelles composed of either detergents or small phospholipid molecules. This is based on the ability of detergents to solubilize and form mixed micelles of membrane lipids and proteins. But the high curvature induced by the micelles as well as the lack of a bilayer structure makes it a not-so-ideal membrane mimic. Unilamellar phospholipid vesicles, whose morphology is similar to that of biomembranes are the other widely used and studied alternative. Their tedious preparation and lack of stability has favored the use of liposomes or multilamellar vesicles (MLVs), which are more easily made. But both MLVs and ULVs have been found to be inadequate for high resolution NMR studies due to the inability to align them in magnetic fields in a controlled manner [20].

Bicelles as Amphiphillic Hosts

A biomimetic system comprised of phospholipid mixtures of long and short chain lipids has received considerable attention due to its unique combination of biocompatibility and of strong orientational properties in magnetic fields. This has led to their importance as alignable liquid crystalline media for nuclear magnetic resonance (NMR) based protein structure determination and studies of membrane associated peptides and proteins [20, 22]

in which applications they have largely replaced lipid based vesicles and detergent based micellar systems. More recently it was also demonstrated that the proton pump transmembrane protein bacteriorhodopsin [23, 24] could be crystallized from suspension in these lipid mixtures. These systems could therefore also play an important role in the production of the crystals needed for high resolution structure determination of membrane proteins. An understanding of the phase diagram of such lipid mixtures should therefore initially furnish a better background for interpretation of NMR results, but could in the future be crucial for systematically tailoring their properties to the goal of crystallizing specific membrane proteins.

1.1   Thesis Outline

The broad objectives of this dissertation are:

1. To understand the structural transitions in lipid mixtures underlying their interesting phase behavior through scattering techniques.

2. To understand lipid mixtures in a way that their properties can be engineered for studying different proteins.

In order to accomplish the above goals, mainly experimental research complimented by extensive modeling and analysis has been conducted in this dissertation. In the first part of the study, the low temperature assembly of the most well documented two component lipid mixture, DMPC/DHPC (Dimyristoyl (or C14), 14 Carbon double tailed and Dihexanoyl (or C6), 6 Carbon, double tailed phospholipids) has been undertaken. Taking full advantage of the information provided by small angle neutron scattering (SANS), the discoidal geometry with its inherent segregation hypothesis for the two lipids has been tested. Furthermore, aspects of lipid packing pertaining to structural changes with temperature have been explored. The role of the melting transition temperature of the long tail lipid and curvature of the short tail lipid in the observed phase behavior has been studied in

detail. In the second, universality of the ideas developed for DMPC/DHPC mixtures, when extended to other systems as a means to tailor the morphology for various biological applications has been studied. Extensive scattering experiments, with both neutrons and X-rays have been employed, aided by other measurements like Differential Scanning Calorimetry (DSC), and Densitometry.

Chapter 2, gives a brief background on the main themes of this work. Ideas of aggregation and self assembly based on Israelachvilli's work [25, 26, 27] and those on the hydrophobic effect by Tanford [28] and others on amphiphillic systems [29, 30] have been outlined briefly. Some of the same ideas can be extended to mixtures also, even though phase transitions in phospholipid mixtures involve much more complicated theories [13]. Background on the existing phase diagram of pure phospholipids followed by our current understanding of DMPC/DHPC (or C14/C6) mixtures is presented. Comparison with studies on related lipid-surfactant assemblies in the literature is undertaken in order to highlighting the context and specific questions answered in this work.

Chapter 3 is based on the experimental techniques used in this study. Key ideas of each technique are briefly reviewed and its instrumentation is described in some detail. As scattering techniques form the main part of this thesis, both neutron and X-ray small angle scattering (SANS and SAXS) techniques have been described in detail.

Following the scattering technique, the main theoretical ideas pertaining to scattering theory have been described in Chapter 4. A discussion on data analysis techniques which vary from simple to more involved techniques is also described. Their key aspects as well as strengths and limitations are reviewed.

Chapter 5 presents the research conducted in this thesis, in understanding assembly and segregation in the two component C14/C6 mixture at low temperatures. In Chapter 6, other mixtures showing similar phase transitions are explored and the lessons learnt from the C14/C6 assembly are applied. Finally, Chapter 7 explores structural and compositional changes with temperature in two mixtures, with significantly different self-assembly.

Chapter 2

Background

In this chapter, a background for understanding self-assembly in bio-mimetic systems consisting of phospholipids and their mixtures is presented. While most model membrane systems under investigation in the literature consist of one of the many bilayer forming phospholipids in naturally occurring membranes [9, 11, 12] or possibly mixtures of two bilayer forming lipids, mixtures of lipids with different self-aggregation properties, have been much less studied. Understanding the phase behavior of a mixed system would be difficult and incomplete without the knowledge of forces that drive self-assembly of the pure single component systems themselves. The following sections briefly describe the self-assembly in long-tailed and short-tailed phospholipids under aqueous conditions and finally in mixtures of the two.

2.1   Amphiphiles in solution

Phospholipids are a class of biological amphiphillic molecules, which have both a hydrophillic and a hydrophobic part. Since many amphiphillic molecules are commonly used as surfactants or detergents (for their ability to change interfacial properties), *detergents,*

surfactants and lipids are used interchangeably in this work, particularly in reference to small phospholipids). They are classified by the nature of their head groups as anionic, cationic, zwitterionic and nonionic. Zwitterionic amphiphiles have both a positive and a negative charge in their headgroup region. Many interesting properties arise as a result of their propensity to self-assemble in solution conditions in different geometries [30].

Amphiphiles are soluble in water as monomers to some extent and that limit depends strongly on the length of the hydrophobic tail, the type of headgroup and on the solution conditions. As their concentration in solution is increased, aggregates of the monomers, called micelles are formed at a certain well defined concentration. This concentration at which micelles first form is the critical micellar concentration (CMC). Above the CMC, a progression of equilibrium phases coexist in equilibrium with a CMC concentration of the monomers in the solution. For double-chain zwitterionic phospholipids, the CMC is very low ($\sim 10^{-10}$)M, whereas typical single chain surfactants have CMC ($\sim 10^{-4}$ - 10^{-1})M. The driving force behind lipid/surfactant aggregation is the *Hydrophobic effect*, which is driven by entropic effects arising from the connected hydrogen bonding structure of water [28, 27]. The hydrophobic effect on its own would favor complete phase separation of the lipid from water. The opposing force coming from the polar head groups hydrophillic nature, forces the system to aggregate such that all the head groups are in contact with water. Following the approach of Tanford and Israelachvilli, the formation of such aggregates of amphiphiles may be thought of as a reversible reaction between the individual monomers and various aggregates

$$nA \Leftrightarrow A_n$$
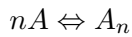
where A is a monomer and A_n is an aggregate consisting of n monomers. At equilibrium, the chemical potential of aggregates of different sizes, $n = (1, 2, 3...)$ is equal, so that

$$\mu_1^0 + k_B T \log(X_1) = \mu_2^0 + k_B T \log(X_2/2) = \cdots \mu_n^0 + k_B T \log(X_n/n) \qquad (2.1)$$

where μ_n^0 is the free energy for an aggregate with n monomers and X_n is the mole

8

fraction of the corresponding aggregate in solution. When the aggregates are very large, this equation reduces to

$$\mu_n^0 - \mu_1^0 = k_B T ln(CMC) \tag{2.2}$$

which relates the free energy of micellization to the CMC. It is the variation of μ_n^0 with n which dictates the aggregation behavior. A necessary condition for aggregates to be formed is that μ_n^0 decreases with increasing n. The functional form of μ_n^0 with n determines the physical properties of the aggregates, such as their mean size and polydispersity [27].

The micellar aggregates formed are an elegant way for the molecules to avoid contact between hydrophobic tails and water. However, several geometrical micellar morphologies like spherical, cylindrical and planar structures can be conceived, which will result in the formation of a micellar aggregate. Then the maximization of entropy dictates the formation of the smallest possible aggregate for a given volume and head group area.With increasing concentration, when the globular micelles can no longer pack, they form array of cylinders followed by lamellar phase [30]. These are general trends seen in any surfactant self-assembly. But for a given amphiphile, what drives the shape of the micellar aggregates formed is the geometry of the monomers themselves and the associated cost of bending a monolayer of the components. The concept of spontaneous curvature and bending energy which defines the local geometry of aggregates is described in the next section.

2.2 Spontaneous curvature and Packing Models

The self-assembly in amphiphiles as a result of 'opposing forces', hydrophobic effect of the tails, and geometrical packing constraints of the head groups [28], has been understood in terms of the Surfactant/Packing Parameter $p = V/al$ of the monomers, where V, a, l are the volume, head group area and tail length respectively of the amphiphillic molecule [27, 30]. For a single component system, simple geometrical relations give the following

9

limits on the packing parameter

$$V/al \quad < 1/3; \text{ globular micelles}$$

$$1/3 < \quad V/al \quad < 1/2; \text{ elongated micelles}$$

$$1/2 < \quad V/al \quad < 1; \text{ bilayers}$$

Within this description, the surfactant aggregate structure is completely determined by the relative sizes of hydrophobic chain and hydrophilic head group parts of the lipid or surfactant molecule. The head group area a is large for molecules with chemically large head groups or with charged head groups resulting in spherical or cylindrical structures. The tail volume is larger for longer hydrocarbons, particularly those with double tails, driving them to bilayer structures.

The packing parameter can be tuned, for instance by addition of salt, which screens electrostatic repulsion between the head groups, effectively reducing a and a progression of the different shapes is indeed observed in ionic amphiphiles [30].

The same progression can be observed by adding a surfactant S ($V/al = 1/3$) with small packing parameter to a lamellar phase of a double tailed lipid L ($V/al = 1$) if a complete mixing of the two components is a possibility. In this case the effective packing parameter is given by

$$\left(\frac{V}{al}\right)_{eff} = \frac{(1/3)X_S + 1(X_L)}{X_S + X_L} \quad \text{X}_S, \text{X}_L \text{ are mole fractions} \qquad (2.3)$$

Such progression of phases has been observed in many different systems of amphiphillic molecules [30]. A brief review of such studies on various lipid-detergent mixtures will be considered in a later section.

Most of the thermodynamic treatment of self assembly of amphiphillic molecules into micelles and mesophases is reduced to the form of μ_n^0 in Eqn. 2.1 in terms of the molecular interactions involved [27, 31, 32, 33]. From the considerations discussed in the previous section, the net effect of the hydrophobic attraction at the hydrocarbon-water

interface, which causes the molecules to aggregate and the hydrophilic repulsion of the head groups, which has the reverse effect, gives the following expression for the total free energy

$$\mu_n^0 = \gamma \cdot a + (C/a) \tag{2.4}$$

where γ is the effective interfacial tension of the water-hydrocarbon interface and C is a constant. Minimization of this free energy per molecule gives the optimal head group area at the interface. Such a description of amphiphillic aggregates in terms of packing parameter works well for closed interfaces ($V/al < 1$). However in general, it is not a sufficient condition to uniquely define the geometry of the interface [30]. It can be shown that the magnitude of the packing parameter fixes only the function of local curvatures given by

$$\frac{V}{al} = 1 - Hl + \frac{Kl^2}{3} \tag{2.5}$$

where H and K are the *Mean* $(C_1 + C_2)$ and *Gaussian Curvatures* $(C_1 C_2)$, respectively for the surface with two principals radii of curvatures $R_1^{-1} = C_1$ and $R_2^{-1} = C_2$. This gives for a sphere of radius R, (the mean and gaussian curvatures are 1/R and 1/R^2), when the chain length l is equal to the radius, packing parameter p of 1/3. Also Eqn. 2.5 shows that both the mean and gaussian curvatures can be varied cooperatively without altering the value of p. The packing parameter provides a *local* constraint upon the curvatures of the interface, while the overall geometry depends on the free energy minimum of the aggregate.

2.3 Bending energy

If a molecule has a preferred average geometry, then departures from it's preferred shape costs energy. An estimate of this energy can be gained by using a harmonic approximation. So that if $p = (V/al)_0$ is the preferred packing parameter, then deviations from

11

this value will incur a 'bending energy' cost given by Helfrich [5] as

$$f_{bend} = k \left(\frac{V}{al_0} - \frac{V}{al} \right)^2 \tag{2.6}$$

where $p = (V/al)$ is the actual packing parameter adopted by the molecule within the aggregate and k is a measure of its flexibility, a molecular analogue of the elastic modulus for the aggregate.

The general concept of bending energy, has been shown to be particularly suited to describing the properties of bilayer aggregates, like lamellaes, vesicles and sponge phases, for which the free energy per unit area can be expressed in terms of the mean and Gaussian curvatures (both scaled by the magnitude of tail length, l) of the interface [5] as

$$f = \frac{1}{2}\kappa \left(\frac{1}{R_1} + \frac{1}{R_2} - \frac{2}{r_0} \right)^2 + \bar{\kappa} \left(\frac{1}{R_1 R_2} \right) \tag{2.7}$$

where κ and $\bar{\kappa}$ are the elastic constants associated with the mean and gaussian curvatures, H and K respectively, in Eqn. 2.5.

The spontaneous curvature $1/r_0$, is non-zero only if there is asymmetry between the different sides of the bilayer. Trends in morphology can be predicted as a function of elastic constants and the spontaneous curvature. The energy required to bend a bilayer away from the spontaneous curvature is proportional to κ, while the energy of a saddle-splay deformation is proportional to $\bar{\kappa}$. The Gaussian contribution is identically zero for lamellar phase, while it's contribution is $4\pi\bar{\kappa}$ for closed vesicles [30]. Theoretically, if $-2\kappa < \bar{\kappa} < 0$ (assuming κ positive), the membrane prefers to be in lamellar phase while for $\bar{\kappa} < \kappa$, the membrane prefers to curve into spherical shape. Thus $\bar{\kappa}$ plays a central role in guiding topological transformations, but has no effect as long as the curvature fluctuations take place at constant topology [30].

2.4 Phospholipids

Phospholipids are amphiphillic molecules that consist of two non-polar acyl chains (tail) which are connected via an ester bond to an alcohol containing phosphate head group as shown in Fig. 2.1. A whole range of phospholipids with head groups made up of different alcohols and tails of different acyl-length are known to exist in nature [34, 35]. Their nomenclature is based on the number of carbons in the acyl-chain, the degree of saturation of the chains and the type of alcohol attached to the phosphate group. Thus lipids with a choline alcohol are called phosphatidylcholine (PCs) while those with a glycerol are called phosphatidylglycerol (PGs). Table 3.1 and Figure 3.1 in Chapter 3 (the Materials section), list all the phospholipids relevant to this work, with their systematic and short names used in this thesis. Under physiological conditions, the phosphate group carries a net negative charge, so that the cholines with a positively charged amine group in phosphatidylcholine lipids are zwitterionic, while phosphatidylglycerols, with no positive charge in the alcohol group, are left with a net charge (neutralized by external salt) [35]. The polar nature of the head groups makes them hydrophilic.

The acyl-chains vary in length and saturation of their carbon-chains. In this work we will be mainly concerned with saturated chains. For reasons explained in the next two section, lipids with chain lengths between 12-20 carbon atoms are as a group considered **Long-tail lipids**, while lipids with tail length of 5-9 carbon atoms are considered **Short-tail lipids**. Tail length of the lipids mainly governs the type of self-assembled structure, while the head group has lesser influence. Table 2.1 lists their properties under aqueous conditions. In general, the maximum tail length (l in Å) of the acyl chains and volume of the tails (V in Å^3) have been known to have the following linear dependence [28] on the number of carbon atoms N (true for any hydrocarbon or surfactant in general)

$$l_c = 0.1265 * (N - 1) + 0.15$$

$$V_c = 2 * (27.4 + 26.9 * N)$$
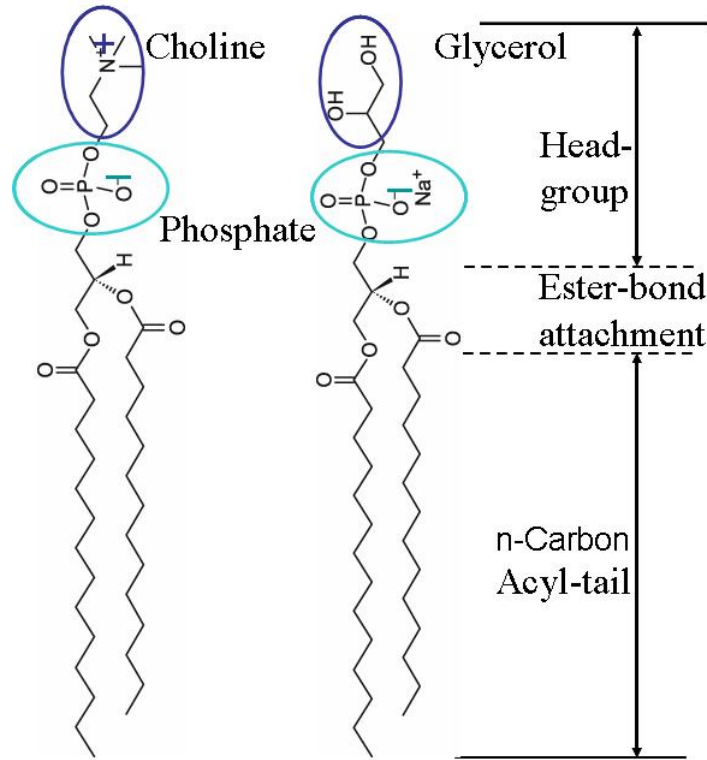
Figure 2.1: Schematic of the chemical structure of two phospholipids: Phosphatidylcholine on the left and phosphatidylglycerol on the right. The n-carbon acyl-tail, ester bond attachment and the head groups with phosphates attached to the respective alcohols are marked.

where the factor of two accounts for the double tailed phospholipids in this study. The size and volume of the head groups depends on the chemical structure (zwitterionic or charged) and the solvent (polar or nonpolar). Lipid (molecular) volumes and head group areas used in this study are based on their measurements in bilayers by Nagle and coworkers ([11] and associated papers). Head group areas in the literature have been assumed to be constant at $\approx$62-66 Å^2 [35]. However, significant deviations in smaller lipids, which do not form bilayers are known to occur where head group areas have been reported to be > 100 Å^2 [36]. As a result, when using head group areas from the literature, particularly in the case of smaller phospholipids, the accuracy issue has to be kept in mind.

Table 2.1: Physical properties of aqueous dispersions of double chain phospholipids used in this study. For completeness, two non-lipidic detergents used in this study are also included.

Name (Carbons)	CMC (mM)	Aggregation No.	Geometry [†] Dimensions(Å)	Chain Melting T_m (in °C)
Phospholipids				
DHPC (6)	14 (24°C)	19	Prolate Ellipsoid a=7.8 b=24	-NA-
DHpPC(7)	1.4(30°C)	27*	Rodlike/Ellip X-section a=9.1 b=9.7	-NA-
DOPC (8)	0.3(30°C)		Rodlike	-NA-
DTPC (13)		-	Bilayers	14.0
DMPC (14)	1.4×10^{-6}	-	Bilayers * $2D_c$=30.3(10°C), 25.4(30°C)	24.3
DPPC (15)		-	Bilayers	33.0
DPPC (16)	0.5×10^{-6}	-	Bilayers $2D_c$=34.4(30°C),29.2(50°C)	41.6
Triton	0.32	143(24°C)	Oblate ellipsoid a=35 b=10[†]	-NA-
Chapso	8	10(24°C)	Prolate ellipsoid a=31.0 b=10.5	-NA-

[†] For micellar aggregates, only inner hydrophobic core dimensions are included; head groups vary ~4-10 Å

[⋆] $2D_c$: inner hydrocarbon thickness

[*] Size and aggregation number varies with concentration, this is for minimum sized micelle
   Geometrical parameters on C6 from [11, 38, 39], on C7 from [37]
   Data on C14 from [11, 38, 39], C16 and others are from [11, 40, 41]
   Chapso from [42, 43] and Triton [44].

2.4.1 Self-Assembly/Polymorphism in Long-tail Lipids

Long-tail phospholipids (12-20 Carbons) are of fundamental importance to biology. Model membrane systems consisting of a such lipids form a variety of interesting structures like, lamellae, cubic, hexagonal, 'rippled' bilayers, etc. under various aqueous conditions. They have been the focus of numerous experimental [45, 46, 47, 48, 49, 50, 51, 52] and theoretical [5, 7, 9, 53] works. The very low CMC of these double tailed phospholipids is attributed to a larger hydrophobic-hydrophillic ratio of the tail and head group parts of the molecule compared to the single tail surfactants. Structural changes can be seen as a function of variety of conditions such as pH, ionic strength, lipid concentration, pressure, and temperature. In this thesis, we are concerned mainly with lipids in excess water conditions with all other variables except temperature being constant. Even the change of a single variable, the temperature results in a sequence of microscopic phase changes in the lipid tail ordering, known as gel, rippled, and fluid phases in phosphatidylcholine(PC) lipid membranes [35]. The microscopic changes in lipid tail order, have to be differentiated from macroscopic phase transitions resulting in structural changes. Under certain conditions of hydration, some lipids have also been known to form bicontinuous cubic phase [9] instead of bilayers. Much of the polymorphism of these phospholipids can be explained by changes in packing parameter as a result of changes in the tail volume due to temperature.

Aqueous dispersions of phospholipids with acyl tail length > 12 carbon atoms, self-assemble into multilamellar structures at $\leq 0.001\%$ of lipid in water. In those macroscopic aggregates, all of the CH-CH bonds in the alkyl chains are saturated and can have an ordered all-trans conformation or a disordered, with -trans and -gauche conformations. This leads to the existence of a chain freezing transition. It has been shown to be a first-order transition in a seminal study using a two-dimensional lattice model by Nagle [53]. Then with increasing temperature, the typical sequence of phase transitions for chain order is gel $L_{\beta'}$, ripple $P_{\beta'}$ and the disordered 'fluid' L_{α} phase above the transition temperature as shown in Fig. 2.2. Typical of most long tail phospholipids, it shows phase changes in a

2% DMPC or C14 lipid with D_2O as solvent, obtained in this work using DSC (differential scanning calorimetry) and densitometry (details of the two methods are given in Chapter 3) to confirm the T_m of the lipids used.

As shown in Fig. 2.2, the 'fluid' L_α phase, above 24.3°C has no long range order within the layers and consists of hydrocarbon chains in a 'melted' state with positional disorder of the molecules in the bilayer plane. While on lowering the temperature, in the gel phase the acyl-chains freeze and the molecules are arranged on periodic 2-D lattices [45, 48]. In the intermediate ripple phase ($\approx$ 15-16°C for C14) [48, 51], the bilayer is characterized by periodic corrugations of the bilayer with the chains being mostly in the ordered phase. The temperature corresponding to this transition is referred to as the *Pre-transition* temperature or $preT_m$ and is also marked in Fig.2.2. The melting temperatures of long-tailed lipids used in this work are included in Table 2.1.
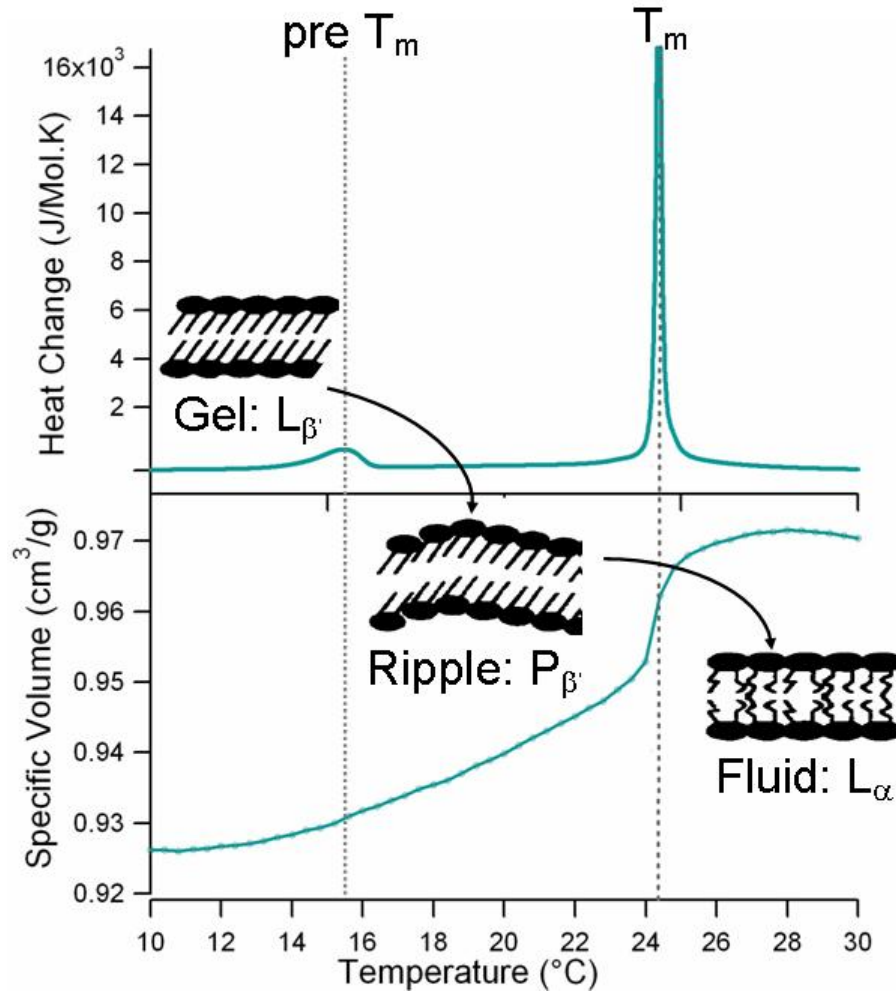
Figure 2.2: . Representative phase diagram of a bilayer forming phospholipid. Phase transitions are indicated by peaks in heat capacity profile and sharp changes in specific volume of the lipid. Data on heat capacity changes obtained by calorimetry (DSC) and specific volume changes obtained by densitometry (details of techniques are in Chapter 3) of pure DMPC/(C14) dispersion (consisting of MLV's) in D_2O are from this work. Chain configurations in the three phases are shown. In D_2O , pre T_m of 15.4°C and T_m of 24.3°C are also indicated.

Besides scattering techniques which have elucidated the chain packing details (listed above) T_m in phospholipids has also been characterized extensively using techniques like DSC [47, 54] and densitometry [54, 55, 56, 57, 58]. The melting transition is now understood to be accompanied by changes in enthalpy (20-40 kJ/mol), volume (about 4%), and area (about 25%) [54]. As shown in Fig.2.2, the sharp changes in volume and heat capacity are related and Heimburg et al. have recently argued that this leads to a simple relation between heat capacity and isothermal volume compressibility [54]. In fact, they have used this proportionality to obtain the elastic constants of lipid bilayers formed of C16 .

The phase state of the lipid has been known to affect the mechanical properties of the bilayer [8, 35]. Hence a quantitative measure of the bending modulus in different phase states of lipids is a critical problem in understanding the correlated mechanical and thermodynamics aspects of membranes. A number of experimental studies which include scattering techniques [38], micropipette methods [59], optical dynamometry [60] and all-optical methods [61] have been employed in characterizing the bending rigidity of lipid bilayers. Even though the elastic constants in the fluid phase have been known for sometime (see [35] for a review), their measurements encompassing the whole temperature range between $\text{pre}T_m$ to T_m has been much more recent [60, 61]. Fig. 2.3 shows temperature variations of κ obtained on DMPC(C14) and DPPC(C16) lipids from these studies both of which show non-linear dependence on temperature.

Fig. 2.3 shows that the rigidity of the bilayers $>$ a few $100 k_B T$ in the gel phase at low temperatures, decreases by an order of magnitude below T_m . Chain melting, results in softening of the bilayer and as we show later in this work, has important implications for lipid mixtures.

One Component Bilayers and Model Vesicles

For a single lipid dispersion in water, at sufficiently high concentrations, two dimensional bilayer sheets are the stable aggregates. The thickness of the bilayer, which is

(a)   (b)
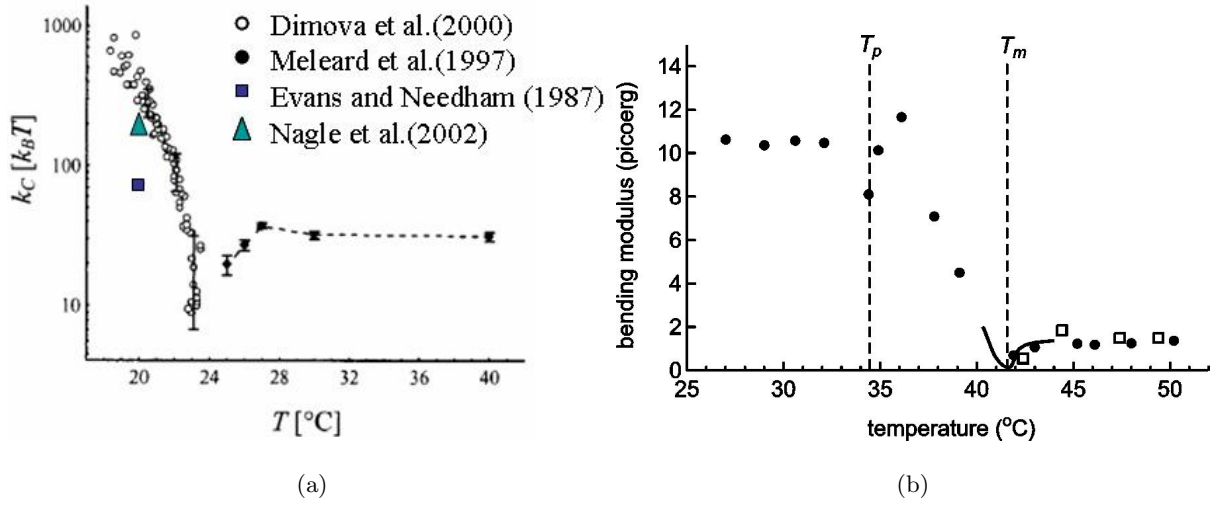
Figure 2.3: Bending modulus as a function of temperature of (a) DMPC(C14) membranes adapted from [60] and (b) DPPC(C16) membranes (reprinted figure with permission from [61]). Both the lipids have similar temperature dependence besides the shift in the transition temperature. Conversion between the two scales is 10 picoerg$\simeq$240k$_B$T .

$\sim$44-50Å for DMPC(C14) lipids, changes by $\sim$ 1.5 Å per carbon atom based on Eqn. 2.8 and the membranes extend for many microns. The edges of the sheets expose the hydrocarbon chains to water and increase its energy. As a result, the bilayers can fold to form unilamellar vesicles (ULV) relatively easily when provided ultrasonic energy by a process called *Sonication* or by extrusion through membrane pores, eliminating the edge energy. The external energy is needed to incur the bending energy cost for the bilayer, against the energy decrease from edge elimination along with the gain in translational entropy (arising from an infinite lamellar sheet going to smaller vesicular system).

Even when formed, vesicles formed from single component phospholipids are generally not stable [29]. Sheet like aggregates are more stable because of the symmetric bilayer which has no curvature preference. However, this situation can be changed dramatically by adding a second component [62]. The presence of another surfactant species can stabilize a phase of large disks, as we show see in section 2.5.

We now consider different effects on the melting transition temperature T$_m$ in

20

such one component lipid mimetic systems before considering their effect on lipid mixtures in Chapters 5-7.

Effect of D_2O on T_m

Deuteration of one component of a system is generally known to have significant effects on its thermodynamic and structural properties [63]. Higgins textbook describes the effect on polymeric systems. In micellar systems, a small difference in hydrophobic effect of H_2O and D_2O has been seen to affect SDS micelle sizes [64]. In phospholipid systems, Nagle and coworkers were one of the earliest to study the partitioning of deuterated solvent between interlamellar and bulk volumes of lipid bilayers. Similar conclusions have also been reached in another recent study on thermodynamic quantities associated with phase transitions in phosphatidylcholine lipids [65]. The main conclusions from these studies on lipid dispersions (MLV) that will be relevant for this study are:

1. Replacement of H_2O by D_2O does not affect the specific volume of the lipid.

2. The interbilayer solvent equilibrates faster than the time scale of measurements.

3. Transition temperature T_m was found to increase by 0.4 degrees in D_2O and an increase in enthalpy of transition of a few kJ/mol for DPPC.

4. Pretransition temperature, $preT_m$ increased by 1.2°C with no change in enthalpy.

Fig. 2.4 shows data taken in this study, from densitometry on DMPC(C14) lipids under different solvent conditions D_2O , H_2O and H_2O with salt, confirming prior results. As we show in the next two chapters, for SANS measurements on lipids, D_2O is the solvent of choice. So from Fig. 2.4, we can safely infer that deuteration effect of solvent has less than a degree effect on the T_m of C14 lipids.

Negligible difference in T_m , but measurable difference in transition enthalpy arise from the difference of interfacial-free energy per molecule in the bilayer in both solvents. These differences are essentially due to the difference in bond strength between deuterium and hydrogen bonds at the bilayer interface [65].
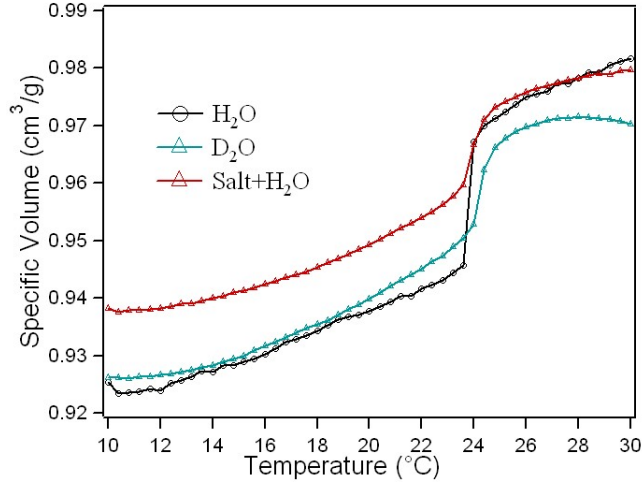
Figure 2.4: Density variation of DMPC lipids measured under different solvent conditions, showing minor effects of solvent on the transition temperature T_m .

Effect of d-Lipid on T_m

The effect of deuteration of the double-tails on the T_m of long-tailed lipids has been considered by Knoll and coworkers in a pioneering study of aqueous lipid dispersions using SANS [66]. For DMPC with deuterated chains only, T_m was found to decrease to $17°C$, while the T_m of a 1:1 mixture was found to be the arithmetic mean of the two T_m 's. In our studies, we have used DMPC which is deuterated in both the headgroup and tails, except for the hydrogens on the ester bond attachments of the tail and headgroup. The T_m of this lipid is $20.2°C$ as obtained by DSC. The data in Fig.2.5 is from a mixture of two separately prepared hydrogenated and deuterated lipid dispersions. The two lipids did not mix and consequently showed two melting peaks, for deuterated lipid at $20.2°C$ and for the regular lipid at $24.3°C$ (the second peak at $24.3°C$ has been subtracted for clarity). Subsequently we verified that a premixed lipid dispersion of the two components showed only one T_m peak at $22.3°C$, approximately at the average of the hydrogenated and deuterated cases (data not shown) in confirmation with Knoll's study. For this study, the shift in T_m has to be accounted for in considering lipid mixtures with deuterated species.

22
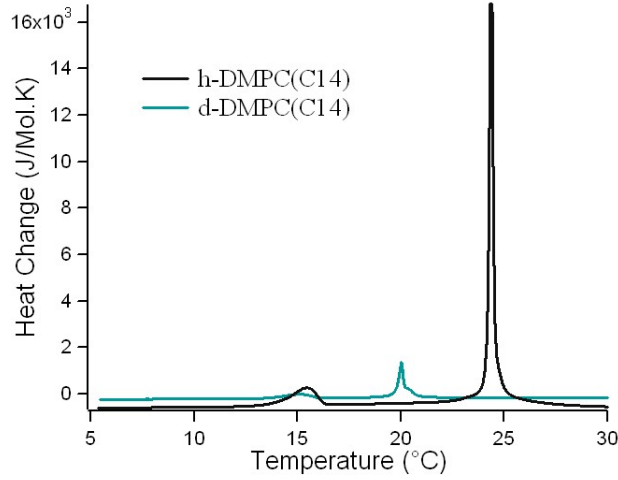
Figure 2.5: Heat capacity changes in pure single lipid dispersions of hydrogenated DMPC and in a mixture obtained by mixing individually prepared hydrogenated and deuterated lipid dispersions from this study.

Size and Curvature Effects on T_m

Current understanding of long range aggregation behavior of phospholipids is based on Nagle's statistical theory for order-disorder transition of the gel to fluid or disordered chain melting process [55, 53] and extensions of his theory. Such models however, assume an infinite system size and work well for MLV containing systems. But other mimetic systems, the 'bicelle' system in particular, are finite in size and composed of single bilayer instead of multi layers. Size effects and preparation techniques have been shown to have a significant effect on the T_m of phospholipids, resulting in broadening and splitting on the melting peak [58, 54, 67, 68, 69]. Fig. 2.6(a) shows the effect on T_m in vesicles of DPPC or C16 lipids in MLV vs ULVs of different sizes prepared by two different techniques, sonication and extrusion. The melting peak in a MLV system is considerably stronger than in the ULVs and there are smaller differences between the ULVs prepared by different techniques. While Fig. 2.6(b) shows the effect of system size on DMPC(C14) dispersions from the work of Heimburg [58, 54], showing splitting of the peak as a result of lipids confined to two different curvatures in the inner and outer part of the bilayer. Ema and coworker's data

23

shown similar peak splits in C12, C13, C14and C15 ULVs, and not in C16 lipids, though they ignore the second peak. Experimental results as well as their theoretical considerations show that finite size or curvature effects can have pronounced effect on the melting transition, though their model predicts only broadening with increased curvature [67, 68]. Phase behavior of long tail lipids clearly depends on the preparation technique and on the size of the bilayer system. In Chapters 7, we will present some consequences of this effect in our lipidic mixtures.

(a)   (b)
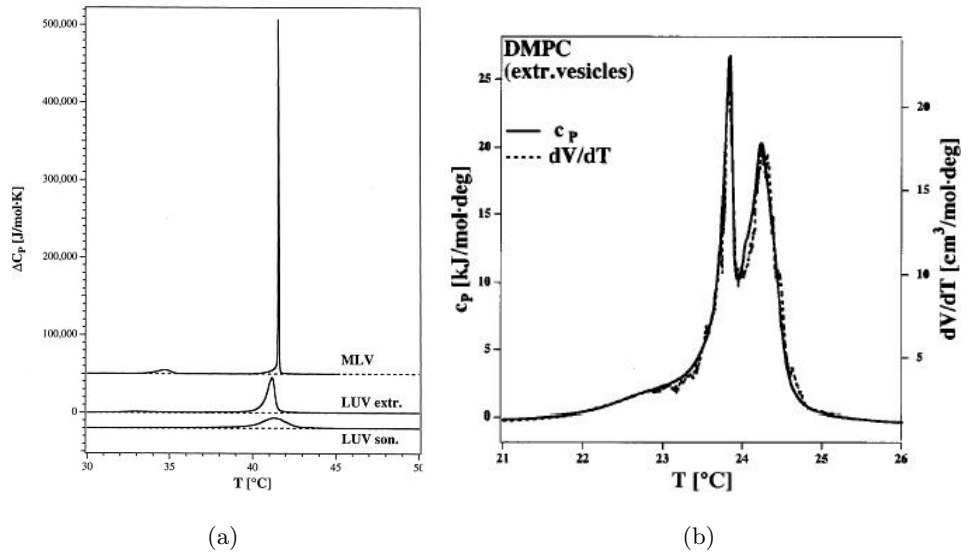
Figure 2.6:   (a) Effect of interactions between bilayers in an MLV system compared to ULVs, and their preparation technique on T_m in DPPC(C16) dispersions. (b) Heat capacity changes in pure DMPC(C14) dispersions of extruded vesicles showing effect of curvature resulting in splitting of the main peak (with permission from [54, 58]).

2.4.2   Self-Assembly in Short-tail lipids

Short chain phospholipids (five-nine carbon chain tails) have been known as useful synthetic lecithins (general term used for lipid membranes). Unlike their longer chain analogues ($\geq$12 carbons per fatty acyl chain), the short chain phospholipids form micelles whose average size depends on the fatty acid chain lengths [28]. Micellar properties of the

small phospholipids used in this study are included in Table 2.1.

The micellar structure formed by C6, C7 and C8 lipids have been studied in detail by Tausk and coworkers, using light scattering and surface-tension techniques [70, 71, 72] and more recently using NMR techniques by Tamm and coworkers [73]. However, their structure and chain packing details could only be obtained by scattering techniques in later studies. C6 micelle sructure has been elucidated in detailed SANS (small angle neutron scattering, the focus of this work) studies by Lin and co workers [36, 37]. More recently, vanDam et al. have shown that the micellar properties of C6 lipids do not change between 15-45°C [74]. A much more recent and comprehensive X-ray scattering study on different classes of detergent, including C6 (and CHAPSO, see next section) has shown that non-spherical or ellipsoidal geometries can explain the micellar structure of different detergents, if their monomer units can be described by a tail and a head group region of different densities [43].

As C6 lipids form the reference among the short lipids/detergents in this study (Chapters 5 and 6), we did SANS measurement to confirm the structure (taken before the publication of [43]). Fig. 2.7 shows SANS data from 0.01 g/ml (or 22mM) of DHPC(C6) in D_2O taken as part of this study. As most of this work is based on SANS techniques, an introduction to the theoretical basis of the method and data analysis techniques is included in Chapters 3 and 4. Guinier analysis of the data gives a radius of gyration of 12.75±0.16 Å which gives a sphere of radius 16.5 Å or an ellipsoid of half axes a=7 Å and b=26.8 Å (the smaller half axes was constrained to the maximum chain length of a 6-carbon acyl chain). Model of poly disperse spheres of radius (15±0.02) Å and polydispersity of 0.2 given by Schulz distribution was found to capture the data very well, except at high scattering vectors (small length scales), where the difference in SLD of the lipids head groups and tail makes the uniform sphere a bad approximation. Good fits over the entire wave-vector were obtained with model prolate ellipsoids of minor and major axes 13.5 and 28.0 Å respectively and only slightly better fits with core-shell ellipsoids of revolution, with inner half axes a=7Å

and b=24Å and outer half axes a=13.8Å and b=31Å. The shape and dimensions obtained, agree well with the detailed contrast matching study by Lin-Chen and coworkers, except for the non-uniform shell (head group thickness varied from 6 and 10 Å in the a and b regions of prolate ellipsoid model) in their study [36], and are within a few Å of that obtained by Lipfert and coworkers [43], likely due to different scattering contrasts with neutrons and X-rays.
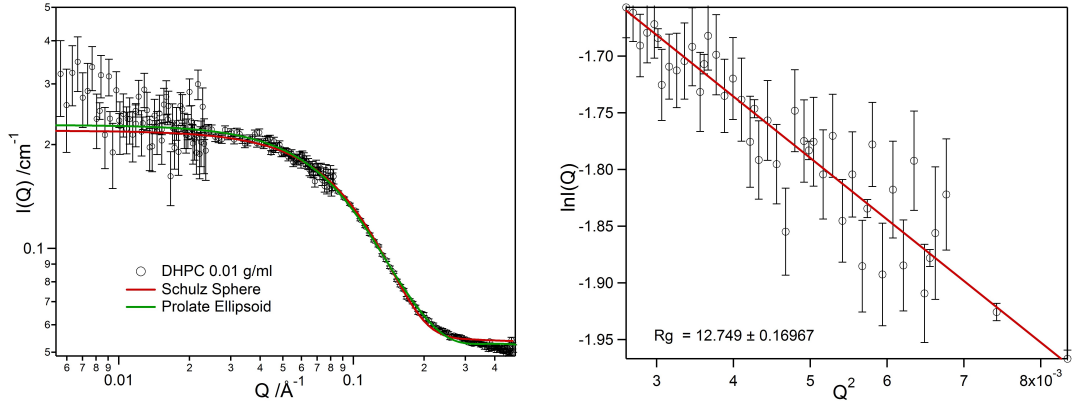
Figure 2.7: (a) Scattering from 0.01 g/ml of DHPC (C6) micelles in D_2O taken as part of this work. Fits using two models- Spheres of radius R= 15 Å with Schulz distribution of polydispersity of 0.02 and Prolate ellipsoids with a=13.7 Å and b=26.8 Å. (b) Guinier fits showing radius of gyration of 12.75±0.16 Å.

Effect of Salt on Short-tail lipids

Tausk and coworkers studied the effect of salt on CMC of 6-8 carbon chain long phospholipids, showing 40-50% decrease in CMC, with addition of 1M of NaCl. Our studies were conducted at 0.2M salt, where the change in CMC is expected to be small. From SANS data taken in this study, the micelle dimensions in salt solution were found to be slightly smaller, within an 1-2 Å of the pure solvent case for C6 micelles. The radius of gyration in this case is only 11.27±0.15Å giving a sphere of radius 14.6Å or ellipsoids of half axes a=7Å and b=23.2Å. Fig. 2.8 shows the scattering data taken by us and fits obtained

in this case.
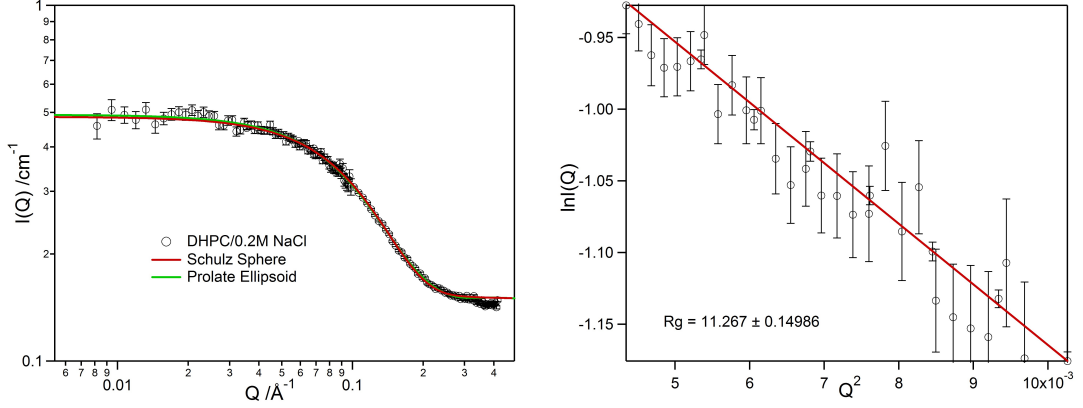
Figure 2.8: (a) Scattering from 0.01 g/ml of DHPC in 0.2M NaCl in D_2O. Fits obtained using two models, Spheres of radius R= 14.1Å with Schulz distribution of polydispersity of 0.023 and Prolate ellipsoids with a=13.5 Å and b=28.0 Å. (b) Guinier fit showing radius of gyration of 11.27±0.15 Å.

2.4.3 Other Detergents

Besides the micelle forming small phospholipids, two other commonly used detergents in membrane protein research, Chapso and Triton (Triton X-100) have been used in this study (see Fig. 3.1 and Table 3.1 for details of chemistry), in Chapter 6. Their micellar properties, listed in Table 2.1 at 10°C are summarized from recent work [43, 42]. Despite decades of study on their aggregation behavior and physio-chemical properties [75, 76, 44], a detailed structural understanding has emerged mostly from scattering studies [44, 43]. Based on the few X-ray scattering studies available on these two detergents, the micellar structures have been found to be consistent with non-spherical micelles. SANS data taken for this study on Chapso (0.01 g/ml, ∼ 16mM) showed prolate ellipsoids of minor and major axes 10.6 and 29.0 Å respectively in agreement with the recent SAXS study [43].

2.5   Self-Assembly in Binary Mixtures

Besides model membrane studies on one component phospholipids in Section 2.4.1, studies of model membranes of lipid mixtures has also been an active research field for the last several decades ([14, 77] and references therein). Mixtures of two bilayer forming phospholipids (that have similar spontaneous curvatures; see Section 2.4.1), has been vigorously pursued using various experimental, theoretical and modeling techniques in the context of domain formation (see for e.g. [78, 79, 80] and [14] for a review and cited references). In the presence of a second component, the local bilayer composition may be distributed in a non-symmetric way and thus the local spontaneous curvature would be non-zero [13, 62]. The implication is that stable (or meta stable, still under debate in the literature [81]) two component vesicles (liposomes) exist leading to their wide applicability in drug delivery [4, 77].

The phase diagram (state of the lipid chains) of such binary bilayer forming phospholipids (like in Section 2.4.1), both of which have melting temperatures T_m , and consequently similar spontaneous curvatures, show typical two component phase diagrams like those of solids [82, 83] with regions of coexistence and single phase regions of fluid and frozen (or solid) lipid chains. Direct and detailed information on lipid domains and understanding of their shape transformations remains a challenging research field [3, 10]. Such two component vesicle phase are not the focus of this work, though they do appear in parts of the phase diagram considered in this work.

In this work instead, we focus on mixtures where the two components have very different spontaneous curvatures. The 'bicelle' system, is a two component mixture of a long and short phospholipid. The idea of a bilayered discoidal morphology, led to their being called the *BICELLE* for 'BIlayered miCELLE'. As we show later in this section, this name has been used in the literature for mixed micellar morphologies that are not even discoids. But we will use the term in reference to the mixtures of lipids that form discoids in a range

28

of temperature-composition phase diagram and *bicelle mixtures* but with no reference to their morphology.

2.5.1 Bicelle Mixtures

The bicelle mixtures have been recognized as potentially important magnetically-alignable substrates for solid-state Nuclear Magnetic resonance(NMR) and neutron scattering studies of membrane associated peptides and proteins (see reviews [20, 22] and their cited references). The interest in the magnetic alignability of such phospholipid mixtures stems from the possibility of using techniques like ^{31}P and ^{2}H- NMR to decipher the local packing and molecular orientation properties of membrane proteins within the aligned assembly [84]. ^{2}H labeling of the lipid acyl chains is used to study structure and interactions in the hydrophobic part of the membrane. While measurement of chemical shifts with phosphorous labeling, where in the line shape of the 100% naturally abundant ^{31}P signal indicates the environment of the phosphorous molecule in the lipid head group, has been used to infer the interactions with in the bilayer polar region. Additionally, the aligned bicelles have been shown to provide a slightly ordered solvent to nonspherical soluble macromolecules, which gives rise to unaveraged, or residual, internuclear dipolar couplings, aiding in their structure determination [19, 85].

The presumed structure of such mixtures, composed of a long-tail and a short-tail phospholipid is discoidal, dependent on the molar ratio $q = [Long]/[Short]$ as shown in Fig. 2.9, with the shorter tail lipids forming the high curvature rim around the bilayer core forming long lipids. In such an assembly, two lipids presumably preserve their individual spontaneous curvatures locally. This picture of a discoidal 'bicelle' should be taken with a note, in that it is not the only possible aggregate geometry that would preserve the individual curvature preferences of the two lipids, as we show in this work. Without the proteins, the same techniques just used for the bicelle mixtures, provide information on the morphology of the aligned phase [86, 87, 88, 89]. The appearance of more than one ^{31}P

chemical shift, has been taken as an indication of segregation of the two lipids in the aligned aggregate.
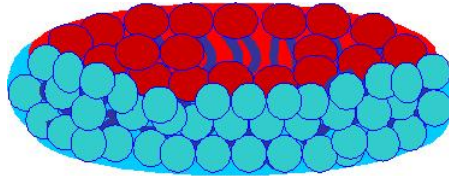
Figure 2.9: Cartoon of the presumed 'bicelle' structure composed of a bilayer forming *long lipid* (red) in the core and a micelle forming *short lipid* (blue) in the edge or rim. Head groups of the two lipids are the same, only the tail length and consequently the spontaneous curvatures of the two species differ. They are colored differently to highlight the packing.

In magnetic fields B_0 greater than 1 Tesla, the aggregate structures formed by the two lipids have been found to orient perpendicular to the magnetic field, typically above the T_m of the lipid at around 30-50°C in mixtures with molar ratio of the two lipids q above 2.3:1 and lipid concentrations 3-40% w/v [87, 85, 88]. An understanding of the field induced alignment in the 'bicelle' mixtures goes back to the measurement of diamagnetic anisotropy of bilayers in the late 70's to early 80's. The orientation in magnetic field has been explained by the anisotropy of the magnetic susceptibility χ, of the phospholipid acyl chains [90, 91]. The anisotropy is the difference between the magnetic susceptibilities parallel $(\chi_{||})$ and perpendicular $(\chi_\perp)$ to the axis of the molecule

$$\Delta_\chi = \chi_{||} - \chi_\perp$$

When $\Delta_\chi < 0$, there is energetically favorable orientation of the molecules perpendicular to the direction of B_0. In the earliest works, such orientation was shown in the case of *non-spherical vesicles* made from DMPC (C14) and also egg-lecithins (phospholipid with unsaturated tails) by Helfrich and coworkers [90, 91], with values χ of (-0.28 to -9)$\times 10^{-8}$ erg.cm^{-3}G^{-2} at 22-23°C . Negative χ makes the lipid molecules and their aggregated states diamagnetic. When the lipid tails are packed parallel in an ordered structure, the energy gain due to orientation of the bilayer is *proportional to the number, N of lipid molecules* as

also the angular difference β, between orientation of the molecular axis and the magnetic field axis.

$$E(\beta) = \frac{1}{2}N\Delta_\chi(\bar{n} \cdot \bar{B})^2 = \frac{1}{2}N\Delta_\chi \cos^2 \beta$$

In case of the bicelle mixtures, the same effect has been used to explain the alignment of the aggregates, thought to be discoids, wherein the long lipid chains are packed in an ordered bilayer structure and there is energy gain due to it's orientation perpendicular to the field [91, 20]. The critical role played by N, however, makes the size of the aggregate structure an important parameter in its alignment in a magnetic field.

Such mixtures were first studied by Gabriel and Roberts using NMR techniques [92, 93, 94]. Initially they showed that unilamellar vesicles(ULV) could form spontaneously by mixing aqueous suspensions of long-chain ($\geq$14) lipids with small quantities of their short-chain analogues (6-8 Carbon). Though their later studies suggested that novel arrangement of the two lipids, forming discoidal aggregates resulted when the molar ratio of the two $q = [Long]/[Short]$ was equal to four, in mixtures of C16 and C7 lipids [95]. We note here that the notation used for the molar ratio q is not to be confused with wave vector Q used in scattering (Chapters 3 and 4).

Later Sanders et. al. showed the magnetically orientable nature of mixtures of bile-salts (biological detergents derived from cholesterol found in the liver) and phospholipids and also of phospholipids and CHAPSO (a detergent, motivated by it's mild nature) [86]. This work led to the use of DMPC (C14) and DHPC(C6) based mixtures by Sanders and a few other research groups as substrates for membrane proteins that can be inserted into the phospholipid bilayer [87, 96, 89, 97, 98, 85, 99, 100]. Furthermore, at around the same time, characterization studies by Vold and coworkers led them to the **Ideal Bicelle Model (IBM)**, proposing a dependence of the bicelle size on the molar ratio q and assuming a complete segregation of the two lipid species [89, 97]. The IBM emerged as a quantitative model for explaining the variation in bicelle sizes [74, 99, 101, 102, 103].
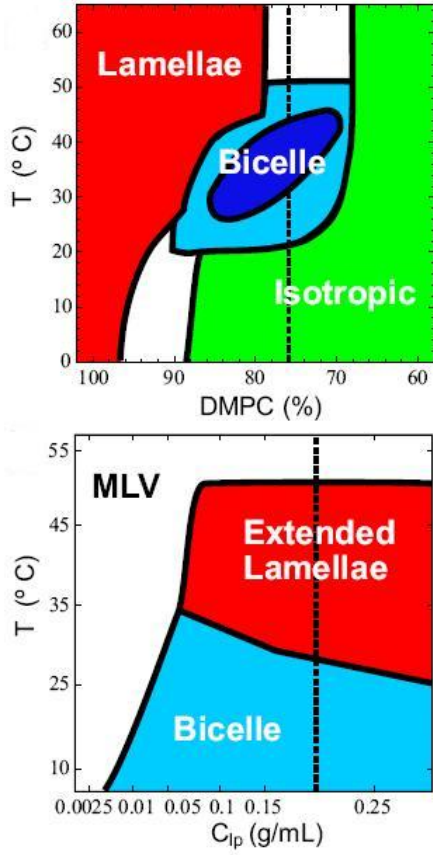
(a) *Top*: Phase diagram of Raffard et. al. [88] obtained by ^{31}P NMR, identifying the alignable 'bicelle' and non-alignable Isotropic phase and *Bottom*: Nieh et. al.'s phase diagram from SANS [104]. Same compositions are indicated by dashed line on the two graphs.
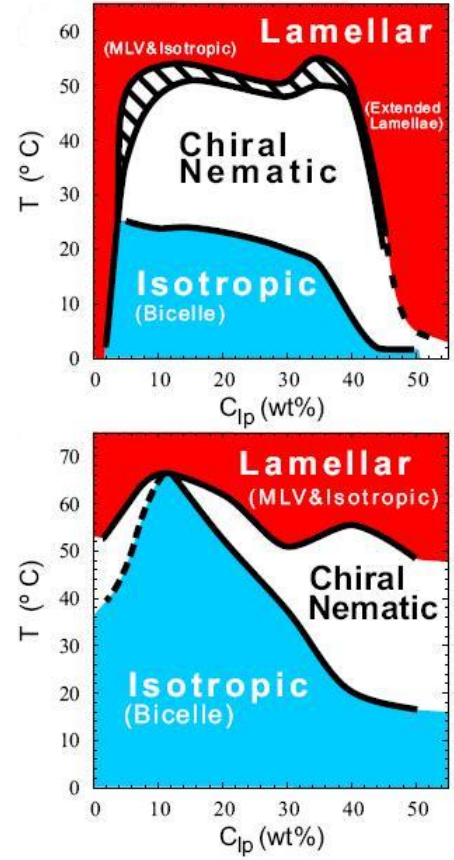
(b) Phase diagram of Nieh et. al. [105] using SANS for two different q values, *Top* $q = 3.2$ and *Bottom* $q = 2$ showing regions of discoidal and other morphologies as a function of total lipid concentration.

Figure 2.10: Phase diagram comparing Raffard and Nieh's studies in 2.10a and recent most phase diagram proposed by Nieh et.al. at two different q values in 2.10b

Raffard et. al. proposed the first temperature-lipid composition phase diagram of bicellar mixtures [88]. Using ^{2}H and ^{31}P solid state NMR their phase diagram showed changes in DMPC/DHPC organization as a function of temperature. As shown in Fig. 2.10a, for 20 wt% lipid mixtures and over a range of temperatures (T = 25 - 45 °C), they showed that bicelles existed in a range of molar ratios $q = [DMPC]/[DHPC]$ of 2.6-6.7. Their study also showed the temperature range where 'Bicelles', meaning aligned aggregates were observed. Besides bicelles, their study also identified regions of 'Lamellar' and 'Isotropic' phases. Extended lamellae were found to exist at higher DMPC/DHPC mole fractions ($q > 6.7$) and higher temperatures. While the isotropic phase, identified for $q < 1.9$ mixtures and lower temperatures, consisted of fast tumbling aggregates with a characteristic phosphorous peak. Later, the single peak in the isotropic phase (showing no alignment) was identified by Triba and coworkers to consist of a split peak in which the ratio of the peak areas is proportional to the q value of the mixture [106] and the two separated with increasing temperature, above T_m , showing alignment of 'discoidal' aggregate.

Fig.2.10a compares the phase diagram obtained by Raffard et. al. and that by Nieh et.al., obtained using SANS for a bicelle mixture of similar composition (same compositions are indicated by dashed line on the two graphs) [101, 104]. The SANS study confirmed the Isotropic phase as consisting of discoidal aggregates. The discoidal morphology at low temperatures was confirmed further more by other experimental techniques, light scattering [99] and cryo-TEM [74]. The SANS study, highlighted the difference in the notation and aggregation states of the aligned 'bicelles' in common practise in the NMR community, which continues even to this day in looking at the number of publications citing 'aligned bicelles' as discoids, among prominent journals.

The same studies also raised additional questions on the morphology of the lipid mixtures near and above the T_m . Structures composed of multilamellar sheets and containing holes formed by the short-chain lipids [85, 101, 104, 107] were more likely candidates that could by oriented by the magnetic field. A more recent and detailed study by Nieh et.

al. [105, 108] undermined the discoidal geometry even more by proposing a 'chiral nematic phase' characterized by worm like micelles above T_m, based on combined polarized optical microscopy (POM) and SANS study. As shown in 2.10b, their study showed that the range of existence of the bicelles at low temperature (and the elongated aggregates close to T_m) dependent upon the over all composition, including the molar ratio q and the total lipid concentration c, in contradiction to the previously observed dependence only on the molar ratio q.

Thus, even though the evidence for the low temperatures discoidal morphology seems strong from Nieh et. al and van Dam et.al's recent studies, details of the lipid packing, lack of quantitative agreement on bicelle sizes between various studies and lack of clear parameters governing the aggregate formation remain unclear. We address these issues with the DMPC/DHPC system in Chapter 5.

The question of segregation and lipid packing, assumed in the IBM (described in detail in Chapter 5), was addressed for the first time in the NMR study by Triba et.al [106]. They claimed that the segregation of the short lipid, DHPC (C6) in the rim and DMPC(C14) in the core is not always complete and found evidence of mixing of the two lipids above T_m. Mixing of both lipids into the other domain was proposed, though their study could only measure the fraction of small lipids in the long lipid core and not that of the reverse i.e long into the edges and at temperatures above T_m, where the aggregates aligned in the magnetic field. Their experiment did not have the resolution to quantify the mixing in the low temperature phase consisting of small discoids. They also proposed a **Mixed Bicelle Model**, where the radius of the disc diverged with increased mixing of the two species, pointing to large alignable aggregates at high temperatures. While the partial miscibility of the two lipids is noteworthy in this study, evidently, the mixing fraction obtained, assuming a discoidal aggregate is at odds with the morphology now known from other techniques [105, 108, 74]. We address the question of the morphology and mixing of the two lipid species at low and high temperatures in Chapters 5-7 respectively.

Triba et. al. have also made connections between the bicelle system and the membrane solubilization studies involving lipid and surfactants [109], showing agreement between their proposed morphologies and that of lipid-surfactant studies. However, it misses on a very important elongated morphology, observed in such studies. Further more, while highlighting the mixing effect (of the short lipid into long lipid), the details of transition between partially mixed phase near the T_m of the lipid to a completely mixed phase at higher temperatures remains inconclusive. Even more unclear is the transition from a completely segregated phase to partially segregated phase in their study. These issues are addressed in Chapter 7.

The story of bicelle mixtures outlined in this section, starting from DMPC(C14) mixtures with -C7 to -bile salts to -CHAPSO and further onto DHPC(C6) mixtures has evolved pretty much following the interests of the NMR, protein communities in finding suitable substrates for membrane proteins and more recently as crystallization hosts (see Chapter 1). But further look into the literature as we describe below, reveals similar questions on the over all morphology in many other lipid-surfactant studies. While the contribution of experimental techniques involving scattering are more recent, the goal in this thesis is to provide further insights into the phase diagram of the mixtures as described in the Thesis Outline (Section 1.1). In addressing the question of the aggregate morphology of C14 with different surfactant sizes and chemistries for our second objective, this research also addresses questions pertinent to a much broader field of investigation.

The following section provides a brief overview of lipid-surfactant studies in the literature, and how it pertains to the work in this dissertation. The discussions in Chapters 5,6 and 7 will make references to this overview also.

2.5.2 Comparison with Lipid/Surfactant Mixtures

As seen in section 2.4.2, short micelle forming phospholipids are known for their detergents properties; and because of their chemistries are naturally the best candidates

for solubilizing lipid bilayers (see Hauser's article in [109]). The process of solubilization of the lipid bilayer, with a wide variety of detergents [109] has been studied in the surfactant community using several experimental techniques like turbidity, light scattering, cryo-TEM and less frequently using X-ray or neutron scattering. However, most of these studies have explored the surfactant effect on phospholipid bilayers in their fluid L_{alpha} phase and the various limits of the solubilization process. The same transitions in the gel state of the phospholipids have been much less studied [110]. In this regard, the bicelle study at low temperature in Chapter 5 addresses the morphology when the lipid is in the gel phase.

Lipid-surfactant mixtures have typically been described by their phase diagrams: for binary lipids and water or lipid-surfactant water mixtures, a ternary or (quasi) three component system in the form of Gibb's triangles [82]. Fig. 2.11(a) shows such a phase diagram of DMPC with Triton (also used in this study; Chapter 6) at 23°C . Among other phases, it shows the small single phase region L_1 where elongated micelles exist [111]. In excess water conditions however, the properties of the system are independent of the water content; so that the ternary system is reduced to a 'pseudo-binary' phase temperature composition diagram (Almgren's article in [109]) wherein the transitions between various aggregate morphologies are understood to be driven by the hydrophobic effect and it's packing models (Section 2.2).

These studies have generally explored surfactant effect on bilayers consisting of model phosphatidylcholine vesicle dispersions and the limits of the solubilization process. As the surfactant concentration is increased in a lipid suspension, the system goes sequentially from a pure lipid bilayer state → bilayer doped with surfactant molecules → bilayer breaks into micellar aggregates → pure micelle phase. This a composition induced *Bilayer/Vesicle-to-Micelle Transition*. This general scheme has been found in several phospholipid-surfactant mixtures like those of DMPC with C12E8[112, 113], SDS and DTAB[114], Octylglucoside[115, 116], Sodium cholate [117, 118] and with Triton[111, 119], and is seen as a step in the membrane breakup process with increasing amounts of deter-

(a)	(b)
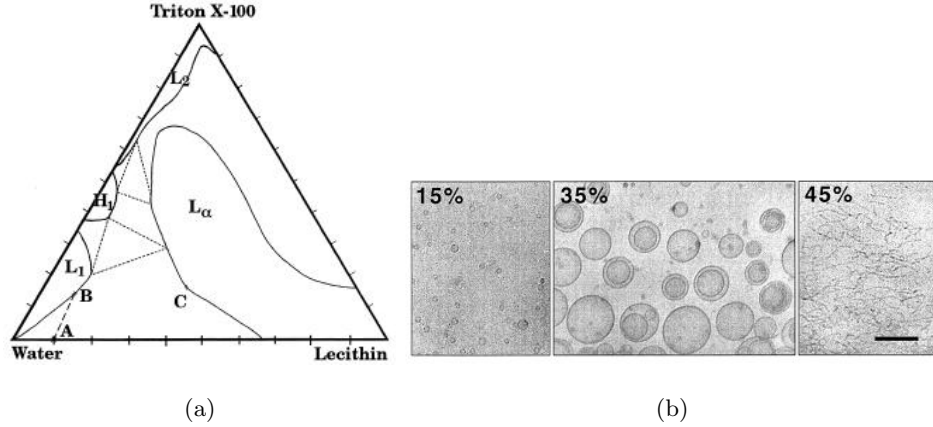
Figure 2.11: (a) Phase diagram of DMPC-Triton mixture at 23°C represented in the form of Gibb's triangle [111]. It shows single phase regions of micelle L_1 solution and lamellar L_α phase among others. (b)Evolution of structures formed with increasing mole fraction of C12E8 (single-tail surfactant) to small sonicated vesicle solution [112]. The elongated aggregates in the last panel are the same as that observed in the bicelle mixtures by van Dam and coworkers [74].

gent. These observations have given rise to the commonly held view of the process of vesicle solubilization with increasing detergent/lipid ratio (inverse of the q ratio used in bicelle studies) is as follows: above the intermicellar concentration (CMC of the mixture) initially fraction of the detergent molecules localize in the vesicles (mixed randomly with in the bilayer), leading to opening of the bilayer structure and, eventually, the formation of small micelles. Intermediate structures such as open bilayers and cylindrical micelles appear after vesicle opening, some of which grow into forming bigger aggregates on dilution. The reverse of this process, i.e. morphological transitions that occur when a mixed micelle is diluted and results in vesicle phase are referred to as *Micelle to Vesicle Transition (MVT)*.

Mixtures of lecithin (naturally occurring mixture of phospholipids found in natural sources like soybean) and bile-salts are another example of a mixed lipid surfactant system where the debate on the morphology of the mixed micelle from discoidal aggregates [120, 121] to elongated cylinders [122, 123, 124] has evolved over the years. Here again, the original description of a discoidal morphology was later found to be flexible elongated worm-

like micelles, in effect being an MVT transition at room temperature. In another work looking at the kinetics of transitions in lecithin bile-salt mixtures, the disk-like structures was established as transient intermediates in the transformation from mixed micelles to vesicles [81].

In this context, the work presented in Chapters 5 and 6 can be seen as an extension of the current understanding of lipid-surfactant assemblies at low temperatures and resolves the global morphology in that part of the phase diagram. Dilution induced growth can however be seen as a general feature of mixed lipid-surfactant systems, whether the lipid is in the gel state or fluid state. The two different states of the lipids result in different packing of the lipids in the aggregates as we show in this work.

Temperature induced changes in lipid surfactant mixtures have been even less studied [110]. In a closely related system of phospholipid and a bile salt, the temperature induced micelle-to-vesicle transition at constant lipid and surfactant concentration has been shown to be analogous to the concentration induced MVT [117, 118, 125] in other mixed lecithin-bile salt systems. This experimental study by Polozova et. al. [117], proposed the transformation of discoidal micelles to elongated micelles and bilayer fragments, but could not shed any light on the structure with in the elongated micelles or on the conditions leading to one of those two structural transformations.

In conclusion, as much of the work in surfactant lipid mixtures has focused on the overall characterization of the micellization process and on the kinetics in some cases without offering details of the aggregation, a lot remains to be understood at both the over all morphology and at the detailed structural levels. The nature of mixed micellar aggregates in concentration or temperature induced transitions, and the question of packing of the two components in the discoidal or the elongated morphologies observed in such transitions are the big questions that remain unresolved. As we show in Chapters 3-4, small angle scattering techniques using neutrons (SANS) and X-rays (SAXS) are best suited to unravel these issues due to the nature of neutron interactions and combined with the range of length

scale probed. In focussing on those two aggregation states, the work described in Chapters 5-7 is a small attempt to understand bicelle mixtures in particular and lipid-surfactant assemblies in general.

Chapter 3

Materials and Methods

3.1 Materials

PhosphoLipids

All the double tailed phospholipids with varying tail lengths used in this thesis work were obtained from one source, Avanti Polar Lipids, (Alabaster, AL) in powdered form. The names of these lipids along with their carbon tail length and product numbers are given in Table 3.1 and their structures are given in Fig. 3.1 . The deuterated lipid used in this study is 'fully' deuterated, since all the hydrogens in glycerol head and ester tails have been replaced by deuterium except for the five hydrogens remaining at the junction between the head and the tail.

All the lipids were obtained as white lyophilized powder. The hydrogenated lipids are claimed to be at > 99% purity, while the deuterated lipid is only of > 98% purity and they are used without further purification. All the lipids are stored in the freezer at -20°C when not in use. Prepared samples are stored at 5°C .

Other Detergents

Besides phospholipids, two other detergents were used in this study.
Chapso (3-[(3-Cholamidopropyl)dimethylammonio]-2-hydroxy-1-propanesulfonate), was purchased from Anatrace Chemicals. Triton-X-100 was purchased from Union Carbide. Their chemical structures are included in Fig. 3.1

Solvents

The heavy water D_2O used in all the neutron scattering experiments was purchased from Cambridge laboratories and used as received. In other experiments regular water, purified by the Milli-Q pure process and with a resistance of 18.2 MΩ was used. All stock samples and other samples were prepared in 0.2M salt solutions of NaCl (from Sigma Co.) prepared by dissolving the appropriate amounts of salt in D_2O or H_2O .
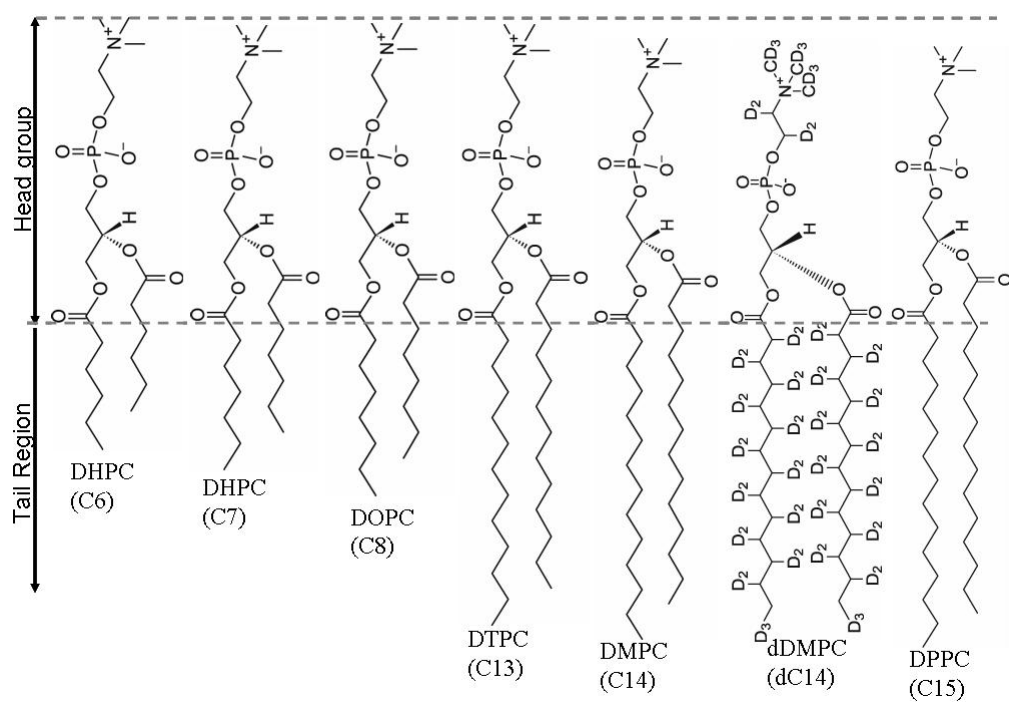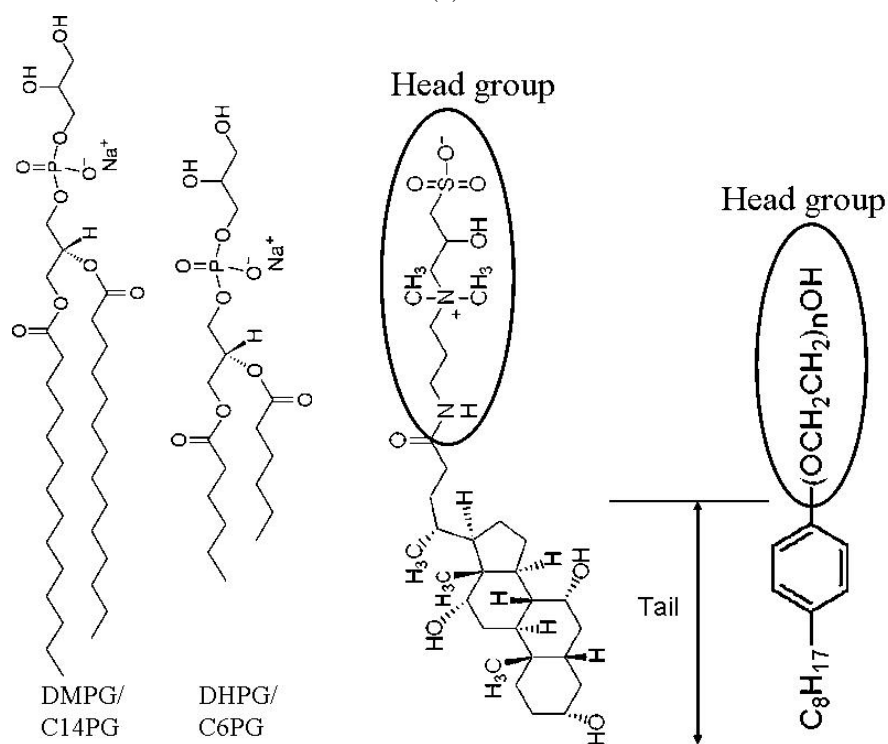
Figure 3.1: Chemical structure of all chemicals used in this study (a) hydrogenated and deuterated phospholipids of varying tail length (b) charged phospholipids (c) non biological surfactants, Chapso (left) and Triton-n100(right).

Table 3.1: Common names and catalog numbers[†] of lipids used in this study

Carbon No.	IUPAC Name	Common/Short Name*	Mol. Wt	Catalog No.
5	1,2-Divaleroyl-sn-glycero-3-Phosphocholine	Pentanoyl, C5PC	425.45	850305
6	1,2-Dihexanoyl-sn-glycero-3-Phosphocholine	Caproyl, C6PC	453.51	850305
7	1,2-Diheptanoyl-sn-glycero-3-Phosphocholine	Heptanoyl, C7PC	481.56	850306
8	1,2-Dioctanoyl-sn-glycero-3-Phosphocholine	Octanoyl, C8PC	509.61	850307
13	1,2-Ditridecanoyl-sn-glycero-3-Phosphocholine	Tridecanoyl, C13PC	649.88	850340
14	1,2-Dimyristoyl-sn-glycero-3-Phosphocholine	Myristoyl, C14PC	677.94	850345
15	1,2-Dipentadecanoyl-sn-glycero-3-Phosphocholine	Pentadecanoyl, C15PC	705.99	850350
16	1,2-Dipalmitoyl-sn-glycero-3-Phosphocholine	Palmitoyl, C16PC	734.04	850350
	Deuterated Lipid			
14	1,2-1,2-Dimyristoyl-D54-sn-glycerol -3-Phosphocholine-1,1,2,2-D4-N,N,N-trimethyl-D9	Caproyl, d-C14PC	745.35	860348
	Charged Lipid			
6	1,2-Dihexanoyl-sn-glycero-3-Phospho-rac-Glycerol	Dicaproyl, C6PG	464.42	840432
14	1,2-Dimyristoyl-sn-glycero-3-Phospho-rac-Glycerol	Myristoyl, C6PG	688.85	840445
-NA-	(3-[(3-Cholamidopropyl)dimethylammonio] -2-hydroxy-1-propanesulfonate	Chapso	630.9	8405
-NA-	(C8H17)C6H4(OCH2CH2)n OH	Triton-X-100	631	

*Unless otherwise stated, phospholipids will be referred by their chain lengths, as C6, C7, or C14.

[†] Anatrace and Union Carbide respectively.

3.2 Methods

3.2.1 Sample Preparation

Due to nature of long hydrophobic tails many of the phospholipids in this study are not easy to dissolve. Mixtures of phospholipids have been prepared using different techniques in the literature. One of them follows the protocol used for preparing single lipid dispersions, where appropriate amounts of the lipid powder are first dissolved in chloroform or acetone and dried in vacuum to get rid of all the water before adding the desired amount of water to obtain the final concentration. In order to prevent any contamination issues with a third component, instead a different preparation technique was followed.

All the samples are prepared in 4-8 ml glass vials with teflon caps. Before using any vials for sample preparation, to remove any dust sticking to the walls of the vials, they are immersed in soap solution and sonicated for 20-30 minutes. Afterwards, they are rinsed repeatedly (at least 5-10 times) with deionized (DVI) water. Subsequently they are immersed in fresh DVI water and sonicated 2-3 times for approximately 30 minutes each to remove any remaining soap. Finally the vials are dried in a drying oven at $\sim100°$C for a few hours. The caps are just cleaned with water and dried on Kimwipes blotting excess water to ensure faster drying.

Before preparing any sample, the lipids are removed from the freezer and allowed to come to room temperature. Only stainless steel spatulas are used for transferring the lipids and any contact of the lipids with plastic is avoided.

For preparing mixtures of two different lipids, first the short tail- hygroscopic lipid is weighed. It is very important to finish this measurement process as quickly as possible for best accuracy and store the lipid back into the freezer with a parafilm on the cap. Then the required amount of longer lipid is added and its mass is recorded. Finally using a micropipette, the appropriate amount of solvent is added and its mass is also recorded. After weighing, the sample vial is closed, parafilm or a thin teflon tape is wrapped around

44

the cap, and then vortexed at maximum speed for a few seconds to break up any loose clumps of undissolved lipid powder. Finally the samples are sonicated to mix them well.

Mixing using Sonication

The samples are subjected to an external sonication process, by immersing the glass vials in a temperature controlled Ultrasonic bath. Each of the samples is floated in the sonicator at $40°C$ for $\sim$20-30 minutes and then at $5°C$ in another bath for the same amount of time. The Branson Models 1510 and 2510 used have temperature ranges from ambient to $\sim70°C$. So the second temperature is approximate because there is no temperature control between room temperature and $0°C$. Ice is placed inside the sonicator to obtain an approximate temperature of $0°C$. After cycling each of the samples three to four times, they are placed in the refrigerating unit at $\sim5°C$ unless they are being used directly. If the sample has been in the refrigerator for over a day, the sonication cycling is repeated but carried out only for $\sim$10-15 minutes each time.

Concentration or $c - series$ samples

For preparing samples of the same molar ratio $q = [Long]/[Short]$, but different total lipid concentrations, a stock sample of high concentration $c = [Long] + [Short]$ $\sim$0.1 g/ml was prepared. Then a series of samples of lesser concentration were prepared by simple dilution. The masses of both the stock and solvent were measured while using a known volume of the micropipette for better accuracy. The high concentration stock sample was kept on ice to maintain its fluidity. After dilution, all the samples were secured with parafilm and subjected to 3-4 sonication cycles at low and high temperatures.

Molar ratio $q - series$ samples

For preparing samples of the same total lipid concentration c but different molar ratios q, two stock samples of different molar ratios (one high and one low), but same concentration were prepared. Then a series of different molar ratio samples were prepared by mixing appropriate amount of the two stocks. After securing the teflon caps with parafilm, all samples were properly homogenized by 3-4 cycles of repeated sonication at low and high

temperatures.

3.2.2 Phase Determination

Simple bulk phase behavior of lipid and surfactant mixtures can be used to get a sense of the aggregate morphology since the macromolecular aggregates have $\sim$ nanometer-micrometer sizes. In this work, crude phase behaviors of various short and long tail lipids were determined by visual observations with the naked eyes, with and without cross polarizers. After preparation, samples were equilibrated to a given temperature for $\sim$30 minutes to an hour, depending on the temperature jump, before recording an observation.

Different morphologies have characteristic visual appearances. Small globular, or spherical micelles are transparent, isotropic and have low viscosity just like water. Rod like micelles will look similar but have a higher viscosity. While samples that are bluish transparent and have very low viscosity are characteristic of small vesicles. Turbid white and weakly birefringent samples are suggestive of $\sim$micron-sized multilamellar vesicles or large bilayer fragments. Birefringent samples indicate oriented domains in the sample consisting of either rod like micelles or packed bilayer fragments. Ultimately, the actual structure can be revealed only by direct microscopy techniques like Differential Interference Contrast (DIC), much higher resolution Cryo-transmission electron microscopy (TEM) and indirect techniques small angle scattering techniques like SAXS and SANS, which the rest of this thesis work is devoted to.

3.2.3 Densitometry

Densitometry or high sensitivity density measurement has been possible since the introduction of a practical model of the 'mechanical oscillator' technique introduced by Kratky in the 60's [126]. Now it is a well established and ideal tool for measuring high precision densities of fluid samples of proteins and lipids. Modern variations of the initial design of vibrating U-tube density meters have accuracies up to fourth and fifth significant figures

and incorporate elements for temperature control (see for e.g http://www.anton-paar.com/). In scattering experiments with neutrons, or X-rays, absolute calibration requires precise values of densities of samples and solvents used [127, 11]. The inverse of density, or specific volume ($v = V/m$) of lipid molecules has also been shown to be of extreme relevance for characterizing the bilayer structures [11]. Study of volumetric changes in lipids with temperature, associated with chain melting are also used to study phase transitions of pure lipids [55, 58, 54]. Examples of such a measurement of density with temperature, (as part of this work) from such measurements on pure DMPC(C14) lipids are shown in Figs. 2.2 and 2.4 in Chapter 2. Such data are of great significance for scattering experiments with neutrons and X-rays in calculating scattering length densities of compounds [63] and will be used in Chapter 5 (see for e.g. Table 5.2). In this study, measurements on pure lipids to characterize the lipids batches, were found to be in conformity with existing literature, particularly those of Nagle and coworkers [55, 56, 128].

Basics and Instrumentation

Vibrating tube density meters are based on the principle of resonance of a column of fluid. The oscillation frequency of a U-shaped boro-silicate glass tube filled with the sample is used to measure the density of the sample.

From basic physics, the natural resonance frequency of a column is inversely proportional to the square root of its mass density; in case of a tube of length L and density ρ_{tube} filled with some sample of density ρ_{fluid}, with an applied tension T_{tube}, it will be given as

$$f_{nat} = \frac{1}{2\pi} \left(\frac{1}{2L} \right) \sqrt{\frac{T_{tube}}{\rho_{tube} + \rho_{fluid}}} \tag{3.1}$$

and is characteristic of the vibrating tube. Since the resonance frequency is inversely proportional to the density, the frequency of a fluid filled tube is related to the natural frequency of the tube itself as

$$f_{fluid} = f_{nat}\sqrt{1 + \alpha} \tag{3.2}$$

where $\alpha = m_{fluid}/m_{tube}$ is the ratio of the mass of the fluid sample to the mass of the tube. This basic theory provides a basis for very accurate measurements when sophisticated electronics is incorporated for providing high precision input signal and measuring output frequencies.

We have used the Anton-Paar DMA 5000 density meter for our experiments. It has a built in solid state thermostat (Peltier) for temperature control and also a built-in air pump for drying the measuring cell. The tube volume is small enough to accommodate sample volumes as small as one milliliter. Typical measurement of a sample takes a few minutes to equilibrate before reading out the density. This instrument has also been used in the 'temperature scanning mode', where the initial and final temperature and the temperature jump unit as well as delay time between two measurements can be specified. For such scans, the measurement times varied between a few hours to a day. Before any measurement, the densities of pure 18M Ω water and air were measured at 20°C for calibration.

Density measurements of Lipids

All the samples dealt with in this work are aqueous samples since the phase behaviors of lipids are reported in aqueous conditions. The DMA 5000 model is very well suited for such samples. In order to extract the densities of the pure component from a measurement of the density of the mixture, we have used the following procedure: For a mixture of two components 1: water and 2: lipid; their respective measured weights are ω_1 and ω_2 and volumes V_1 and V_2, such that the individual densities are respectively $\rho_1 = \omega_1/V_1$ and $\rho_2 = \omega_2/V_2$. If the two components mix ideally, then the density of the mixture is given as

$$\rho = \frac{\omega_1 + \omega_2}{V_1 + V_2} = \frac{\omega_1 + \omega_2}{\omega_1/\rho_1 + \omega_2/\rho_2} \qquad (3.3)$$

This can be rearranged to give:

$$\frac{\omega_1 + \omega_2}{\rho} = \frac{\omega_1}{\rho_1} + \frac{\omega_2}{\rho_2}$$

In terms of mass fractions, the mixture density can be rewritten as

$$\frac{1}{\rho} = \frac{f_1}{\rho_1} + \frac{f_2}{\rho_2} \qquad (3.4)$$

where $f_1 = \omega_1/(\omega_1 + \omega_2)$ and $f_2 = \omega_2/(\omega_1 + \omega_2)$ respectively.

In order to determine the density of pure lipids, they were dissolved in milli-pure water in three to four different concentrations and mixed well until they formed a whitish dispersion of multilamellar vesicles. Lipid and solvent mass were measured by weight and this was used to determine the mass/weight fraction for each sample. Density measurements were made at 10°C . The measured density of the sample was used to plot $(1/\rho - f_1/\rho_1)$ vs f_2, where f_1 and f_2 are the measured mass fractions of water and lipid. The density ρ for H_2O was taken as 0.99969 g/cm^3 at 10°C compared to 0.99818 g/cm^3 at 20°C . Linear fit was used to obtain the slope $1/\rho_2$ for each pure lipid from the above equation. Figure 3.2, shows results of such measurements on pure C14, C6 and dC14 lipid dispersions.
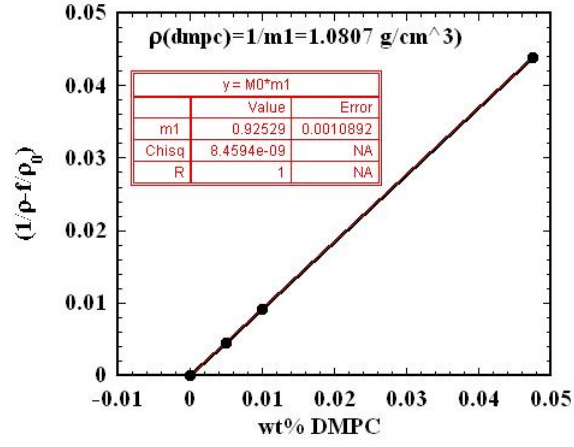
(a)
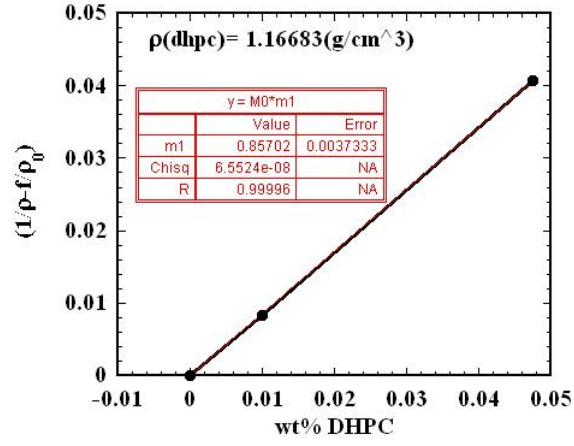
(b)
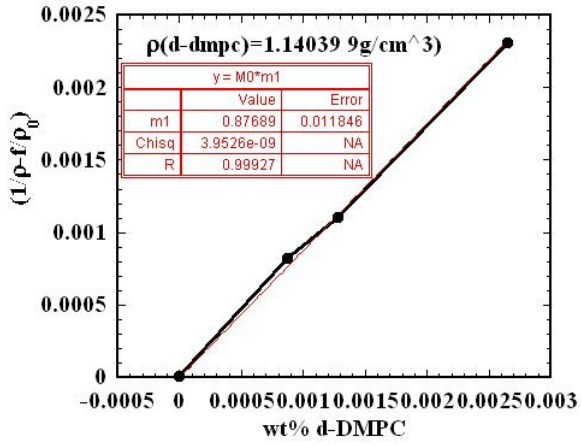
(c)

Figure 3.2: Densities of pure lipids used in this study (a) DMPC (b) DHPC (c) d-DMPC.

The same idea from equation 3.4, is used to obtain the temperature dependent density of the components as

$$\frac{1}{\rho_2(T)} = \left[\frac{1}{\rho(T)} - \frac{f_1}{\rho_1(T)}\right] \frac{1}{f_2} \tag{3.5}$$

3.2.4 Differential Scanning Calorimetry

Differential scanning calorimetry is a technique for measuring heat changes in a sample with controlled variation in temperature. The instrument measures the energy needed to maintain a zero temperature difference between the sample and an inert reference material. When the sample undergoes a phase transition, more (or less) heat will need to flow to it than the reference to maintain both at the same temperature. The amount of heat flow to the sample determines whether the process is exothermic or endothermic. Melting of a solid to a liquid is a exothermic transition, as the sample releases heat to undergo the transition, while crystallization is an endothermic transition; heat is absorbed as the sample undergoes crystallization. Pure phospholipids undergo phase transitions at the chain melting temperature and show a strong peak in their heat capacity profiles as shown in Fig. 2.2 [47]. Pure lipid samples to verify their T_m (see Chapter 2), and lipid mixtures to test the effect of of another component on the phase transitions, have been measured using this technique (Chapter 5-7).

A MicroCal VP DSC instrument in Prof. David Draper's laboratory at Johns Hopkins and in Dr. Ed Schwarz's laboratory at CARB, NIST were used for DSC measurements. In this instrument, the cells are fabricated from Tantalum 61, which has excellent chemical resistance properties. The cells themselves are coin shaped and can hold sample volumes of 0.5 ml. The operating temperature range of the instrument is 10°C to +130°C and is based on an internal Peltier mechanism no external heating or cooling devise is required. Scan rates in the range of a few °C to 90°C per hour can be employed with this setup.

3.2.5 Small Angle Neutron Scattering

The small angle neutron scattering (SANS) technique derives its name from the use of small angles and/or the use of long wavelengths to achieve small scattering-vectors defined by $Q = (4\pi/\lambda)\sin\phi/2 \approx 2\pi\phi/\lambda$, where ϕ is the scattering angle and λ is the wavelength of radiation (neutron, photon in case of SAXS) used. The main design requirement of any small angle scattering instrument is obtaining small scattering angles. With the detector a distance L from the sample, the scattered radiation striking the detector at a distance D from its center defines the lowest limit of scattering angle ϕ. If the distance L is large compared to D, the scattering wave vector can be written as

$$Q = \frac{4\pi}{\lambda}\sin\phi/2 \approx \frac{4\pi}{\lambda}\tan\phi/2 = \frac{2\pi}{\lambda}\frac{D}{L} \qquad (3.6)$$

This section describes the experimental aspects of this technique, while the underlying theoretical aspects and analysis techniques associated with SANS experiments, are described in Chapter 4.

SANS experiments described in this work have been carried out at the National Institute of Standards and Technology (NIST) Center for Neutron Research (NCNR) on two instruments, the NG3-SANS and NG7-SANS. A schematic diagram of the Guide Hall with the cold neutron instruments and the SANS instrumentation are given in Fig.3.3. The neutron source is a 20MW nuclear reactor. Neutrons are produced in the reactor core from fission of ^{235}U, and is surrounded by moderators like H_2O and D_2O . The thermal neutrons are further cooled to lower temperature by using a small volume of liquid or superfluid hydrogen at temperature of $\sim$20 K. The cold neutrons are transported from the source to the instrument by using neutron guides, which are coated by Nickel and operate by total internal reflection of the neutron beam. Beam filters consisting of Beryllium (for neutrons) and high Z-material like Bismuth (for gamma rays) are used to cleanup the beam from unwanted fast neutrons and gamma rays.
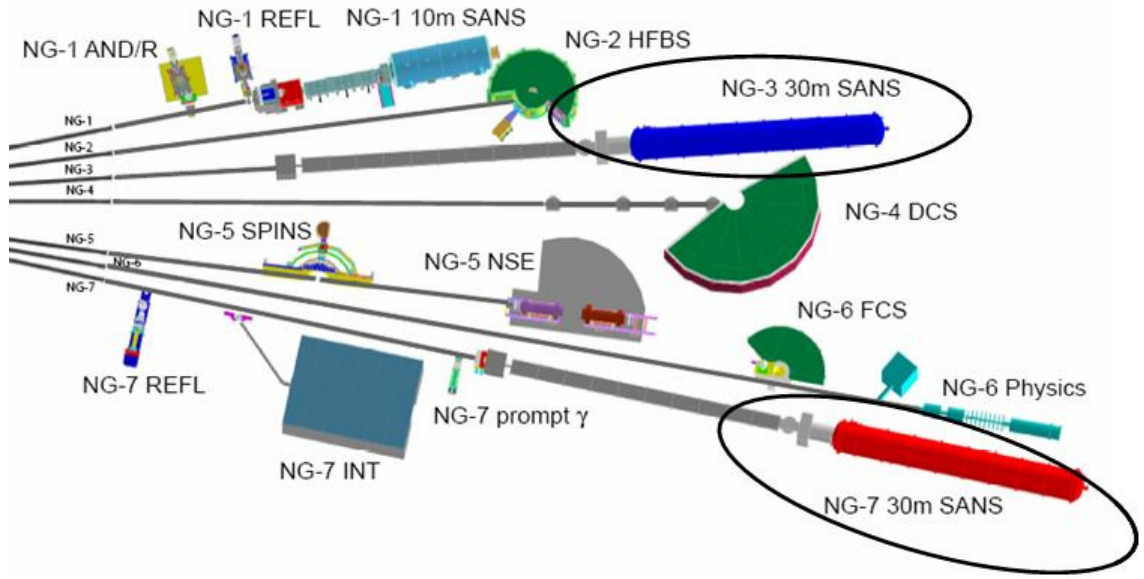
(a)
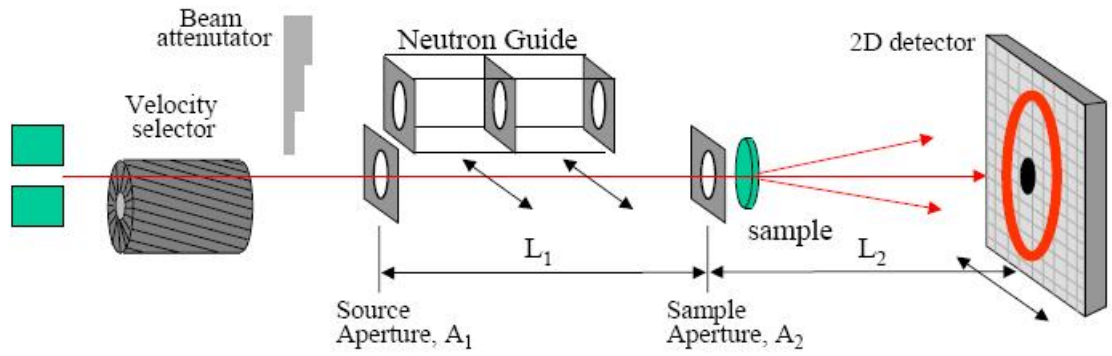
(b)

Figure 3.3: (a) Schematic of the guide hall showing all the cold neutron instruments. The two SANS instruments used in this work are marked. (b) Schematic of a SANS instrument showing important components [129].

Briefly, as shown in the schematic in Fig. 3.3, the key components involved in SANS instrumentation are as follows: Multi-disk mechanical velocity selectors, with variable speed and pitch are used to obtain monochromatic beam with wavelength between λ between 4-20 Å and $\Delta\lambda/\lambda$ between 10-30%. The monochromatic beam is collimated by circular pinhole slits in a 15 m long evacuated pre-sample flight path. Pre-sample flight paths lead to the experimental sample station which can accommodate, multi-sample translation blocks, temperature control, cryostats, and other sample environments. Between the velocity selector and the pre-sample collimation system, a low-efficiency fission chamber detector is used to monitor the neutron beam during data acquisition. The sample position is followed by a post sample evacuated flight path which ends in an area detector 64 cm×64 cm. The detector itself is a ^{3}He position-sensitive proportional counter with 0.5cm×0.5 cm spatial resolution. The area detector can be positioned using rails, and can be moved to attain sample to detector distances of ~1-15 m in length. Built into the detector is also an adjustable beam stop, for protecting against damage of the detector from the high intensity of transmitted beams.

Once the incident neutron beam has been scattered off of the sample and collected by the detector, it is corrected for efficiencies of each detection unit on the detector. The efficiency of the detector is determined in a separate experiment by measuring a strong isotropic scatterer like plexiglass. Measurements are also taken from an empty cell (to account for scattering from the cell and windows), a blocked beam (to account for detector dark current, stray neutrons etc.) along with beam flux measurement in transmission mode for absolute scale calibration ([129], SANS tutorials at http://www.ncnr.nist.gov/SANS).

The cross section of a scattering sample $d\Sigma/d\Omega$, is related to the measured count rate I(Q) on a detector by

$$I(Q) = \phi \cdot A. \cdot d \cdot T \left(\frac{d\Sigma(Q)}{d\Omega} \right)_{sample} \Delta\Omega \cdot \epsilon \cdot t \qquad (3.7)$$

where

$\phi=$ incident neutron flux; $\Delta\Omega =$ solid angle of each pixel

$A =$ sample area ; $\epsilon =$ detector efficiency

$d =$ sample thickness ; $t =$ counting time

and T is the transmission efficiency of the cell with the sample in it.

From this relation, using the beam flux measurement or a standard reference measurement, SANS data is corrected and rescaled to give an absolute scale for the macroscopic cross-section in units of cm^{-1}. When the 2-D data is isotropic, it is circularly averaged (in case of anisotropic scattering, sector averages are used) to obtain one-dimensional intensity pattern as a function of wave vector Q.

SANS measurements on all the samples were taken in cells of 1-2 mm path length with quartz windows and neutron wavelengths in the range 6-8 Å and wavelength spread $\Delta\lambda/\lambda \sim 8-20\%$. Sample to detector distances ranged from 1 m to 15 m giving a Q range of 0.001-0.5 Å^{-1} .

3.2.6   Small Angle X-ray Scattering

Small Angle X-ray scattering (SAXS), like SANS is a small angle geometry instrument. SAXS measurements were done in collaboration with Dr. Ursula Perez-Salas at the Advance Photon Source on beamline 12-1D. The synchrotron X-ray source at APS has a continuous spectrum, high flux ($\sim 10^{13}$ photons/s) and high coherence needed for high resolution scattering measurements. With photons in the energy range 3-27 keV ($\lambda \sim 0.7$-6 Å) and $\Delta E/E$ of 10^{-4}, the beamline on sector-12 is especially suited for SAXS. For the measurements described in this work, 12 KeV beam with two detector positions at 2m and 70 cm was used, giving a Q-range of 0.004-0.4 Å^{-1} . An X-ray phosphor detector optically coupled to 3x3 mosaic charge-coupled device (CCD) read out is used on this beam line as described elsewhere [130]. The same cells as used in SANS, with 1 mm path length, but with thin mica windows (weak scatterer for X-rays) were used along with a sample and

temperature block,of the same design as the one used at NIST. Unlike the SANS measurements, water scattering was measured as standard for absolute scale calibration, similar to the procedure used by Glatter and coworkers [127]. Sample exposure times were optimized to five 1s shots to avoid sample heating and better sampling.

Chapter 4

Scattering Theory and SAS Data Analysis

4.1 Introduction

Scattering techniques, and small angle scattering (SAS) techniques in particular, have become widely used tools for characterization of condensed matter systems, including biological systems over the last twenty years or so with the advent of many powerful neutron and X-ray facilities around the world [63, 131, 129]. Unlike microscopy techniques which probe surfaces and interfaces, scattering techniques probe bulk properties. Combined with the length scales probed, in the 10-1000Å range, the range of interest in this work, SAS has become indispensable for studying structures in soft matter, more appropriately, the colloidal domain. The typical structures studied are complex macromolecular aggregates, consisting of protein assemblies, organic polymers, membranes and micellar dispersions.

In this chapter, basics of scattering theory as it applies to Small Angle Scattering

(SAS), the main experimental technique used here, being neutrons and X-rays, are summarized. In order to facilitate interpretation of the experimental results presented in Chapters 5-7, basics of the analysis techniques are also presented.

Scattering measurements can be done with light, X-rays or neutrons. Scattering results from the variations within the sample of refractive index in case of light, electron density in case of X-rays and of nuclear density, in the case of neutrons. While the theoretical basis of scattering remains the same, the choice of radiation fields or a combination of them is dependent on the strength of the respective fields. Most of this Chapter is based on scattering using neutrons, but easily extended to X-rays with some differences as outlined in the last section.

Scattering techniques have been employed for decades to study structures in macromolecules that have a crystallinity via **Bragg's law:** $\lambda = 2d \sin \phi/2$, where d is the distance between the atomic unit, λ is the wavelength and ϕ is the scattering angle. Even though scattering from macromolecular systems encountered in soft matter are much more complex, basic understanding of the length scale can be obtained from the simple Bragg's law. In the literature, 2θ is the more commonly used to denote angle of scatter. The scattered intensity is measured as a function of the momentum transferred $\boldsymbol{Q}$ as

$$Q = |\boldsymbol{Q}| = \frac{4\pi}{\lambda} \sin \phi/2 \tag{4.1}$$

so that, the length scale probed by radiation of wavelength λ is given by $d^{-1} \sim Q = (4\pi/\lambda) \sin(\phi/2)$.

4.2   Neutron Scattering

Neutron scattering, in principle, was born in 1932, with the discovery of neutrons by Chadwick. In practise though, Bertram Brockhouse and Clifford Schull brought this technique to the forefront, and for their pioneering work in this field, they were awarded the Nobel Prize in Physics in 1994. Due to the deeper penetrating power of the neutron, its

isotope sensitivity and the magnetic moment of the neutron, it has been used extensively to study 'hard' crystalline materials. However, recently with biological sciences becoming more quantitative in nature, scattering techniques have found many new applications [131]. Biologically relevant materials have length scales bigger than the atomic length scale. Their study has also become possible by the advent of 'cold' neutron sources that emit longer wavelengths, lower velocity neutrons, compared to the 'thermal' neutrons. In such systems, it is the technique of choice for a number of reasons including-

1. Neutron probes are non destructive. This is very important for most fragile, soft matter and biological systems, where large energies of X-rays can cause damage.

2. Since neutrons are highly penetrating, neutrons can be employed to study thick samples that cannot be studied with the X-ray techniques.

3. Neutrons can distinguish isotopes, since neutron scattering lengths vary randomly with atomic number. This is because neutrons interact with atomic nuclei instead of the diffuse electron cloud for X-rays. Isotopic labeling can be used to probe structural information in greater detail.

A number of books [63, 132, 133, 129] and articles (see for e.g *Journal of Applied Crystallography*) have been published that describe the basis of this technique. This section briefly describes the theoretical basis of scattering, following the discussion in Higgins's and Glatter's and textbooks highlighting the main results relevant for this work.

4.3 Scattering Theory

A scattering experiment measures the intensity of scattered waves by different units in the system. In an elastic scattering experiment, the incident and the scattered waves have the same energy or wavelength, and the time averaged structure of the system is obtained. When the scattering is inelastic, change in energy of the neutron is measured

to obtain information about the dynamics of the system. In this work, we will be concerned with structure determination and hence focus on elastic scattering only.

Scattering from a Single Atom

For non-magnetic systems, neutron scattering results from the strong nuclear force between the nucleus and incident neutrons. The range of the nuclear force being on the order of 10^{-15}m which is about five orders of magnitude smaller than the wavelength of the neutrons in typical experimental studies. This means that the neutron cannot resolve the internal structure of the nucleus.

In the simplest case of scattering from a fixed atom, the incident neutrons are represented by a plane wave

$$\Psi_i = \exp(i\boldsymbol{k_0} \cdot \boldsymbol{r}) \tag{4.2}$$

The scattered wave, far from the origin at a point $\boldsymbol{r}$ can be considered as a spherical wave with an amplitude decreasing as $1/|r| = 1/r$ and written as

$$\Psi_{sc} = -\frac{b}{r}exp(i\boldsymbol{k_1} \cdot \boldsymbol{r}) \tag{4.3}$$

where r is distance of the scattering unit to the detector. The quantity $bb^\star$ ($b^\star$ is the complex conjugate of b) gives the probability that an initial plane wave of amplitude unity will be scattered in the direction r. So the quantity b, which has units of length is referred to as the *scattering length* and is a measure of the strength of the interaction between the neutron and the nucleus. It depends on the type and spin of the nucleus and 'varies seemingly randomly' across the periodic table, based on quantum mechanical eigen states. The unit of the scattering length, b, is the fermi (1 fermi = 10^{-15} m).

In a typical elastic experiment, the number of scattered neutrons in a particular direction are counted ignoring any changes in energy. When the distance from the detector to the sample r is large, then in a small solid angle $d\Omega$ subtended by the detector, the probability of a neutron being scattered into the detector, is defined as *differential scattering*

cross-section

$$\frac{d\sigma_s}{d\Omega} = \frac{\text{Neutrons/unit time scattered into } d\Omega}{\text{Number of incident neutrons per area per second}} \tag{4.4}$$

and is equivalent to the effective area that the nucleus presents to the incident neutron in the direction $d\Omega$. The *total scattering cross-section* σ is obtained by integrating over all solid angles

$$\sigma_s = \int \frac{d\sigma_s}{d\Omega} = 4\pi b^2 \tag{4.5}$$

so that σ_s has dimensions of area. It is expressed in units of 10^{-12} cm or *barns*. Physically, the cross-section represents the effective area presented by the target nucleus to the incident beam of neutrons for elastic scattering. The value of the scattering length depends not only on the type of nucleus, but also on its spin state. A detailed discussion is given in all standard texts and will not be considered here. If the value of b varies in a system of single element due to the presence of isotopes and/or varying nuclear spin states and the value of b_i occurs with relative frequency f_i, then average values for b and b^2 can be defined as

$$\bar{b} = \sum_i f_i b_i, \qquad \bar{b^2} = \sum_i f_i b_i{}^2 \tag{4.6}$$

As a result the scattering cross section can be broken into two terms, a coherent part and an incoherent part

$$\sigma_{tot} = \sigma_{coh} + \sigma_{inc} \text{ where}$$

$$\sigma_{coh} = 4\pi \bar{b}^2, \qquad \sigma_{inc} = 4\pi(\bar{b^2} - \bar{b}^2) \tag{4.7}$$

Only the coherent part of the scattering cross section contributes to the Q-dependent or structural signal from a system while the incoherent part contributes to Q-independent background to the scattering. As photons do not have any spin, there is no strict analog in SAXS or light scattering of incoherent scattering of neutrons. Compton scattering in X-rays is similar in the sense that it contains no information from interference effects, or

Table 4.1: Scattering lengths and cross-sections of some common elements

Element	$\bar{b}(10^{-12}\text{cm})$	$\sigma_{coh}(\text{barns})$	$\sigma_{inc}(\text{barns})$
Hydrogen	-0.374	1.76	79.7
Deuterium	0.667	5.597	2.04
Carbon	0.665	5.59	0
Nitrogen	0.930	11.1	0
Oxygen	0.580	4.23	0
Sodium	0.363	1.66	1.62
Phosphorous	0.513	3.31	0
Chlorine	0.958	11.53	5.9

structural features and forms a background to the coherent signal. This background is usually neglected in SAXS studies, since it goes to zero in the limit $Q \to 0$.

Table 4.1 shows the scattering length, coherent and incoherent scattering cross-sections for a number of common elements, most of which we will encounter in this research. Values for b vary essentially randomly through the periodic table, but their range is limited. For biological and soft matter, the first two entries listing hydrogen and deuterium are the most important entries. Their scattering lengths vary in sign and magnitude, with the deuterium cross-section being bigger by more than a factor of three. The other bigger difference is the huge incoherent cross-section of hydrogen, nearly $40\times$ greater than that of deuterium. These differences have played a key role in the application of neutrons to study biological matter via Small Angle Scattering techniques as we describe later in Section 4.4.

Scattering from Multiple Unit System

In a typical experiment, scattering is the result of interference of waves scattered by multiple scattering units/atoms that compose the object. For coherent scattering, the amplitudes of the scattered waves add and scattering intensity is the square of the resulting amplitude. Consider the scattering from two points separated by a distance $\boldsymbol{r}$ as shown
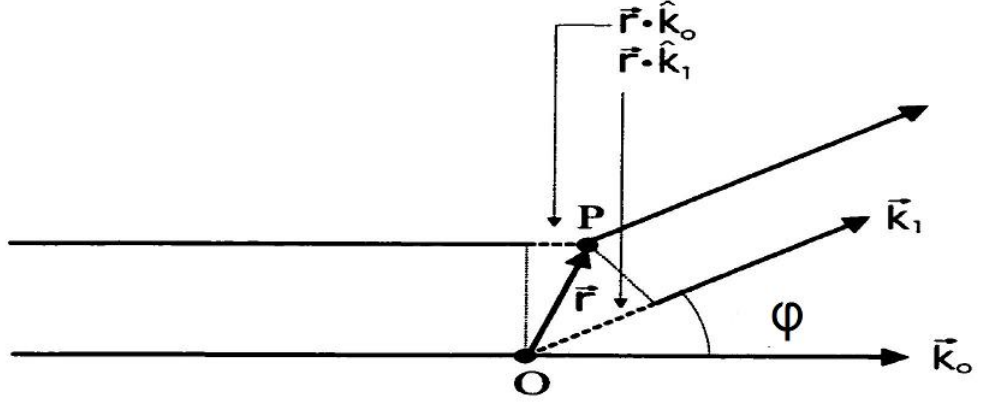
Figure 4.1: Scattering geometry of incident waves from two points.

in Fig. 4.1. An incoming wave with wave vector k_0 scatters off the points O and P such that the scattered beam is in the direction given by k_1 as shown in Fig. 4.1. In complex notation, a scattered wave can be written as $e^{i\phi}$, where the phase ϕ is $2\pi/\lambda$ times the distance traveled from some arbitrary reference point. With a path difference of r, the phase difference between the waves scattered from the two points is $\frac{2\pi}{\lambda} r \cdot (k_0 - k_1)$. The scattering amplitude in the direction k_1 from the two point scatterers is then given by

$$A(Q) = \sum_{\text{all points}} b(r) e^{iQr} \tag{4.8}$$

where $Q = (k_0 - k_1)$ is the scattering vector and $b(r)$ is the bound scattering length of the object at r. In using the bound scattering length, the *static approximation* has been used, which assumes that the target molecule is fixed and there is negligible energy transfer from the neutron.

For a macroscopic object the number of scatterers is large and the sum can be replaced by an integral

$$A(Q) = \int d^3r \rho(r) e^{iQr} \tag{4.9}$$

where $\rho(r)$ is the **Scattering Length Density**, or the *scattering length per unit volume* (used from hereon, as opposed to the mass density used in Chapter 3) and the integral is

over the volume of the object. It is better expressed in terms of the molecular properties, rather than the atomic properties. The SLD for a molecule composed of N known elements can be calculated using Table 4.1 and the density of the constituents as

$$\rho = \sum_i^N \frac{b_i}{\bar{V_i}} = \frac{dN_A}{M_W} \sum_i^N \frac{b_i}{\bar{V_i}} \tag{4.10}$$

where $\bar{V_i}$ is the volume of component i; d is the density and M_W is the molar mass of the molecule, and N_A is Avogadros number ($N_A = 6.022 \times 10^{23}$ moll^{-1}).

The scattering intensity is the absolute square of the scattering amplitude

$$I(Q) = A \cdot A = \int \int d^3 \boldsymbol{r}_1 d^3 \boldsymbol{r}_2 \rho(\boldsymbol{r}_1) \rho(\boldsymbol{r}_2) e^{i\boldsymbol{Q}(r_1 - r_2)} \tag{4.11}$$

Since the double integral involves only the relative distance $|\boldsymbol{r}_1 - r_2|$ between every pair of points in the object, the integration can be divided into two steps: (1) integrate over all points with equal relative distances, and 2) integrate over all possible relative distances. The first integral can be written as

$$\bar{\rho}^2(r) = \int d^3 r \rho(r_1) \rho(r_2) \text{with } r = (|\boldsymbol{r}_1 - r_2|) = constant \tag{4.12}$$

We can see that $\bar{\rho}^2(r)$ is a measure of the correlation between the scattering length densities at all points in the sample separated by a distance r. The second step gives an integral over all separation points

$$I(Q) = \frac{1}{V} \int d^3 \boldsymbol{r}_1 \bar{\rho}^2(\boldsymbol{r}) e^{i\boldsymbol{Q}r} \tag{4.13}$$

4.3.1 Small Angle Scattering (SAS)

Small angle scattering offers some simplification to the results derived in the previous section. They are based on the assumption

1. System is statistically isotropic.

This would be true for specific types of material only, but if true, it would mean that

$\bar{\rho}^2(r)$ depends only on the magnitude of r and the phase factor $e^{i\boldsymbol{Q}r}$ can be replaced by its orientational average as

$$\langle e^{i\boldsymbol{Q}r} \rangle = \frac{\sin Qr}{Qr} \tag{4.14}$$

2. There is no long range order, i.e., there is no correlation between points separated widely enough.

This would mean that the SLD would become independent (uncorrelated) at large r and can be replaced by a mean value $\bar{\rho}$.

Based on the these considerations, SAS data analysis can be analyzed using the following different approaches.

4.3.2 SAS Data: Asymptotic Limits

The simplest way is to look at limiting values of I(Q). In the limit of $Q \to 0$, so that we are looking at the scattering object from a length scale much bigger than the object itself, the orientational average of the phase factor or the exponential term in the expression in Eqn. 4.14 can be approximated as $\frac{\sin(Qr)}{Qr} \sim 1 - \frac{1}{3}(Qr)^2 + \cdots$ as shown first by Debye in the early nineties [132].

Then the expression for I(Q) can be rewritten as

$$I(Q) = \frac{1}{V} \left(\int_V \rho(r)d^r \right)^2 \left[1 - \frac{1}{3}Q^2 R_g^2 + \right]$$

$$\text{or } I(Q) \cong I(0)e^{-\frac{1}{3}Q^2 R_g^2} \text{ where } R_g^2 = \frac{\int \rho(r)r^2 d^3 r}{\int \rho(r)d^3 r} \tag{4.15}$$

Here R_g is the **Radius of Gyration** and $I(0)$ is proportional to the SLD per unit volume. This is called the **Guinier Approximation**. The R_g obtained from the simple linear relation of ln(I) to Q^2 can be used to obtain the radius of a spherical object or the relationship between the two dimensions of non-spherical objects. These values are listed in Table 4.2 for some common shapes.

65

Table 4.2: Guinier Radius for some common shapes

Particle Shape	R_G^2
Sphere (R=radius)	$\frac{3}{5}R^2$
Cylinder (R=radius, L=length)	$\frac{R^2}{2} + \frac{L^2}{12}$
Disc (R=radius, t=thickness)	$\frac{R^2}{2} + \frac{t^2}{12}$
Prolate Ellipsoid (Axes a,b)	$\frac{1}{5}(a^2 + 2b^2)$
Parallelpiped (Edge length A,B,C)	$\frac{1}{12}\left(A^2 + B^2 + C^2\right)$

For elongated (cylinder) or flattened (disc/sheet) like structures, with two different length scales, their are two Guinier regions. At the lowest Q for the largest dimension and at another higher Q for the smaller dimension. Those two can be separated easily, if the two dimensions are far apart.

In case of scattering from a cylinder, for values of $Q > 1/L$, the scattered intensity is insensitive to L and depends only on the cross-section and internal structure. This allows separate orientational averaging of the length and radial contributions. Since the length scales inversely with Q, the **Modified Guinier approximation** becomes

$$QI(Q) = I_c(0)exp(-\frac{Q^2 R_{CG}^2}{2}) \tag{4.16}$$

where R_{Cg} is the cross-sectional radius of gyration and $I_c(0)$ is the SLD per unit length. Now a plot of $ln(QI(Q))$ vs Q^2 is linear over the range of $1/L < Q < 1/R$ and the slope from R_{Cg} is related to the radius of the particle as $R_{Cg} = R/\sqrt{2}$ for a circular cross-section.

In case of scattering from an extended plate like (discoidal) structures, the structure at high Q is dominated by the smaller length scale, or the thickness. At distance bigger than the thickness, or for low Q, scattering is proportional to $1/Q^2$ and in this case the

66

Modified Guinier approximation gives a linear relationship between $ln(Q^2 I(Q))$ vs Q^2. In this case the slope is proportional to the $t^2/12$ and would thus give a measure of the thickness of the plate like structure.

At the highest values of Q, when one is looking at length scales smaller than the dimensions of the object itself, small-angle scattering probes the interface between the particle and the solvent. At sharp interfaces, the intensity falls of as Q^{-4} [63, 133, 129] and the measured intensity at high Q can be approximated as $I(Q) \approx AQ^{-4} + B$ where A is proportional to the coherent scattering cross-section and B is the constant background. This limit is called the **Porod Scattering** from Porod's work on scattering from the asymptotic limit [133].

4.3.3 Data Analysis: Model Free Analysis

SANS data in Q space is difficult to visualize, particularly if the scattering is from objects of irregular shapes. A complimentary way of data analysis by Glatter, Svergun in the late 70's helps to mitigate this problem. This is achieved by Fourier transforming I(Q) into a pair distribution function P(r) according to

$$P(r) = \frac{1}{2\pi^2} \int_0^\infty I(Q) Qr \sin(Qr) dQ \tag{4.17}$$

Since this transform is infinite with respect to Q, and indirect Fourier transform (IFT) method was proposed by Glatter [133] and by Svergun [134, 135] in independent implementations. In the work presented in this thesis, a free version of this technique, an implementation by Svergun, called GNOM has been used (see http://www.embl-hamburg.de/ExternalInfo/Research/Sax/gnom.html).

IFT uses a least squares fit of the amplitudes c_i of a set of N Fourier-transformed equidistant B-spline functions ϕ_i [1], or other basis functions, like Hermite polynomials [134, 134] which form a complete set, to the measured scattering curves for obtaining the smoothest function $P(r)$ that will fit the scattering data the best.

$$I(Q) = \int_0^{D_{max}} P(r) \frac{\sin(Qr)}{Qr} dQ, \text{ where } p(r) = \sum_{i=1}^{N} c_i \phi_i(r) \tag{4.18}$$

In the above equation, the integral over r is limited to D_{max}, i.e., it puts a limit on the system to consist of non-interacting particles with a maximal dimension D_{max} at low concentrations. In this regard, the method requires an independent estimate of D_{max} before hand. For particles with a center of symmetry, this technique can also be deconvoluted, to obtain the radial scattering length density profile $\rho(r)$ [1]. Also, the radius of gyration R_g is calculated from $P(r)$ using

$$R_g = \frac{\int_0^{D_{max}} P(r)r^2 \, dr}{2 \int_0^{D_{max}} P(r) \, dr} \tag{4.19}$$

4.3.4 Data Analysis: Model Based Fitting

The main result from the previous section relevant for scattering from a molecular aggregate of some shape can be summarized as

$$I(Q) = \frac{d\Sigma}{d\Omega}(Q) = \frac{N}{V} \frac{d\sigma}{d\Omega}(Q) = \frac{1}{V} \left| \int \bar{\rho}(\boldsymbol{r}) e^{i\boldsymbol{Q}r} d^3\boldsymbol{r}_1 \right|^2 \tag{4.20}$$

To clarify our notation $\sum = \sigma/V$ is the **Macroscopic Cross section** For a two phase system, for instance a collection of objects immersed in a solvent, the SLD variation in the scattering process results in

$$\frac{d\Sigma}{d\Omega}(Q) = \frac{1}{V}(\rho_1 - \rho_2)^2 \left| \int_{V_1} e^{i\boldsymbol{Q}\cdot\boldsymbol{r}} d^3\boldsymbol{r}_1 \right|^2 \tag{4.21}$$

The integral in Eqn. 4.21 is referred to as the **Form Factor** or just P(Q) and is a characteristic of only the geometry and shows that scattering from a two phase system is proportional to the square of the SLD difference. The term $(\rho_1 - \rho_2)^2$ is termed as the **Contrast Factor**. However, if the object has a non-homogeneous composition, i.e the SLD varies between different parts, then the SLD variation also has to be included in the integral.

Table 4.3: Form Factors for some common geometries relevant to this work from [1]

Geometry	P(Q)
Sphere (R=radius)	$\left(3\frac{\sin(QR)-Qr\cos(QR)}{Q^3R^3}\right)^2$
Cylinder/Disc (R=radius, L=length)	$\int\left(\frac{J_1(QR\sin\theta)}{QR\sin\theta}\frac{2\sin(QL\cos\theta)}{QL\cos\theta}\right)^2\sin\theta\,d\theta$
Ellipsoid (Axes a,b)	$\int\left(\frac{J_1(x)}{x}\right)^2\cos\theta\,d\theta$ with $x=Q[a^2\sin^2\theta+b^2\cos^2\theta]^{1/2}$
Lamellar (Thickness=δ) (σ: variation in $\delta\equiv\delta\times$Polydispersity)	$\frac{2}{q^2}\left[1-\cos(Q\delta)e^{-Q^2\sigma^2/2}\right]$
Parallelepiped (Edge lengths A,B,C)	$\int\int\left(\frac{\sin(QA/2\sin\alpha\sin\beta)}{QA/2\sin\alpha\cos\beta}\frac{\sin(QB/2\sin\alpha\cos\beta)}{QB/2\sin\alpha\cos\beta}\right)^2\times$ $\left[\frac{\sin(QC/2\cos\alpha)}{QC/2\cos\alpha}\right]^2\cdot\sin\alpha\,d\alpha\,d\beta$

For simple geometrical shapes with some symmetry, the integrals can be evaluated analytically. For anisotropic shapes like ellipsoids and cylinders, the scattering intensity depends on the relative orientation of the particle and the scattering vector. So a final numerical integration over all possible orientations in solution scattering, also has to be performed [1]. A list of form factors for some of the common shapes, particularly relevant to this work are included in Table 4.3.

The scattering length density is usually not constant throughout the volume of macromolecular aggregates. In the case of lipids (the primary sample component in this work) in particular, the head groups and tail are known to have very different SLDs. For such compound objects, the form factors have to be modified. Several illustrations of this calculation for core-shell disc models and parallelepiped models are included in **Appendix B and C**.

Armed with a list of analytical expressions for form factors, a non-linear least-squares fitting of the data can be performed to obtain the characteristic dimensions of the particle. The SANS Analysis package, written in Igor Pro (http://www.wavemetrics.com)

developed at the NIST Center for Neutron Research (NCNR) [136], as well as extensions developed in this work, have been used to do model fits to the scattering data in this work. Non-linear least squares fitting has mostly been done using an implementation of the Leveneberg-Marquardt algorithm in Igor-Pro.

4.4 Contrast variation in SANS

From the previous section, it is clear that for composite materials containing phases with different chemical compositions (or different SLD's), the 'macroscopic' scattering equation is a function of the average spatial distribution of SLD of its constituent phases (in Chapter 5, SLD's with neutrons and X-rays, for the constituents of lipids used in this study are included; see Table 5.2).

From Eqn. 4.14, for a composite object, composed of two units of some shape and component volumes V_1 and V_2, the resultant scattering intensity is given by

$$
\begin{aligned}
I(Q) &= \frac{1}{V}\left\langle\left|\int(\bar{\rho}(r)-\rho_0)e^{i\boldsymbol{Q}r}d,\vec{r}\right|^2\right\rangle \text{ where } V = V_1 + V_2 \\
&= \frac{1}{V}\left\langle\left|(\bar{\rho}(r_1)-\rho_0)\int e^{i\boldsymbol{Q}r_1}d,\vec{r_1} + (\bar{\rho}(r_2)-\rho_0)\int e^{i\boldsymbol{Q}r_2}d,\vec{r_2}\right|^2\right\rangle \\
&= (\bar{\rho}(r_1)-\rho_0)^2 P_1(Q) + (\bar{\rho}(r_2)-\rho_0)^2 P_2(Q) + \text{ cross term}
\end{aligned}
$$

Due to the large difference in scattering length densities between D_2O ($6.36 \times 10^{-6}\text{Å}^{-2}$) and H_2O ($-0.6 \times 10^{-6}\text{Å}^{-2}$), the solvent SLD term ρ_0 in the above equation can be varied, such that either

1. $\bar{\rho}(r_1) = \rho_0$ so that I(Q) $= (\bar{\rho}(r_2)-\rho_0)^2 P_2(Q)$
2. $\bar{\rho}(r_2) = \rho_0$ so that I(Q) $= (\bar{\rho}(r_1)-\rho_0)^2 P_1(Q)$

By selective choice of the solvent, the form factors for the two components can be separated. Similarly in a multi-component aggregate, by changing the SLD of the sol-

vent, which can be achieved by altering the ratio of D_2O and H_2O , size and shape of individual components can be obtained. This is called **External Contrast variation**. As an extension of this idea to more complex shapes, one can also selectively deuterate particular functional groups in a large macromolecular aggregate, resulting in **Internal Contrast Variation**. These two contrast variation techniques can be used very effectively to highlight/emphasize selected parts of the macromolecular sample. The internal contrast variation technique is particularly relevant, when the SLD of the composite object is very small, so that external contrast variation would require large amounts of hydrogenated solvent which would also give rise to huge incoherent background. In order to keep the background minimum, deuterated solvent in conjunction with deuteration of parts of the composite object is preferred. We emphasize here that such 'contrast variation' by isotopic substitution does not change the chemical properties of the system, while some physical properties show slight variations (see for e.g. Section 2.4.1) from the regular hydrogenated components. Since lipids, the primary sample component in this work, are hydrogenated and have a very small overall SLD of $0.67Å^{-2}$, hence in this work, we use internal contrast variation, by selectively deuterating one component of the assembly.

4.5   Xray Scattering

The scattering concepts presented in the earlier sections apply equally well to X-rays as well with some modifications that will be noted here. Foremost, X-ray scattering is an older field than neutron scattering as the first X-ray diffraction from a crystalline sample was produced way back in 1912, many years before Chadwik's discovery of the neutrons. As X-rays are electromagnetic radiation, they will interact strongly with the electron cloud of an atom, necessitating a quantum mechanical treatment of the scattering problem. But as shown by Warren [137], a classical calculation, like the neutron case is sufficient. The main differences between the two sources are:

1. Since X-rays scatter from electron cloud, the scattering strength of an atom scales with its atomic number Z. As a result light atoms like hydrogen that are one of the main components of biological matter, are very weak scatterers. So, unlike neutron scattering, one cannot vary the contrast of a sample without substitution by a heavier element which can drastically affect the phase behavior of the system.

2. As X-rays scatter from electrons through electromagnetic interaction, there is no incoherent scattering associated with different spin states as there is in the neutron case. Incoherent contribution comes due to Compton scattering, but as it varies directly with scattering angle, it can easily be accounted for.

3. Ionization effects from intense X-ray irradiation can damage biological samples.

X-ray scattering is in fact used to great advantage in this work, due to the improved resolution at small length scales (higher Q) where incoherent scattering start dominating with neutrons. As X-rays and neutrons scatter differently from different components of the same system based upon the contrast factor, the information obtained is in essence 'complimentary'. For instance, a barely visible peak with neutrons (due to large background) may be easily distinguishable with X-rays.

Chapter 5

Low temperature Assembly in DMPC/DHPC Mixtures

5.1 Introduction

'Bicelles' or discoidal micelle forming mixtures, in particular the combination of DMPC(or C14)/DHPC(or C6) phospholipids, have been widely studied for various applications ranging from substrates for hosting membrane proteins and their crytallization to alignment media for high resolution NMR based protein structure determination. Consequently, their characterization has been undertaken by many groups in the literature. To name a few, Arnold and coworkers reported disc of diameter $\sim$300-500 Å [138] based on scanning electron microscopy (SEM) images and nuclear magnetic resonance (NMR) (in conjunction with a disc based model); Glover and coworkers have reported 30-100 Å radii discs based on dynamic light scattering (DLS) and NMR [99]; Edwards and coworkers reported 40-200 Å radii based on DLS and cryo-TEM [74], while Nieh and coworkers reported bicelles ranging in size from 100-250 Å [105, 101, 108] (also reported a concentration depen-

dence in the latest study) based on small angle neutron scattering (SANS) measurements. These studies, conducted in different ranges of the lipid composition and temperatures, have interpreted their results with the predictions of the Ideal Bicelle Model (IBM, discussed further in the next section), which would give a linear relationship of the aggregate size on the molar ratio of the two species mixed, assuming they are completely segregated [89, 98]. Clearly there is lack of agreement between results obtained by different techniques and based on different sample conditions.

From the discussion in Chapter 2 (see Section 2.5.1), the presumed discoidal aggregates and their measured radii in studies conducted above 24°C is questionable. Consequently the recently proposed 'Mixed Bicelle Model' in place of the IBM, by Triba and coworkers is somewhat suspect, even if its assumptions are valid [106, 139]. In fact, as shown by Nieh's recent study and included in Fig. 2.10b, it is quite clear that the range of existence of discoidal aggregates, even in the low temperature part of the temperature-composition phase diagram is highly dependent upon the molar ratio $q = [Long]/[Short]$ of the two lipid species. Nieh's, Glover's and van Dam's data are the only ones conducted at low temperatures between 10-20°C , in the supposed discoidal phase. But on assuming the IBM for a segregated discoidal aggregate, the role of the other sample and thermodynamic parameters, concentration and temperature, in defining the aggregate size becomes immediately questionable. Additionally, in it's current form, the IBM does not place any limit on the disk sizes obtained in such mixtures. While recent results from TEM suggest an upper limit of disk sizes obtained from such mixtures [74, 140].

From the work of Nieh and coworker's, even if the existence of the discoidal geometry at low temperatures is accepted, it is imperative to clarify the difference in the predictions of the quantitative models currently used in the literature [89, 106], and even more to clarify details of lipid packing, in the IBM or the Mixed Bicelle scenarios. This would also serve to quantify the results from samples of different composition and by different groups. This chapter is thus based on the DMPC/DHPC or C14/C6 (used interchangeably,

see Chapter 3) lipid mixtures in the low temperature phase only at 10°C .

5.2 Ideal Bicelle Model (IBM)

First, we briefly review the main ideas of the *Ideal Bicelle Model*(IBM), its under-
lying assumptions and limitations. Then we apply it to our mixed lipid system, and finally
propose corrections to the model based on our results.

The discoidal morphology has been explained in the literature via the IBM pro-
posed by Vold and Prosser [89, 97] and assumes complete segregation of the two lipids
based on their curvature propensities. Such a segregated aggregate, where the short chain
phospholipid favoring high curvature, sits in the rim and the long tail phospholipid favoring
zero or negligible curvature sits in the planar part of the disk, was originally proposed in
phospholipid mixtures by Gabriel and coworkers for their DPPC/DHeptanoylPC (C16/C7)
system [92, 141, 95]. Building on the segregation hypothesis, Vold and coworkers identi-
fied the molar ratio of long-tail to that of the short tail lipid in the mixture q as the key
parameter governing bicelle sizes. For a disc of core of radius R_c and thickness t with a
hemispherical curved rim of radius of curvature s as shown in Fig. 5.1 (so that $t = 2s$),
areas of the core and rim A_{core} and A_{rim} are

$$A_{core} = 2\pi R_c^2, \qquad A_{rim} = 2\pi(R_c + 2s/\pi)\pi s \qquad (5.1)$$

Further, the molar ratio of the two lipids $\frac{[C14]}{[C6]}$, was assumed to be equivalent to
the ratio of those two areas, giving

$$q = \frac{A_{core}}{A_{rim}} = \frac{2\pi R_c^2}{2\pi(R_c + 2r/\pi)\pi r} \qquad (5.2)$$

Denoting $q \to q_A$ and solving for $R_c \to R_A$, the **Vold Eqn.** for total bicelle radii
is

$$R_A = R_c + s = \frac{q_A s}{2}\left(\pi + \sqrt{\pi^2 + 8/q_A}\right) + s \qquad (5.3)$$

While in another recent study by Triba and coworkers, it was proposed that volumes ratios of the bilayer disk and rim should be used as a measure of the molar ratio of the two lipids [106]. They also proposed an ellipsoidal rim in place of the hemispherical rim, in light of the chain length difference between the two lipids. As shown in the geometry in Fig. 5.1, besides the bilayer core of radius R_c and thickness t, now there is also a rim of curvature r, where $r \neq t/2$. For such a geometry, using the expressions for the volumes of the core and rim given by

$$V_{core} = \pi R_c^2 t, \qquad V_{rim} = 2\pi \left(R_c + \frac{4r}{3\pi} \right) \frac{\pi r t}{4} \tag{5.4}$$

and by a similar argument of proportionality of q to volume ratios V_{core}/V_{rim}, and denoting $q \to q_V$ and $R \to R_V$, **Triba Eqn.** for the bicelle radius is given as

$$R_V = R_c + r = \frac{q_V r}{4} \left(\pi + \sqrt{\pi^2 + \frac{32}{3 q_V}} \right) + r \tag{5.5}$$

The Triba expression, Eqn.5.5 is seen to have similar dependence as the Vold expression, Eqn. 5.5 except for the factor of two difference. Also drawn for reference is a discoid with a rim of rectangular cross-section of width ΔR and same thickness. This model will be used later in section 5.4.3. For such a disk, referred as *Pcshl disk*, the volume argument would give the **Pcshl Equation.**

$$R_{PV} = R_c + \Delta R = \frac{q_V \Delta R}{4} \left(1 + \sqrt{1 + \frac{1}{q_V}} \right) + \Delta R \tag{5.6}$$

All the three geometries have been drawn such that the net disk dimension is the same

$$R = \text{core radius } (R_c) + \text{ rim curvature } (s, r, \Delta R)$$

The three expressions in Eqn. 5.3, 5.5 and 5.6 are plotted in Fig. 5.1(b) for s=22 Å, (for t= $2 \times s$= 44Å, corresponding to bilayer thickness of C14 lipids [38, 142]) and $r = \Delta R = 17$ Å (for radius of curvature of C6 lipids, Table 2.1). All of them show the direct proportionality of disc radii to q. While the Triba and Pcsl models are reasonably

close, as both are based on the volume packing argument, the factor of two difference as noted above, from the Vold Eqn. which is based on area argument is obvious. This point of difference will be taken again in the discussion section.
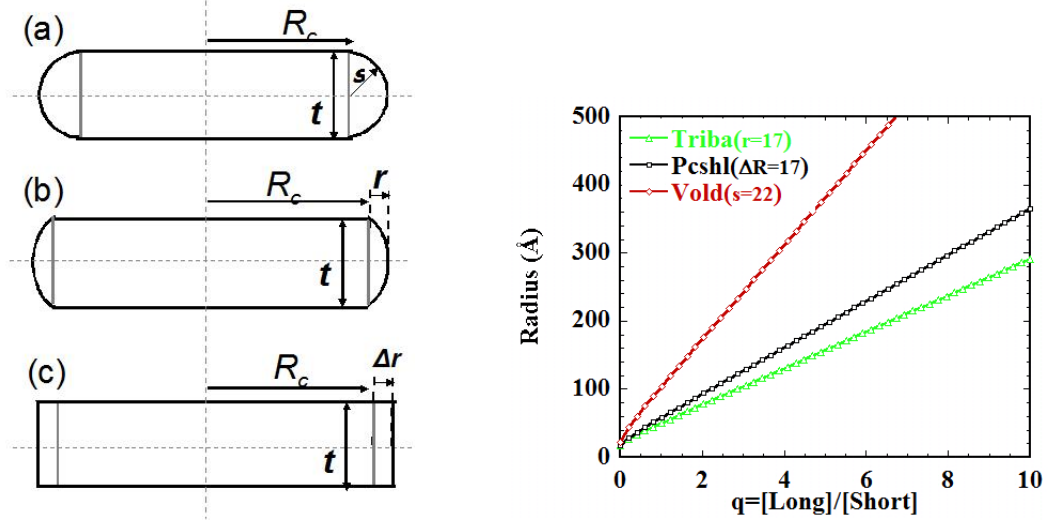
Figure 5.1: *Left*: Proposed geometries for a discoidal bicelle: circular bilayer core of radius R_c and thickness t surrounded by rim of different cross-sections (a) hemispherical rim of curvature $s = t/2$, (b) ellipsoidal rim $r \neq t/2$ (c) rectangular rim $\Delta R \neq t/2$. *Right*: IBM variation of bicelle radii from Vold (Eqn. 5.3) Triba's (Eqn. 5.5) and Pcshl (Eqn. 5.6) expressions.

In both the Vold and Triba expressions for bicelle radii, there is a fundamental problem. The expression for R_A will hold true, if and only if the head group areas of C14 and C6 lipids are the same. To a first approximation C14 and C6 have the same head group chemistries, so they should have same areas. But from surfactant literature [143, 144, 30] we know that based on packing parameters and geometry of the final aggregate, effective head group areas can differ significantly. Similarly R_V will hold true if and only if the volumes of the two lipids are same, which is clearly not the case.

In light of the above discrepancies as well as absence of a satisfactory model correlating results on the discoidal phase for different sample parameters, we have done a systematic study in the low temperature regime at 10°C , exploring the variation of those

77

two key parameters:

1. The total lipid concentration $c = [Long] + [Short]$.

2. The molar ratio of the two lipids $q = [Long]/[Short]$.

As noted in Chapter 2, we emphasize again the difference between Q and q. While Q as defined in Chapter 4 refers to the scattering vector, from this chapter onwards the notation q with small letter, is used to denote the measured molar ratio of the long to the short lipids. Thus q and Q are not related and we have just adopted the literature notations for both the quantities. In this chapter q refers to the C14(or DMPC) and C6 (or DHPC) lipid mixtures and in the following chapters, it will be used to denote molar ratios of other long/short lipid mixtures.

In the following section, we describe our experiments and the results obtained followed by a discussion on how our data clarifies not just the morphology, but also details of the molecular packing in the aggregate. Further, we attempt a brief analysis of existing theories on stability and occurrence of the discoidal phase in lipid mixtures.

5.3 Experimental Details

In order to understand the structure of the aggregates formed, and the parameters driving their self-assembly, we did systematic SANS measurements on a relatively dilute system of DMPC(C14)/DHPC(C6) system at 10°C varying total lipid concentrations $c = [C14] + [C6]$ in the range 0.005-0.10 g/ml at fixed $q = [C14]/[C6]$. These $c - series$ samples were made by dilution from a stock solution at each of the fixed q values: 1.5, 2, 2.6 and 3.2 and 4.0; and the initial 0.10 g/ml as well as the diluted samples at c=0.025 g/ml form a $q - series$ at fixed concentration. We note here that the samples were made up of hydrogenated lipids in 0.2M salt solution of D_2O (as described in Chapter 3), since that gives the maximum contrast between the fully hydrogenated lipid assembly and the

solvent and also the lowest background. The salt solution was chosen to avoid inter-particle interactions from residual charges on the zwitterionic head groups (seen in early work, but later found to be from impurities). As discussed in Section 2.4.1, for the purpose of the experiments discussed in this work, use of such a solvent does not change the properties of the assembly.

To elucidate details of the internal structure and its composition, the 'contrast enhancing' technique with SANS is used (see Chapter 2 and Section 4.3.4). This involves samples with head group and tail deuterated-C14 (dC14, see Fig. 3.1(a)) and hydrogenated C6 of $q = 2$ and c=0.02, 0.03 and 0.05 g/ml, in deuterated solvent. This unique combination of lipid deuteration gives the best contrast between the components to understand the local structure and lipid distribution in the aggregate as we show further in this chapter. The use of deuterated C14 changes only the T_m and does not affect the assembly in this study at 10°C (see Section 2.4.1). This is the first such study using internal contrast variation in phospholipid 'bicelle' mixtures probing the details of the composition in the assembly. We mention here that the only other study using contrast variation on phospholipid mixtures, used partially deuterated lipids in mixtures of H_2O and D_2O , and in a very limited range of wave vectors, unlike this study [95]. All measurements were at T=10°C on NG3 and NG7 SANS instruments as discussed in Section 3.2.5.

5.4 Results and Analysis

5.4.1 DMPC(C14)/DHPC(C6) $q - series$

First we report results from the C14/C6 samples prepared with different molar ratios of the long and short lipids $q = [C14]/[C6]$ but having the same total lipid concentrations $c = [C14] + [C6]$ of c=0.025 g/ml and c=0.01 g/ml. We call both these series as $q - series$ at different total lipid concentrations. Scattering intensity as a function of the wave vector Q from the two q-series are shown in Fig. 5.2(a) and (b).
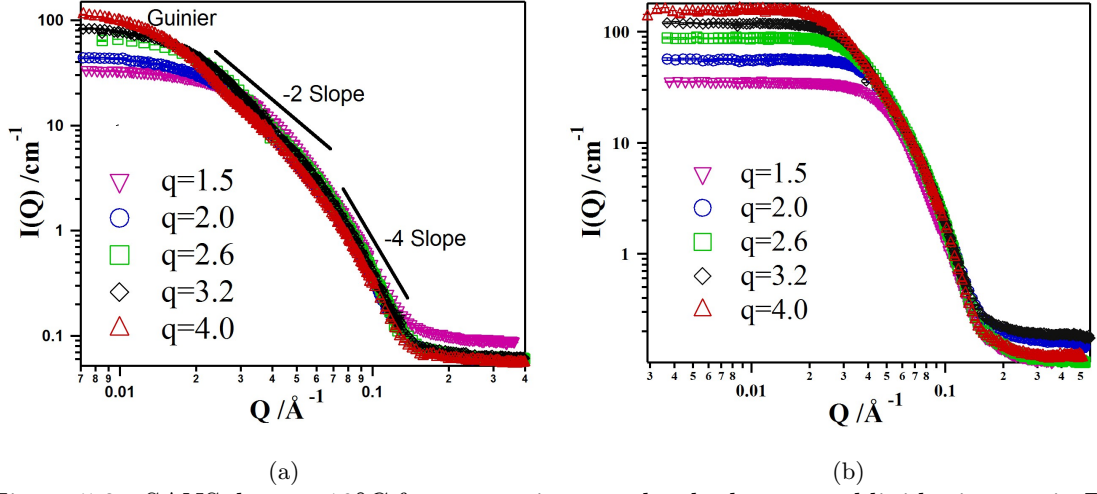
Figure 5.2: SANS data at 10°C from $q-$series samples, hydrogenated lipid mixtures in D_2O , at two different total lipid concentrations c=[C14]+[C6]. (a)c=0.025 g/ml and (b)c=0.1 g/ml

From Fig. 5.2, it is clear that all the samples show similar scattering profiles: a flat Guinier regime at the lowest Q, characteristic of discrete objects, followed by a Q^{-2} dependence in the intermediate regime, characteristic of scattering from planar objects, and ending with a steep decay at large Q, where $QR \gg 1$ (at the highest Q, the Q independent incoherent background from the hydrogens, overtake the scattering from the sample) [133, 63]. This is consistent with the predicted discoidal morphology. We also see an increase in the low Q scattering and a shift of the Guinier regime to lower Q, indicating that the scattering units in both these series of lipid mixtures are increasing in size with increasing q. This is also consistent with the expectations of the IBM.

The data at intermediate scattering vectors in all the samples overlap, indicating that they have similar cross sections, while there are smaller variations at the highest wave vectors, due to the effect of hydrogen content of the lipids (in the sample) on the background. The cross-sectional variation, if any can be quantified by measuring the cross-sectional Guinier radius of these samples (Section 4.3.2). This approximation is valid for objects whose length/width dimension is bigger than the thickness. Fig. 5.3(a), shows the

modified *Guinier* plot, also called the *Kratky − Porod* plot for the two q-series, obtained by plotting $ln(Q^2I(Q))$ vs Q^2. All the samples show the linear regime in the intermediate Q-range (0.035 < Å $^{-1}$ Q < 0.13 Å $^{-1}$) with the same slope R_t. The cross-sectional Guinier radius obtained from the slopes of the fitted line are related to the total thickness of a planar object by $R_t^2 = t^2/12$ (Table 4.2). Results from these fits are listed in Table 5.1.

It is important to point out that the disc thickness, which really corresponds to the thickness of the (long) lipid C14 bilayer (at the center of the discoids), obtained by this method at ≈ 44 Å, is less than the 50 Å obtained by Nagle and coworkers from X-ray diffraction measurements on multi-lamellar (MLV) dispersions of pure C14 lipids [38, 39] and also our own results from core-shell model fits to the SANS data (explained further in this chapter). As has been noted before, this systematic difference comes from the first order approximation of the SLD (scattering length density, see Chapter 4) variation across a bilayer. It corresponds to the head-to head distance in the bilayer [142], which is composed of head and tail of very different SLD. In this context, we use 44 Å as a measure of relative changes in the disc thickness across different mixtures, and not as the absolute thickness.
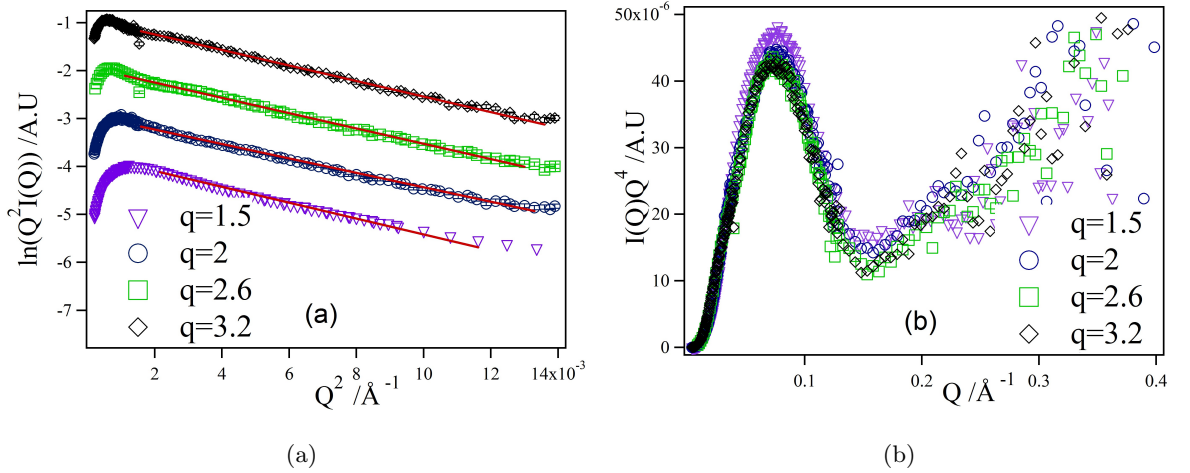
Figure 5.3: All samples in the $q−$series have the same cross-section. (a) Modified Guinier Plots of $q − series$ at 0.025 g/ml showing same slope of $t^2/12$ (b) IQ^4 vs Q plots (here I stands for $I(Q) − Background$; background is obtained from the high Q limit of the scattering data) in the Porod regime and highlighting the same cross-sectional thickness.

Table 5.1: Bicelle dimensions for $q-series$ obtained from Guinier Fits.

c (g/ml)	q	t*	Full R$_g$	Disk Radius[†]
0.03	1.5	44.6	46.5±0.09	63.5
0.03	2.0	45.5	59.2±0.17	81.9
0.03	2.6	43.4	66.3±0.13	92.0
0.03	3.2	44.1	72.1±0.16	100.2

*   Less than half an Å uncertainties are not included

†   Uncertainty in radius, propagated from that in R$_g$ is less than a percent and not included.

Furthermore, features of the scattering curve in the intermediate to high Q limit, can be enhanced by plotting $(I-Bgrd)\times Q^4$ vs Q as shown in Fig. 5.3(b). By looking at the Porod limit, the smallest length scale in the aggregate is highlighted (Section 4.3.2). The constant peak position in the intermediate Q shows constant thickness of the aggregates. While the surface to volume (S/V) ratio of discs, of radius R and thickness t in the highest Q limit, which varies as $(1/R + 1/t)$, is not resolvable given the level of statistics in this region.

Finally, Guinier fits $lnI(Q)$ vs Q^2 are used to obtain the overall dimensions of the disk R using the relation $R_g^2 = \frac{R^2}{2} + \frac{t^2}{12}$ (see Section 4.3.2) and an average thickness of $t = 44$ Å, from Table 5.1 for the disc thickness. The difference in radii obtained by using a 44 vs 50 Å thickness from this methods, is only between 1-2 Å or lower. Further, as expected from the contributions of the radius and thickness terms in the R$_g$ relationship, the difference is highest when the disc dimensions are nearly the same as its thickness, which is true for only a few of the samples considered in this study. Dimensions of the $q-series$ samples are also included in Table 5.1.

5.4.2   DMPC(C14)/DHPC(C6) $c-series$

Fig. 5.4, shows data from two different $c-series$ made out of stocks of lipid concentration c=0.1 g/ml at molar ratios (a) $q = 2$ and (b) $q = 4$. All the samples were made by dilution to the final concentration. The samples shown in Fig. 5.4 were transparent

and had minimal viscosity like that of water. Though the lowest concentration samples for each series, $c \sim 0.005$ g/ml were turbid white and, scattering results from those are discussed later in section 5.4.5.

Data from both the series, show that although the molar ratio remains fixed, the Guinier regime clearly shifts towards lower Q as the total lipid concentration is reduced, again indicating increasing sizes of the scattering units. These observations are consistent with those of Glover [99], but clearly contradict the expectations of the fully segregated IBM, since in that model an increase in bicelle size demands an increase in q: the ratio of long chain lipid to the short chain lipid in the sample, as the presumed parameter governing their growth.

(a)   (b)
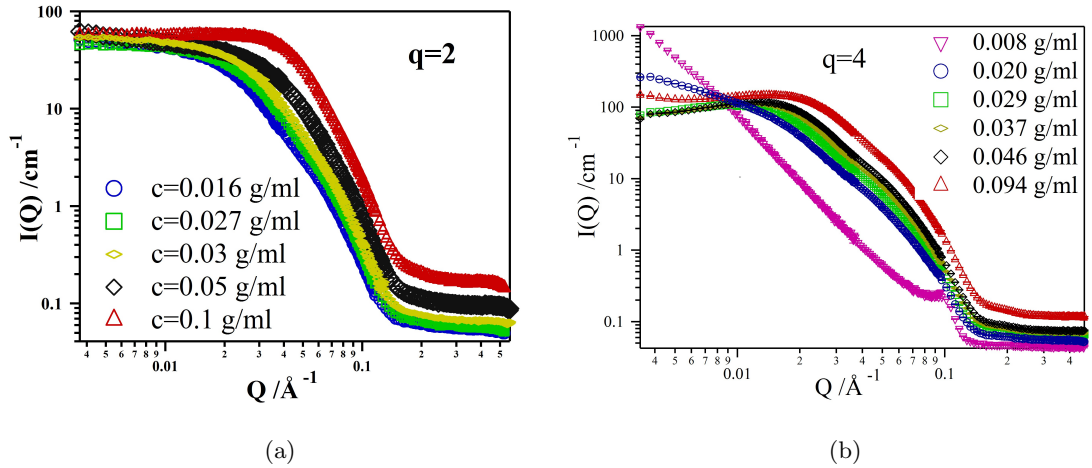
Figure 5.4: SANS data at 10°C from c-series samples: hydrogenated lipid mixtures in D_2O , at the same molar ratio (a) $q = [C14]/[C6] = 2.0$ and (b) q=4.0, but at different total lipid concentrations $c = [C14] + [C6]$.

A Guinier analysis of the overall size variation provides a simple quantification of this effect. Figure 5.5 shows Guinier plots ($lnI(Q)$ vs Q^2) of the low Q scattering data from a few of the samples of the $q = 2$ series. For each sample the linearity of lnI vs Q^2 is consistent with scattering from single particles, falling from a maximum intensity at $Q = 0$ as $exp[-(QRg)^2/3]$. Then for aggregates with disc-like structure, the radius of gyration R_g

is used to obtain the aggregate dimensions as noted before and given in Table 4.2.

From the changing gradients of the fits to the data in Fig. 5.5 we may infer that the radius of gyration, R_g of the scattering particles through the series c=0.016, 0.024 and 0.05 g/ml decreases from 67.6 Å through 58.9 Å to 43 Å. Results from Guinier fits to all the samples are included in Table 5.3. Assuming discoids with a thickness equal to that of bilayer formed by the long chain C14 $t \sim 44$ Å, these results would indicate that as the concentration increases by a factor of three from 0.016 to 0.05 g/ml, the overall radii far from remaining constant at the q value must be nearly halved, changing from 93 Å to 57 Å. In the context of the IBM we can interpret this as a lower availability of short chain rim lipid relative to the core lipid at lower concentrations than the constant ratio we might expect from relative solution concentration in the sample series (discussed further in this Chapter). Similar results were obtained for other $c - series$ at fixed q values of 1.5, 2.0, 2.6, 3.2 and 4.0. The overall aggregate dimensions obtained from the Guinier fits to all the samples measured, assuming rectangular cross-section, are included in Table 5.3. For disks with hemispherical, elliptical or rectangular cross-sections, **Appendix A**, includes the derivation and results for the relation between the overall dimensions and the R_g. Only a few Å difference is observed in the overall dimensions, so that, for the rest of the discussion in this chapter and elsewhere, only the simpler rectangular cross-section is assumed.

5.4.3   Disk Form Factor Analysis

In order to fit the scattering intensities shown in Fig. 5.2, and in Fig. 5.4 over the entire Q range, we developed the Polydisperse Core-shell Disc model (Pcshl disk), a slight variant of the Core-shell Cylinder (or disc in the appropriate limit of its length) model used by Nieh and coworkers [101, 104]. Details of these models (and other types of SLD variation) are included in **Appendix B**. A schematic description of the commonly understood shape of the bicelle with in this scattering geometry is shown in Fig. 5.6. It also shows the variation of scattering length density (SLD) across and perpendicular to the bilayer, based
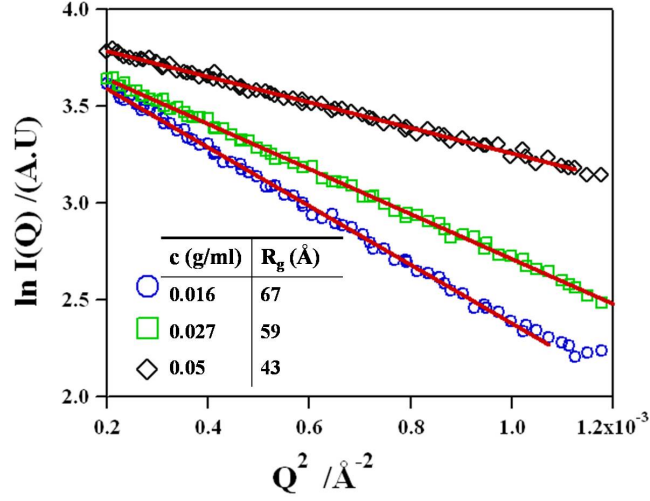
Figure 5.5: Guinier fit to the scattering data at 10°C from $c - series$ samples for $q = [C14]/[C6] = 2$ at varying total lipid concentrations $c = [C14] + [C6]$.

on the composition of the constituent elements of the lipid tail and head groups (Chapter 4). A table of SLD for the different lipids and their tail and head groups, used in this study are listed in Table 5.2. This table includes some values derived from our measured densities, while others are estimates from theoretical values of the density (assuming volume of the lipid from Tanford's formulae, Eqn. 2.8 and mass from formula weight). For hydrogenated lipids, our measured values are in good agreement with those reported in the literature [56] and more recently by Pencer and coworkers [145] (even though there is some difference in choosing wether the glycerol carbon should be part of the headgroup or the tail region). For deuterated dC14 lipid, no literature references for its molecular volume, or SLD were found for comparison.

The Polydisperse core-shell disk form factor models the disks with the internal structure of the lipids by assigning the hydrophobic lipid core of thickness t_c and radius R_c with a uniform scattering length density (SLD) ρ_c. Notice the similarity of the *two-step SLD profile* in both the planes of the disc in Fig. 5.6. This SLD profile is the next best

approximation to the *one-step* profile assumed in the R_g calculations before, and has been shown to be a good approximation [142, 146] of the detailed underlying profile for a lipid molecule. The hydrophilic head groups of the lipids are represented by a face shell thickness Δt, a radial shell thickness ΔR and a SLD of ρ_s; so that the overall radius of the bicelle is $R = (R_c + \Delta R)$ and the thickness $t = (t_c + 2\Delta t)$. Even though the shell thicknesses on the face and the rim are independent, the SLD of the shell ρ_s is uniform. In contrast to the core-shell disc model used by Nieh et al., where the entire shell, on both the face and the rim is of uniform thickness, this model is better suited to capture variations in shell thickness. This feature of the model is particularly relevant for modeling data, when the contrast in the radial and perpendicular directions of the disc are very different, as we show in the next section.

A mentioned before, the total radius R of the bicelle is the sum of the core radius R_c and the rim curvature s, r or ΔR for the differently shaped rims (Fig. 5.1). For ease of modeling the scattering data, instead of a bicelle with hemispherical rim of curvature with $s = t/2$ or an ellipsoidal rim of curvature r, this model assumes a rectangular cross-section ΔR and the thickness t of the bicelle is equal to the C14 bilayer thickness.
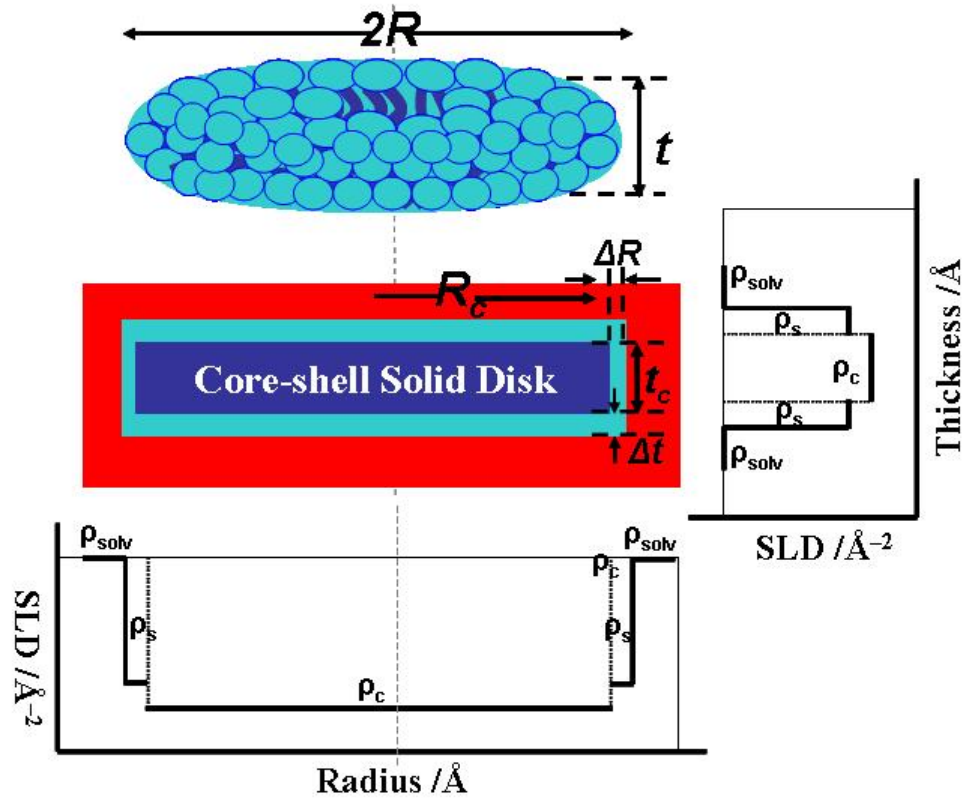
Figure 5.6: Cartoon of a core-shell disk illustrating the geometry and SLD variations. Color coding highlights the inhomogeneous nature of the assembly. Dark blue lipid tails form the interior core, light blue head group form outer shell. The disc is immersed in red D_2O solvent. SLD variation across (radial) and perpendicular to the bilayer plane are similar and follow two-step density profiles.

Table 5.2: Densities and SLDs of phospholipids and their constituents at 10°C used in this study.

Lipid	Formula	ρ (g/cm^3)	SLD$_{Neutron}$ (10^{-6}Å^{-2})	SLD$_{X-ray}$ (10^{-6}Å^{-2})	Density Method
C14	C36H72NO8P	1.0807	0.295	9.68	Densitometry
-"-		1.09	0.307		Estimate from Mol. wt & lipid volume from Nagle [38]
Tail	C28H58	0.814	-0.382	7.92	Estimate from Mol. wt. & double tail volume
Head	C8H14NO8P	1.69	2.21	15	Estimate from Mol wt. & HG Vol.
dC14	C36H5D67NO8P	1.1404	6.71	9.74	Densitometry
-"-		1.196	7.06	10.3	Estimate from scattering length ratio h/d-DMPC
-"-		1.24	7.31	10.7	Empirical: $1.15 \times \rho$ h-DMPC
Tail	C28D58	0.934	7.11	7.89	Estimate from Mol. wt. & double tail volume
Head	C8H5D9NO8P	1.74	5.57	15	Estimate from Mol wt. & HG vol.
C6	C20H40NO8P	1.1668	0.686	10.7	Densitometry
Tail	C12H26	0.752	-0.464	7.36	Estimate from Mol. wt. & double tail volume

Because both C14 and C6 head groups have identical chemical composition, we assigned the same SLD for the face and rim shells. The quality of fits obtained by using Δt and ΔR as free and independent parameters was tested from that of the core-shell disc model (for which $\Delta t = \Delta R$), as it would also minimize the number of floating parameters in our fits. These two conditions might not be absolutely true as

(1) Water penetration can cause significant changes in the SLD values of the lipid head groups [147]. With C14 and C6 occupying the face and the curved rim of the bicelle, the SLD of their head group is expected to be different as more water can penetrate the C6 hydrophilic part because of curvature.

(2) The molecules in the curved rim might experience less stress and their head group extension might be slightly different.

The quality of fits in those two cases (Pcshl disc and core-shell, ours vs Nieh models) was not substantially different when used for the SANS data of the fully hydrogenated samples. We also found that the computational cost of a more sophisticated model using different SLDs for the rim and central core head groups (to account for the points 1-2 above) did not result in significant improvement in the quality of fits for the SLD profile. (**Appendix B**: Form factors for inhomogeneous core-shell discs). On the same lines, the effective resolution of our SANS measurements also does not allow us to resolve details of a curved rim. In fact, excellent fits to our data were obtained with bicelles represented as a solid disk with a *two step SLD profile* showing contrast between tail and head groups and between the lipid head groups and the solvent- with the curved rim represented by a flat edges as in Fig. 5.6. In order to capture the high Q scattering accurately, we added a polydispersity in the disk radius. This polydispersity is included by integrating the form factor over a Schultz distribution [148, 149] of the cylinder radii. There is an excellent agreement between the data and this model over the entire Q range for both the c- and q-series data, which confirms the essentially discoidal shape of these self-assembled aggregates in these

lipid mixtures. Figure 5.7 shows some representative SANS data with the core-shell model fits. The fits were performed with the SLD of the tail of the lipids and the solvent fixed to the values listed in Table 5.2.
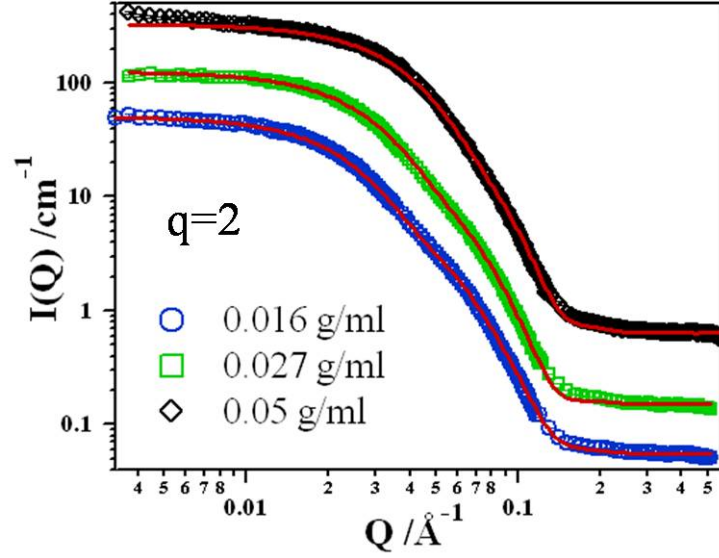
Figure 5.7: Core-shell disk fits to $c-$series data over the entire Q range of the measurement.

For the fits shown in Fig. 5.7, the core thickness was fixed to the hydrocarbon chain thickness [38] and equal to 30 Å and both shell thicknesses Δt and ΔR were constrained to be equal. The shell SLD was left as a free parameter, though constrained between its theoretical value $2.21 \times 10^{-6} \text{Å}^{-2}$ and a value of $5 \times 10^{-6} \text{Å}^{-2}$. The fit SLD of the shell at $\sim 3.2 - 3.8 \times 10^{-6}$ Å^{-2} is higher than the pure lipid head group SLD and is in confirmation with prior studies which show $\sim 30\%$ water penetration in the hydrophilic head groups [101, 104, 147]. Polydispersity values for all the samples radii were around 20%. The disc thickness is ~ 50 Å over all the samples measured, with shell thickness of $\sim 10 \pm 1$ Å. As noted before, it compares well with the bilayer thickness obtained by Nagle and coworkers [38] and is bigger than 44 Å obtained when a one-step SLD profile is assumed.

In fitting the data with free fit parameters limited to the radius, radius polydispersity, shell thickness and shell SLD, we also found that relatively poor fits were obtained

when the volume fraction was fixed to the experimentally measured volume fraction. The fits shown above, required us to treat the lipid volume fraction as a fitting parameter, although we did apply constraints as described below. Essentially this was required because the volume fraction of the scattering particles and the contrast terms are coupled (see **Appendix B**) and indicates that the availability of each lipid species to segregated discoidal aggregates is not simply related to their relative molar fraction, but also varies with the total lipid concentration. The upper limit on the volume fraction of the scattering units was obtained from an estimate of the mass of each species and its density, assuming all lipids went into forming aggregates. So for a sample of concentration c(g/ml) and composition given by

$c = x_1(gm)C14 + x_2(gm)C6$ in $x_3(gm)$ of solvent

the volume fraction is given by

$$\phi = \left(\frac{x_1/\rho_{C14} + x_2/\rho_{C6}}{x_1/\rho_{C14} + x_2/\rho_{C6} + x_3/\rho_{D2O}} \right) \tag{5.7}$$

Since some amphiphillic molecules can also exist as free monomers, the lower limit on the volume fraction constraint was obtained from an estimate of the amount of $[C6]_{free}$, calculated from the discussion in section 5.5.1 (where we also show that $[C14]_{free}$ is almost negligible). The measured and fit volume fractions as well as the total radius of the bicelles are listed in Table 5.3 for all the measured samples. The trend in the radial sizes of the bicellar aggregates, increasing with q and with increasing dilution, are identical to those obtained from the simple Guinier analysis.

5.4.4 Contrast Enhanced Mixtures

While our results in the previous sections are in agreement with the discoidal shape assumed in the literature [20, 89, 97, 98], the obtained sizes are not exactly the sizes reported in the literature, except at high total lipid concentration. Also, the concentration dependence is completely uexpected from the predictions of the geometrical IBMs. Clearly,

Table 5.3: Bicelle radii of $c-series$ samples obtained from Guinier and Form-factor Fits.

q	c (g/ml)	ϕ	C6$_{free}$ %	ϕ_{fit}	R$_g$(Å)	Radius (Å) (R$_g$ fit)∗	Radius (Å) (FF fit)
1.5	0.01	0.0084	50	0.0071	78.4	108.9	105
	0.019	0.0154	34	0.0139	51.4	69.7	63
	0.029	0.0244	24	0.0227	44.5	59.5	59
	0.038	0.0312	19	0.0294	37.9	49.5	53
	0.078	0.0648	10	0.0629	27.8	33.4	44
2.0	0.005	0.0042	68	0.0035	MLV		-NA-
	0.016	0.137	37	0.0125	67.9	93.8	97
	0.027	0.0231	25	0.0217	59.2	81.1	81
	0.03	0.0255	23	0.0241	56.1	76.7	76
	0.05	0.0416	15	0.0401	45.4	60.8	58
	0.10	0.0835	8	0.0805	29.2	36	54
d-$q2\star$	0.02	0.017	31	0.016	-	-	89
d-$q2\star$	0.02	0.017	23	0.023	-	-	77
d-$q2\star$	0.047	0.039	15	0.038	-	-	61
2.6	0.010	0.0084	50	0.0076	MLV	-	-NA-
	0.025	0.0212	27	0.0201	66.2	91.3	105
	0.04	0.0335	19	0.0320	55.75	76.2	67
	0.10	0.0856	8	0.0836	33.6	42.9	78
3.2	0.01	0.0856	49	0.0078	MLV		-NA-
	0.018	0.0147	35	0.0138	75.5	104.8	110
	0.025	0.0213	27	0.0204	71.1	98.4	104
	0.103	0.0865	8	0.0850	38.6	50.6	77

∗ Obtained using ractangular cross-section, see text.

$\star$ R_g estimates are not included, due to limited range of low Q-data and flat Guinier regimes.

there are problems in the details of the complete description of the system, which means that perhaps the complete segregation hypothesis itself should be verified more directly.

In order to do so, we took advantage of the large neutron contrast difference between hydrogenated and deuterated lipid species, performing SANS measurements on high contrast or 'contrast enhanced' mixtures: deuterated C14 and hydrogenous C6 at a molar ratio $q = [dC14]/[C6] = 2$, for concentrations c= 0.05 g/ml. The scattering length density (SLD) for d-C14 is $6.7 \times 10^{-6} \text{Å}^{-2}$ and is now close to that of the solvent, deuterated salt solution at $6.3 \times 10^{-6} \text{ Å}^{-2}$, so that if lipid segregation occurs in these aggregates, the main scattering contrast will come from a hydrogenous C6 (SLD $0.67 \times 10^{-6} \text{ Å}^{-2}$) rim - thus the scattering object should now be essentially a hollow disk or ring rather than a solid disc. A schematic of such a disk with the SLD variations in the radial and perpendicular (to the disc plane) directions, is shown in Fig. 5.8. The SLD profile in the radial direction is a *two-step profile*, with a large difference between the core and shell (6.7 to 0.67 Å^{-2}) while in the perpendicular direction, both a *one-step and two-step profile* (to account for the difference in the tail and headgroup SLD of dC14 lipid) are shown.

We note here that while replacing the long tail hydrogenated C14 lipids with deuterated dC14, decreases the overall contrast between the overall lipid assembly and the surrounding solvent, as shown in Fig. 5.8, the contrast in the radial direction is 'enhanced' in comparison to the perpendicular direction, hence the name 'contrast enhanced' samples. We emphasize that this is not a 'contrast matched' condition as used in the literature [63, 131, 129], since the SLD of the core lipid is not exactly matched to that of the solvent. But the large difference in the SLDs of long deuterated and short hydrogenated chain lipids makes the SLD of the core and rim in these samples quite sensitive to mixing within the aggregate.

Figure 5.9 compares the scattering from the q=2 and c=0.05 g/ml samples in the two different contrast cases. The fit to the regular C14/C6 sample is that presented previously for this sample in Fig.5.7 indicating a total radius of ∼58 Å as indicated in
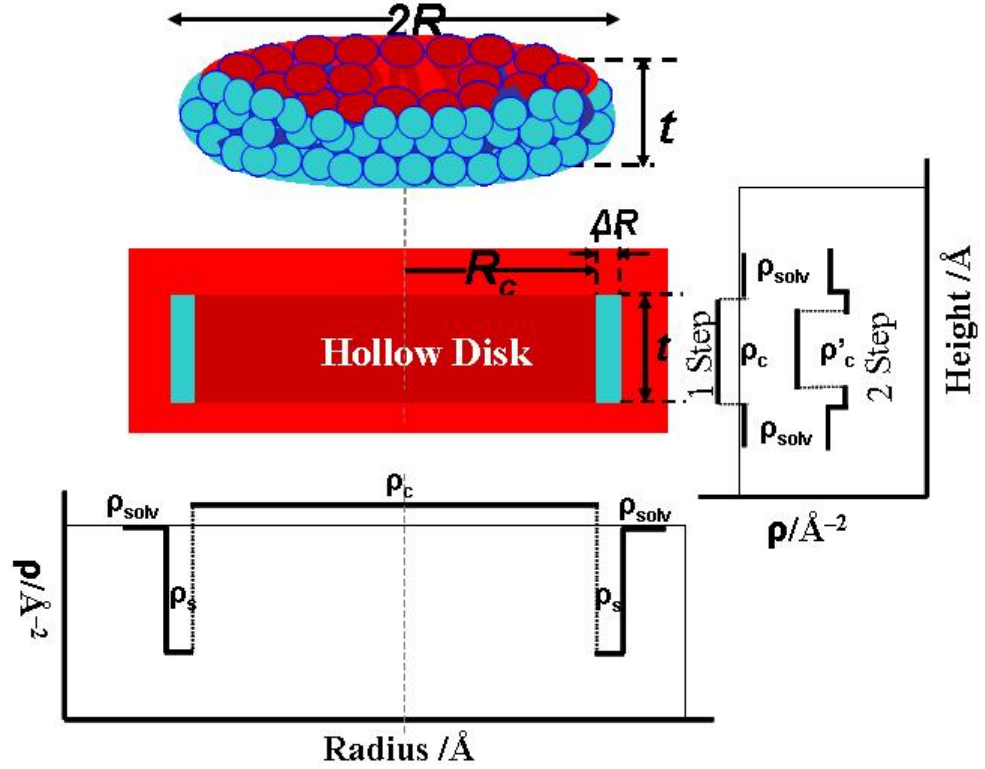
Figure 5.8: Cartoon of a core-shell disk with SLD variations in the contrast enhanced case: the contrast between the core lipid and the solvent has been changed by using deuterated-C14. The slightly higher SLD of the core is indicated in dark red in contrast to the light red solvent, while blue colored small C6 forms the rim. Notice the difference between the SLD profiles in the radial and perpendicular directions.

Table 5.3. If the two lipids were similarly mixed within the aggregate structures, then the scattering from dDMPC/hDHPC would be identical to those of C14/C6 albeit with a somewhat lower intensity due to an overall decrease in the contrast between the solvent and the aggregate (see SLD values in Table 5.2). The scattering from this hypothetical mixed discoid is shown in Fig. 5.9. For comparison, a fully segregated model, based on the SLD profile shown in Fig. 5.8 is also shown. The observed scattering curve from the dC14/C6 sample is very different and more than an order of magnitude weaker at low scattering vector - which in itself clearly supports strong segregation within the discoidal aggregate and consistent with a large volume of the aggregate (a central dC14 disc) having

94

low contrast with respect to the solvent. Further, this weaker scattering is dominated by a peak at Q=0.06 Å$^-$1 $\sim 2\pi/100$ Å, which we may identify as scattering from hydrogenous C6 rim of $\sim$100 Å diameter, around the deuterated lipid core immersed in the solvent. However, the overall intensity is at least two fold less than the ideally segregated case and hints to two possibilities: (1) mixing of some deuterated species (dC14) into the rim (2) mixing of deuterated solvent in the rim, or their combination, which would lower the overall contrast between the rim and the solvent resulting in lower intensity as shown by the data.
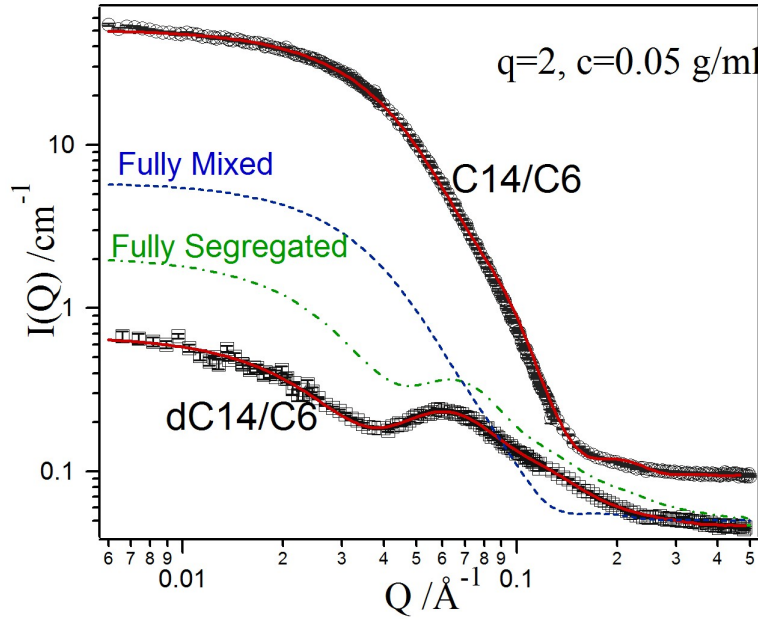
Figure 5.9: Scattering intensity as a function of wave vector comparing a regular sample and a contrast enhanced sample for c=0.05 g/ml and q=2.0. Symbols are data from the two samples and solid red lines are fits to the two sets using the poly-disperse core-shell disc geometry. Dashed and dotted-dashed lines show scattering on absolute scale from fully mixed and fully segregated cases respectively.

To distinguish between those two possibilities, we fit the contrast enhanced sample with the polydisperse core shell disk form factor, described previously. In using this model, we consider a zero face shell thickness for the core of dC14 with an overall SLD of 6.7 $\times 10^{-6}$Å^{-2} . With a single step SLD variation in the perpendicular direction and a two-

Table 5.4: Fit parameters and disc characteristics in the contrast-enhanced mixtures, d-C14/C6 =2.0, and different total lipid concentrations using the Polydisperse core-shell form factor.

Sample	SLD_{core} (Å^{-2})	Thickness (Å)	Radius R+ΔR(Å)	SLD_{shell} (Å^{-2})	Mixing (fraction)
0.05 g/ml					
	6.7	44(0)+0	56.6(0.11)+7.34(0.12)	1.93	0.21
	6.7	40(0)+0	56.5(0.3)+ 7.0(0.49)	1.61	0.16
	7.11	34.6(0.32)+0	49.8(0.19)+12.73(0.25)	2.29	0.27
0.03 g/ml					
	6.7	44(0)+0	70.1(0.39)+7.0(0.64)	1.71	0.17
0.02 g/ml					
	6.7	44(0)+0	85.1(0.6)+7.0(0.2)	1.55	0.14

step in the radial direction, the SLD of the rim consisting of hydrogenated C6 (SLD of 0.67×10^{-6} Å^{-2}) and any mixed deuterated lipid species, is a fit parameter. Besides the shell SLD, the other fitting parameters in this case are the core radius, its thickness and polydispersity and the rim shell thickness, while the volume fraction was constrained as described as for the hydrogenated mixture.

The fit results from three different concentration samples, all of molar ratio 2.0, at c=0.05, 0.03 and 0.02 g/ml are listed in Table 5.4. Now consider just the 0.05 g/ml sample: the disc dimensions are in agreement with the fits shown previously on the purely hydrogenous samples; the disc radius of 62±2 Å is within a few Å of that obtained in the fully hydrogenated lipids sample at 59±1 Å. Thus, the dimensions of the disks in the two cases are the same within errors. However, the fit SLD of the rim shell at 1.93×10^{-6} Å^{-2} is higher than 0.67 Å^{-2} and implies $\sim$ 20% mixing of the deuterated lipid into the rim. On fixing the core length to a few Å bigger (smaller) values, the quality of fits reduces (improves) and changes the mixing fraction by $\sim$10%. The radial shell thickness obtained from the fit at $\sim$ 7 Å, shows that only the hydrophobic part of rim lipids is visible. Then, considering the high SLD over that of C6 lipid tails (-0.4Å^{-2}), implies $\sim$30% of the core lipid tails are mixed into the rim lipid tails. From these considerations, we put a 15-20%
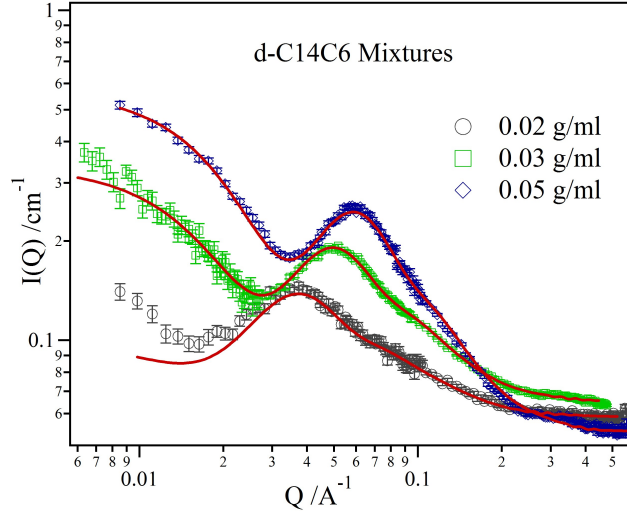
Figure 5.10: SANS data from contrast enhanced samples of dC14/C6=2.0, for different total lipid concentrations $c = [dC14] + [C6]$=0.02, 0.03 and 0.05 g/ml. Data are fit with Polydisperse core-shell disk model with SLD contrast as shown in Fig. 5.8.

uncertainty on the mixing estimate by this fitting procedure.

In order to decouple the effect of water penetration in the rim, we also use a slightly different fitting procedure, making use of the fact that the scattering intensity depends mainly on the contrast between the deuterated and hydrogenated tails of the lipids relative to the solvent, if the head groups are largely hydrated and do not contribute to the signal. This is reasonable assumption for the two step SLD in the perpendicular direction in Fig 5.8, since with the deuterated head groups at 5.5×10^{-6}Å^{-2} , even 10% water mixing into the face, would increase its SLD to that of the solvent making the face shell invisible making it essentially like the single-step SLD profile. Doing so, we fixed the core SLD to that of the deuterated- hydrocarbon chains at (7.11×10^{-6}Å^{-2}) but its thickness along with the rim SLD vary. The fit thickness at ~ 34 Å is close to that of the hydrophobic tail length. The quality of the fit is even better, but in this case, a thicker rim thickness at $\sim$12Å is obtained, and the rim SLD is now 2.29×10^{-6}Å^{-2} . This would mean that both the rim lipid tail and part of the headgroup are visible, so that with a 25-30% water in the rim

97

lipid headgroup (shown before in Section 5.4.3), $\sim 15\%$ dC14 tail would have to be mixed to obtain the fit SLD of the shell. The mixing fraction obtained by the two approaches are consistent within the uncertainty estimate and proves the validity of the mixing argument, in addition to providing a quantitative estimate.

Fig. 5.10 shows fits to all the contrast enhanced samples, where similar fitting procedure was applied and the fit results are included in Table 5.4 (for the c=0.02 and 0.03 g/ml samples, results of only the first fitting procedure are included). With decreasing total lipid concentration, or increasing aggregate size, mixing ratio shows decreasing trend, even if we account for the uncertainty in those estimates. We discuss its implications further in this Chapter and in Chapter 6. In summary, the SANS data on the contrast enhanced mixtures not only proves the segregation hypothesis, but also leads to quantification of the mixing of the core lipid in the rim, defined from now on as *mixing fraction* $x \sim$ (number of d-C14 molecules in rim)/ (Total number of C6 + d-C14 in rim).

5.4.5 DMPC(C14)/DHPC(C6) c-series: Dilute Regime

In section 5.4.2, we alluded to a few dilute samples in each c-series which were whitish and not included in the list of isotropic, fluid like bicelle samples. Unlike all the other samples in Section 5.4.2 which were clear and transparent like water at 10°C , these samples were turbid, indicating the presence of big objects. Figure 5.11 shows the SANS from the lowest concentration samples from each q-series. The scattering pattern of the samples from all the three series are similar, showing a lamellar peak at $Q = 0.098 \pm 0.005$ Å $^{-1}$. The presence of the peaks represents scattering from multilamellar samples with a D-spacing of 64±3 Å and is consistent with bilayer spacing in MLV samples of pure DMPC lipid [11]. With bilayer thickness of ~ 50 Å, this means that only about 20% of the MLV is water. MLV formation at low lipid concentrations in the same mixtures, has been seen before [104] and confirmed to be the same as that of pure C14 dispersions. Our data from the three q-series show that neither the total lipid concentration nor the initial molar ratio q

has an effect on the peak position and hence on the interlamellar spacing within the MLVs.
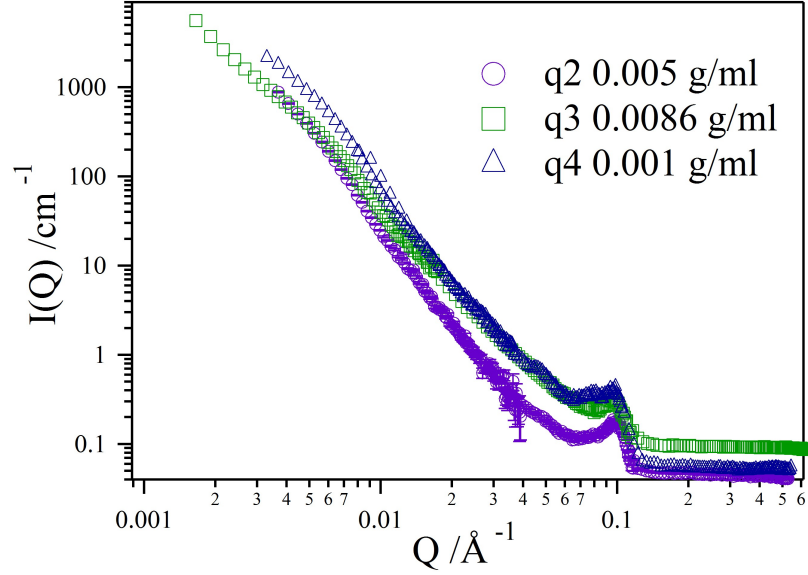
Figure 5.11: Scattering intensity as a function of wave vector for the lowest concentration sample in different $q-$series. All the curves show a peak at $Q = 0.1$ Å^{-1}, indicative of multilamellar vesicles.

5.5   Discussion

SANS data on the lipid mixture from both the $c-$ and $q-$ series with the hydrogenated samples together with the contrast enhanced sample, confirm the essentially discoidal model of bicelle formation, but the size variation with total concentration at constant molar ratio indicates that some of the assumptions of the IBM must be modified to explain the details of the packing behavior. This implies that there is more core lipid and less rim lipid then expected from the molar ratio of the two, especially at low total lipid concentration. This could be either due to unavailability of C6 lipids, or due to mixing of C6 in the core. This section is devoted to understanding those discrepancies to obtain a quantitative model for bicelle growth.

Before explaining the trend in our data and developing a quantitative model, it is important to note that since both the Vold Eqn. 5.3 and the Triba Eqn. 5.5 are based on packing the two lipids based on their curvatures (segregated), they should give equivalent results. However, as shown in Section 5.2 (see Fig. 5.1), those expressions differ by a factor of two, since they incorrectly assumed equal head group areas a_{C6} and a_{C14} and equal molecular volumes, v_{C6} and v_{C14} for the two lipids respectively. Clearly, if the molecular parameters were correctly accounted for, those two expressions should be equivalent. The ratio q is correctly defined as

$$q = \frac{n_{C14}}{n_{C6}} \equiv \left(q_A = \frac{A_{core}}{a_{C14}} \times \frac{a_{C6}}{A_{rim}} \right) \equiv \left(q_V = \frac{V_{core}}{v_{C14}} \times \frac{v_{C6}}{V_{rim}} \right) \tag{5.8}$$

where a_{C14}, a_{C6}, v_{C14} and v_{C6} are the head group areas and full lipid volumes of the two lipids C14 and C6 respectively and define k_A and k_V as the following ratios of the molecular parameters

$$k_A = \frac{a_{C14}}{a_{C6}} \qquad k_V = \frac{v_{C14}}{v_{C6}} \tag{5.9}$$

Then by substituting k_V and k_A for the volume and headgroup area ratios, we can once again solve for R_c, the central bilayer core radius. The total bicelle radius can now be expressed as the following modifications to Eqns. 5.3, 5.5 and 5.6

$$R_A = \frac{k_A q r}{2} \left(\pi + \sqrt{\pi^2 + \frac{8}{k_A q}} \right) + s \tag{5.10}$$

$$R_V = \frac{k_V q r}{4} \left(\pi + \sqrt{\pi^2 + \frac{32}{3 k_V q}} \right) + r \tag{5.11}$$

$$R_V = k_V q \Delta R \left(1 + \sqrt{1 + \frac{1}{k_V q}} \right) + \Delta R \tag{5.12}$$

The relative accuracy of the radii obtained above, are limited by the certainty of the measured headgroup areas and volumes of the two lipids. Head group areas and volumes of various lipids have been studied extensively in the literature [11, 70, 71, 73]. Nagle and coworkers have studied the gel and fluid phases of C14 and evaluated it's structural details in a series of papers ([38, 39] and references there in) using X-ray diffraction techniques on

multilamellar vesicles and also oriented multilayer samples. Currently, the accepted value of C14 volume is 1041 Å^3, while it's head group area is 47.2$\pm$0.5 Å^2 in the gel phase at 10°C (they are 1090 Å^3 and 60.6$\pm$0.5 Å^2 in the fluid phase at 30°C !). It is important to note that we are using those values at 10°C , the temperature for all the SANS data. Similarly for C6, Lin and coworkers, studied the micellar structure using SANS and obtained a value of $\sim$ 670 Å^3 for the volume and 100 Å^2 for the headgroup area [36]. However, questions about the accuracy of the headgroup area of C6 in pure micellar aggregates have been raised [73, 143, 144], since the head group area per molecule is critically dependent on the curvature of the aggregate.

Using the above noted values for the volumes and head group areas, leads to a k_V value of 1.55 and a k_A value of 0.47. Fig. 5.12 shows a plot of the expectations from the various modified IBM Eqns. 5.10, 5.11 and 5.12 for the upper and lower limit of the curvature values for the rim discussed below. The shaded area between solid and dashed lines, the overlap region, represents the limited region where k_V and k_A are consistent. The Solid lines are for the lower limit of r and ΔR, corresponding to the hydrophobic semi axis of a prolate ellipsoidal micelle formed by C6, and the lower limit on headgroup size 4 Å) and s of (bilayer thickness/2) equal to 20 Å (see Section 2.4.2). The dashed lines represents those values for maximum extended length from Eqn. 2.8 upper limit on headgroup size of 9 Å. Combined with the accuracy issues associated with headgroup areas (in contrast to the more precise volume parameter), from here on, for the rest of the discussion that follows, the modified Eqn. 5.11 is used as the minimal model for growth of C14/C6 and other binary mixtures (in Chapter 5).

In the IBM Eqns. 5.3-5.6 or the modified IBM Eqn.s 5.10-5.12, the bicelle radius R is independent of the lipid concentration regardless of the value of k_V or k_A, unless one takes the molar ratio q to be concentration dependent, since k_V and k_A are both molecular parameters. Thus in order to relate a purely geometrical model, defining the radius of a disc
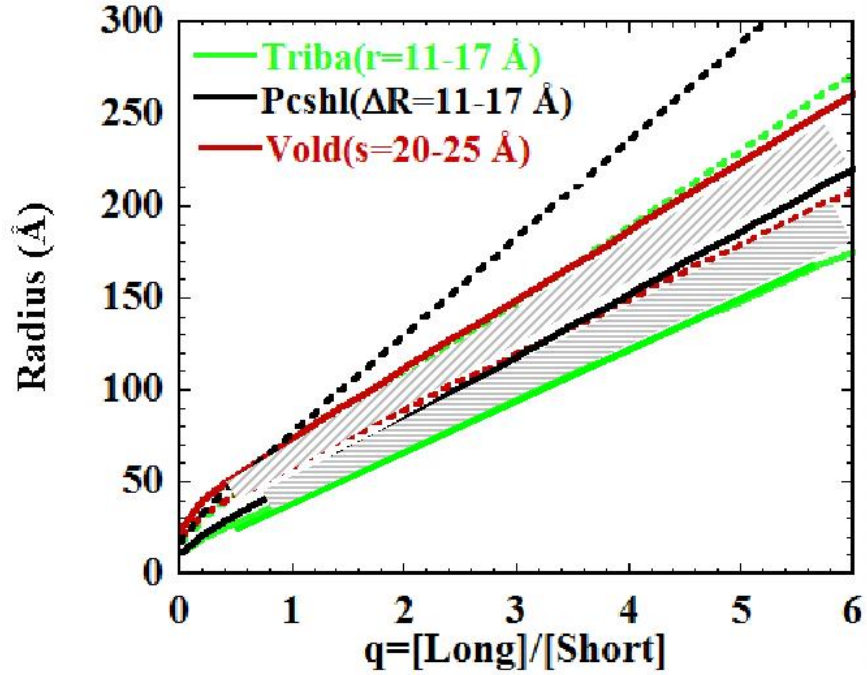
Figure 5.12: Modified Ideal Bicelle equations, based on Vold, Triba and Pcshl geometry of the rim. All the three expressions are equivalent within limits of uncertainty of the lipid head group areas, volumes and curvatures of the rim. Limits of each model is shown within solid and broken lines for varying rim dimensions. For Vold Eqn. s:20-25 Å, Triba en. r:11-17 Å and Pcshl Eqn. ΔR :11-17 Å.

to the thermodynamics of a self-aggregating system, the definition of the molar ratio in the IBM equation has to be modified. We define the ratio 'q_{eff}', which must be concentration dependent, to account for the amphiphillic characteristics of the C14 and C6 lipids, since the IBM arguments, clearly hold only for the ratio of the two lipids in the aggregate, and not their ratio in the mixed solution. The basis of this proposition, explained further, lies in the knowledge from amphiphillic science, that in fact micellar aggregates are equilibrium structures where some 'free' monomers are in equilibrium with those in the aggregates, above a *critical micellar concentration*, CMC.

Vold and Prosser first proposed the idea of free C6 in the bicellar mixtures in order to explain the stability of their discotic nematic phase at concentrations much smaller than

102

predicted by Onsager's theory [98]. Later Glover and coworkers estimated the free C6 from their NMR measurements to account for observed chemical shifts in the phosphorous signal in bicelle samples as opposed to the shift of C6 in it's monomeric form. The free C6, which is in a rapid exchange between the monomeric and bicelle associated states, was obtained by extrapolation of the observed line shifts between it's micellar and monomeric values. van Dam and coworkers also used similar concept to explain the size dependence in their DLS measurements [74]. However, all these studies assumed a constant amount of free C6 in solution estimated at 5-7 mM, which is approximately half the critical micellar concentration (CMC) of pure C6 in water. This is consistent with the traditional single amphiphillic system in which the free monomer concentration is equal to or slightly greater than the CMC, if one assumes the CMC of the mixture is equal to the average of the two CMCs for all compositions. However, due to the cooperative thermodynamic nature of the self assembling systems, the CMC of mixtures is a function of both the CMC and concentration of each component and cannot be estimated quantitatively in this way [150, 151, 32, 152]. In the next section, we obtain a quantitative estimate of the free C6 in solution in order to explain the observed growth trend in our data.

Borrowing theoretical work from surfactant science and considering the C14/C6 phospholipid system as a binary amphiphillic mixture, the observed physical properties of this system can be modeled by using the pseudo phase separation approach [150]. By treating the micelle as a separate infinite phase in equilibrium with the monomer phase, predicted CMCs of mixture have been tested experimentally for many other binary mixtures, including binary mixtures of nonionic detergents [151], cationic and anionic surfactant [153], and bile-salt lecithin mixtures [124, 81] to name a few. However to our knowledge, it has never been applied to obtain a quantitative value of free C6 in phospholipid mixtures.

5.5.1 Clint Theory and Modifications to IBM

We follow the approach derived by Clint [150] in assuming a simple phase separation model and essentially ideal mixing within the bicelles. The latter assumption is a reasonable first approximation based on similar head group chemistries of the two lipids [28] and also as a consequence of the bicelle hypothesis itself in that each component in the bicelle is predominantly aggregated in a way similarly to its pure solution form- the body forming lipids as a lamellar section and the micelle forming lipids in the highly curved rim, and may therefore be expected to have similar rates of exchange with the free lipid monomer in solution. In such a mixture, for total monomer concentrations c_L and c_S in a mixture of total lipid concentration $c = c_L + c_S$, the CMC of the mixed solution C_M is related to those of the pure components C_{ML} and C_{MS} as:

$$\frac{c}{C_M} = \frac{c_L}{C_{ML}} + \frac{c_S}{C_{MS}} \tag{5.13}$$

Thus in terms of the ratio of components $q = c_L/c_S$ (where L denotes the 'Long' component, C14 and S denotes the 'Short' component (C6)

$$C_M = \left(\frac{q/(q+1)}{C_{ML}} + \frac{1/(q+1)}{C_{MS}} \right)^{-1} \tag{5.14}$$

In the present case, the CMC of C14 at 2.7×10^{-6}mM is far less than that of C6 at 14 ± 1mM (Chapter 2), and thus at the mixing ratios and concentrations used here dominates the expression for the total CMC, effectively:

$$C_M \cong C_{ML}(c/c_L) = C_{ML}(q+1)/q \tag{5.15}$$

The CMC of the mixture is very small, for the q values in this study, and is only a little higher than that of pure C14, which is consistent with our observation of aggregate formation at very small total lipid concentrations. Clint showed that thermodynamically the ratio of each free monomer concentration to its (pure) CMC was equal to its concentration fraction within the ideally mixed aggregate micelles. Above this concentration micelles form

in the mixture, in equilibrium with concentrations of free lipid components derived by Clint as:

$$c_L^{free} = C_{ML}\left\{[(c-\Delta)^2 + 4c_L\Delta]^{1/2} - (c-\Delta)\right\} \tag{5.16}$$

$$c_S^{free} = C_{MS}(1 - c_L^{free}/C_{MS}) \tag{5.17}$$

where Δ denotes the difference between the CMC of the first and second components of the mixture, $\Delta = C_{M2} - C_{M1}$, which in the present case is very close to the CMC of pure C6. From equation we can see that the ratio of free lipid concentrations in solution will be the same as the ratio of their CMCs. Thus the very low CMC of C14 means that a negligible amount of the free lipid will be in solution. However, the much higher CMC of C6 means that free lipid concentrations are significant over the range of q values and total concentration explored in this study (see Table 5.3.

With a little algebra we derive the consequent expression for the effective molar ratio available to the bicelle aggregates as a function of our sample variables: the total molar ratio q and concentration c:

$$\begin{aligned} q_{eff} &= \frac{c - c_L^{free}}{c - c_S^{free}} \\ &= \frac{1}{2}\left((q+1)\left[\Delta/c + \sqrt{1 + 2\frac{(q-1)\Delta}{(q+1)c} + (\frac{\Delta}{c})^2}\right] + (q-1)\right) \end{aligned} \tag{5.18}$$

Even from this very inconvenient expression, we can see that as we should expect from the thermodynamic ratio that led to its derivation the effective lipid ratio, q_{eff}, within the bicelles will only be equal to the measured molar ratio for the total solution, q, when the CMCs of both components are equal, which is far from the present case. For $\Delta > 0$, as in this case, we see that q_{eff} will always be greater than q, with a high concentration $c/\Delta >> 1$ limit approaching q as $q_{eff} \rightarrow q(1+\Delta/c)$. The low concentration limit $c/\Delta << 1$ of this expression $q_{eff} \rightarrow (q+1)\Delta/c = \Delta/c_2$. Further in the current case since $\Delta \cong C_{M2}$ we see that this limit if it were approached, depends only on the short chain lipid parameters.

Figure 5.13 shows a plot q_{eff} derived from Eqn. 5.18 for the concentration range and lipid ratios covered in this study. As we would expect from the limits presented above, at high total lipid concentrations c, in our case 0.1g/ml, q_{eff} and the measured molar ratio q are nearly identical. However at low concentrations the c^1 behavior of q_{eff} causes the effective lipid ratio to diverge from the total solution ratio - the increasing proportion of C6 in free solution can in turn be expected to significantly reduce in the relative amount of short chain lipid material available to form the rim of a bicellar aggregate leading to the inverse proportionality we observed between bicelle size and c at a fixed q.
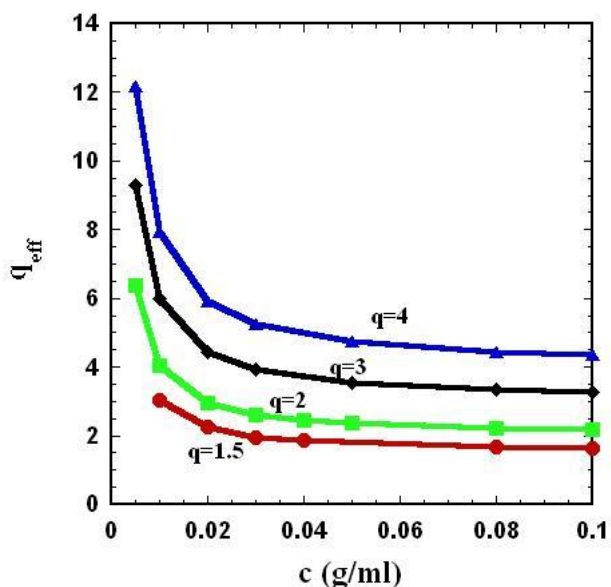
Figure 5.13: Variation of q_{eff} as a function of total lipid concentration for different values of measured molar ratio q calculated using 5.18.

Thus the single key parameter q_{eff} in the expressions for bicelle radii R, Eqn.5.10, 5.11 or 5.12 properly calculated includes the contributions from both the variables c and q. Table 5.3, lists the percentage of calculated free C6 for each of the samples used in this study using equation 5.17. Previously unaccounted for, we see that for a given q, the amount of free C6 could range between 8-70% for c varying from 0.005-0.1 g/ml. We used these estimates for the concentration of $[C6]_{free}$ in calculating the lower limit on lipid

volume fractions while fitting the data using the Poly-disperse core-shell model. The fitted volume fractions are within very good limits of the estimated correction for the lipid volume fraction.

Figure 5.14 shows a plots of the measured bicelle radii obtained from the different $c - series$. Besides the samples listed in the Experimental section, another preparation of $c - series$, for $q = 2.0$, 3.0 and 4.0, by a SURF student in the group are also plotted, showing reproducibility of the results. As expected, when plotted against q in 5.14(a), there is considerable scatter in the radii obtained from different concentration samples. Measured radii vary almost by a factor of two. This can explain the variability in measurement obtained by different groups for the same q. But when plotted against q_{eff} for each of the c-series samples, they all follow the linear trend very well, and yet, the observed growth is short of that expected from the completely segregated modified IBM Eqns. 5.10- 5.12. All the measured radii are short of the expected growth rate, shown by the hatched region in Fig. 5.12. (Note that the radii plotted in 5.14(b) are those obtained by form-factor analysis; as the Guinier and Form factor analysis give radii within 2-3 Å of each other and follow the same trend (see Chapter 6 for more on comparison between different techniques), only the form factor values are plotted for clarity.

If Eqn. 5.11 were a good mathematical description of the bicelle formation, then we should expect all the data points to collapse to one single line. However, the scatter in the data points for all the series hints to additional corrections. The fact that disk sizes are smaller than the IBM predictions implies that less lipids are available for forming the disk core, hinting to subtle mixing effects. Previously unaccounted for, this mixing is critical in understanding the quantitative size dependence of the discoids in C14/C6 mixtures. In order for bicelle radii to follow the ideal growth rate, we next apply mixing corrections described in the following section.

107

(a)	(b)
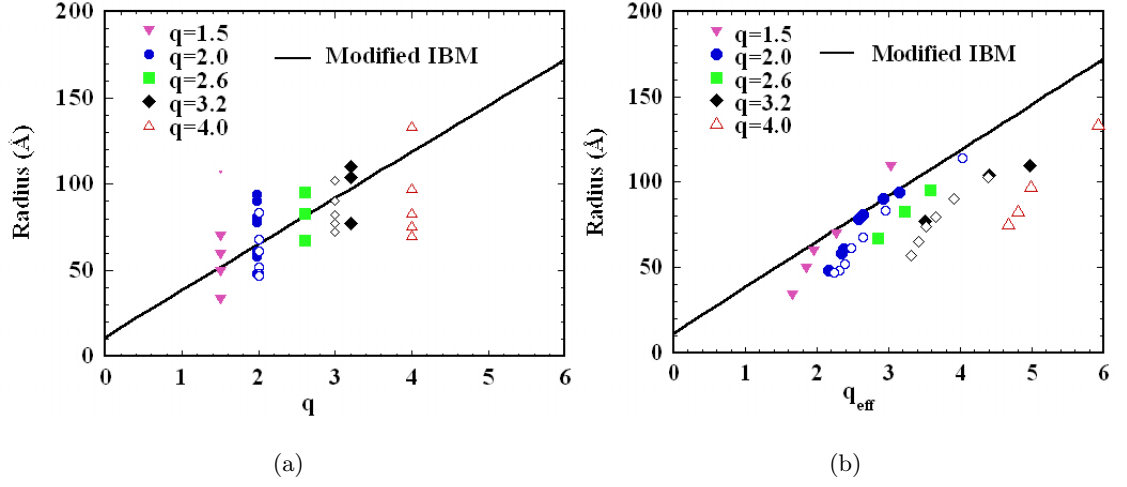
Figure 5.14: Measured bicelle radii for four $c - series$ plotted as a function of (a) the measured molar ratio q and (b)q_{eff}, the molar ratio in the aggregates accounting for free lipids. Solid symbols are from form factor fits to Poly-core-shell disc model. Error in fits cannot be seen on the scale of the graph. Hollow symbols are radii calculated from Guinier fits on q=2.0, q=3.0 and q=4.0 $c - series$ from another preparation of those series and showing reproducibility. The modified IBM (Eqn. 5.11) equation of Triba, with k_V of 1.55 and rim curvature of $r = 11$ shows the growth rate in all the mixtures is below that expected from the modified IBM.

5.5.2 Segregation and Mixing Modifications

From the measured radii of the bicelles in Fig. 5.14(b), it is clear that disc radii are smaller than expected from even the lowest estimate of the completely phase segregated, Triba's modified Ideal bicelle model. The fact that the observed growth on dilution is smaller than expected, hints to the non-availability of bilayer forming C14 for forming the bicelle cores. Similar conclusion was reached by Lin and coworkers in aggregates formed by mixtures of C16/C7 lipids using light scattering and SANS and a partial segregation model was suggested [95] to explain slower growth rate than expected. However no quantitative estimates or dependence on the composition in such a model were undertaken.

This leads to our second proposed correction to the IBM, which comes from the dynamic nature of the discoidal aggregate. Besides the constant exchange of lipids between the aggregate (bicelle) and the free monomeric state, the two lipids can also exchange between the bilayer and the rim section of the bicelle. Mixtures of two bilayer forming lipids (i.e both lipids undergo gel-to-fluid transition), differing only by their hydrophobic chain lengths are known to mix above the main transition temperature of the two lipids, as a pseudo binary mixture [82, 83]. The mixing is ideal or non-ideal depending on the interaction between the head groups and the tails. For C14/C6 mixtures with a tail length difference of six carbon atoms, the mixing behavior is expected to be highly non-ideal. While C6 tails are fluid at all temperatures, C14 tails go through the crystalline gel to fluid transition at T_m via a complex phase transition (as described in Section 2.4.1).

From entropic arguments, we expect to see a small fraction of C6 molecules going into the bilayer and a small fraction of C14 molecules going into the edges, even at 10°C . If N_{C6}^T and N_{C14}^T are total number of C6 and C14 molecules in the aggregate, then the fraction f_1, of C6 mixing into bilayer and f_2, of C14 mixing into rim, with respect to the total number of the respective species

$$f_1 = \frac{N_{C6}^{bil}}{N_{C6}^{bil} + N_{C6}^{rim}} = \frac{N_{C6}^{bil}}{N_{C6}^T}$$

$$f_2 = \frac{N_{C14}^{rim}}{N_{C14}^{rim} + N_{C14}^{bil}} = \frac{N_{C14}^{rim}}{N_{C14}^{T}}$$

So that the experimentally accessible mixing, defined as the fractional impurities in rim and bilayer will be given respectively by

$$x \equiv n_{C14}^{rim} = \frac{N_{C14}^{rim}}{N_{C14}^{rim} + N_{C6}^{rim}} = \frac{f_2 q}{f_2 q + (1 - f_1)} \equiv \text{ C14 as impurity in edges} \tag{5.19}$$

$$y \equiv n_{C6}^{bil} = \frac{N_{C6}^{bil}}{N_{C14}^{bil} + N_{C6}^{bil}} = \frac{f_1}{f_1 + (1 - f_2)q} \equiv \text{ C6 as impurity in bilayer} \tag{5.20}$$

Using NMR measurements, Triba et. al. have estimated the fraction of C6 impurities in the bilayer Eqn. 5.20 as a function of temperature *above* T_m [106]. For temperatures lower than T_m, their measurements did not have the sensitivity to detect either of the two mixing given by Eqn. 5.19 or 5.20. In fact, the fraction of C14 mixing into the rim was apriori taken to be negligible over the whole range of temperatures studied, below and above T_m. In contrast we argue below, that in the low temperature discoidal phase, C14 going into the fluid C6 edge (at all temperatures), as defined by Eqn. 5.19 is not negligible and is in fact responsible for the slower growth than expected from the fully segregated models seen in Fig. 5.14.

In order to incorporate mixing into the bicelle model, we further modify the definition of molar ratio in the aggregates as follows- for the partially segregated model, q_V is appropriately defined as

$$q_V = \frac{V_{core}}{V_{rim}} \equiv \frac{N_{C14}^{bil} V_{C14} + N_{C6}^{bil} V_{C6}}{N_{C6}^{rim} V_{C6} + N_{C14}^{rim} V_{C14}} \tag{5.21}$$

which can be written in terms of mixing fractions f_1 and f_2 as

$$q_V = \frac{(1 - f_2)q k_V + f_1}{1 - f_1 + f_2 q k_V} \rightarrow \frac{(1 - f_2 q_{eff} k_V)}{1 + f_2 q_{eff} k_V} \text{ when } f_1 \rightarrow 0 \tag{5.22}$$

The above definition of q_V when used in Eqn .5.11 is expected to be the correct scaling for bicelle radii. Again, using $k_V = V_{C14}/V_{C6}$ the effective molar ratio of the two

lipids in the aggregate q_{eff} , q_V is now related to q_{eff} in any of the IBM equations, for instance to the Triba Eqn. as

$$q_V = \frac{(1 - f_2 q_{eff} k_V)}{1 + f_2 q_{eff} k_V} = \frac{\pi R_c^2 t}{2\pi (R_c + 4r/3\pi) (\pi r t/4)} \tag{5.23}$$

This equation can be solved to give an equation similar to Eqn. 5.11, or Eqn.5.12 with q_V defined as in Eqn. 5.22. Conversely, the **mixing fraction** f_2 for each mixture can be estimated by its deviation from the fully segregated case. For a given mixture, using its the measured radius R, estimates of q_{eff} , r and k_V, f_2 solved as $\sim f(k_V, q_{eff}, R, r)$ in a simple Mathematica program to obtain a quantitative estimate of the mixing of C14 into the rim (**Appendix D**). Fig. 5.15, shows an estimate of the mixing fraction obtained as a function of the excess molar ratio q_{eff} /q (to normalize for different qs) for each $c - series$ sample measured; using k_V of 1.55, r of 11 Å. This is only a lower estimate of the mixing, since a rim with curvature $r > 11$ Å would have more sites for mixing and result in a higher estimate. The relative trend in such an estimate of mixing should however be comparable to experimental results from the contrast enhanced mixtures.

In direct confirmation of the mixing defined by Eqn. 5.19, fit results from the contrast-enhanced samples (Section 5.4.4), indeed show composition dependent fraction of the core d-C14 lipids mixed into the hydrogenated C6 rim (as listed in Table 5.4). The estimated trend in decrease in mixing with increasing excess molar ratio q_{eff}/q obtained from regular hydrogenated samples, matches well with the experimentally measured mixing from the contrast enhanced samples. The mixing fraction obtained 0.05 g/ml and 0.02 g/ml match well with the estimates, while the 0.03 g/ml sample is seen to be more than the estimate and could be possibly the result of a separate preparation.

We point out here that the mixing of C6 into the C14 core defined by Eqn. 5.20 and estimated to be $< 5\%$ by Triba and coworkers has less discernible effect on our results. Based on the SLD for d-C14 core (Table 5.2), our fitting results indicates that at 10°C , accounting for 1-2% mixing of C6 lipids mixing into the core or flat bilayer section, changes

the mixing fraction only by a few percent and hence was neglected. In the next section, we show that this is a reasonable assumption at 10°C even on energetic grounds. Its the mixing in the rim, which has more dramatic consequences at low temperatures seen in the growth trend with dilution in Fig. 5.14.
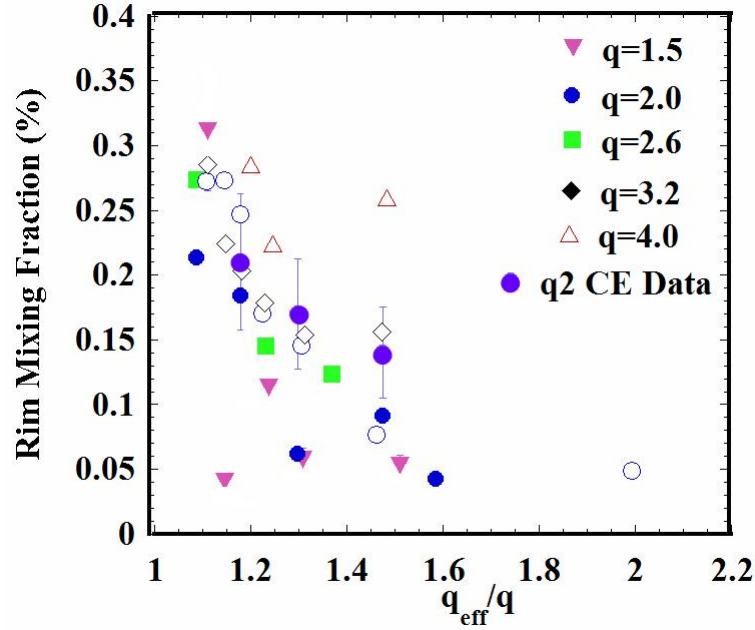
Figure 5.15: Estimates of core lipid C14, mixing into C6 rim at 10°C for all the samples measured in this study, plotted as a function of excess molar ratio, or 'q_{eff}/q'. Also indicated are mixing estimates from fitting the contrast enhanced samples from section 5.4.4. Decrease in mixing with excess ratio or aggregate size is clear from both the approaches.

Thus partial mixing of C14 ensures that there are no abrupt curvature changes in going from curved rim to the flat bilayer core, and also ensures that the dilution induced growth of the discs takes place at a smaller rate than that predicted by the completely segregated models. In such partially segregated aggregates (possible as long as the curvature strain on the long lipids mixed into edges is compensated for by the entropy of mixing), smaller discs would be favored in lieu of the expected disc sizes for the translational entropy gain. The fact that a small fraction of C14 goes into the rim and provides stability has also been observed in a simulation study of edge behavior [154] and also confirms to Fromherz's

view of edge stabilization in lipid bilayers [155].

5.5.3 Why Discoids Are Favored at low T ?

The question of morphology of a mixed system of lipids and detergents has been widely studied in many systems (see Section 2.5.2). Discoidal aggregate structures are a rare form of self-assembly not usually observed in micellar aggregates [30, 29, 143, 144]. While for the lecithin-bile salt system, now it is more or less clear that elongated micelles are the dominant morphology [122, 123, 124] at the molar ratios considered, their occurrence and stability in other lipid-surfactant mixtures is still debated (Almgren's article in [109]). The structure of such mixed systems has also been studied theoretically by many groups and precludes the discoidal micelle ([156, 157, 81] and cited references). Then what is the origin of the stable discoidal phase seen in the C14/C6 mixtures?

The occurrence of a flat bilayer with a curved edge and partial mixing in the components in the rim, requires a local minimum of free energy, which is the net sum of bending energy, the edge energy and the entropy of mixing. In order to explain the discoidal aggregates seen in the C14/C6 mixtures, we turn to the study of Kozlov et al., where they addressed the question of the most stable aggregate structure, when increasing amounts of a surfactant is added to a long tail lipid vesicles [156]. They accounted for the thermodynamics of the system by using the Helfrich energy of curvature (see Section 2.3) for the amphiphillic mixture and also their entropy of mixing.

To analyze the resulting structures for each possible aggregate geometry, they considered the free energy as a function of the given aggregate composition in solution. Finally for a given composition, the geometry with the lowest free energy is taken as the equilibrium structure. Based on their analysis, the transition from bilayered vesicular to discoidal, or a mixed elongated micelle is dictated by the parameter λ, which depends on the difference of the spontaneous curvatures of the lipid and surfactant $\Delta c = c_S - c_L$, and on the material properties of the mixed monolayer (forming the closed surface), namely the

bending rigidity κ, the Gaussian curvature modulus $\bar{\kappa}$ along with head group area of the short surfactant a_S as

$$\lambda = \frac{\bar{\kappa}}{\kappa} \left(\frac{k_B T + (1/4)\kappa a_S (\Delta c)^2}{k_B T} \right) \qquad (5.24)$$

For simplicity, they considered κ or $\bar{\kappa}$ to be independent of the composition: a strong assumption found to hold true in some cases (for e.g. mixed monolayers of reveres phases in [158]), but not in many other mixed systems [49, 159]. Since the role of $\bar{\kappa}$ in the parameter for the final morphology is critical, in the absence of reliable experimental value for the modulus of Gaussian curvature of mixed monolayers, their study referred to theoretical predictions of the same. Considering, typical values for a_L=60 Å^2, $\Delta c = 1/15$ A^{-1} (with the spontaneous curvature of long lipid at $c_L = 0$ and of short lipid at $c_S = 1/15$, when it forms micelles of semi axis 15 Å), $\kappa = 10k_B$T (at room temperature for the experimental system they considered), disc like aggregates were seen to occur if $\bar{\kappa}/\kappa < -0.2$. Based on the argument that typical values of $\bar{\kappa}$ are negative and much larger in value than needed, they ruled out discoidal micelles. But their analysis also showed that at small mole fractions of the surfactant $\phi \sim 0.1$-0.3, discs are more stable, while at higher mole fractions > 0.6, elongated cylinders are the more stable aggregates (see Fig. 3 in Ref. [156]).

However, for the mixtures in this study, considering C14 is in the gel state (with $\kappa \sim$ few 100 k$_B$T) at 10°C , Kozlov's analysis cannot be applied directly, as there are several issues in their calculation that need a reconsideration

1. Independence of κ and $\bar{\kappa}$ from the composition of the mixed system. For the C14/C6 system, a large difference between the hydrophobic thicknesses of the two lipids would make such an assumption invalid in the first place.

2. The assumption of ideal mixing that goes into calculation of mixing entropy may not necessary hold true, particularly if the two lipids have very a big hydrophobic mismatch and one of the lipids is in a gel state while the other is in fluid state.

3. Based on ideal mixing conditions, the spontaneous curvature taken as the average values

of the lipid and surfactant may not hold true.

4. The gaussian curvature for such a non-ideally mixed system, cannot be predicted accurately (see for e.g [159, 15]).

Inspite of the lack of suitable theoretical models with molecular level energy considerations, the segregated and partially mixed aggregation state of the C14/C6 system with formation of discoidal aggregates can be rationalized on energetic arguments in a continuum model, first proposed by Fromherz [155] (and described further in the next section). It is based on the fact that, below the melting T_m , due to the frozen gel state of lipid tails, C14 has high bending rigidity κ of the order of a few 100 of $k_B T$ (see Section 2.3). The ordered chains thus preclude mixing of C6 which form the rim around the bilayer tails of C14. In such a system, the driving force for formation of discs is mainly entropic. The micelle forming short lipids prevents the edge of the bilayers with edge tension $\sim 0.5 k_B T$ /Å from exposure to water, lowering the edge energy in the process; and leading to the formation of discoidal aggregates as small as possible, based upon the availability of the smaller lipid species and increasing the net (translational) entropy of the system in the process.

For the same entropic reason, the growth rate on dilution is smaller than what is expected from the fully segregated modified IBM models (see previous discussion in Section 5.5.2). In order to increase the mixing entropy term, for the same molar ratio q of the two lipids, smaller partially segregated discs are formed instead of fully segregated discs at the expense of some bending energy cost in mixing of the two lipids in the edges.

In the room temperature measurements of lecithin bile salts cited by Kozlov et al., discoids are not the preferred mixed micelle structure. However, the original prediction for the discoidal morphology in those mixtures, still stands if the experiment is conducted at low temperature, the temperature range used in our experiments. The bending rigidity of C14, is lowered by atleast two orders of magnitude above T_m , as the lipids go into the fluid phase, causing C6 to mix with the softening of the bilayer. Structures formed by

chain melting and consequent mixing of the two lipid species will be discussed Chapter 7. Similar mechanism with frozen chains, molecular segregation and molar ratio variation has been found to be the shape controlling mechanism in a very different system of catanionic mixtures as well [153, 160].

5.5.4   Maximum Disk Sizes: Bicelle to Vesicle Transition

For a range of q and c values, we experimentally confirm that nano-sized disks are the most stable aggregate structure at $10°C$. Our results also hint to the possibility of a limiting size, beyond which discoidal aggregates are not stable and fold onto themselves to form closed vesicles, irrespective of the initial composition. In previous studies using DLS, vanDam et. al. have observed a maximum possible disk size, so that no matter which combinations of q or c was used, disks with diameter >20nm could not be observed [74]. Previous observations of nano-disks in other systems have also found a limited range of molar ratios where discoidal aggregates can be formed [153, 160]. These observations agree well with our results in Table 5.3, where the range of disk sizes, vary from $\sim$ 40 to 120 Å for $1.5\leq q_{eff} \leq6$ (at the highest dilution limit). Above this higher q_{eff} limit, the discoidal phase is no longer stable in comparison to the vesicular phase. This transition between discs and vesicles, has been described as a first order transition by Fromherz in his analysis of the stability of bilayer fragments by edge-stabilizing agents [155, 161].

The existence of discoidal aggregates, and their limit of stability was obtained by Fromherz by balancing the elastic and line energy associated with the deformation of a disk [155]. The total energy f_{frag} of a membrane fragment of area A, length (contour length or perimeter) L and radius of disc R, which can be folded to form vesicles, can be written as the sum of its elastic energy f_{el} and edge energy f_{ed} given respectively by

$$f_{frag} = f_{el} + f_{ed}$$
$$= \frac{1}{2}(\kappa + 1/2\bar{\kappa})(2/R)^2 A + \Lambda L$$

where f_{ed} is characterized by Λ, the edge tension and gives the free energy of an edge, due to the change in interactions of the lipid molecules at the edge of a bilayer. It has contributions from 1. the hydrocarbon water contact and is positive due to the Hydrophobic effect 2. the changed headgroup environment.

f_{el} is characterized by $\tilde{\kappa}$ so that $8\pi\tilde{\kappa}(= (\kappa + \bar{\kappa}/2))$ is the elastic energy of a closed vesicle and the ratio $V_f = R\Lambda/4\kappa$, called the 'vesiculation index' is the ratio of line energy to bending energy and characterizes the relative stability of disks over closed vesicular structure.

A better understanding of the energetics involved is obtained by writing the f_{frag} in terms of Ω, the shape parameter which is defined as the ratio of the radius of a closed spherical shell (or vesicle) to the radius of the corresponding open disc [155]. By this definition, $\Omega = 0$ for a planar disk and $\Omega = \pm 1$ for closed vesicle. In terms of V_f and the shape parameter Ω, the net energy of a fragment associated with the deformation of a disc of radius R is given by

$$f_{frag}(\Omega) = 8\pi\tilde{\kappa}\Omega^2 + 2\pi R\Lambda(1 - \Omega^2)^{1/2}$$
$$= 8\pi\tilde{\kappa}\left[\Omega^2 + \frac{R\Lambda}{4\bar{\kappa}}(1 - \Omega^2)^{1/2}\right] \qquad (5.25)$$

Vesiculation indices V_f are shown in Fig. 5.16 in a (R, Ω) plane, for typical values of line tension $\sim 0.5k_B T$ / Å (19-20 pN) for long lipid like C14 [81, 154], and for different modulus of elasticities $\kappa \sim 100$, 200 and 10 $k_B T$ and radii between 50-500 Å. Also shown are representative curves for 50 and 400 Å fragments, showing their stability behavior in (a) where increasing radii makes fragments increasingly unstable. With increasing $\kappa \sim 200$ $k_B T$, V_f, the zone of stability increases as shown in (b). While decreasing κ to 10 $k_B T$, makes all except for the smallest 50 Å case unstable resulting in $V_f > 2$.
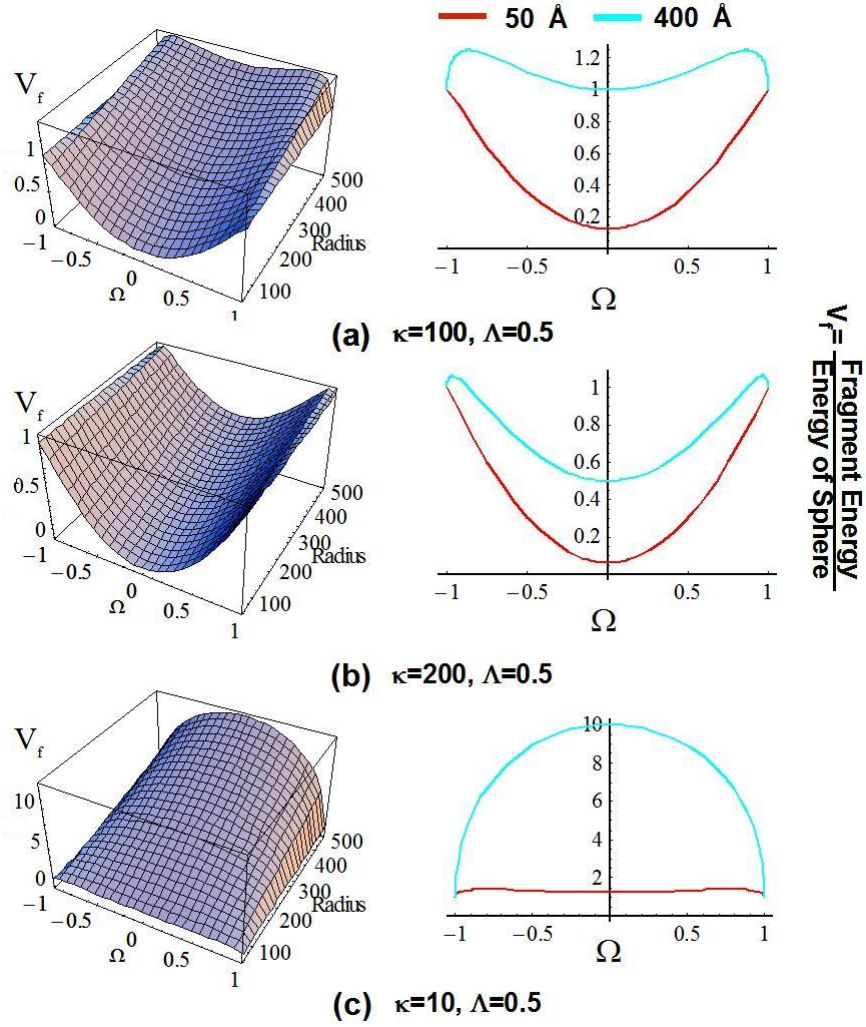
Figure 5.16: Stability of bilayer fragments (discs, $\Omega = 0$) vs. closed spherical shells ($\Omega = \pm 1$), or V_f, as a function of size, membrane rigidity and line tension of the assembly. *Left:* Stability as observed in (R, Ω) plane and Right: Two cuts at 50 and 400 Å showing V_f for discs of those dimensions for the same parameters. (a) For $\kappa =100$ k$_B$T and $\Lambda = 0.5$ k$_B$T / Å, V_f increases monotonically making 400 Å fragments unstable. (b) Increasing the membrane rigidity makes even the largest fragments, the 400 Å case stable. (c) Decreasing κ leads to instability in all the cases.

While the effect of κ is seen to be critical to the stability of bilayer fragments, for given bending modulus κ, increasing the fragment size, R, increases V_f, and decreases the stability of the disc phase as compared to the closed vesicle phase, confirming our experimental observation. In the gel state of C14 lipids, discs or bilayer fragments exist when the bending energy is commensurate with the edge energy.

Since the line tension Λ is another parameter defining V_f, this discussion also gives a strategy to control the line tension and hence the size of bilayer fragments in solution. By changing length of the bilayer forming lipid, as also by addition of second component, smaller lipids with lower line tension, the line tension of the bilayer aggregates can be modified. In the next chapter, we systematically explore the role of κ and Λ on V_f and hence on the discoidal bicelle phase.

5.6 Conclusions

This chapter focusses on the low temperature phase in C14/C6 'bicelle' mixtures for which there is growing evidence of discoidal aggregates only below the melting temperature T_m of the long lipid. In this regard, the magnetically alignable phase, considered in the literature to be composed of few 100 Å radius discoids, and only recently shown to elongated aggregates are considered in a later chapter (Chapter 7).

By focussing on the low temperature phase, we question the validity of the fully segregated ideal bicelle models (IBM) in the literature by using SANS techniques on lipid mixtures of the same composition but different contrast with respect to the solvent. In the first kind, where both the lipids are hydrogenated, SANS results from the contrast between a composite aggregate and the deuterated solvent, and a discoidal geometry is seen to be a good description of the aggregates in confirmation with prior studies. In the second, a direct evidence of the segregated discoidal morphology is obtained in experiments with mixtures of hydrogenated and deuterated lipids. By enhancing the contrast between lipids and the

solvent (CE samples) in the radial (in plane) direction as opposed to the perpendicular (normal to the bilayer) direction, the central assumption of the bicelle hypothesis, i.e. the long chain lipid forming the core of the bicelle while the short chain lipids form the rim is established.

Furthermore, since the segregated models in the literature do not have any dependence on thermodynamic parameters, we investigated them by characterizing the mixtures at 10°C . Growth of the discoidal aggregates is understood quantitatively with concentration and molar ratio dependence of the bicelle radii and a packing model consistent with the structural characteristics of the two lipids. The measured molar ratio q, shown in prior studies to be the defining parameter of the bicelle sizes using the IBM hypothesis, is shown to be inadequate description of the lipid mixtures. We derive a modified definition of q based on mixed surfactant theories and defined as the molar ratio with in the aggregates or q_{eff} . This parameter is shown to account for the first order growth of the discoidal aggregates. The observed growth rate however, falls short of that predicted by the fully segregated models implying that the segregation of the two lipids is not complete and an overall mixing of long-core lipids in the rim takes place. An estimate in such a mixing scenario, is obtained by quantifying the departure of the observed growth from that of the fully segregated case. It is found to be in good agreement with the result from the CE sample, obtained by fitting a polydisperse core-shell model with appropriate scattering length densities (SLD) to the SANS data in this case. Moreover, the mixing trend in the different concentration series is found to scale inversely with the excess molar ratio of long chain lipids, independent of the initial sample composition.

In the absence of adequate theoretical work on such non-ideal systems consisting of phospholipids, the driving force for the discoidal assembly is understood from Fromherz's continuum description of bilayer-vesicle stability, making it entropic in origin. The local minimum in the total energy of an aggregate is achieved in the discoidal geometry with a net partial mixing of the long lipids in the rim. The limiting size of the discoidal aggregates in

such lipid mixtures is seen to be a consequence of the balance of edge and bending energies of the aggregate and mixing entropy of the constituent lipids. Their transition to closed vesicular structures, seen experimentally in the limit of very low total lipid concentrations, is analogous to a first order transition based on the Fromherz argument.

Chapter 6

Low Temperature Assembly in Other Mixtures

6.1 Introduction

In Chapter 2, DMPC/Chapso (C14/Chapso) and DPPC/DHPC (C16/C7) mixtures were alluded to as the early progenitors of the bicelle mixtures. Both mixtures have been understood as forming discoidal micelles [86, 141, 95] and implicated in membrane protein crystallization [23, 24] and NMR applications. Although questions of packing and lipid segregation within the aggregates remain unanswered, just like in the C14/C6 case. In the bigger picture, the question of structural changes accompanying bilayer solubilization using various surfactants, a frequently studied problem in both physical chemistry and membrane protein communities (Almgren's article in [109]), also remains. While the discoidal aggregates frequently show up in phase diagrams of other lipid-detergent mixtures, their origin and variables governing their formation remain unexplained [109, 110]. In this chapter and the next, we present a detailed study of the morphology of various short and

long-tail phospholipids and of phospholipid-surfactant (non-lipidic) mixtures, using a combination of neutron and X-ray scattering techniques. The goal is to apply the lessons learnt from the previous chapter to other similar systems, in order to achieve the following:

1. To test the validity of the ideas driving the self assembly in the model C14/C6 mixture and verify their generalities.

2. To better understand the role of the two lipidic components in driving the aggregation behavior, so as to extend their applicability to newer membrane protein crystallization problems and a better understanding of any given lipid-detergent mixture.

As the tail length of the smaller rim lipid species is increased, the edge stabilization provided by the lowering of line tension from the smaller species, is expected to break down and increasing lamellar propensity is expected to overtake the aggregate morphology from finite size discoids to infinite bilayers, when the two species are of the same tail length. Also, from the phase transitions proposed by Katsaras and coworkers [105, 105, 22], lipid chain melting temperature T_m has a critical role in the phase transitions observed in these mixtures. Moreover, as shown in Chapter 5, since the bending rigidity of the core lipid was seen as a key ingredient for disc formation in, the question of aggregate morphology on enhancing this rigidity is expected to lead to further insights into their phase behavior. Hence, investigation of lipid mixtures with varying chain length of the long tail, core lipid and the short tail, rim lipids becomes necessary. From the discussion in Chapter 5, these studies, directly test Fromherz's arguments on stability of discoidal aggregates based as a competition between edge and bending energies.

In order to address the above issues, we report on two different series of experiments at 10°C in this chapter, using small angle neutron and X-ray scattering (SANS and SAXS) techniques.

1. Effect of increasing sizes of rim lipids: We investigated mixtures of DimyristoylPC (C14) with DiheptanoylPC (C7) and DioctanoylPC (C8) which are known to have order

of magnitude smaller CMC then that of C6 lipids and also the micellar sizes are larger and concentration dependent (Chapter 2). As both C7 and C8 are known to form polydisperse elongated micelles in solution due to their respective packing parameters, the question of their packing properties on rim curvature and stabilization of the aggregates naturally arises. Even more interesting is the question of segregation of the two lipids as the size of the short lipid chains increases.

2. Effect of increasing sizes of core lipids: We investigate mixtures of DihexanoylPC(C6) with DitridecanoylPC(C13) and with DipentadecanoylPC(C15). Both lipids are known to be bilayer forming and show chain melting transition from ordered to disordered states at 14 and 33°C respectively [47]. Also, chain length of the lipids is known to manifest in the bending modulus of the bilayers formed in a linear relation [162].

In this chapter, we obtain complimentary information from Small angle neutron scattering (SANS) and small angle X-ray scattering (SAXS) to get detailed information on both the global and local structure. For future reference, Fig. 6.1 summarizes the SLD profiles (see Chapter 4 and Section 4.4) in the radial and vertical directions of a disk like aggregate, offered by the small angle scattering (SAS) geometry, with neutrons and X-rays. SANS, with hydrogenated lipids is expected to answer questions of the global morphology. In fact, with the range of wave-vectors used in this study in SANS, $(0.002\text{-}0.6)\text{Å}^{-1}$ and in SAXS $(0.005\text{-}0.3)\text{Å}^{-1}$, being nearly the same, both can be used to probe the global morphology. But, with the SLD profile shown in Fig. 6.1, SAXS is expected to provide independent and detailed information at large scattering vectors or smaller length scales, since the background effect predominates in the neutron case. While we have already used a contrast enhanced sample of C14/C6 mixture in Chapter 5 to prove segregation and quantify mixing of the core lipid into the rim, it will be extended further in this chapter.
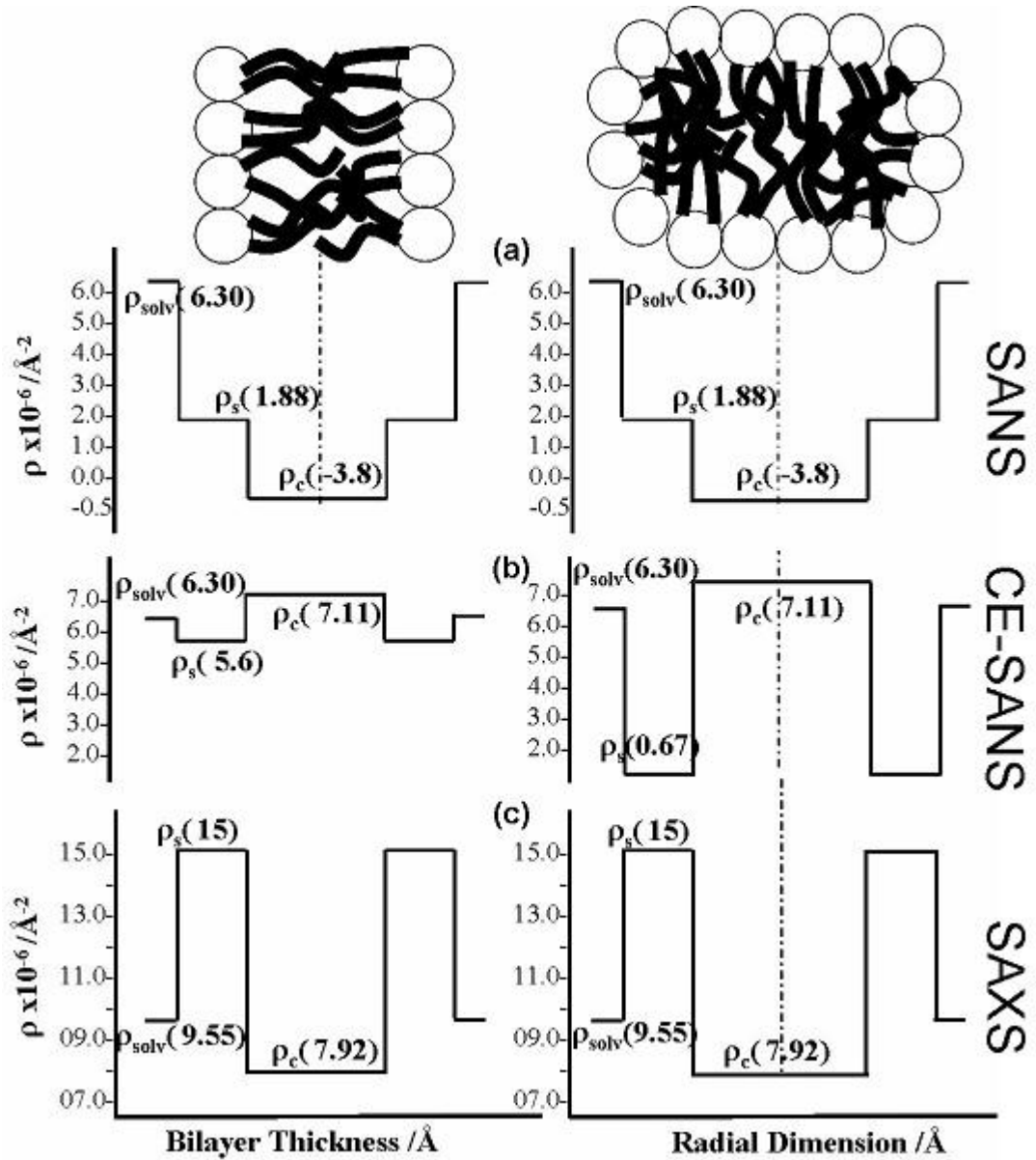
Figure 6.1: Variations in scattering length density across and perpendicular to a bilayer using neutrons and X-rays. (a) With neutrons on regular hydrogenated lipid samples or regular contrast (b) With neutrons on deuterated core bilayer forming lipid or contrast enhanced samples (c) With X-rays on regular or contrast enhanced samples. The difference in SLD contrast variation in case (b), across and perpendicular to the two planes, leads to 'contrast enhancement' across the bilayer plane. Lipids are shown without color to account for the different contrasts seen.

6.2   Experimental Details

Five different series of mixtures with varying rim lipid (the shorter species) were prepared: hydrogenated DMPC (C14) with C6, C7, C8, Chapso and Triton at molar ratio $q = [C14]/[Cx] = 2$ and total lipid concentration $[C14] + [Cx]$ of 0.1 g/ml by our usual sample preparation technique with 0.2M NaCl in deuterated solvent (Chapter 3). Each sample was diluted to give at least 4-5 *c-series* samples and sonicated at low and high temperatures a few times to ensure good mixing. Samples were stored overnight before measuring with neutrons. Contrast enhanced samples, one each with deuterated d-DMPC and hydrogenated C6, C7 and C8 in deuterated solvent, with $q = [dC14]/[Cx] = 2$ and c=0.03 g/ml were also prepared. These samples were measured with X-rays, neutrons and differential scanning calorimetry (DSC) within a few days of each other. Due to smaller volumes of sample prepared in this case, DSC measurements were done first and the same sample used again in SANS. Part of the original stock sample was used in SAXS. At 10°C c-series of each of the mixtures, except the C14/C8 case, are seen to be fluid and non-viscous like water.

For core lipid variation, the samples were prepared by a SURF student in the group. Samples with varying chain length of core lipid(the longer species) included hydrogenated C13, C14 and C15 mixtures with C6PC. The stock sample in this case was also made with $q = [Cy]/[C6] = 2$ and a total lipid concentration $c = [Cy] + [C6] = 0.1$ g/ml. Samples were diluted to obtain final total lipid concentrations between 0.001-0.08 g/ml for each mixture.

6.3   Results and Analysis

6.3.1   Mixtures with Rim Lipid Variation

For understanding trends with rim lipid variation, our reference point is the C14/C6 mixture, for which a detailed study was presented in Chapter5. Fig. 6.2, com-

pares SANS data on the absolute scale, from the molar ratio $C14/Cx \equiv q = 2$, and to-
tal lipid concentration $C14 + Cx = 0.03$ g/ml sample for each of the mixtures, C14/C6,
C14/C7, C14/C8, C14/Chapso and C14/Triton. The pair distance distribution function,
P(r) for each mixture, which is obtained from the indirect fourier transform (IFT) (Chapter
4) of the SANS data is also included in this figure. The P(r) distribution gives the global
structure of the aggregates without any assumptions of the geometry [[133, 134, 163, 164].

Similar to the C14/C6 case, all the samples, except for C14/C8, show the Guinier
regime at low scattering vectors, followed by a $\sim Q^{-2}$ decay. While the C14/Chapso mixture
shows the smallest R_g among all the mixtures studied, the intensity of the C14/C8 mixture
shows a -1 scaling after a barely visible Guinier regime, and is expected to have a very
different morphology than the rest of the mixtures. The Guinier regime in C14/C8 is seen
to occur almost at the lowest limit of the wave vector attained, and indicates the presence
of much larger aggregates than the other mixtures. This is even more evident from the P(r)
distribution for each mixture, shown in Fig. 6.2(b). At c=0.03 g/ml, all the other mixtures
are seen to have 100-150 Å aggregates while C14/C8 mixture has aggregates larger than
400-500 Å. However, the intermediate Q range data in all the samples are similar, pointing
to a similar cross-section in all the mixtures. The scattering data also agrees well with
visual inspection of all the samples at 10°C . At this temperature, all the mixtures except
for the C14/C8 mixture are transparent, fluid like water and non-birefringent, implying
the presence of small aggregates. The C14/C8 mixtures on the other hand were clear, yet
slightly viscous even at 10°C pointing to the presence of elongated structures.

Figures 6.3 and 6.4, show the SANS data and the corresponding P(r) distribution
for c-series in each of the lipid mixtures considered. Since the cutoff distance, at which
P(r)$\longrightarrow$ 0, gives an estimate of the largest dimension of the scattering object, existence of
finite sized globular aggregates, ≤ 200 Å in size is clearly seen. The C14/C8 mixtures on the
other hand show aggregates extending from 600Å in length to even larger values, which are
beyond the limit of resolution of the SANS instrument. Furthermore, evidence of growth

(a)

(b)
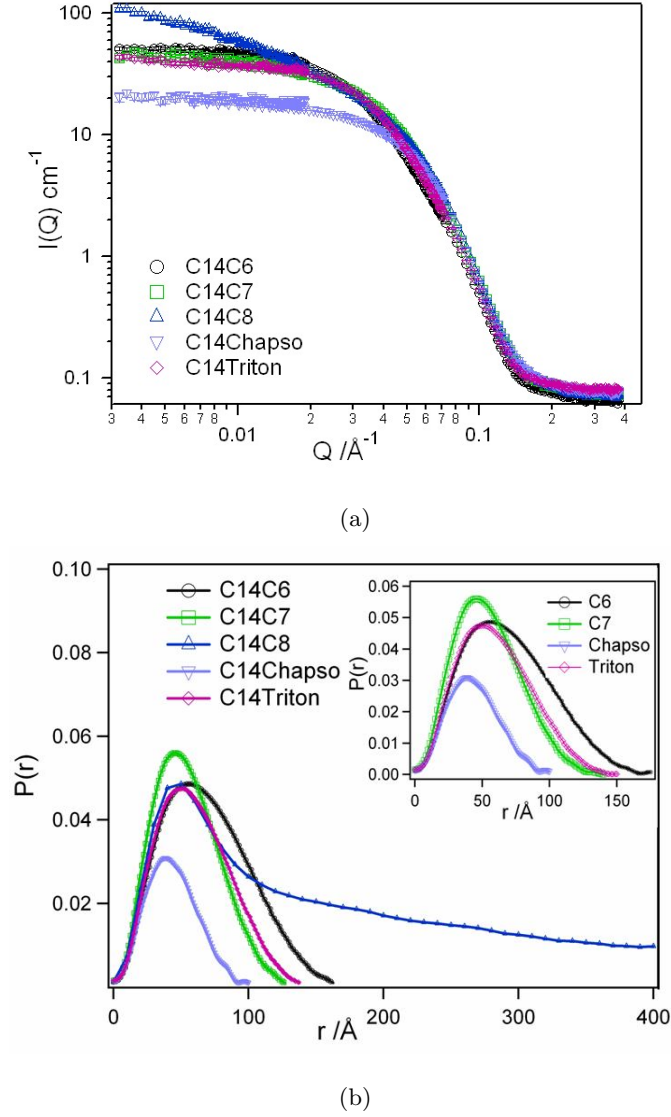
Figure 6.2: (a) Scattering data on an absolute scale, for the rim variation samples. All samples are of the same molar ratio $q = [C14]/[Cx] = 2$ total lipid concentration $c = [C14] + [Cx]$=0.03 g/ml. (b) Pair distance distribution function P(r) corresponding to each mixture. Inset shows the mixtures forming globular aggregates only.

with increasing dilution, similar to the one in C14/C6 mixtures is seen from the shift in Guinier regime to lower wave vectors, and even more from the change in P(r) distribution to larger distances in each lipid mixture. The elongated aggregates in C14/C8 mixtures are also seen to grow in size with increasing dilution. In this case, the cross-section given

by the point of inflection [133, 163] to a linear regime, extrapolated to zero (indicated in the C14/C8 case), shows that the cross-section remains constant even though the overall aggregate size undergoes elongation on dilution.
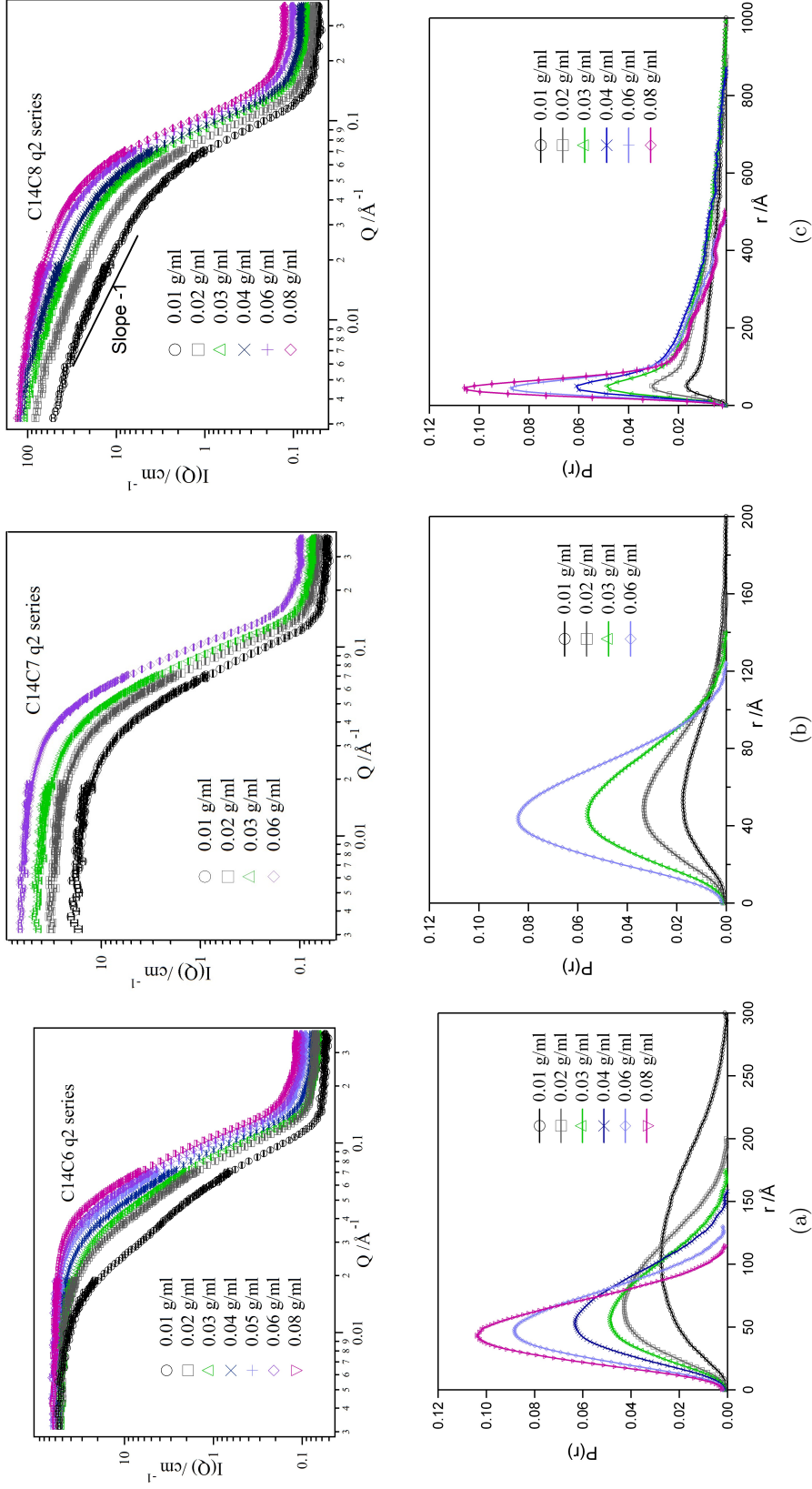
Figure 6.3: Scattering data and distance distribution functions P(r) from rim variation samples (a) C14/C6 (b) C14/C7 and (c) C14/C8. All samples are of the same molar ratio $q = [C14]/[Cx] = 2$ and total lipid concentrations $c = [C14] + [Cx]$ vary. Different morphologies P(r) corresponding to each series.
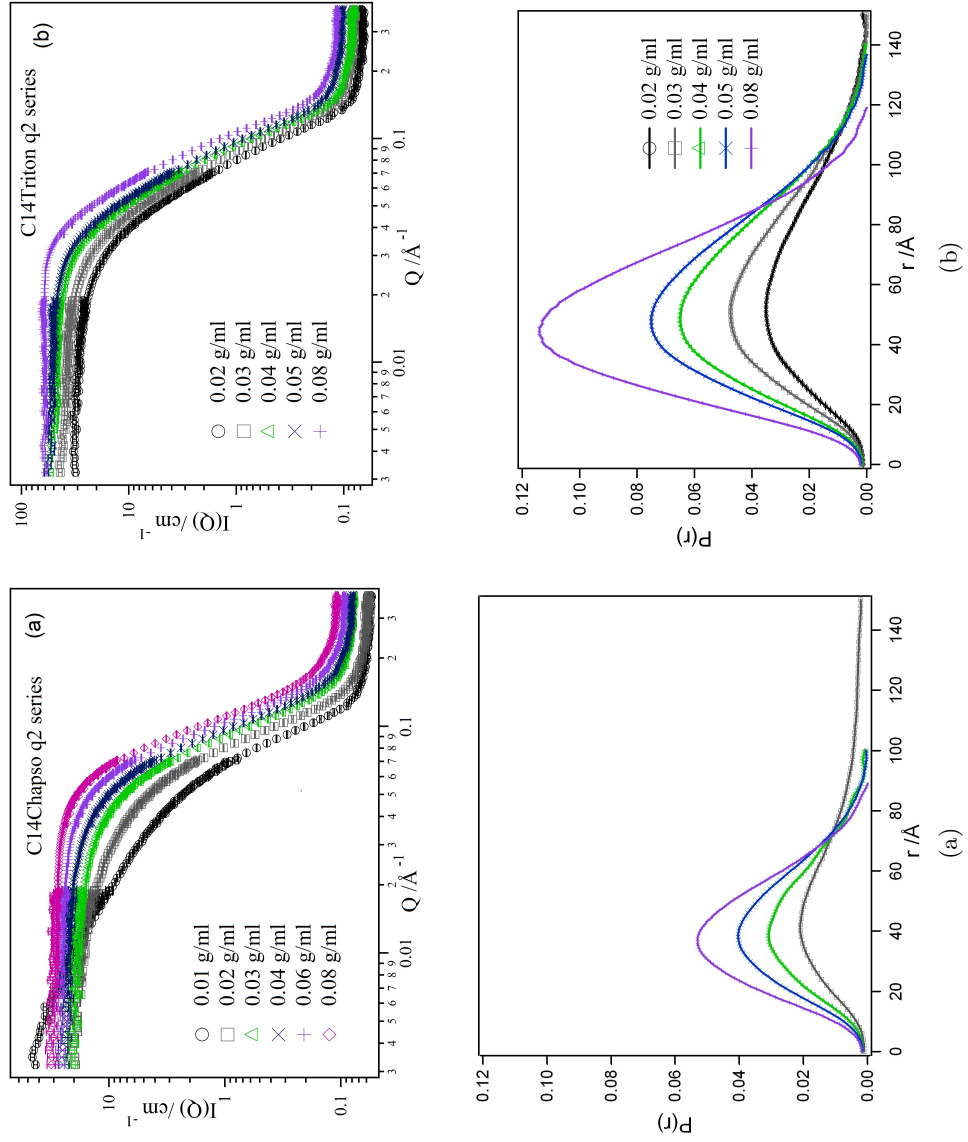
Figure 6.4: Scattering data from rim variation samples, C14/Chapso and C14/Triton. All samples are of the same molar ratio $q = [C14]/[Cx] = 2$ and total lipid concentrations $c = [C14] + [Cx]$ vary. Distance distribution functions P(r) corresponding to each series.

In order to characterize all the mixtures, particularly the one showing large aggregates (the C14/C8 c-series), one would like to use the R_g estimates obtained from the P(r) analysis to obtain aggregate sizes before using an appropriate model to do a tedious fit over the whole Q range. To do so, before applying this method on the spectra showing elongated aggregates, it's accuracy is tested first in the well studied C14/C6 case, for which the aggregate structure has already been established.

Fig. 6.5 shows variations in measured disk radii for the C14/C6 $c-series$ obtained using three different analysis techniques; namely the P(r) method, the Guinier estimate, and the non-linear least squares fits to models. R_g values obtained from the P(r) analysis are within 10-15% of those obtained from Guinier fits, and give a few Å difference in the calculated radii. Furthermore, the dimensions obtained from R_g estimates are in good agreement with those from form factor fits (Polydisperse core-shell). Thus all the three methods give fairly close results. As discussed before in Chapter 5, the radius of gyration obtained from the P(r) method and Guinier estimates were used to obtain the radius based on a discoidal shape with a rectangular cross-section and a thickness of 44 Å.

Consequently, in all the samples showing globular aggregates (and their spectra following the behavior of C14/C6 mixtures over the entire Q range), which includes the C14/C7, C14/Triton and C14/Chapso mixtures, the aggregate dimensions are obtained from the radius of gyration R_g by assuming discoidal shape with vertical rim. In the C14/C8 case, R_g was used to obtain length of the aggregates assuming an elongated structure, with rectangular or circular cross-section (discussed further in Chapter 7). For further discussion in this chapter, all the dimensions reported will be based on radii calculated from R_g estimate. To account for the differences obtained from the different analysis techniques, we put $\sim 10\%$ error bar for the rest of the discussion.
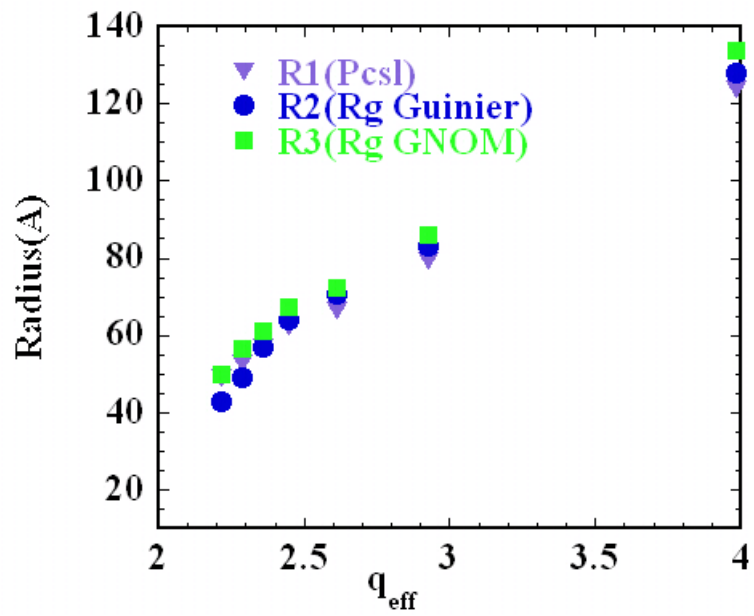
Figure 6.5: Radii of disks from the C14/C6 mixtures, obtained by three different techniques, form factor analysis using Pcshl fits to the full data, and from radius of gyration estimates obtained from Guinier fits and from P(r) analysis using the GNOM package.

Table 6.1: Aggregate sizes (in Å) of all mixtures obtained by different analysis techniques.

Composition	q_{eff}	P(r) Analysis			Guinier Analysis		Model Fitting†
$q = [C_{14}]/[C_x]$ $[C_{14}] + [C_x] = c$(g/ml)		R_g	Size (Largest)	R_{max}	R_g	Size	
C14/C6=2, 0.03	2.61	52.0	70.6	-	51.8	70.4	66.7(0.4)
C14/C7=2, 0.01	2.17	49.6	67.1	-	53.3	72.5	58.4(1.2)
C14/C7=2, 0.02	2.09	45.2	60.6	-	46.6	62.6	54.4(1.4)
C14/C7=2, 0.03	2.06	43.0	57.3	-	43.5	58.0	50.9(0.9)
C14/C7=2, 0.06	2.03	37.4	48.8	-	39.1	51.4	47.8(0.5)
C14/C8=2, 0.01⋆	-	-	-	-	-	-	-
C14/C8=2, 0.02	-	243±11.2	1084	1000	198.7 ± 8.5	671	-
C14/C8=2, 0.03	-	238±9.3	1062	1000	182.6 ± 6.3	614	-
C14/C8=2, 0.04	-	216±10.4	963	1000	162.7 ± 8.4	543	-
C14/C8=2, 0.06	-	123±2.2	545	500	141.4 ± 8.9	465	-
C14/C8=2, 0.08	-	115±3.5	508	500	116.9 ± 2.4	375	-
C14/Chp=2,0.02	2.68	51.3	69.6	-	43.6	58.2	-
C14/Chp=2,0.03	2.48	33.7	43.0	-	33.3	42.52	-
C14/Chp=2,0.04	2.37	32.5	41.2	-	31.4	39.44	-
C14/Chp=2,0.06	2.28	30.6	38.1	-	28.2	34.26	-
C14/Chp=2,0.08	2.16	-	-	-	27.4	32.94	-
C14/Tri=2,0.02	2.040	48.0	64.7	-	46.9	63.11	-
C14/Tri=2,0.03	2.017	46.3	62.2	-	44.0	58.95	-
C14/Tri=2,0.04	2.031	44.6	59.7	-	40.1	52.91	-
C14/Tri=2,0.05	2.030	43.4	57.8	-	37.8	49.41	-
C14/Tri=2,0.08	2.027	39.1	51.4	-	35.6	46.02	-

* Assuming a triaxial parallelepiped aggregate (Table 4.2) of thickness and width 44 and 63 Å respectively.

† Fitting errors are less than an Å and not included.

⋆ Guinier regime is beyond the low Q resolution of the instrument.

In going from C14/C6 to other mixtures, the first question one has to answer is weather the bilayer structure of the long lipid, forming the inner core, and the discoidal geometry are maintained in other mixtures. If that is indeed true, then we can apply much of the analysis in Chapter5 to model the growth of disc radii and mixing of the lipid species in edges. For the C14/C8 mixtures on the other hand, an elongated cylinder, can be used to estimate the length from the measured R_g by assuming a circular cross-section with constant radius. That this is not entirely true, is shown in the following discussion.

To clarify the cross-sectional details of the various mixtures, we first check their local structure by analyzing the data at the largest scattering vectors. Multiple contrasts from neutron and x-ray scattering data are used to get complimentary information as follows.

Cross-section from SANS data at large wave-vectors

Kratky-Porod (KP) analysis for locally two-dimensional objects and IQ^4 vs Q plots for all the samples, obtained from SANS data are shown in Fig. 6.6. Since the R_g obtained from a KP analysis is related to the thickness as $t^2/12$, the constant slope obtained by linear fits in KP graph in (a) as well as the same peak position in IQ^4 analysis in (b) shows that the smallest dimension of the aggregate, corresponding to the thickness of long tail bilayer core, is the same. The fit results are included in Table 6.2. Locally, all the mixtures maintain the bilayer structure of the long lipid C14.

Furthermore, in case of the C14/C8 mixtures, which shows a -1 power law scaling, implying elongated 1-dimensional objects, the modified Guinier analysis, $lnQI(Q)$ vs Q^2 (Chapter 4) can be used to estimate the rod diameter. Fig. 6.7 shows a few representative fits in the C14/C8 mixture. The rod diameter at ~ 63 Å is clearly much longer than a bilayer thickness and points to a third dimension in these aggregates. The cross-sectional diameter can be used to estimate the second dimension, like 'width' by assuming a thickness of 44 Å and using the radius of gyration of a rectangle given by $R_g^2 = 1/12(A^2 + B^2)$, where A, B are the edges of the rectangle. Hence in Table 6.1, the length dimension of the aggregates

135
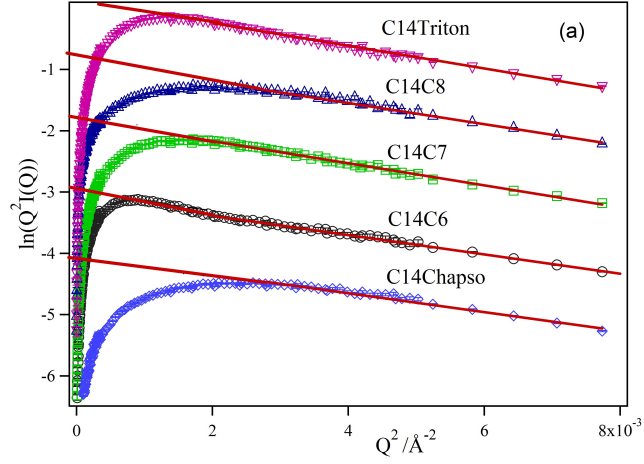
(a)
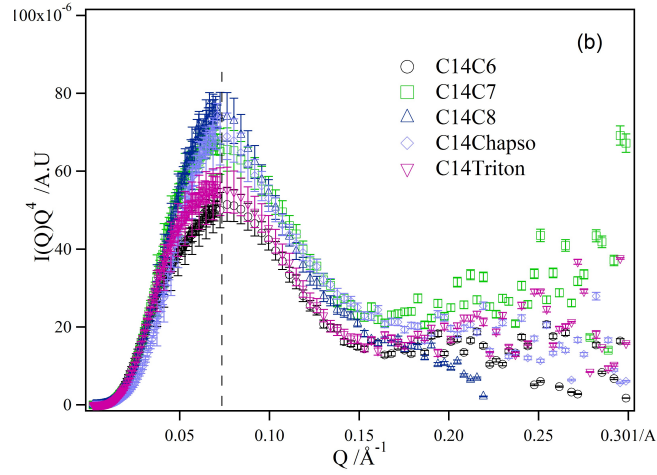
(b)

Figure 6.6: All samples have the same local geometry/ cross-sectional thickness. (a) Kratky-Porod Plots of rim variation samples showing same slope (data have been shifted on y-axis for clarity) (b) IQ^4 vs Q plots showing same peak positions implying same bilayer thickness. All samples are of the same molar ratio $q = [C14]/[Cx] = 2$ and total lipid concentration $c = [C14] + [Cx] = 0.03$ g/ml.

are obtained from the R_g by assuming an elongated triaxial ellipsoid (Chapter 4), with axes $2a = 44$Å(thickness) and $2b = 64$Å(width), instead of a cylinder with circular cross-section and of diameter equal to the bilayer thickness.
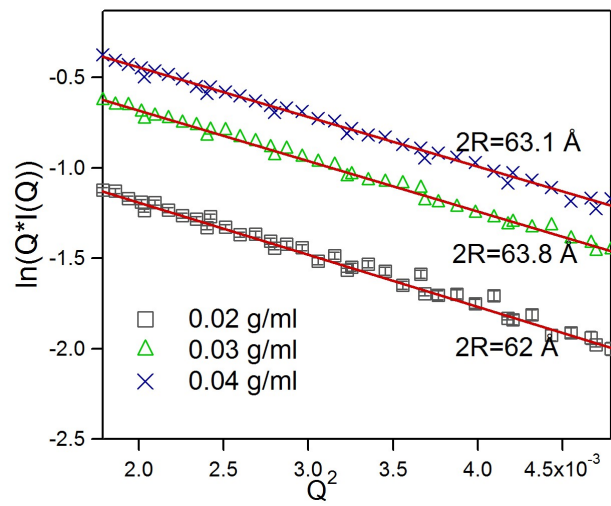
Figure 6.7: Modified Guinier fits to few data sets of C14/C8=2, $c-series$, showing rod diameters bigger than the fully extended size of a C14 lipid bilayer.

Cross-section from SAXS data

To obtain complimentary cross-sectional information, SAXS measurements were also taken on a few samples. As shown in Fig.6.1(c), the SLD profile with X-rays, in both the radial and perpendicular direction (both are 2-step profiles), is entirely different from those with neutrons in both contrast cases shown in Figs. 6.1(c)(a) and (b). The SLD difference between the head group and tails is the largest with X-rays ∼(15-7.92) (c), ∼(6.3-0.67) (b) and ∼(1.88+0.38) (a) in units of Å^{-2} . The samples included mixtures of composition $q = 2$, c=0.03 g/ml in all of dC14/C6, dC14/C7 and dC14/C8. Fig. 6.8 shows the SAXS data with the smallest dimension indicated. Since in neutron scattering, the oscillations in the bilayer form factor are hidden due to the large incoherent scattering from hydrogen, with X-ray scattering, even in the limited $Q-$range of our data, they can be seen clearly upto second order (this is in contrast to five and six orders of peaks obtained by Nagle and coworkers with oriented multilamellar bilayer samples and with much smaller wavelengths). The samples used for these measurements, included d-C14 (instead of the regular hydrogenated species) to be used also with neutrons. For X-ray scattering itself though, changing C14 with the deuterated C14 does not change the contrast and the SLD of tails in both the cases in $7.92{\times}10^{-6}$Å^{-2}. Data with neutrons is discussed further in this section.

Fig. 6.8 shows the SAXS data and the Q vector corresponding to smallest dimension in all the three mixtures. The second peak has been argued to be the head to head spacing when the SLD profile has a core-shell variation as shown in Fig. 6.1 [43].

Fig. 6.8 shows results from an IQ^4 vs Q analysis of the X-ray scattering data. All three samples show the same peak positions but vary in peak intensities. In this form, the data at high Q is amplified and we could apply the core-shell lamellar form-factor, with poly dispersity to fit this data (Chapter 4). The results of these fits are also included in Table 6.2. The half bilayer thickness is fixed to 30Å based on X-ray data of Nagle and coworkers [38], giving a headgroup region of 6Å, slightly smaller than expected. However,

the bilayer thickness is seen to remain constant with varying rim lipids, indicating that the bilayer core, in either the discoidal or the elongated aggregates remains unperturbed.

(a)

(b)
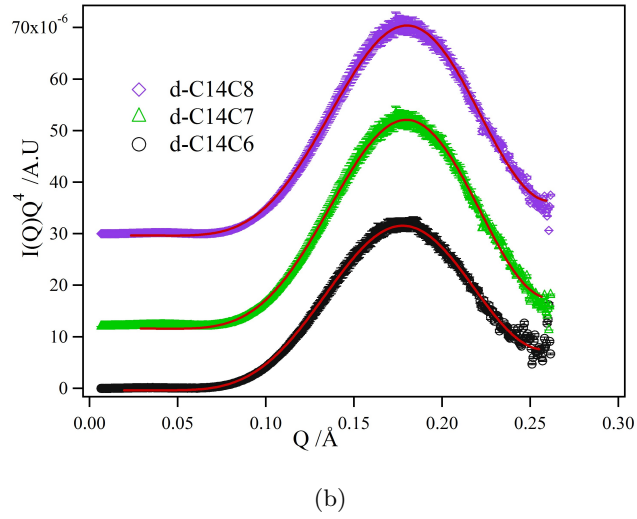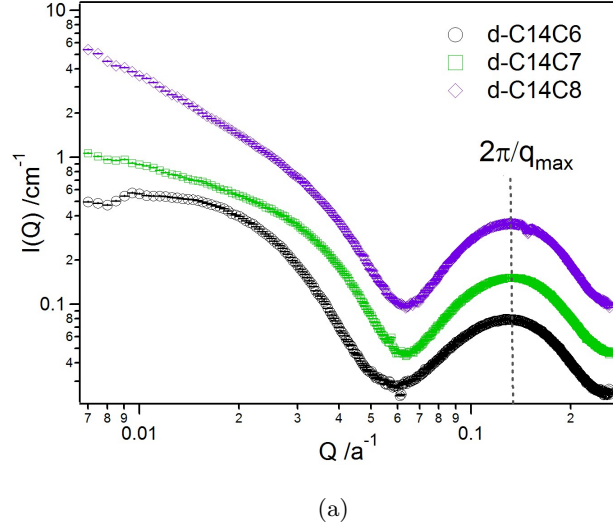
Figure 6.8: All samples have the same cross-sectional thickness. (a) SAXS data showing same high Q profile. (b) IQ^4 vs Q plot of SAXS data showing no shifts of peak positions and implying a constant bilayer thickness. Fits were obtained using the lamellar form factor (Chapter 4) written in IQ^4 format. All samples are of the same molar ratio $q = [dC14]/[Cx] = 2$ and total lipid concentration $c = [dC14] + [Cx] = 0.03$ g/ml.

Table 6.2 is a compilation of cross-section information obtained using both neutrons and X-rays. It is clear that the thickness of the bilayer core does not change as one

Table 6.2: Bilayer characteristics of representative rim lipid variation samples at 10°C used in this study (all samples are of molar ratio $C14/Cx = 2$ and total lipid concentration $c = C14 + Cx = 0.03$ g/ml

Method	Sample	Core (Å)	Head Group (Å)	Bilayer Total (Å)	Polydispersity
Neutron KP	C14/C6			46.37 ± 0.14	
	C14/C7			47.18 ± 0.07	
	C14/C8			45.35 ± 0.08	
	C14/Chapso			43.64 ± 0.12	
	C14/Triton			49.34 ± 0.12	
Neutron IQ4*	C14/C6	15 ± 0	7.6 ± 0.33	45.2	0.29
Xray IQ4*		15 ± 0	6 ± 0.06	42	0.11
		15 ± 0	6 ± 0.06	42	0.08
		15 ± 0	6 ± 0.06	42	0.09

* Fit using Lamellar form factor (Chapter 4) which gives only half the bilayer thickness

changes the lipid species in the rim. The variations between 45-50Å are mainly due to the approximation of the actual SLD profile of a bilayer shown by Nagle and coworkers, to that of single step or two step SLD profile used (Fig.6.1). Such differences have been observed before in scattering on unilamellar vesicles of pure C14 and C16 lipids ([142] and references therein). The simplifications to the SLD profile, in terms of step changes, even if not a good representation of the actual bilayer, give quantitative trends for the mixtures in this study, since we are interested in the over all changes in the aggregate morphology.

Discoidal aggregates in other mixtures

Having established that the central bilayer core is maintained in C14/C7, C14/Chapso and C14/Triton series, like in the C14/C6 mixtures, the radius of gyration data from linear fits is used to calculate the overall radial dimensions of the aggregates using a thickness of 44Å (less than 1Å difference is found by using 40 or 50Å as the disc thickness). As noted in Chapter5, for binary mixtures, the CMC of the mixture plays a key role in the effective molar ratio of the two species that goes into forming the aggregate in a mixture of molar

ratio q and total lipid concentration c. The relevant parameter for a binary lipid mixture of given composition is thus q_{eff} given by Eqn.5.18, in that it is this parameter that governs the growth of the discoidal aggregates. The q_{eff} , of each sample after correcting for free lipids in solution and the radial dimensions are included in Table 6.1.

As discussed in detail in Chapter 5, the aggregate dimensions of C14/C6 mixtures fall short of the growth predicted by the *modified ideal bicelle model (IBM)* in Eqn. 5.11, and call for a net mixing of the long species C14 into the edges. Use was made of Eqn. 5.23, to estimate the mixing into the rim in each of the c-series mixtures. Before extending the same analysis to the rim variation mixtures in this chapter, we checked the predictions of the modified IBM on the mixing estimates simply on variations of the rim curvature and the overall radial dimensions.

Fig. 6.9 shows that the maximum uncertainty in the estimate comes not from the uncertainty in the radial dimensions (based upon the measurement method, Guinier, P(r) or form factor), but instead from the curvature. This is understandable, since the curvature decides the number of edge/rim sites and hence the percentage of long lipid that can go into the edges. This is particularly relevant for the following discussion, since the hydration of the head group, which is dependent upon the curvature and varies for each species, makes it difficult to separate the total dimensions of the rim lipid (head group + tail length) from the radial dimensions of the disc, particularly in the C14/Chapso case, as Chapso is known to form micelles where its head group and tail region cannot be distinguished[43]. So for the rest of the discussion, a 15-20% uncertainty in the mixing estimates is assumed.

For the rim curvatures, we obtain approximate values from semi-minor, or the smallest axis of the micelle formed in solution. From Table 2.1, we see that the hydrophobic tail length of C7 is 9.5Å giving the shortest dimension of its aggregation state at ~ 13 Å, and ~ 10 Å in case of Chapso and Triton. Then using the measured radii, q_{eff} , the volume ratio of the long to short lipid species $k_V = Volume_{C14}/Volume_{CX}$ along with the estimated rim dimensions, mixing estimates as a measure of deviation from the fully segregated case,

141
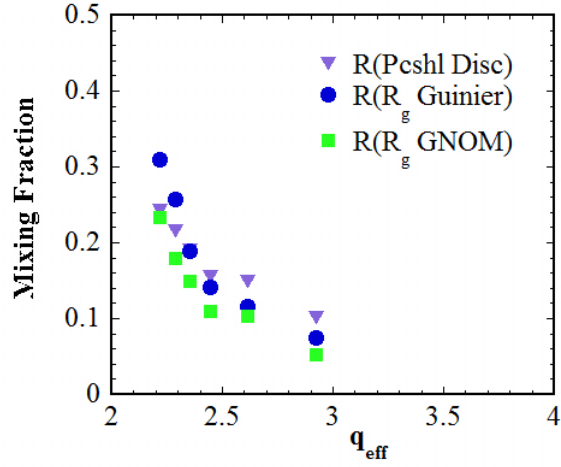
(a)
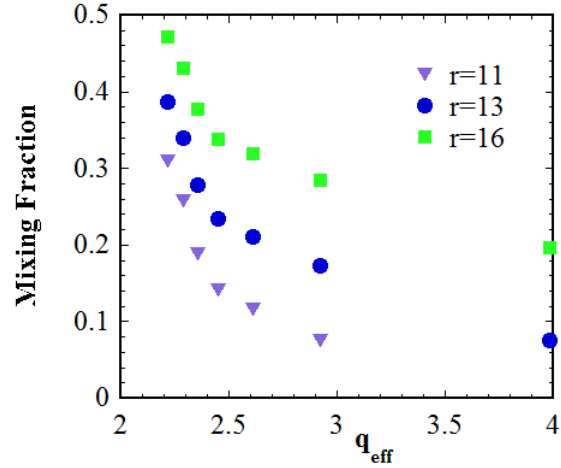
(b)

Figure 6.9: Uncertainty in mixing estimates. (a) From analysis techniques: disc radii calculated from radius of gyration R_g and obtained via Guinier fit or model independent P(r) analysis and compared with form factor fit to polydisperse core-shell model (b) From curvature of the rim: shows large differences, upto $\sim$ 30-50% based on the composition.

are obtained for each mixture. Based on the molecular volumes of the rim species (Table 2.1), k_V values used were as follows C14/C6: 1.55, C14/C7: 1.45, C14/Chapso: 1.25 and C14/Triton: 1.80.

Fig. 6.10 shows disc radii in all the rim variation samples. Disc radii are plotted against q_{eff} , where q_{eff} is the effective ratio of lipids in the aggregates, as defined in

Chapter 5. Disc radii scale with q_{eff} but with different slopes. From this figure, it is clear that for the same range of concentration changes, the disc sizes obtained in C14/C6 mixtures have the largest size implying the best edge-actant nature of C6 lipids (see also Fig. 6.2(b)). The fact that the C14/C6 mixtures form the largest discoidal aggregates for a given composition is not very surprising considering it has the highest CMC of 14mM, and also the smallest hydrophobic length C6, C7 and C8, so that on dilution, the free monomer effect from Clint's theory is biggest in this case. In the C14/Triton case, it is unclear weather the sharp growth on dilution (see inset) is a result of uncertainty on its CMC value, or non ideality terms in the Clint model used. Trends in these mixtures will be taken up further in the discussion section.

(a)

(b)

[Disc radii and mixing estimates for the rim variation mixtures.]
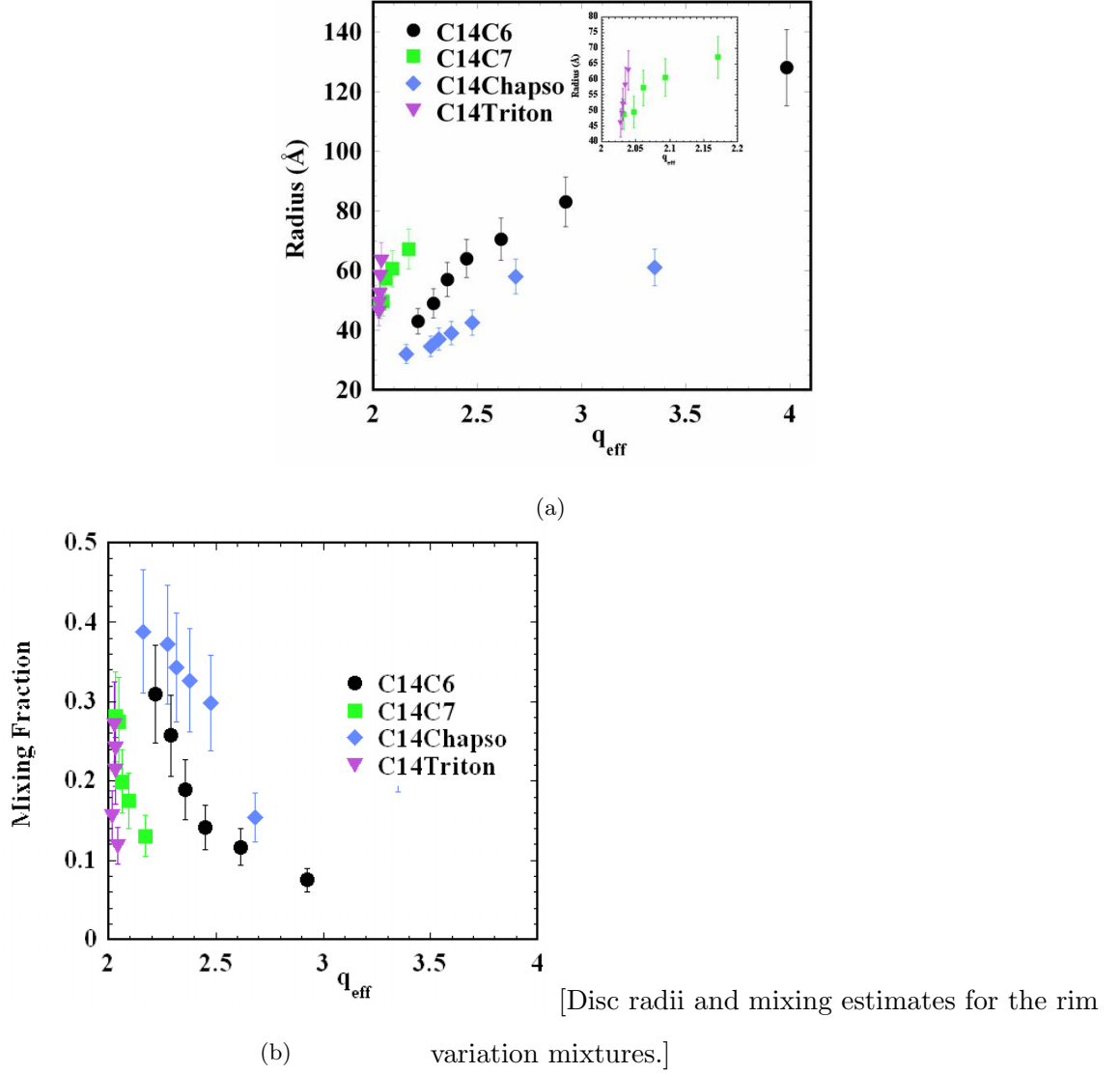
Figure 6.10: Disc radii and mixing estimates for the rim variation mixtures. (a) Radius of discs obtained in all the series plotted as a function of q_{eff} for each sample. Radius values are those obtained from radius of gyration using Guinier fits. 10% uncertainty (from 6.5) is included. (b) Mixing estimates of the long tail lipid C14 into the rims. 15% uncertainty is included as a lower limit on the uncertainty in rim curvature.

144

Mixing verifications from contrast enhanced samples

By extending the contrast enhancing technique used in Chapter 5 and Sec.5.4.4, where the first proof of the segregation hypothesis for the two lipids was shown, Fig. 6.11 shows proof of segregation in two of the other mixtures in this study. Irrespective of the geometry, (discoidal in C14/C6 and C14/C7 or elongated in C14/C8 mixtures), the presence of correlation peaks, indicates the segregation of the two lipids. The peak position in C14/C8 is at higher wave-vector than in the C14/C6 mixture. This suggests that in the C14/C8 mixture, with elongated morphology, the segregation is in a smaller dimension then the radial dimension of the C14/C6 mixture at ∼140 Å diameter. From the analysis of the cross-section outlined before, this could be the width of the elongated aggregates.

The polydisperse core-shell disc (or cylinder) form factors described in Chapter 5, were used to fit the data in the dC14/C6 and dC14/C7 case as described in Chapter 5, but not in the dC14/C8 case. Since that model requires a shell of uniform SLD, it would not work for the elongated aggregate in the dC14/C8 mixture, if there the lipids are segregated. For this reason, in the next chapter, we develop a model for such elongated aggregates. As for the dC14/C6 data, the polydisperse core-shell model fits the dC14/C7 data very well, except at low Q, possibly due to some elongation of the aggregate, that we ignored by fixing the disc thickness. Fit in this case indicate about 35% mixing in the edges, significantly larger than in the dC14/C6 case for the same composition of the mixture. Fit to the dC14/C6 data is as obtained in Chapter 5, which gave a mixing estimate of ∼ 15%. Even with the 15-20% error bar on these results as described in Chapter 5, the trend is quite clear.

Ideally, similar SANS data on contrast enhances mixtures with C14/Chapso and C14/Triton would have further added credence to the trend in rim variation mixtures, nevertheless the segregation and mixing trends obtained from the current data can be correlated to the data from regular samples. Contrast enhanced SANS on other mixtures is left for future investigation.
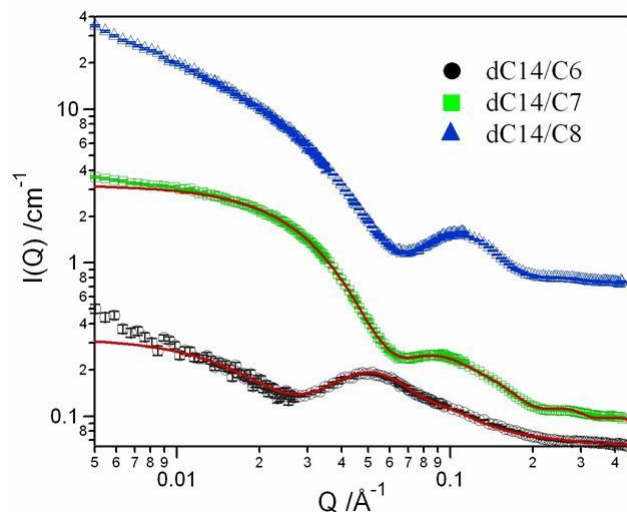
Figure 6.11: SANS data from contrast enhanced samples in $q = 2$, $c = 0.03$g/ml mixtures of dC14/C6, dC14/C7 and dC14/C8 (shifted on the y-axis for clarity). Correlation peak in all the mixtures show segregation irrespective of the overall morphology. dC14/C6 and dC14/C7 mixtures, with small discoidal aggregates are fit with the polydisperse core-shell disk model.

6.3.2 Mixtures with Core Lipid Variation

Variations of the long-tailed core lipid is expected to confirm ideas developed in previous and the current chapter on the crucial role played by the bending rigidity of the long tail lipid in discoidal formation at low temperatures. Fig.6.12, shows SANS data obtained from mixtures with variations of the core lipid, C13, C14 and C15; and their corresponding pair distance distribution function.

From the scattering data and the P(r) results, the trend of increasing aggregate sizes with decreasing total lipid concentration is quite clear. Since these measurements were also taken at 10°C , below the melting temperatures of both C13 (15°C) and C15 (33°C) lipids, it is reasonable to assume that the aggregates are discoidal in shape. This means that all the ideas developed in this as well as the previous chapter on the growth and partial segregation of these lipid mixtures can be easily extended. Fig. 6.13 shows radius as well as mixing variations in the C13/C6 and C15/C6 mixtures when compared to the reference

phospholipid mixture of C14/C6. Aggregate sizes in C13/C6 are smaller than in C14/C6, which in turn are smaller than those on C15/C6. Though the difference between C15/C6 and C14/C6 mixtures is not as pronounced. Further, decreasing sizes of the aggregates for the same composition between those mixtures is seen to result in increased mixing.
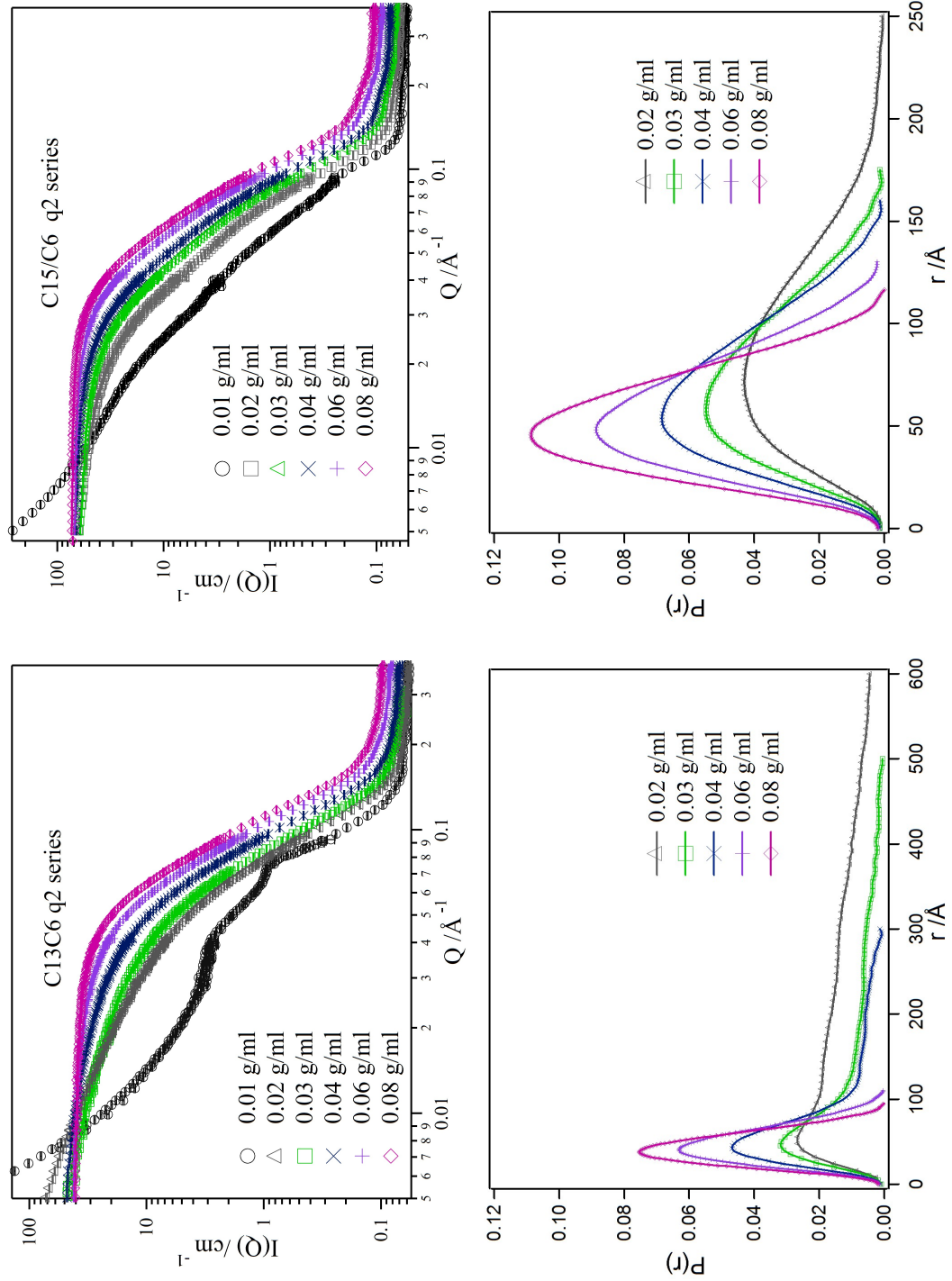
Figure 6.12: SANS data and corresponding pair distance distribution functions P(r) from core lipid variation samples. (a) C13/C6 and (b) C15/C6.
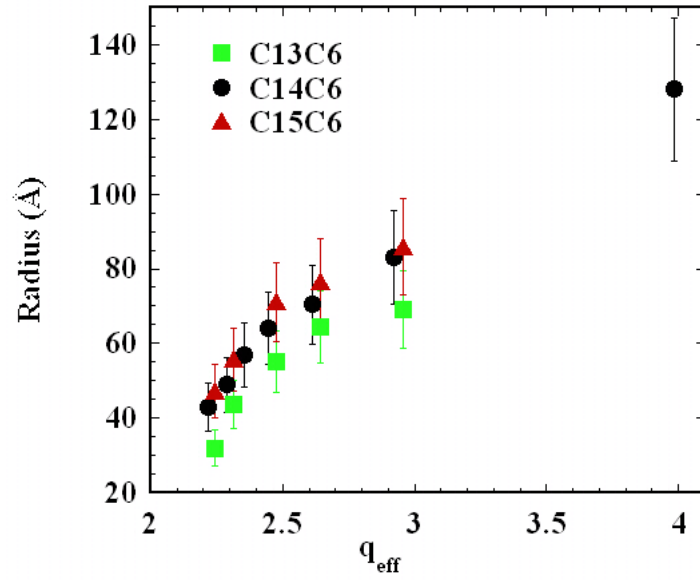
(a)
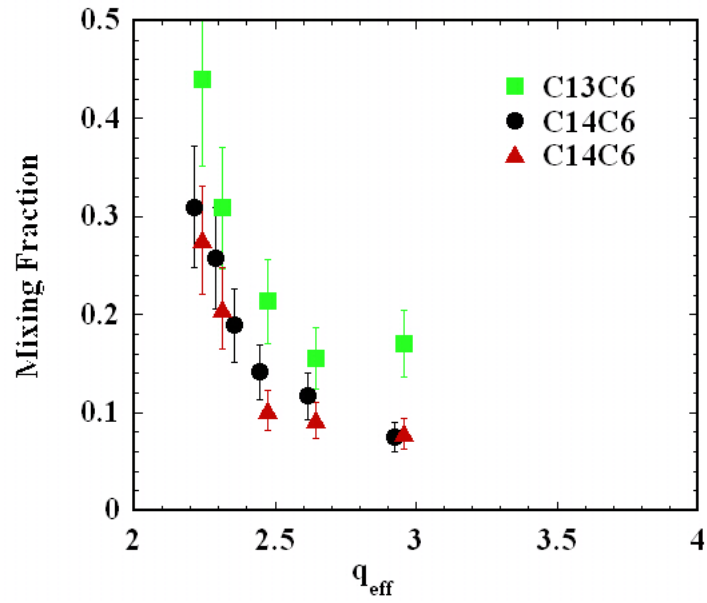
(b)

Figure 6.13: Discoidal phase in core lipid variation samples. Growth of the aggregates with decreasing concentration or increasing q_{eff} in (a) and estimate of core lipids mixed into edges in (b).

6.4 Discussion

In the following sections, a discussion of the results and other more general characteristics of the low temperature phase behavior from the two studies and their implications for the goals of this study are presented.

6.4.1 'Universality' of Segregated Phase Below T_m

The morphology of different phospholipid mixtures and phospholipid-surfactant mixtures at low temperatures, presented in this chapter, are consistent with small discoidal aggregates. The results are a strong indication that the segregated, with partial mixing in the rim, discoidal phase is a common feature in mixtures of long and short lipids at low temperatures where chains of the long-tailed lipids are in the gel state. In fact, data from Chapso and Triton, indicate that it may be an even more general feature of mixtures of bilayer forming long lipids and short chain micelle forming surfactants. The main criterions for the formation of these discoidal aggregates, appears to be the presence of a phospholipid species with large bending rigidities ($\sim 100k_BT$ for DMPC or C14 lipids), characteristic of most phospholipids with a melting temperature T_m ; and the presence of a second component, another smaller phospholipid or a detergent which has detergent properties such as to lower the line tension of long lipid edges and thus stabilize the discoidal aggregates. If such segregated, mixed micelles have been considered 'unusual' in prior literature [165, 113], than our study shows the rather 'usual' occurrence of these aggregates. Formation of much larger segregated, discoidal aggregates has also been shown in a very different system of mixtures of catanionic surfactants, by a similar mechanism [153].

The mixing behavior of the two species with large differences in their spontaneous curvatures in the aggregate (read disc) edges shown in this study is the first such result with regard to prior studies on mixed lipid phases. As expected from detailed reports on lipid mixtures [82, 83] and also proposed in recent study by Triba et. al. [106] on the same

system, our results confirm that mixing of the short lipid species into the core is negligible when the long tail lipid is in the frozen gel phase below T_m. In addition, our results show previously unexplored mixing behavior in the edges. While mixing of short lipid species into the long lipid core is unfavored due to the frozen nature of those lipid chains, the short tail lipids lower the free energy of the disk by self-assembling with the long-tail species, covering the edges to reduce the edge energy.

The results presented in this section can be seen better in light of prior experimental work in mixed bilayer systems [49] which have considered the effect of cosurfactants with different chain lengths and focussed on the stability of bilayer phase to vesicle formation. Similarly, prior theoretical studies in mixed lipid-surfactant systems [62, 157, 156] have focussed mostly on lipids in the fluid phase, where transitions from mixed bilayers to mixed micelles have been observed experimentally[115, 116]. Theoretical studies using molecular theories of mixed systems with varying chain lengths have considered effect on bending rigidity and spontaneous curvatures with regard to bilayer stability [15, 159, 162], but the mixing terms have been considered ideal.

6.4.2   Mixing Increases with Decreasing Chain Length Difference

Fig. 6.14 shows mixing estimates as a function of the disc radii or more generally the aggregate sizes in both the rim variation and core-variation samples. For the $c-$series in each lipid mixture of molar ratio $q = 2$, the mixing estimates obtained as deviation from the fully segregated model are plotted against the corresponding aggregate size. It clearly shows, that the fraction of long lipid species, mixed into the curved edges, scale inversely with the aggregate size, independent of the smaller or longer lipid species, as long as the larger lipid species forms a rigid core with its frozen chains (measurements at 10°C in all the mixtures, ensures a rigid core). This observation is similar to the mixing trend in C14/C6 $c - series$ of different molar ratios, in Chapter 5, where the mixing fraction was shown to

151

scale inversely with the *excess molar ratio*, an indicator of the aggregate size over and above that expected from the molar ratio. In addition, Fig. 6.14, which compares mixing in the C14/C6 case, to mixing in both the rim and core variation mixtures, shows the 'universality' of the mixing behavior in the segregated lipid-surfactant phases.

The trend in mixing seen in the regular C14/C6 and C14/C7 mixtures and confirmed further by the corresponding contrast enhanced SANS data, is a first quantitative study of the mixing behavior of short and long lipids in an overall segregated aggregate. Even though contrast enhanced samples of the other combinations (dC14Chapso and dC14Triton) have not been measured in thus study, the overall trend in segregation and scaling of the partial mixing behavior seems to be a fairly general across discoidal aggregates of any two mixtures with the characteristics listed above. Furthermore, the inverse scaling of mixing behavior (for instance in the rim variation samples) and shown to be a result of curvature strain, can be explained more generally as a consequence of the hydrophobic mismatch between the long-core and short-rim species, as discussed below.

As discussed before in Chapter 5, since for a given composition of the lipid mixtures, for entropic reasons, mixing of the two species into each other is expected to increase the mixing free energy contribution as the difference between the tail length decreases (lipids with similar sized tail lengths mix ideally [82, 83]. Triba et al. have shown increased mixing with decreasing chain length difference between the rim species [139], for temperatures above T_m of the long lipid. Fig. 6.14 compares the mixing behavior between rim variation mixtures for the same core lipid C14 and core lipid variation with the same rim lipid C6. In confirmation with those results, our results show the same mixing behavior even at low temperatures when the majority of long lipids are in the gel phase core. For the same composition, increased mixing of the longer species in the rim, with decreasing chain length difference is seen in both the cases in the trend $x_{C6} < x_{C7} \sim x_{Triton} < x_{Chapso}$ and $x_{C13} > x_{C14} > x_{C15}$.

While we have argued before for mixtures showing discoidal aggregates, that the
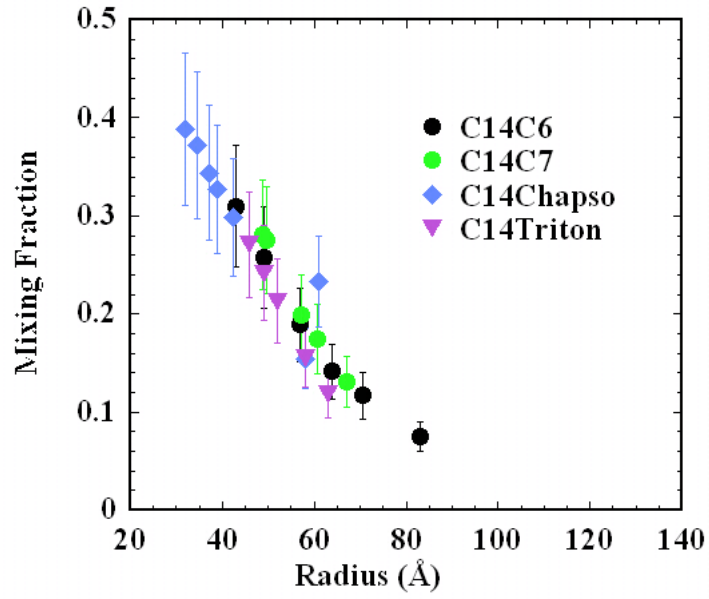
(a)
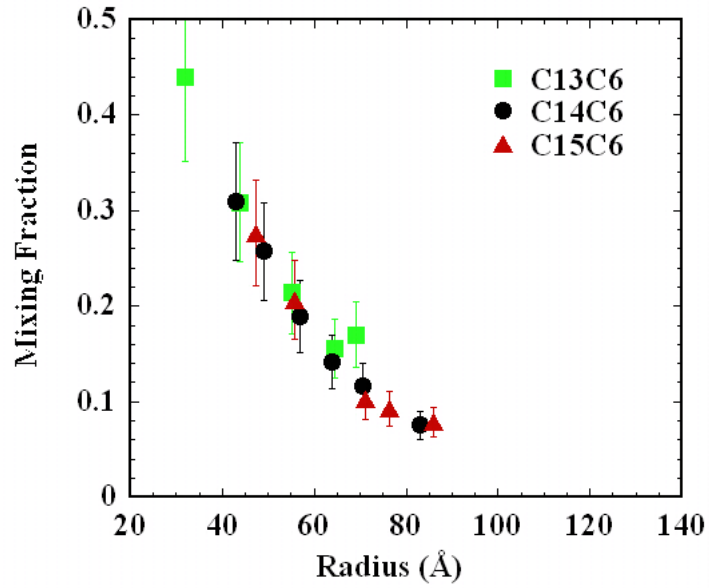
(b)

Figure 6.14: Mixing of long tail lipid into rims of short lipid species scales with disc radii (a) In rim variation samples (b) In core variation samples.

smaller growth rate then the ideally segregated case observed experimentally is evidence of the longer species mixing into the edges (note that two mixing fractions were defined in

Section 5.5.2, of long mixed into short x in rim, and of short mixed into long y in the core). But this may not be absolutely true, particularly in the case of C14/C8, (as argued in the next section). In the other mixtures also, it is only likely that a smaller mixing in the core also takes place, and it is the net effect that is seen in the observed growth rate.

We discuss the rim variation mixtures: C14/C6, C14/C7, C14/Triton and C14/Chapso mixtures and the core variation mixtures, C13/C6 and C15/C6 first, before discussing the C14/C8 mixture, which has a very different morphology than the rest.

The mixing trend seen Figures 6.10(b) and 6.13(b), a consequence of the decreasing hydrophobic mismatch or curvature difference between the two lipid species can be understood by Fromherz's vesiculation argument (see Section 5.5.4). The 'vesiculation index' which defines the stability of a bilayer fragment (over a closed vesicle phase) of radius R and of bending rigidity κ and line tension Λ and expressed as $V_f = R\Lambda/4\kappa$, can be lowered by decreasing the line tension of the aggregate with the addition of 'edge-active species'. Fromerz also proposed a Gibb's isotherm like phenomenon [161] to describe their accumulation in the edges. Imagine a lipid bilayer of the long tail lipid species, of some bending modulus κ and line tension Λ_{CLong0}. The decrease in the line tension as a consequence of the adsorption of the rim lipids on the edges can be described by Gibb's equation as

$$\Lambda = \Lambda_{CLong0}\left[1 + \frac{k_BT}{\alpha_b}ln(1 - \phi_r)\right]$$
$$\Lambda = \Lambda_{CLong0}\left[1 + \frac{k_BT}{\alpha_b}ln(x)\right] \tag{6.1}$$

where ϕ_r, the mole fraction of the small edge-active lipid in the rim, is (1-fraction x) of long lipid mixed into edges obtained experimentally from our SANS data. While the parameter α_b is the energy gain when one rim lipid binds to the edges and is a measure of the edge stabilizing characteristic of the molecules that can lower the line tension by providing a rim of high curvature. Based on this argument, and the fact that line tension is known to decrease inversely with the hydrophobic tail lengths [154, 27], one can expect

154

the following trends

1. For the edge-active rim lipids, since the hydrophobic tail lengths are for C6: ~ 7.5, C7 ~ 9; Triton ~ 9, Chapso ~ 10.5 Å respectively; (see Chapter 2), their effectiveness in reducing Λ in Eqn. 6.1 would increase with decreasing tail length, so that for a given composition q_{eff}, the line tension at the edges would vary as $\Lambda_{C6} < \Lambda_{C7} \sim \Lambda_{Triton} < \Lambda_{Chapso}$. From the discussion in Chapter 5, this leads to large aggregates being stable with C6 in the rim compared to Chapso in the rim $R_{C6} > R_{C7} \sim R_{Triton} > R_{Chapso}$, which is the experimentally observed trend in Fig. 6.2. This trend is qualitatively captured in Fig. 6.15, using the Fromherz's arguments. It shows the stability of bilayer fragments of different sizes, as a function of changing line tension at the edges. For comparison, the effect on two fragments, 50 and 400 Å are compared and show that for the lowest line tension, even 400 Å size bilayer fragments are stable to vesiculation.

Further, between varying rim species, for same size fragments to be equally stable (same V_f), following the effectiveness in reducing the line tension of the bilayer fragments, the fraction of long species in the rim, x would be essential inverse of that order from Eqn. 6.1.

$$x_{C6} < x_{C7} \sim x_{Triton} < x_{Chapso}$$

and explains the trend seen in Fig. 6.10(b).

This is an important result, expected to be relevant in mixed lipid-surfactant studies in predicting aggregate sizes and detergent effects on protein insertions.

2. For core lipid variation, the edge tension of C13 lipid bilayers is expected to be smaller than in the longer C15 lipids, so that for a given composition of the mixture, C13 could mix more with C6 than could C15. In this case, both Λ_{CLong0} and κ decrease with decreasing chain length of the core lipid, the argument is not direct. Qualitatively though, since Λ falls inversely with chain length, while κ decreases as a higher power of chain length [27], overall, smaller V_f would be expected for fragments of longer lipid tails. Essentially this means that the increase in rigidity of the bilayer core, makes the elastic energy larger
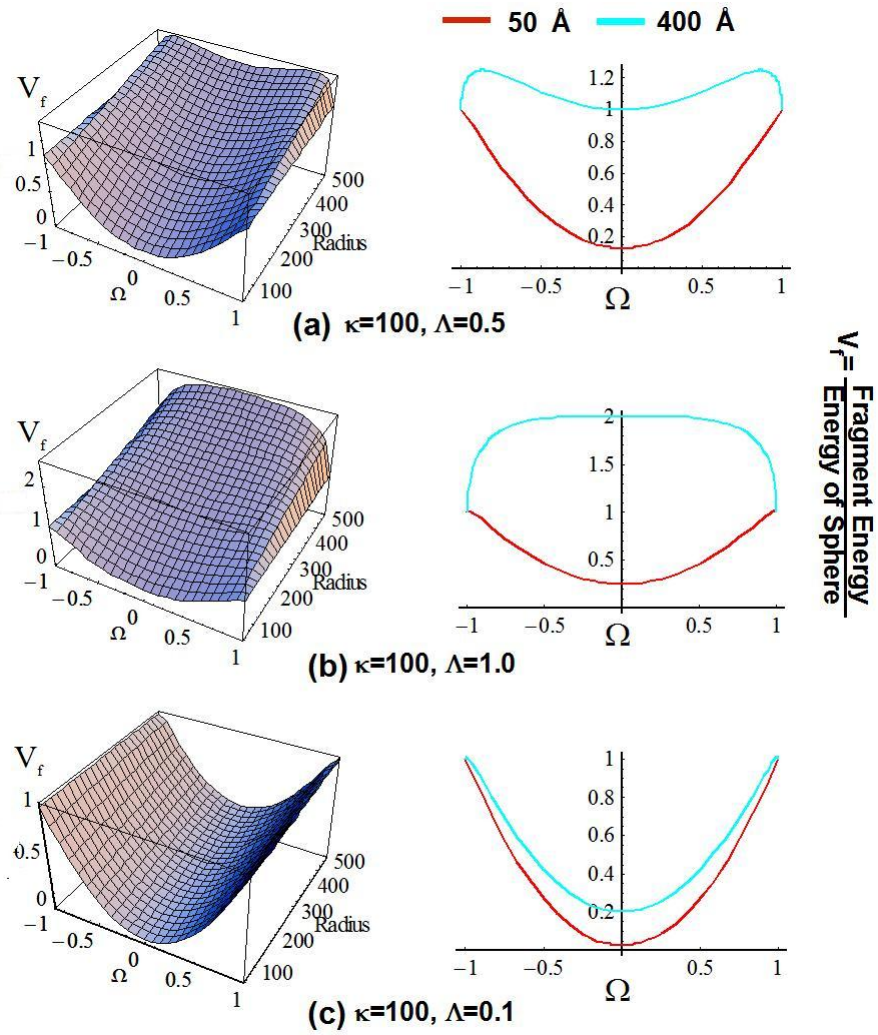
Figure 6.15: Effect of line tension on the stability of bilayer fragments. Vesiculation indices are drawn for the indicated κ and Λ as a function of radius and shape parameter. Particular cases of 50 and 400 Å fragments are shown separately. Smaller line tensions, achieved with appropriate rim species, makes large fragments stable.

than the edge energy, so that for the same composition, larger fragments of C15 mixtures with C6 are stable than those with C13, in line with the trend seen in Fig. 6.13.

Again, if one were to take the trend in aggregate sizes from Fig. 6.13, then for the same decrease in edge tension using Eqn. 6.1 (on addition of C6 in the rims), with $\Lambda_{C13} < \Lambda_{C14} < \Lambda_{C15}$, it would imply that the $(1 - \phi_r)$ or the fraction of longer species

156

mixed in the rims, x, can be higher in C13/C6 case than in the C15/C6 case, making

$x_{C13} > x_{C14} > x_{C15}$

3. In C14/C6 mixtures, the disc radii increase and mixing of the long lipid into edges, decreases with decreasing concentration of total lipid. But if discs are stable for any of these combination of c and q, this means that for increasing concentration $c_1 < c_2 < c_3$ resulting in $R_{c1} > R_{c2} > R_{c3}$, the line tensions of those aggregates would be $\Lambda_{c1} < \Lambda_{c2} < \Lambda_{c3}$

Then Eqn. 6.1 implies that $(\phi_r)_{c1} > (\phi_r)_{c2} > (\phi_r)_{c3}$. Again, this shows that the fraction of C14 in the edges decreases with increasing aggregate sizes as $x_{c1} < x_{c2} < x_{c3}$.

What does this mean for any given two component lipid mixture? Larger fragments can be stable only if the line tension at the edges is very small. One way to achieve lower line tensions is by addition of another component that has a very low line tension of its own. As line tensions of lipids decrease with decreasing hydrophobic tail length [27, 154], the smaller C6 lipids do exactly this, when added to C14 aggregates, with their fluid tails. For the DMPC/DHPC mixtures, this implies that smaller discs can be stable even if the rim lipids have some long lipids mixed into them, while for larger disc sizes, only a pure rim, with only the smaller DHPC molecules would provide the necessary stability.

6.4.3   Appearance of Elongated Morphology

In the previous section, trends in the mixing behavior of the two lipids in the edges was shown and argued to be the net mixing effect, i.e both the mixing fractions, core lipids in the edges, x and rim lipids in the core, y as defined in Section 5.5.2, could be non-zero, and the quantification from our analysis in the last chapter as well as this, is perhaps the resultant of those two competing effects, since at even the smallest temperatures, one could expect some mixing of the rim lipid into the core for entropic reasons [82, 106]. The growth law for the other mixtures (discussed above) derives from the net direction of mixing, which in all the mixtures, except C14/C8 is in the rim. If decreasing hydrophobic mismatch increases the mixing of the two lipids, then how would that affect the structure of C14/C8

mixtures?

The elongated aggregates seen in these mixtures possibly includes the answer to this question. When the chain length difference between the two lipid species decreases, their propensity to mix, increases [82, 83, 106, 139], with ideal mixing in the limit of equal chain lengths. In such a scenario, even small fraction of C8 lipids in the core, could modify the bending rigidity of the bilayer as is known from theoretical studies [159, 162], which in turn affect the packing properties of lipids.

6.5   Conclusions

Rim lipid variation (with C14/C6, C14/C7, C14/C8, C14/Chapso and C14/C8) and core lipid variation (with C13C6, C14/C6 and C15C6) studies on lipid mixtures and lipid-detergent mixtures have been undertaken in this chapter. SANS data on all the mixtures, except the C14/C8 case, show evidence of small, globular discoidal aggregates. Similar to the C14/C6 mixtures, dilution induced growth occurs in all of these mixtures independent of the lipid and detergent species. SAXS data on three of those mixtures confirms that the cross-section does not change on varying the rim lipid, and contrast enhanced SANS on the same samples shows evidence of segregation. These results are strong evidence that the long debated segregated discoidal phase is universal in binary phospholipid mixtures with ~6-8Å chain length difference between the two species in the low temperature parts of their temperature-composition phase diagram. The main criteria required for the formation of discoidal aggregates is the presence of a phospholipid species with a well defined melting temperature T_m , or equivalently negligible spontaneous curvature and the presence of a second amphiphillic component, another smaller phospholipid or a detergent, which forms globular micelles and can support finite curvature.

Similar to the C14/C6 mixtures, the growth rate on dilution in all the other mixtures (except C14/C8) is smaller than the fully segregated modified ideal bicelle model

derived in Chapter 5. Deviations between the observed and ideal case are again used to quantify the net mixing effect of long lipids into the edges. It is found to scale inversely with aggregate sizes and independent of the rim or the core lipid. Mixing in the rims, based on the curvature, leads to more mixing in smaller discs. Additionally the observed trend in mixing between mixtures of the same composition, for different rim or core lipids, are seen to agree with the idea of hydrophobic mismatch. The larger the difference between the hydrophobic parts of the rim and core species, smaller is the mixing. These observations were also shown to be in qualitative agreement with Fromherz's idea of edge activity in stabilizing a bilayer fragment.

With increasing chain length, the appearance of elongated morphology is observed. Evidence of a third dimension, or 'width' is seen, while contrast enhanced mixtures indicate segregation of lipids in the cross-section of the elongated aggregates. This mixture if left for further investigation in the next chapter.

Chapter 7

High Temperature Phases in Lipid Mixtures

7.1 Introduction

Having established the segregated discoidal morphology in various phospholipid mixtures, at temperatures well below the T_m of the long phospholipid in Chapters 5 and 6, the question of the lipid packing and the overall aggregate morphology with increasing temperature naturally arises. As pointed out in Chapter 2, the magnetically alignable 'bicelle', originally postulated to be discoidal aggregates is now understood as elongated aggregates, consisting of thread like, commonly referred to as worm like micelles (WLM), near the T_m of the long tail C14 lipid and perforated lamellae at even higher temperatures [105, 108, 74, 140]. Combined SANS and POM study and Cryo-TEM images have highlighted the difference between the aggregation states in the aligned 'bicelles' commonly used in NMR studies. Understanding the structure of the lipid mixtures at these temperatures is essential as they are implicated in aiding membrane protein crystallization [23] and also

their alignability in magnetic fields is crucial for NMR based studies of membrane bound proteins and peptides [20]. In that regard, this Chapter will continue further on the goals outlined in Chapter 6.

While the question of the general morphology at higher temperatures (depending on the composition and temperature, see Fig. 2.10) as proposed by Nieh et al. and Dam et al. appears to be similar to those found in other lipid-surfactant mixed systems [109, 110] the questions of *lipid packing* within the elongated micelles and the proposed lamellar phase with holes, still remains an open question. Close to T_m, the phase diagram proposed by these authors become even less clear. Nieh et. al.'s SANS study speculated on the cross section of the elongated and long flexible micelles to consist of a DMPC bilayer with edges coated by DHPC monolayer [105, 108]. This cross section is similar in profile to that of a discoidal aggregate at low temperatures, with the two lipids ideally segregated in the two different curvature parts of the assembly (bilayer and edges). This proposed structure could also explain why ^{31}P NMR data, which shows the segregation of the DMPC and DHPC lipids, has been interpreted in terms of a bicelle model. However, TEM data of vanDam et al. seem to indicate the micelles to be nearly cylindrical. The diameter of the micelles seen by TEM and SANS are well below the ≈ 100 Å radius for $q > 2.0$ mixtures, strongly indicating that micelles are unlikely to form a phase of stacked discoidal bicelles as proposed earlier to be the magnetically orientable phase. On further increase of temperatures above T_m, the shift to a lamellar phase perforated by holes (with the detergent-like short lipids DHPC forming the edges of the holes) is similar to the discoidal bicelle, in that such a structure also explains the presence of two NMR peaks, corresponding to the two lipids localized in different curvature regions of the aggregate formed, again illustrating the fact that distinguishing morphologies with the same local packing, but different overall assembly, using spectroscopic techniques like NMR is limited.

As noted before and in Chapter 2, the idea of lipid-surfactant mixtures forming elongated micelles is hardly new outside the 'bicelle' literature. In fact, the presence of

elongated rod like or flexible worm like micelles has been shown in other phospholipid-surfactant mixtures like those of DMPC with C12E8[113], Octyl-glucoside[115, 116], SDS and DTAB[114], Sodium cholate [118] and Triton[119] as a step in the membrane breakup process with increasing amounts of detergent, if one looks at the colloid and surfactant literature ([109] and references therein). Such mixtures and their phase behavior have typically been described as *concentration induced Micelle to vesicle transition (MVT)*. Temperature induced changes in lipid surfactant mixtures have been much less studied [110] in such mixed systems. In a closely related system of phospholipid and sodium cholate (a bile salt), the temperature induced micelle-to-vesicle transition at constant lipid and surfactant concentration has been shown to be analogous to the concentration induced micelle-to-vesicle induced transition [117, 113] in other mixed lecithin-bile salt systems. These studies have proposed the transformation of discoidal micelles to elongated micelles and bilayer fragments, but could not shed any light on the structure with in the elongated micelles or on the conditions leading to one of those two structural transformations. A large part of the work in surfactant-lipid mixtures seems to have focused on the kinetic and overall structural characterization of the micellization process using techniques like cryo-TEM and electron microscopy ([119, 124, 81], Almgren's article in [109]).

The melting temperature T_m has been implicated in the structural transitions observed in a few lipid-surfactant studies before [113, 165, 166], but there is no clear understanding of what drives the transition of a segregated two dimensional object like a disc to a phase of elongated, one dimensional rods which further transition to segregated two dimensional sheets. In this work however, we do not focus on the two dimensional 'perforated lamellar phase', which occur at much higher temperatures, and instead focus on the structures close to and about $\sim$ 10-15°C above T_m of C14 lipids. By isotopic labeling certain parts of the assembly, leading to enhanced contrast, small angle neutron scattering (SANS) technique offers the possibility of resolving these questions. Aided by simultaneous small angle X-ray scattering (SAXS), we investigate structural changes in temperature steps

162

of a few degrees from ∼10-40°C . The scattering studies are supplemented by a continuous temperature variation study, using the differential scanning calorimetry (DSC) technique, which probes molecular level cooperative events. This combined study offers the opportunity to resolve some of the outstanding questions on the structure and composition of phospholipid bicelle mixtures in this Chapter.

7.2 'Universality' of Phase Behavior in Lipid Mixtures

In order to correlate the observed morphologies and sequence of phase transformations in mixed lipid-surfactants near room temperature, relevant for crystallization studies, as well as for the magnetically alignable phase in NMR studies, we investigated the temperature induced phase behavior in the lipid-mixtures considered previously in Chapter 5. The temperature-morphology phase diagrams were first constructed on the basis of visual observations, before any SANS measurement. The same composition, $q = 2$, c=0.1 g/ml samples of each of the core-lipid variation mixtures, C13/C6 and C15/C6; and the rim-lipid variation mixtures C14/C6, C14/C7 and C14/C8, were studied in temperature intervals of 1-2°C between 10-40°C by visual observation. While crude in nature, in the sense that the underlying aggregate structure is not known exactly, they give rough information about the length scale of the underlying aggregates.

The most pronounced aspect of the universality discussed in the previous chapter at low temperatures, is seen particularly well in core-lipid variation samples with varying temperature. For a given composition, with reference to Katsaras et al.'s phase diagram (Chapter 2), the observed morphological transformations with temperature is seen to be scalable, based on the T_m of the core lipid as shown in Fig. 7.1. It shows crude phase diagrams of core-lipid variation mixtures, with C6 as the short lipid and C12 (T_m =-1°C), C13(T_m =14°C), C14(T_m =24.3°C) and C15(T_m =33°C) as the core lipid. The observed sequence of aggregate morphologies are seen to be just shifted on the temperature axis.
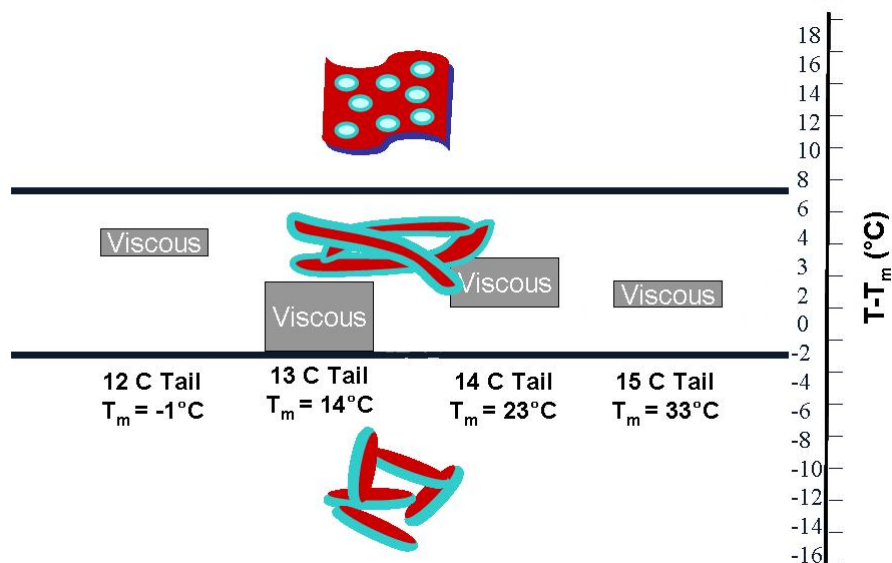
Figure 7.1: Various phases observed in mixtures of long and short tailed lipids can be rescaled to T_m .

Water like, isotropic, discoidal phase exists at temperatures $\sim$ 10-12°C below the melting temperature of the lipid, while a viscous phase, whose morphology we tentatively ascribe to elongated micelles (and studied in detail in this chapter), lies in a 8-10°C temperature range around T_m . More than 15-20°C above, a turbid and fluid phase, possibly a lamellar or vesicular phase is observed. The low and high temperatures referred in this thesis work, are in reference *rescaled* to the melting temperature T_m of the lipids.

Based on the above considerations, the observed phases in other lipid-surfactant mixtures in the literature discussed previously, are most likely the intermediate temperature phase seen in Fig. 7.1. This study thus offers the possibility of shedding light on those and other mixed systems of relevance to membrane protein crystallization and also NMR studies.

As shown in Chapter 6, rim variation mixtures, C14/C7, C14/Chapso and C14/Triton, showed similar morphology compared to C14/C6 at low temperatures, while the C14/C8 mixtures did not. Regular hydrogenated samples of the rim variation mixtures, studied as a function of temperature were seen to follow similar sequence of phase behavior as in

Fig. 7.1. Since only the C14/C8 mixtures showed significantly different behavior from the C14/C6 mixtures, in this chapter, we focus on the temperature dependence of C14/C6 and C14/C8 mixtures only.

7.3   Experimental Details

In order to resolve details of the morphological and packing changes in the phospholipid assemblies, we have studied two different phospholipid mixtures, C14/C6 and C14/C8, as a function of temperature. As in Chapters 5 and 6, samples consisting of both lipids hydrogenated, have been investigated first to obtain the overall morphology. As before, these samples are referred to as the *regular samples*. The following samples were studied in this category using SANS and DSC-

1. C14/C6: $q = 2$, c=0.03 g/ml; T=10-38°C

2. C14/C6: $q = 2$, c=0.05 g/ml; T=10-38°C

3. C14/C6: $q = 3$, c=0.03 g/ml; T=10-24°C

4. C14/C8: $q = 2$, c=0.03 g/ml; T=10-22°C

SANS measurements on these samples were conducted in increasing temperature steps of a few °C from ~10-40°C , with at least 30-45 minute equilibration time, for a 2°C temperature change. Following the increase, sample temperature was lowered down to 10°C and another scan at this temperature was taken to confirm complete reversibility of the structural transition.

Finally the *contrast enhanced* samples consisting of deuterated long lipid dDMPC (or dC14) in place of the hydrogenated lipids, and forming mixtures dC14/C6 and dC14/C8, were studied to answer questions of lipid packing and segregation. These samples are the same as those described in Chapter 6. In this category, results on the following samples using SANS, SAXS and DSC were conducted-

165

1. dC14/C6: $q = 2$, c=0.05 g/ml; T=10-30°C

2. dC14/C6: $q = 2$, c=0.03 g/ml; T=10-20°C

3. dC14/C8: $q = 2$, c=0.02 g/ml; T=10-30°C

Temperature change protocols in SAXS were similar to the one followed for the hydrogenated samples. Prior to the SANS and SAXS measurements, bulk phase behavior, studied by visual inspection on both the regular and contrast enhanced samples, showed that the phase boundaries for the contrast enhanced samples were shifted by a few degrees compared to the regular samples. DSC measurements on some of the regular and contrast enhanced samples were taken from 10-35°C (and from 10-50°C for a few samples) at scan rates of 5°C /hour. Higher scan rates were found to give broader transitions.

7.4 Results and Analysis

Fig. 7.2 shows results from heat capacity measurements in both the regular and the contrast enhanced sample in various C14/C6 and C14/C8 mixtures. For each mixture, the regular hydrogenated samples and the contrast enhanced deuterated samples show similar melting phenomenon, slightly shifted due to the changes in T_m in going from hydrogenated to deuterated lipids (from Chapter 2, $T_m \sim$ 24°C for DMPC and $\sim$20°C for dDMPC). This implies that the contrast enhanced samples go through the exact same morphological transformations as the hydrogenated ones, justifying our use of deuterated lipids without perturbing the underlying phase behavior. In addition, all the C14/C6 mixtures show complex heat capacity profiles, most prominent of which are the broad melting peaks at $\sim T_m$ of C14 in addition to multiple shoulder peaks below T_m . This implies that the bilayer packing of the long tail lipid remains until T_m , even if its intensity is not as strong as in the pure lipid case. However, in the C14/C8 mixtures, a fairly sharp melting peak $\sim$ 4°C below T_m and a much smaller peak at $\sim$ 28°C are observed. In order to correlate

the complex calorimetry profile with structural changes, next we look at scattering data on these mixtures at higher temperatures.
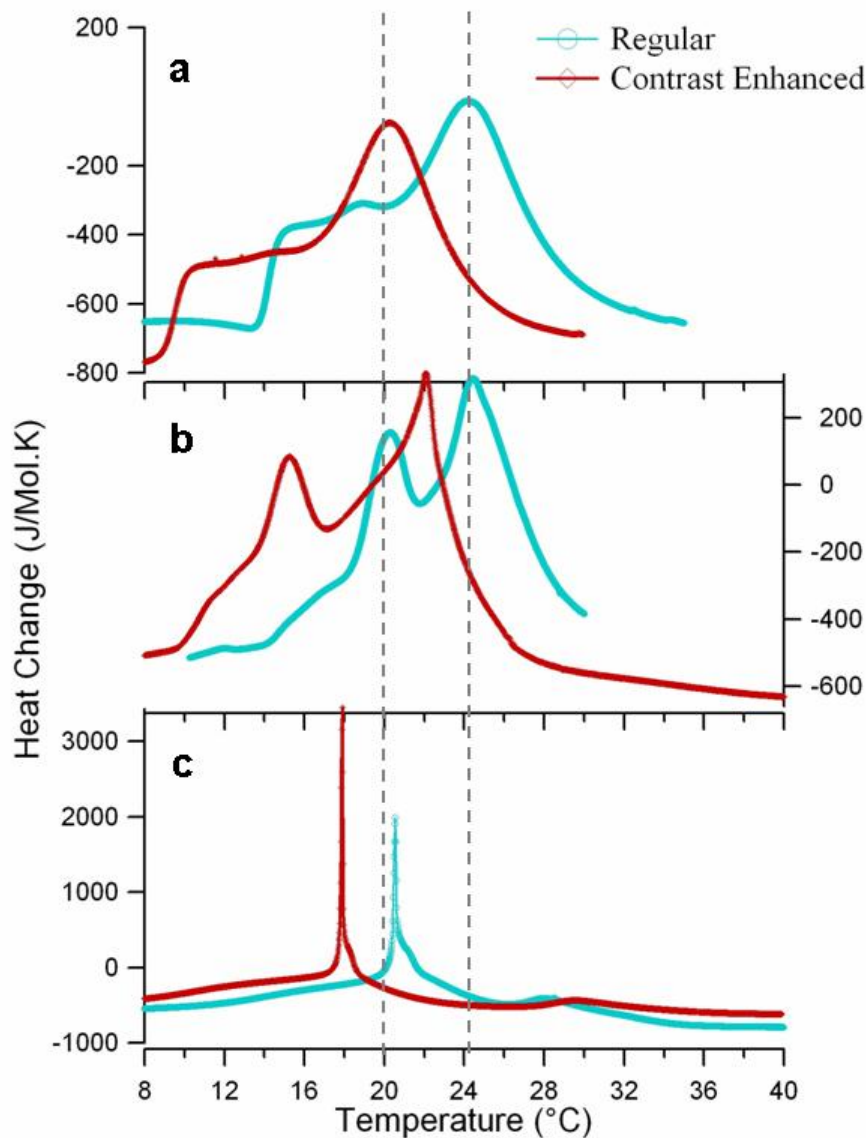
Figure 7.2: Comparison of DSC scans in regular and contrast enhanced samples of different mixtures at scan rates of 5°C /hour (a) C14/C6=2, c=0.03 g/ml (b) C14/C6=2, c=0.05 g/ml and (c) C14/C8 =2, c=0.03 g/ml. For reference, melting temperatures of pure C14 and dC14 are shown as dotted lines.

7.4.1 Aggregate Morphology

Fig. 7.3 shows the SANS data on an absolute scale and the pair distance distribution function, for the three regular (both lipids are hydrogenated) samples with increasing temperature: $q = 2$, c=0.03 and c=0.05 g/ml samples of C14/C6 and $q = 2$, c=0.03 g/ml of C14/C8 mixtures. Similar scattering profiles were also obtained for the C14/C6 $q = 3$, c=0.03 g/ml samples (data not shown). In the C14/C6 mixture, the flat Guinier exists uptil $\sim$ 16-17°C after which, the low Q scattering starts to increase, and eventually at $\sim$ 24°C , shows a Q^{-1} behavior extending uptil the lowest Q values. Close to this temperature, visual observation shows that the clear fluid sample between $\sim$10-23°C , suddenly becomes semi-viscous. This is characteristic of typical sphere-to-rod (small aggregates/discoids in this case to elongated aggregates) transitions as long rods start to entangle. At high scattering vectors all the data coincide, and show small variations at intermediate wave-vectors. The form factor oscillations are however not visible due to high hydrogen background in the SANS data. Any subtle changes at these wave vectors can be resolved only by SAXS, which would be free of the incoherent background, as we show below.

As described before in Chapter 6, in order to follow changes in the geometry of the aggregates with temperature, without a priori assumptions of the shape, the indirect fourier transform, which yields the pair distance distribution function [167, 164, 127, 135] is used. With increasing temperature, the C14/C6 mixtures clearly show transition from small globular aggregates about 100-200 Å in size to elongated objects 500-800 Å in length uptil 24°C and even longer at further high temperatures 30-38°C , as can be seen in Fig. 7.3. Depending upon the original composition of the mixture (and hence the aggregate sizes at low temperature 10°C), the growth proceeds more rapidly, above some critical temperature (compare for e.g., Fig. 7.3(a) and (b)). Above this temperature, the decay to large r values is seen in the P(r) profile, which are not linear but slightly convex (only 30°C data shown in Fig. 7.3(b)), which indicates polydispersity in length [133, 1]. Length scales above 1000 Å, are beyond the resolution limit of the instrument and the aggregates could

be even longer.

The C14/C8 mixtures on the other hand, showed slightly higher viscosity even at 10°C as observed before. The scattering data on these samples taken till very low scattering angles $Q = 0.002\text{Å}^{-1}$, show Guinier regimes at the lowest wave-vectors, which disappears with increasing temperature. The small viscosity at 10°C increases sharply at 20.5°C (and 17.9°C in the deuterated case). The P(r) profile at low temperatures, which indicated aggregates about 700 Å long extends to even larger distances on increasing the temperature. The maximum distance, D_{max}, increases slowly till 22°C , at which point, the P(r) profile shows a hump, possibly due to increased flexibility of such long aggregates, which is not accounted for in the calculation.
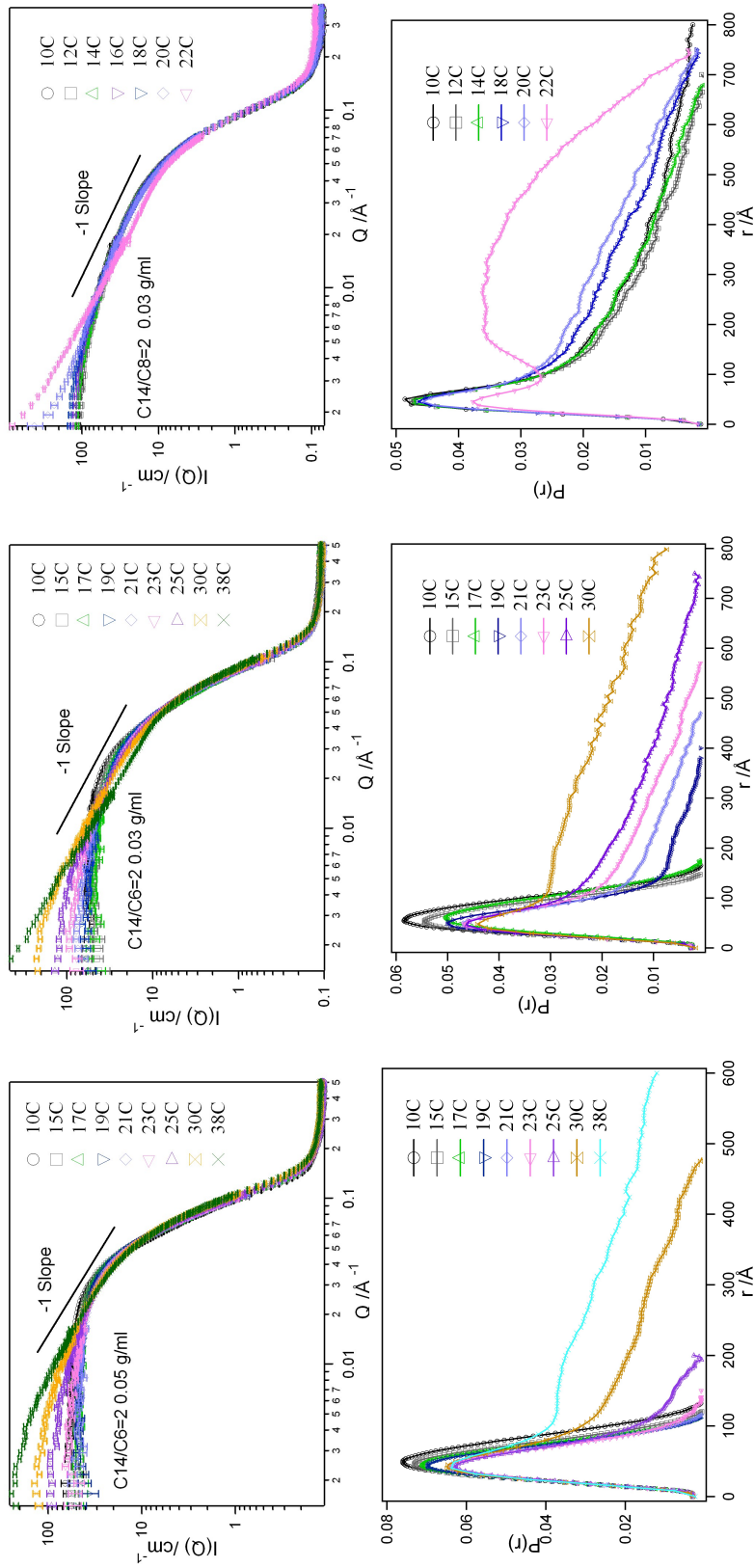
Figure 7.3: SANS data on regular hydrogenated lipid mixtures and their corresponding Pair distance distribution functions P(r), using the indirect fourier transform technique (a) C14/C6 $q = 2$ c=0.05 g/ml (b) C14/C6 $q = 2$ c=0.03 g/ml (c) C14/C6 $q = 2$ c=0.03 g/ml (d) C14/C8 $q = 2$ c=0.03 g/ml mixtures.

7.4.2   Local Morphology

Fig. 7.4 shows results of SANS measurements on two contrast enhanced samples, a dC14/C6 mixture and a dC14/C8 mixture. As noted in Chapter 5, the correlation peak at intermediate wave vectors is a strong indication of segregation in both of these samples at 10°C . This data clearly indicates that the segregation, with possible mixing, continues even to higher temperatures. If the two lipids were mixed, the observed scattering pattern would be similar to that obtained with both the lipids hydrogenated, as seen in Fig. 7.3, except for a lower intensity due to a reduced overall contrast. With increasing temperatures, the correlation peak in the C14/C6 case, shifts to higher wave vectors, in agreement with the data in Fig. 7.3, indicating decreasing size of the segregated region in the aggregate, while I(0) increases, indicating increasing overall sizes of the aggregates. Such a segregated aggregate, would likely have a non-circular cross-section; on the other hand, if the two lipids were randomly mixed, then a circular cross-section mixed body with end caps rich in the short lipid would be anticipated. We investigate the cross-section and lipid packing within these aggregates further.
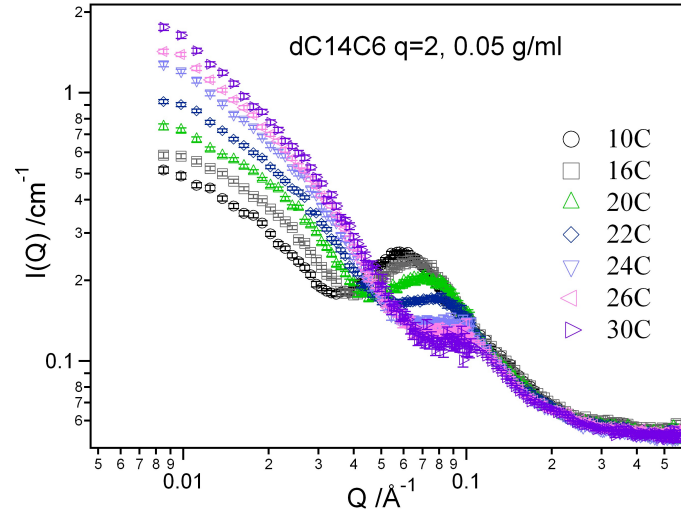
(a)
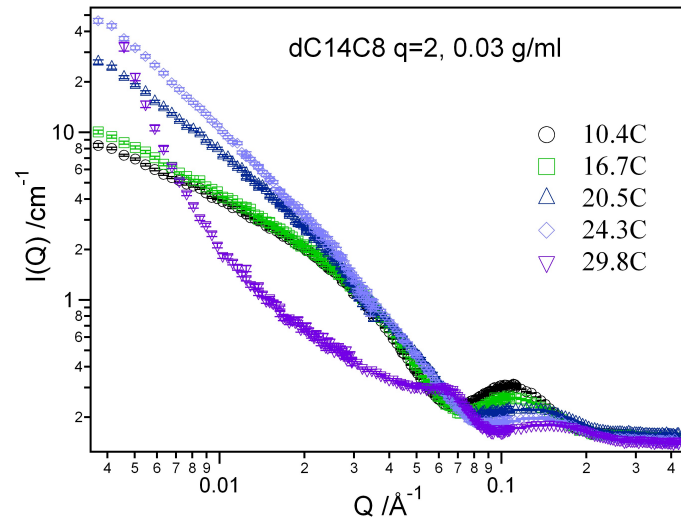
(b)

Figure 7.4: SANS data on the contrast enhanced samples taken from 10-30°C on (a) dC14/C6=2.0, c=0.05 g/ml and (b) dC14/C8=2.0, c=0.03 g/ml mixtures. The correlation peak, indicative of segregation of the two species is maintained over the entire temperature range studied here in both mixtures.

172

As shown in Chapter 6, the cross-section of the elongated aggregates in C14/C8 mixtures at 10°C is not circular. If the C14/C6 mixtures at temperatures above ~16°C (when deviations from Guinier region at low Q start appearing), are indeed elongated aggregates, then the modified Guinier approximation (see Chapter 4), assuming a rod of circular cross-section, can be used to obtain their cross-sectional dimensions as a function of increasing temperature. Fig. 7.5 shows variations in the rod diameter of the mixtures obtained by this method, as a function of temperature. In the temperature range of our measurement where elongated micelles exist, the effective diameter of a C14/C6 rod-like aggregate varies from 72 Å at the onset of elongation, down to ~60 Å. While the C14/C8 diameter starts at 64 Å already at 10°C and decreases more slowly to about 60 Å as well. Inset shows one such fit, in the C14/C6, c=0.05 g/ml sample at 30°C (see Fig. 7.3) where the SANS data and the P(r) showed clear signature of elongated aggregates. As noted before, since the cross-sectional dimension of the elongated aggregates in Fig. 7.5 is bigger than twice the length of a C14 lipid with a fully extended chain, it suggests that the bilayer may still be present and that the elongated shape maybe a ribbon (or a tablet, depending on the aspect ratio), rather than a rod.

In order to correlate the cross-sectional changes with temperature seen from the SANS data, we also look at complimentary information from SAXS at large wave vectors (corresponding to the bilayer thickness $2\pi/50 \sim 1.1$ Å^{-1}). At these high Q's, while the SANS data in Fig. 7.3 showed overlapping profiles, with SAXS, oscillations due to core-shell nature of the bilayer are visible [43]. X-ray data on dC14/C6 and dC14/C8 mixtures, between 10-30°C are shown in Fig. 7.6. As noted before, the presence of deuterated core-lipid, does not have any effect on the SAXS data, so that it would have had the same profile had we used C14/C6 instead of the deuterated mixture, and in fact the information obtained compliments that from SANS. Local changes in bilayer structure of the aggregates can be followed by fitting the peaks at 0.13 Å^{-1} which are characteristic of a single bilayer form factor oscillations, arising from electron density differences between the inside of the
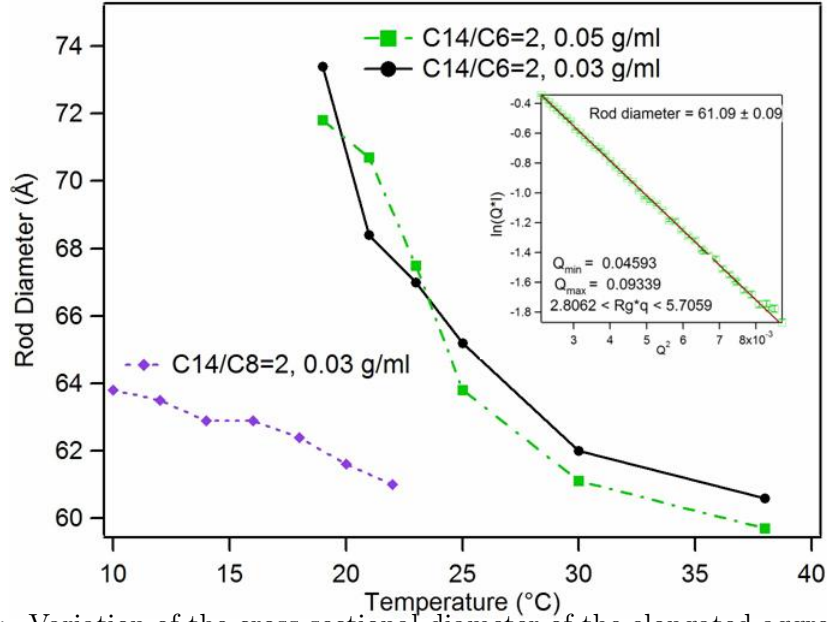
Figure 7.5: Variation of the cross-sectional diameter of the elongated aggregates, obtained by using the modified Guinier approximation to the SANS data in Fig. 7.3. In both C14/C6 and C14/C8 mixtures, the diameter is larger than a bilayer thickness and tends towards ~60 Å with increasing temperature. Inset shows fit at 30°C of a C14/C6 sample.

bilayer and the outside head group part. The minor changes in bilayer thickness, seen in the maximum of the second peak, is also seen by looking at IQ^4 data over the entire Q range. The slight thinning of the bilayer, as seen in the IQ^4 profiles, in going from the ordered gel phase with straightened tails to disordered fluid phase is as expected from the known thinning of about 4-5 Å, that occurs in pure C14 bilayers on such a transition [11]. This, then is a strong indication that indeed bilayers still exist in the structures, that therefore must have the bilayer thickness as *one* of their dimensions. Combined with melting peaks in the calorimetry data of Fig. 7.2, this is a strong evidence of bilayer arrangement of the long lipids in the elongated aggregates.

(a)

(b)

(c)

(d)
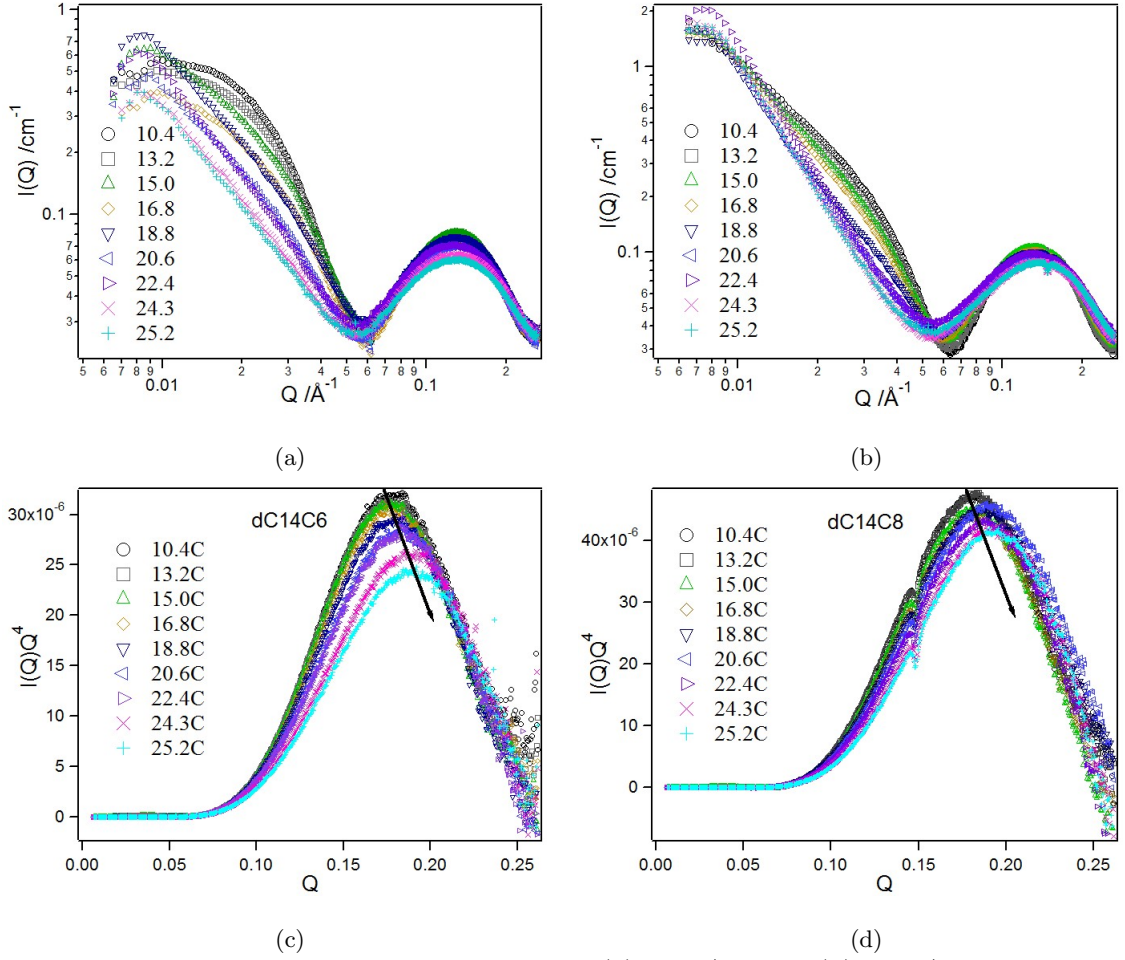
Figure 7.6: Intensity vs Q data from SAXS on (a)dC14/C6 and (b)dC14/C8 mixtures. For each mixture, IQ^4 data is plotted against Q showing minor variations in bilayer thickness with increasing temperature.

7.4.3 Scattering Models for Elongated Aggregates

As pointed out previously, details of the cross-sectional composition and overall structure of the phospholipid mixtures at higher temperatures cannot be resolved with the currently available models in the literature, such as the cylinder, and worm-like models [63, 129], of circular cross-sections and their core-shell versions (listed in Chapter 4). The shell structure in all these models is uniform and would assume an average SLD over the entire shell. Similarly, elongated cylinders with ellipsoidal cross-sections are not any use-

ful for the same reasons, since they allow only for non-homogeneous shell thickness, but uniform shell SLD by geometry. In order to account for *non-circular cross-section and non-uniform SLD* in different parts of the cross-section of the elongated structure, a Core-shell Parallelepiped (CsPP) model has been derived. Such a model is essential to fit the contrast enhanced samples, (like the use of Poly-disperse core-shell disc for the low temperature data in previous chapters), while the simple rectangular parallelepiped (PP) model [1], with a single-step SLD profile is sufficient (see Fig.6.1 for the contrast definitions) for the regular hydrogenated samples.

One can define a homogeneous PP with a single SLD, and of dimensions such that length>width>thickness, or as shown in Fig. C.2, a core-shell PP with varying SLDs forming shells on the faces of the PP for a more realistic description of the internal structure of the lipids. The derivation and simple comparisons with other models have been given in **Appendix C**. Here we just give the main results.
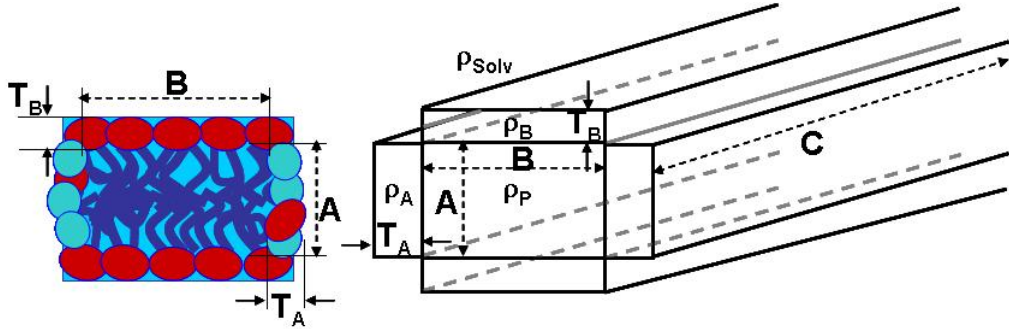
Figure 7.7: A schematic of the Coreshell Parallelepiped (CsPP) model, showing the rims on sides A and B of thickness T_A and T_B and SLDs ρ_A, ρ_B respectively. The interior of the CsPP, is a parallelepiped (PP) of edges $A < B < C$ and uniform SLD ρ_P. The CsPP is immersed in a solvent of SLD ρ_{solv}. Lipid packing (with color coding as in Chapter 5) is also shown.

The form factor for a rectangular parallelepiped of edge lengths A, B and C, is given by the orientational average of the square of the phase factor. When, the scattering vector Q vector is oriented at angle α from z-axis and β from the y axis, it can be written as the double integral [1]

$$F_{(A,B,C)}(Q)$$

$$= \int_0^{\pi/2} \int_0^{\pi/2} \left(I_{(A,B,C)}(Q) \right)^2 \sin\alpha \, d\alpha \, d\beta$$

$$= \int_0^{\pi/2} \int_0^{\pi/2} \left(\frac{\sin(QA/2\sin\alpha\sin\beta)}{QA/2\sin\alpha\cos\beta} \frac{\sin(QB/2\sin\alpha\cos\beta)}{QB/2\sin\alpha\cos\beta} \right)^2 \left[\frac{\sin(QC/2\cos\alpha)}{QC/2\cos\alpha} \right]^2$$

$$\times \quad \sin\alpha \, d\alpha \, d\beta \tag{7.1}$$

For a core-shell Parallelepiped, of edge lengths $(A + 2T_A, B + 2T_B, C + 2T_C)$ (the rims of lengths T_A, T_B and T_C extend out on each face), and of SLDs (ρ_A, ρ_B, ρ_C) and ρ_P in the core, the phase factor has additional terms besides the core term. This gives the form factor as the sum of inner core term plus extra terms for each edge with the correct SLD term variation and volumes as

$$\begin{aligned}
F_{(A+T_A, B+T_B, C+T_C)}(Q) &= \frac{1}{V_{ot}} \int_0^{\pi/2} \int_0^{\pi/2} \{ (\rho_p - \rho_0) I(A, B, C) ABC \\
&+ \quad (\rho_A - \rho_0)[I(A + T_A, B, C) - I(A, B, C)] 2T_A BC \\
&+ \quad (\rho_B - \rho_0)[I(A, B + T_B, C) - I(A, B, C)] A2T_B C \\
&+ \quad (\rho_C - \rho_0)[I(A, B, C + T_C) - I(A, B, C)] AB2T_C \}^2 \sin\alpha \, d\alpha \, d\beta
\end{aligned}$$

$$(7.2)$$

where V_{ot} is the total volume of the parallelepiped, and is equal to

$$V_{ot} = ABC + 2T_A BC + A2T_B C + AB2T_C$$

Like the poly disperse core-shell disc used in Chapter 5, any mixing of the long lipid DMPC into the edges can be quantified by fitting the SLD of the edges, ρ_A, ρ_B or ρ_C.

7.4.4 Form Factor Fits

Based on the information from the previous two sections, about the overall aggregate structure, as well as their cross-sectional structure at higher temperatures, we used

Table 7.1: Comparison of aggregate sizes (in Å) of C14/C8 $c-series$ mixtures obtained by different analysis methods.

Sample	P(r) Analysis			Guinier Analysis		PP Model
c (g/ml)	R_g	Length*†	R_{max}	R_g	Length*	A, B, C
0.01	-	-	-	-	-	43.2, 67.8, 700
0.02	243±11.2	828	1000	198.7 ±8.5	684	42.8, 64.7, 600
0.03	238±9.3	810	1000	182.6 ± 6.3	628	42.0, 61.8, 500
0.04	216±10.4	733	1000	162.7 ± 8.4	558	41.9, 61.7, 425
0.06	123±2.2	398	500	141.4 ± 8.9	483	42.0, 59.6, 300
0.08	115±3.5	368	500	116.9 ± 2.4	398	-

*   Assuming a cylindrical aggregate with circular cross-section of radius 62/2 =31 Å.
†   Errors propagated from R_g are not included.

the parallelepiped (PP) model to represent the triaxial aggregate geometry of the elongated aggregates in both C14/C6 and C14/C8 mixtures. In order for a single geometrical model to fit the data from the contrast enhanced and the regular hydrogenated samples at higher temperatures, SANS from the regular samples are fit with the rectangular parallelepiped (PP), before using the core-shell PP on the contrast enhanced SANS data.

First we test this model on the $c-series$ of C14/C8 at 10°C for which Guinier fits and P(r) results were obtained in Chapter 6. This is for a quantitative comparison of the results from form factor fits, to that obtained from the previous model independent estimates. Good quality fits over the entire Q range, except at the highest Q values (likely the effect of sharp edges) are obtained using the PP model. Results of fits at 10°C using this model are shown in Fig. 7.8 and included in Table 7.1. Results from the PP fits, show that the long axis are $\sim 10\times$ the other two dimensions and the width is approximately 1.5× the thickness. Due to the low Q limit of the SANS data, large error bars are seen in the R_g estimates for the overall dimension of the particle. Thus the absolute dimensions of the length of the aggregates are only approximate numbers from all the analysis techniques. Nevertheless, the increase in overall aggregate size with increasing dilution, while its cross-section remains unchanged, is captured very well with the PP model fits.

Having shown that the PP model can be used to describe elongated aggregates
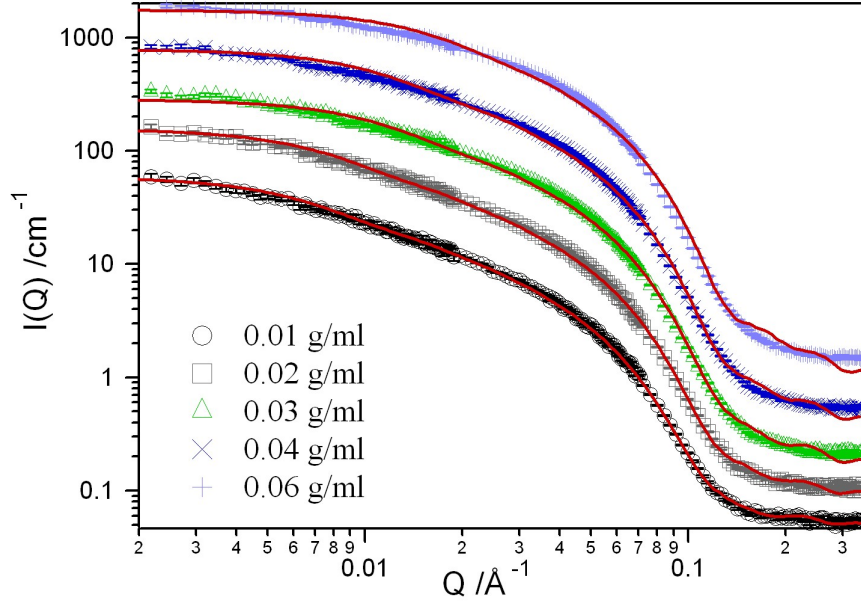
Figure 7.8: Fits to SANS data on regular samples, concentration series of [C14]/[C8]=2 mixtures using the Parallelepiped model giving the thickness, width and length of elongated aggregates.

very well, atleast those in the C14/C8 mixtures at 10°C , we fit the temperature dependent SANS data of the C14/C6 and C14/C8, $q = 2.0$, c=0.03 g/ml mixtures in Fig. 7.3 over the entire measured temperature range. Fits using this model are shown in Fig. 7.9 and the fit results are included in Table 7.2. In C14/C6 mixtures, the same PP model works well for the whole temperature range between 10-38°C . The largest dimension, length, increases gradually from 136 Å to 275 Å at 21°C and then begins to increase dramatically to ∼400 Å at 25°C , and by 38°C , the dimensions have grown beyond the low Q resolution of the instrument.

Fig. 7.10 compares the largest dimension of the aggregates with increasing temperature, from the PP model with the estimate from the P(r) calculation in a C14/C6=2, c=0.05 g/ml sample. Even though there is few tens of Å difference between the two estimates, the same relative changes with temperature are seen in both the results. The result of fits on the other C14/C6 samples compare similarly to the corresponding P(r) results,

Table 7.2: Results from SANS data on C14/C6 and C14/C8 mixtures between 10-30°C using Parallelepiped form factor.

Temperature	C14/C6			Temperature	C14/C8
(°C)	$q = 2$		$q = 3$	(°C)	$q = 2$
	0.03 g/ml	0.05 g/ml	0.03 g/ml		0.03 g/ml
10	A=45	A=43.5	A=43.9	10	A=42.2
	B=111	B=92.1	B=132.5		B=62.8
	C=136	C=111.8	C=170		C=400
15	A=43.2	A=45.5	A=43.8	12	A=41.6
	B=102.8	B=82	B=133.7		B=61.5
	C=124.0	C=105	C=174		C=450
17	A=45.4	A=46.1	A=43.6	14	A=41.4
	B=79.0	B=79.4	B=126.4		B=61.6
	C=175	C=102	C=163		C=450
19	A=44	A=45.8	A=43.7	16	A=40.9
	B=73	B=77.8	B=80.9		B=61.1
	C=200	C=100	C=500		C=500
21	A=43.4	A=44.3	A=42.9	18	A=40.3
	B=68	B=75.4	B=73.4		B=61
	C=275	C=100	C=500		C=600
23	A=41.6	A=42.5	A=42.4	20	A=39.7
	B=65.3	B=67.1	B=71.3		B=60.3
	C=400	C=130	C=950		C=1200
25	A=41	A=39.6		22	A=38.3
	B=64.8	B=59.2			B=57.8
	C=475	C=250			C=1800
30	A=40	A=40			
	B=63.4	B=58.3			
	C=1000	C=350			
38	A=40	A=40			
	B=56	B=58.1			
	C=2000	C=600			
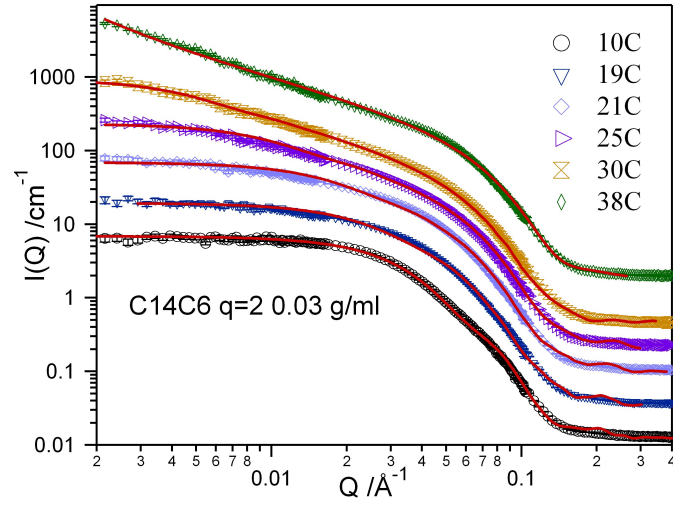
(a)
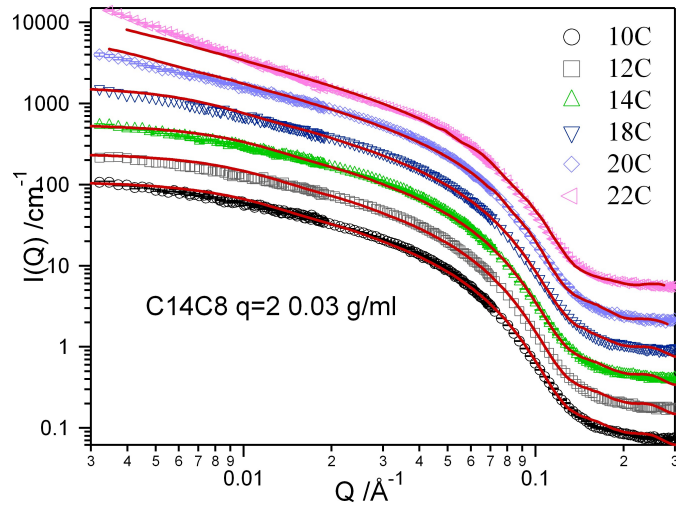
(b)

Figure 7.9: Fits to regular, hydrogenated C14/C6 and C14/C8 mixtures of q=2.0, c=0.03 g/ml, using the parallelepiped model.

showing the growth of aggregates from a few 100 Å below T_m to about 1000Å, $\sim$ 5-10°C above the T_m .

The PP model works well for the $c-series$ in C14/C8 and also gives very good fits over the temperature range 10-24°C (upper temperature range is limited in this case) above the melting peak at $\sim$20°C , except for a slight underestimation at the lowest Q (see Fig.

181
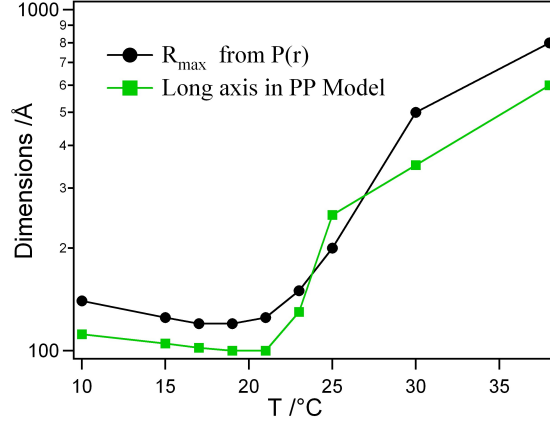
Figure 7.10: Comparison of largest dimension obtained from fits using parallelepiped model and R_{max} in the pair distance distribution function of a C14/C6 mixture. Small error bars (less than 1-2 Å in the PP model fit) cannot be seen on the scale of the graph.

7.2). This may indicate the onset of flexibility, which is not accounted for in this model.

Based on the temperature dependent SANS data, and borrowing the terminology from Bergstrom and coworkers for triaxial ellipsoids, aggregates in both the mixtures can be described as small 'tablets' and as 'ribbons' [168], when the tablets grow more than ∼400 Å in length to form more flexible structures, implying aggregates with three independent length scales: *thickness, width and length*, unlike a disc with only two independent length scales: *radius and thickness*.

At first look, the geometry of a parallelepiped is different from the discoidal geometry, but as shown in Fig. 7.11, the quality of fits using this model, or using the discoidal models at low temperatures (used in Chapters 5 and 6) are equivalent from 10°C until ∼16-17°C . In fact, from SANS basics, a parallelepiped with $width \equiv length$ can be seen as a 'square disc'. Above this temperature, deviations between the two models can be clearly seen. Results comparing the fits using those two geometries on SANS data from both regular and CE mixtures are also included in Table 7.3. The discoidal model, unlike the PP model, cannot be used once the length grows beyond $\approx$ 150 Å, giving a ratio of 150:50 or 3:1 between the biggest (length) and smallest (thickness) length scale. The presence of two

Table 7.3: Comparison of aggregates sizes at 10°C (in Å) in C14/C6 mixtures from the discoidal and elongated parallelepiped geometries.

Sample q, c(g/ml)	R_{max} in P(r)	Core-Shell Disk 2(Radius+Shell)	Parallelepiped Length	Width
C14/C6=2, 0.03	175	2×67=134	136	111
C14/C6=2, 0.05	140	2×57=114	112	92
dC14/C6=2, 0.03	-	2×70.5=141	202.4(0.63)+6.8	118(1.3)+6.92(0.65)
dC14/C6=2, 0.05	-	2×61=122	167.2(0.47)+6.3	80(0.6)+5.8(0.43)

dimensions, width and length, is thus in an average sense like the ellipticity parameter in ellipsoidal models, or an average diameter with some polydispersity. From the surfactant literature, ellipticity bigger that 3 is the rule of thumb for an ellipsoid to be distinguished from spherical aggregates using scattering techniques [30, 124]. The advantage of this model is that it can be used to fit the data over the whole temperature range and leads to a mechanism of growth; secondly, even without the use of any 'polydispersity' factor (like in the poly-disperse cylinder/disc models), it can fit the data in the whole Q range quite well. Ofcourse, real aggregates would not have sharp edges as in this model, neither is SANS sensitive to such small features, as in sharp or curved edges. Nevertheless, it is a good representation of the biaxial cross-section and can capture the trends with temperature changes well.

Overall, from the PP model fits to the SANS data in Table 7.2, elongation of the tablets is seen to be accompanied by local changes, only in the width dimension [168, 143]. The cross-sectional dimensions, width and thickness of the tablets for the four regular samples are plotted as a function of temperature in Fig. 7.12 and show significant change in the width dimension and negligible changes in the thickness. These changes in the cross-section will be taken up further in the discussion section.
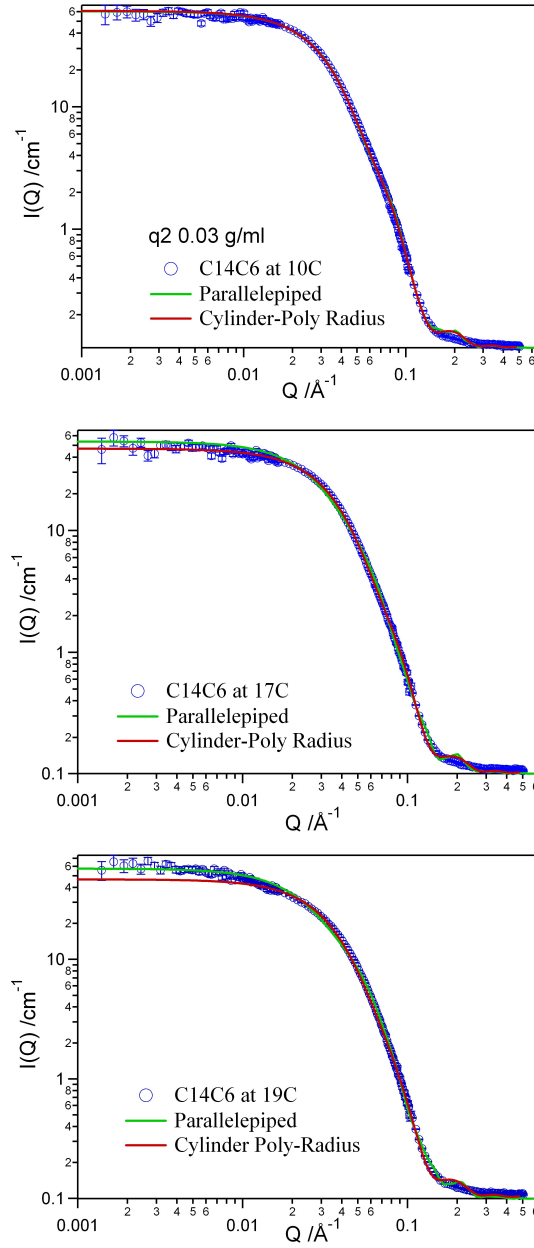
Figure 7.11: Comparison of fits to SANS data on regular hydrogenated mixture C14/C6=2, c=0.03 g/ml mixture, using a parallelepiped (pp) model and the model of a disc with polydispersity (Pcshl). Below ~16-17°C , the quality of fits using both the models is same. At 19°C , deviations between the quality of fits can be seen.
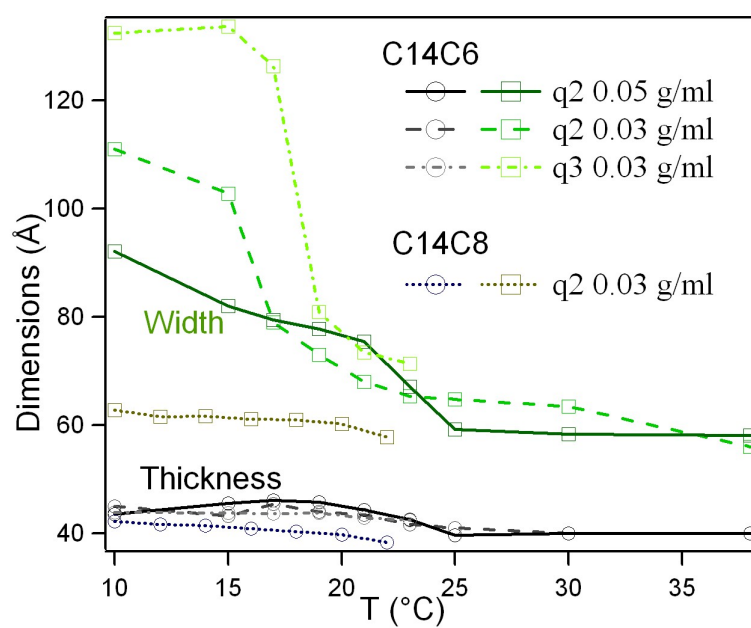
Figure 7.12: Comparison of width (open squares) and thickness(open circles) variations in C14/C6 and C14/C8 regular samples of different composition as a function of temperature from PP model fits.
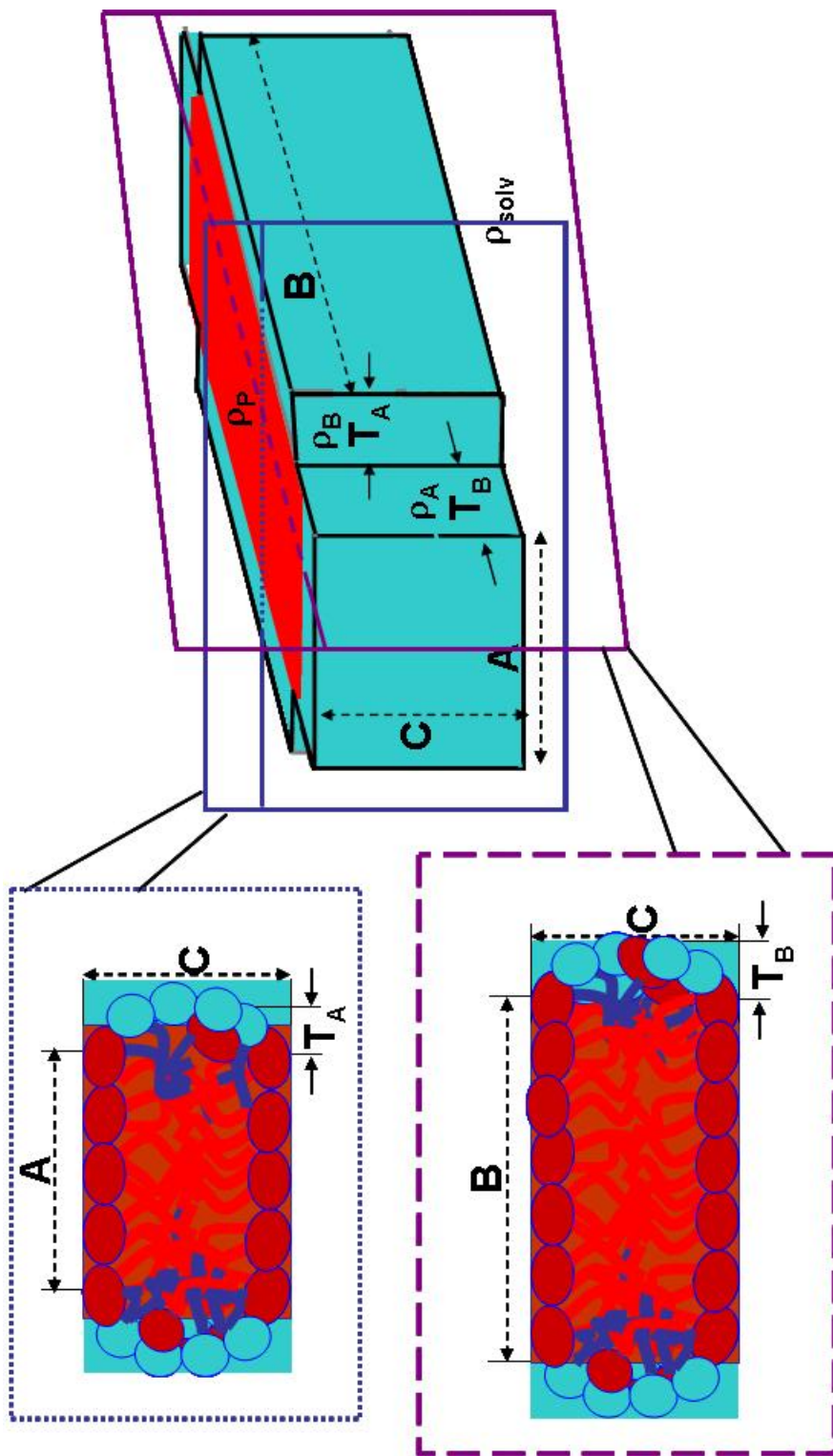
Figure 7.13: Lipid packing in the elongated geometry and orientation of the core-shell parallelepiped model used in fitting. Cuts through two perpendicular planes shows the deuterated C14 lipid forming the bilayer (thickness C) and the short lipid (C6/C8) in the edges modeled by shells on sides A(width) and B(length). Long tail and short tail lipids are color coded as in Chapter 5, to represent the CE mixtures with deuterated lipids forming the core.

7.4.5 Lipid Packing in Elongated Aggregates

In order to elucidate details of lipid packing with increasing temperature, we fit the SANS data from the contrast enhanced samples shown in Fig. 7.4 using the core-shell parallelepiped model. The scheme outlining the cross-sections in the width and length dimensions, as also the orientation of the three axes, used in fitting the data is shown in Fig. 7.13.

As already shown before, using calorimetry, and SANS and SAXS data at high Q's on the regular hydrogenated mixtures, since the cross-section consists of 50 Å bilayer structure and a temperature dependent width (which stabilizes to ∼62-60 Å), it precludes worm-like mixed micelles used in the literature [124, 1, 122] (used particularly in the lecithin bile-salt mixtures). Such mixed micelles have been modeled as core-shell cylinders with circular cross-section, with the long tails consisting of the core and the mixed heads and bile-salts consisting of the shell. Fig. 7.14 compares the schematic of such a packing model to that in the segregated case.

However, since the difference between the width and thickness dimensions is not very big, before applying the segregated packing model, captured by the core-shell PP geometry, to the CE SANS data, we ensured it's validity as opposed to the mixed models in the literature. To do so, we tested the results of both the models on two representative data sets where the aggregates are elongated as seen from the P(r) data.
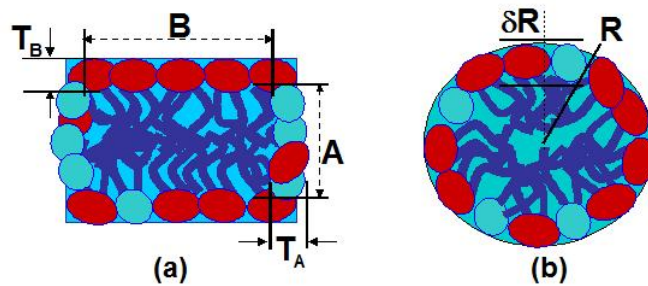
Figure 7.14: Compositional variation of the cross-section and lipid packing in (a) mostly segregated cross-section (the core-shell parallelepiped geometry) (b) mixed cross-section (polydisperse core-shell cylinder) geometry.

When the mixed worm-like micelle is applied to the phospholipid mixtures in this study, the inner core radius is expected to be no longer than the tail length of dC14, at ∼15 Å. The shell region on the other hand, consisting of full molecule of the smaller species, C6 or C8, and the head groups of dC14 can be expected to be bigger 9-10 Å. The results of such a mixed model as compared to our proposed segregated model, are shown in Fig. 7.15, which shows fits to a dC14/C6=2.0, 0.05 g/ml mixture at 22°C and to a dC14/C8=2.0, 0.03 g/ml mixture at 10°C . Both these samples show elongated morphologies at the respective temperatures in their P(r) profile.

Effectively, both the segregated and mixed models give similar quality of fits. The difference lies however in the fit results! For the mixed model, we used the poly-core shell disk model (see Chapter **??**) with the thickness/length as a free parameter to allow for an elongated geometry, unlike in the previous chapters, where the length (thickness for discs) was fixed to be ∼44 Å. The core SLD was fixed to 7.11×10^{-6} Å^{-2} for the deuterated lipid tail of C14. The radius, radial shell, length and shell on the length direction (cap), as well as the shell SLD were fit parameters. As can be seen from the results in Table 7.4, the radial dimensions obtained from these fits, are $\sim 30(core) + 6.8(shell)$ Å in C14/C6 and $\sim 26.6(core) + 6.9(shell)$ Å in C14/C8; both are bigger than the fully extended dC14 tail length, making the results physically unreasonable. Even though the fits are of decently good quality, their not being physically acceptable lets us reject the mixed model in favor of the segregated one.
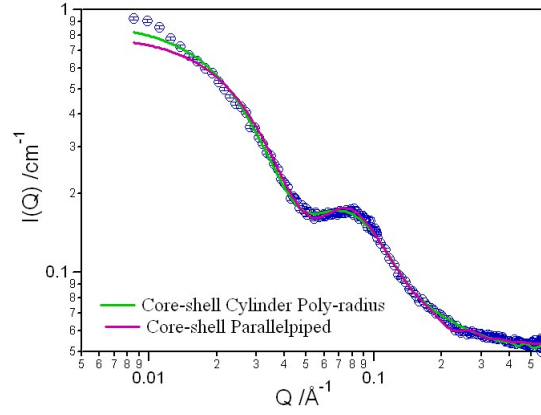
(a)
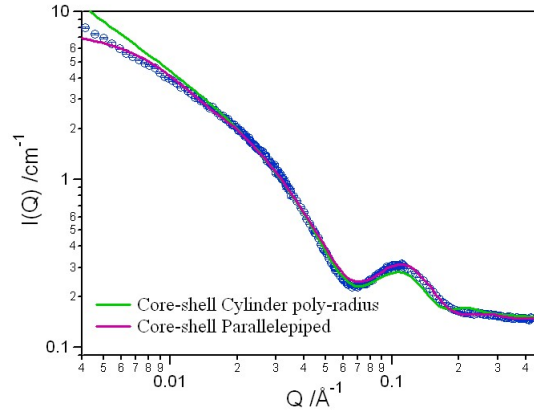
(b)

Figure 7.15: Comparison of fits from a mixed model (using the core-shell cylinder form factor) and segregated model (using the core-shell parallelepiped form factor) on two representative data sets (a) dC14/C6 mixture $q2$ c=0.05 g/ml at 22°C and (b)dC14/C8 $q2$ c=0.03 g/ml mixture at 10°C .

189

Table 7.4: Comparison of results from a mixed and a segregated model on two mixtures used in this study

Sample	Mixed Model (All dimensions in Å)		Segregated Model (All dimensions in Å)		
	Radius+ Radial shell	Length+shell	Thickness	Width + Shell$_{width}$	Length+Shell$_{width}$
dC14/C6 @22°C	30(0.2)+6.78(0.02)	150.5(1.7)+5(0.16)	35(0.75)	76.5(0.98)+7.1(0.5)	431.7(0.44) +3.2(0.33)
dC14/C8 @10°C	26.6(0.18)+6.91(0.49)	3413(4)+ 6.9(0.49)	50(0.64)	75.5(0.11)+5(0.48)	507.4(2.94)+6.26(0.08)

Fits to the segregated model were obtained with the orientation of the core-shell PP as shown in Fig. 7.13. The parallelepiped core of 6.7×10^{-6} Å^{-1} at 10°C and 6.56×10^{-6} Å^{-1} at 20°C was oriented to coincide with the bilayer, of fully deuterated lipids, with no shell in this direction. The shell thicknesses and SLD in the other two directions (length and width) were free parameters. With increasing temperature, the core SLD was also left as a free parameter to include mixing of hydrogenated rim species in the core. Deviations from the core SLD at 20°C , showed about 5% mixing of short lipids in dC14/C6 above that temperature and in also in dC14/C8 at 10°C . The rims on the other hand showed significant deviations from that of a pure rim of short lipid, like the disc case in Chapters 5-6, indicating mixing in both the shells, along the body and at the end caps (length and width) of the aggregate.

Fig. 7.15 shows good quality fits using this model in both the dC14/C6 and the dC14/C8 mixtures. The rims on both edges were between 6-7 Å while the shell SLD varied between $\sim$ 2.3-4 Å^{-2} , with slightly higher values for the shell along the width. This would mean an increase in mixing of the long lipids from about 15-20% (at 10°C with the discoidal model) to more than 60% and slightly more in the caps with increasing temperature, a reasonable trend considering the curvature of the rim in the end caps is more than that along the length (body). The volume fraction in this model however was found to have some inconsistency, so that mixing changes with temperature would have large uncertainty. This leads us to draw only qualitative trends from the fits at present.

7.5   Discussion

Figs. 7.17 and 7.18 summarize the results of this study on the temperature induced changes in the C14/C6 and C14/C8 mixtures of the same composition, molar ratio q=2.0 and c=0.03 g/ml as the temperature of the system is raised from 10-40°C and 10-25°C respectively. Both the figures correlate 'macromolecular changes' in aggregate size
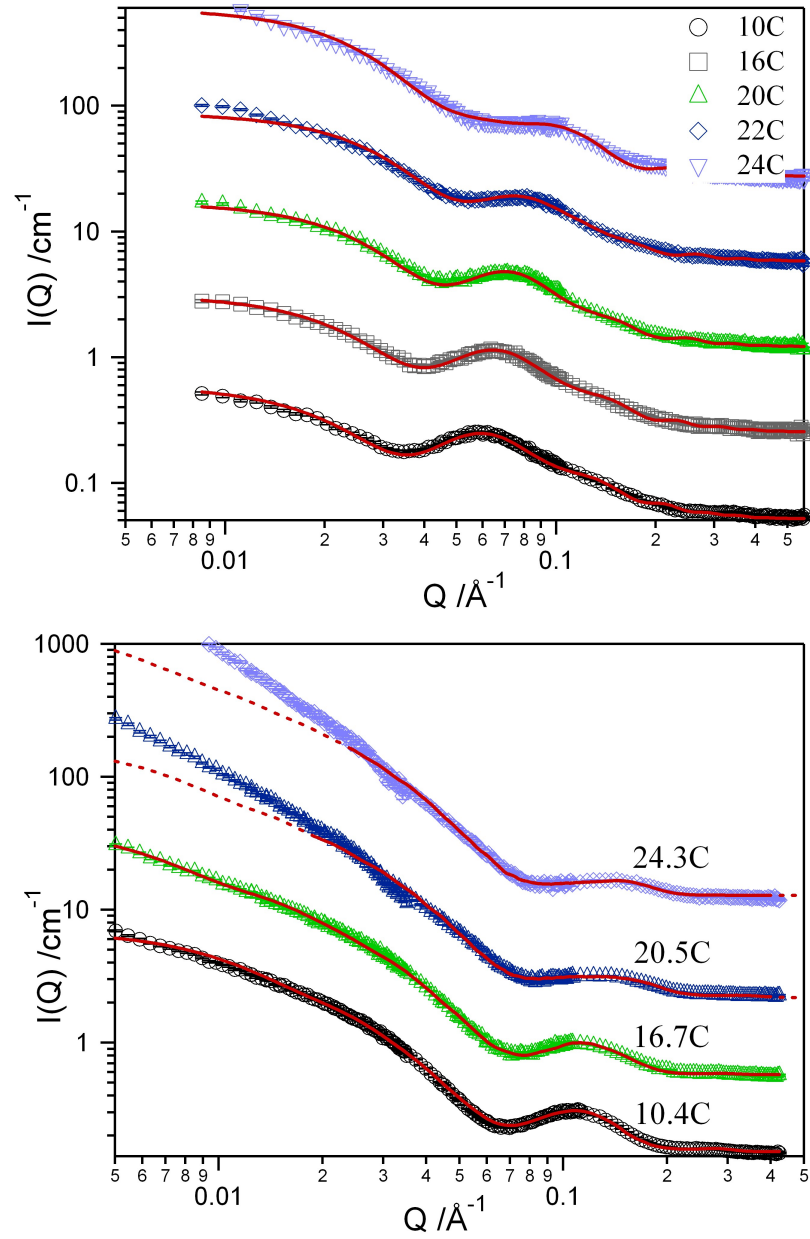
Figure 7.16: Fits to the contrast enhanced samples in (a)$q2$ c=0.05 g/ml dC14/C6 and (b)$q2$ c=0.03 g/ml dC14/C8 mixtures using the core-shell geometry in Fig.7.13.

from visual inspection and SANS to cooperative 'molecular' changes in the lipid molecules from calorimetry data on those mixtures. In C14/C6 mixtures, below a characteristic temperature (determined by it's composition), the mixtures are discoidal, but beyond that

temperature, they start to grow. The discoidal geometry, with the segregation of the two lipids and partial mixing of DMPC into the short lipid edges as understood in chapters 5 and 6 before, can be better understood as tablet shaped aggregates of rectangular cross-section that can grow in one dimension to form elongated objects, and which could also grow in two dimensions to form bilayer fragments eventually forming vesicles at further higher temperatures (not part of this study). The C14/C8 mixture on the other hand consist of elongated aggregates at even the lowest temperature in this study, $10°C$, leading up to a very sharp melting peak at $20.5°C$ (and $17.9°C$ in the deuterated case), concomitant with a very sharp increase in viscosity, which is seen to be correlated with a sharp increase in elongation and possible entanglement of the flexible aggregates. The sharp melting peak is analogous to that in pure DMPC lipid dispersions, except for the shift in temperature.A much smaller shoulder like peak, observed near $28°C$ coincides with a visible change to milky white fluid (we do not have corresponding SANS data to correlate this peak).

Similar results, correlating the visual appearance to the calorimetry and scattering data and further to the macromolecular organization of the aggregates can be established for the all the mixtures at other compositions of total lipid concentration c and molar ratio q in this study as well. Next we discuss the correlation observed in Figs. 7.17-7.18 and a general scheme for structural transitions in lipid mixtures, based on those two systems.

7.5.1 Temperature Induced 1-D Growth of Segregated Aggregates

The temperature induced growth of small discoids, to elongated and more flexible aggregates seen with increasing temperature in our lipid mixtures, can be rationalized in terms of changes in the 'material properties' of the aggregates. Recent work by Bergstrom, Pedersen and coworkers have theoretically studied the free energy of micelle of 'tablet' geometry, as a function of the spontaneous curvature, and elastic constants $\kappa, \bar{\kappa}$ and line
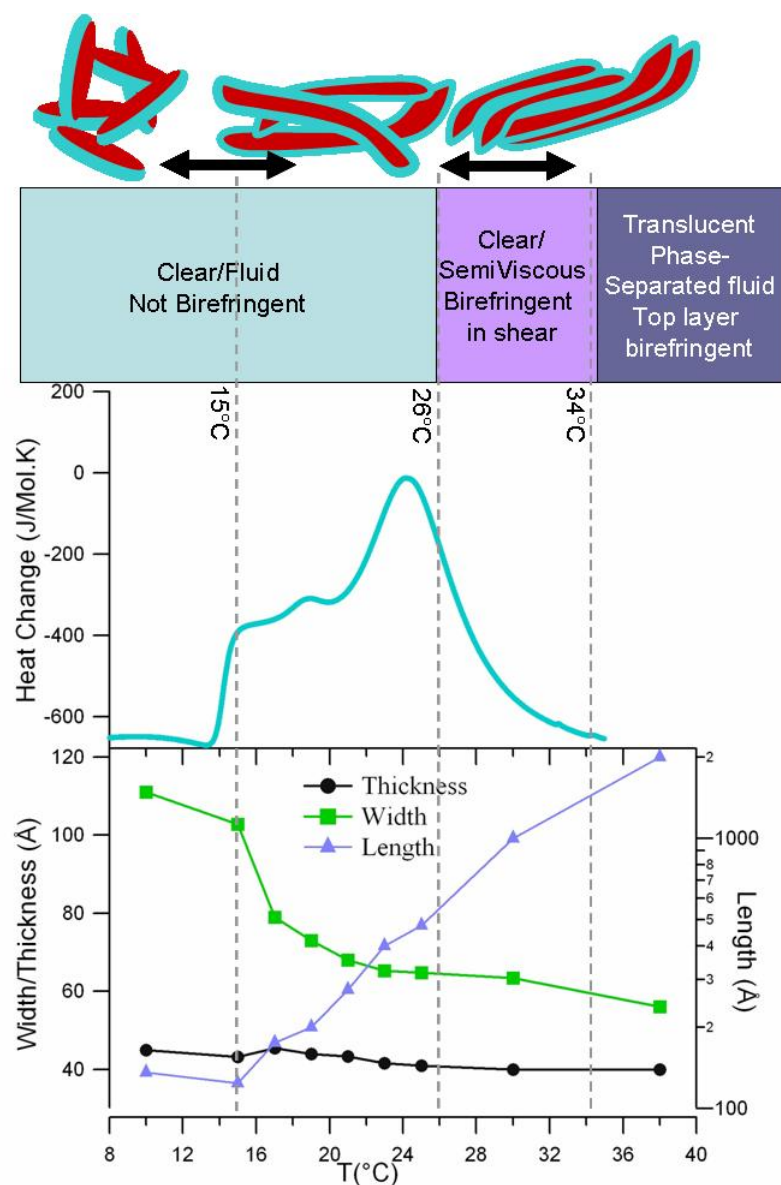
Figure 7.17: Temperature induced changes in a regular C14/C6, q=2 and c=0.03 g/ml mixture, when the temperature is varied from T=10-40°C , as seen in the measured aggregate parameters obtained from SANS data, calorimetry and optical phase behavior. Possible aggregate morphologies range from small tablets (approximate discs), $\sim$ 10-15°C below T_m , to elongated tablets near T_m and flexible ribbons at 10-15°C above T_m .

tension of the molecules composing the aggregate [143, 144], as an alternative approach to

the widely used packing parameter ideas by Israelachvilli.

194
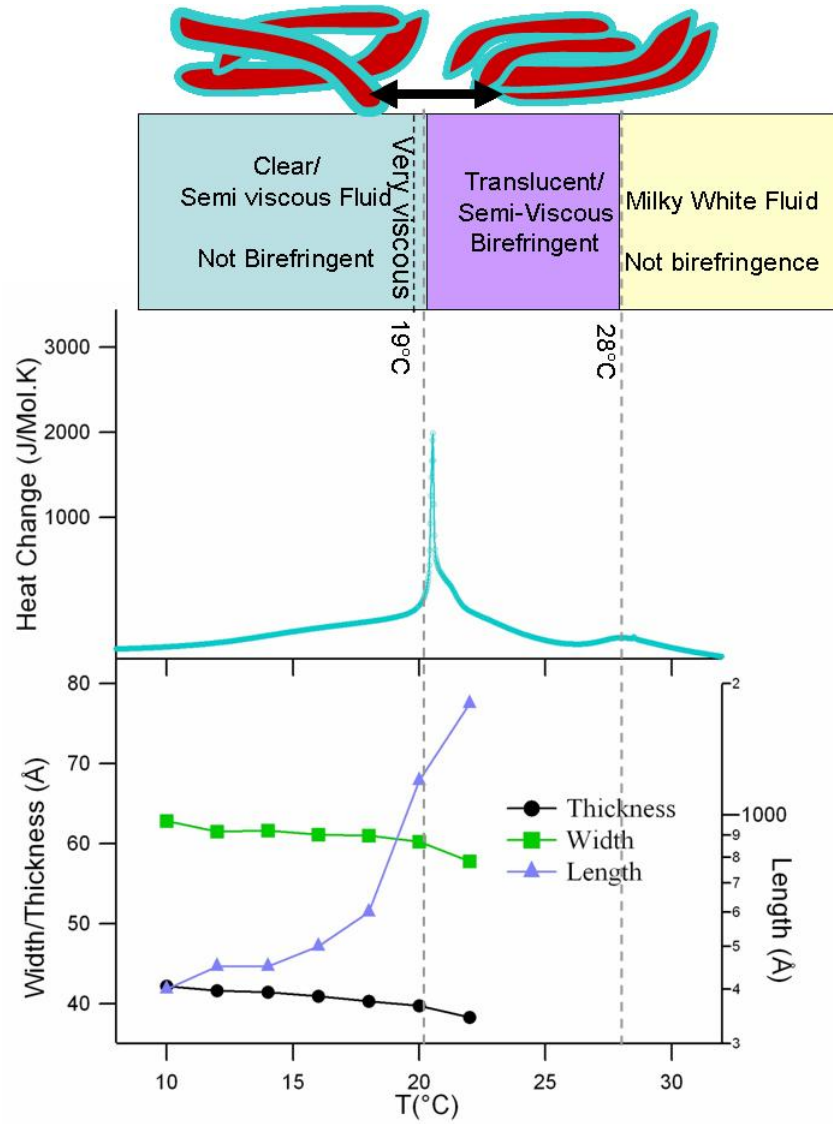
Figure 7.18: Temperature induced changes in a regular C14/C8 mixture of molar ratio q=2 and c=0.03 g/ml mixture, when the temperature is varied from T=10-22°C , as seen in the measured aggregate parameters obtained from SANS data, calorimetry and optical phase behavior. Possible aggregate morphologies range from elongated tablets ~10-15°C below T_m , to flexible, entangled ribbons near and above the modified T_m for this mixture.

Without going into the details of their calculation, we point out the main result of their formalism, which predicts the growth of small globular aggregates to polydisperse elongated aggregates as the bending rigidity approaches $k_B T$. By accounting for free energy

of formation of the curved edges and the bilayer, Bergstrom and coworkers have shown that for large values of the elastic constant κ, disk like globular aggregates, the limiting case of a tablet with $length \equiv width$ are expected, while at small values of κ, polydisperse rodlike micelles are expected. Though the experimental system studied by these authors, mixtures of charged surfactants, showing existence of triaxial aggregates [168, 169, 170], and salt effects on the bending rigidity of the aggregates driving the transitions, is different than our mixed lipid system, the theoretical ideas can be extended to the case of phospholipid mixtures.

For the lipid mixtures in this study, it is the thermodynamic effects on bilayer properties of the long lipid, resulting in more than an order of magnitude difference in bending rigidity (see Chapter 2), that can be seen as driving the observed mesomorphic transitions in Figs 7.17-7.18. In direct analogy to their system, in C14/C6 mixtures, the elastic behavior of the bilayer forming core lipids, drives the elongation of the tablet and its transition to flexible ribbons with temperature. With reference to the quantitative data on such changes by Dimova et al. [60], shown in Fig. 2.3, the small increase in aggregate size of the tablets between preT_m and T_m could be accounted for by smaller decrease in bending rigidity, since between 10-24°C , when κ decreases steadily, so that the tablets are still rigid rod like, while above T_m , κ falls by more than an order of magnitude which leads to the rods suddenly becoming flexible and worm like, and better described as 'flexible ribbons'.

Fig. 7.19 compares the temperature dependent changes in the length, width and thickness of the various mixtures in this study.
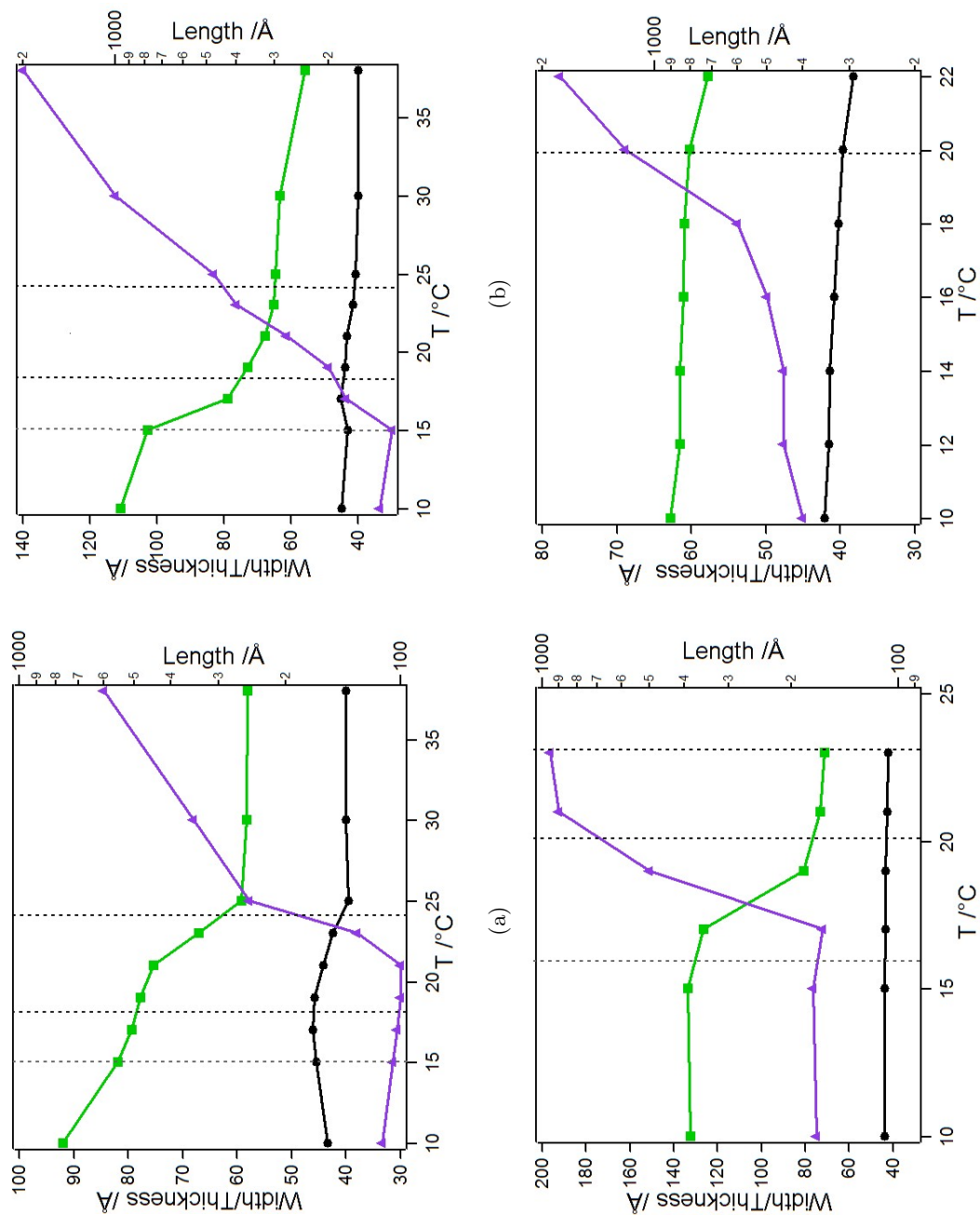
Figure 7.19: Dimensional changes showing thickness (*circles*), width (*square*) and length (*length*) obtained from fits to neutron data using parallelepiped model in different samples (a) C14/C6 $q2$ c=0.05 g/ml (b) C14/C6 $q2$ c=0.05 g/ml (c) C14/C6 $q3$ c=0.05 g/ml and (d) C14/C8 $q3$ c=0.03 g/ml. Peaks from calorimetry data are indicated. Note the composition dependent temperature at which the small disc/tablet to elongated tablet morphology takes place.

197

7.5.2 Structural Changes Associated with Melting Transition

The ideas that T_m of the lipids which represent the tail ordering and hence a molecular parameter, could also be correlated to the 'macromolecular' structural changes (as shown in Fig. 7.1) in the mixed aggregates is natural, but not so far a very clear. It has been explored before based on combined calorimetry, light scattering and NMR studies in DMPC-C12E8 mixtures [113, 165, 166], but a clear understanding of how those two changes could be related has not emerged so far. In fact, evidence of such a coupling even in the case of a single charged lipid has been recent [171]. As shown in Chapter 2, several other studies of bilayers with finite curvature (as in SUVs) of zwitterionic lipids have implicated broadening of the melting peaks (compared to flat bilayers) due to changes in the lateral pressure experienced by the lipids and consequent differences in packing between the inner and outer monolayer [67, 68]. The origin of split peaks in extruded vesicles of C12-C15 phospholipids however, is not clear [58, 54]. Recently 'in plane' density fluctuations have been implicated for the observed peak split in ULVs of C13 and C14 lipids [69].

Fig. 7.20 shows calorimetry data on the contrast enhanced mixtures of dC14/C6 of different composition, varying in the molar ratio of the two lipids (two of these are from Fig. 7.2). Besides the shift due to deuterated lipids, all the scans, except the one for $q = 0.5$, show a very broad melting regime, starting from near the preT$_m$ all the way to T$_m$, spanning almost 10-15°C in temperature. As the molar ratio of the long lipid to the short lipid is increased, a clear splitting of the main T$_m$, the magnitude and size of both of which are related to the aggregates size and their polydispersity, and a not so clear effect on preT$_m$, is observed. The low end of the split peak, near ~ 18-20°C is clearly visible as the aggregates sizes grow with increasing molar ratio; so the $q = 3.0$ sample shows a well defined lower second peak, which becomes much smaller in $q = 2.0$ samples and completely merges in $q = 1.0$ samples. The important question one has to answer is wether mixing of C14

lipids into the curved edges (shown before at low temperatures) could be responsible for the splitting of the main T_m, since those lipids experience a very different curvature. If that is true, it would also shed some light on the mixing behavior in the elongated aggregates along with the SANS data.
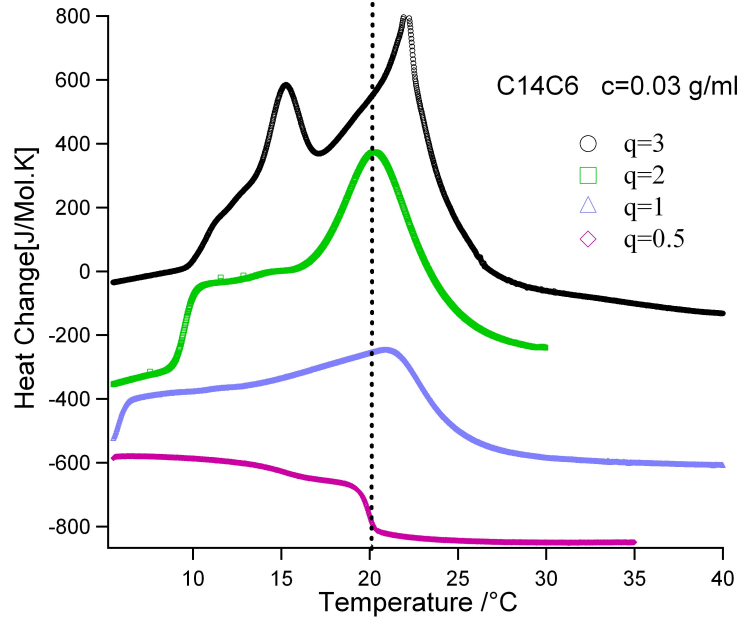
Figure 7.20: DSC scans on c=0.03 g/ml mixtures of dC14/C6, at varying molar ratios in the contrast enhanced samples. For reference T_m of deuterated C14 is indicated. Scan rate was 5°C /hr.

In order to understand the underlying cause for the broad melting in our calorimetry data, the melting curve of two mixtures was deconvoluted as shown in Fig. 7.21 for C14/C6 mixture of two different molar ratios q=2.0 and 3.0, both of the same total lipid concentration 0.03 g/ml. Three Lorentzian peaks were fit to both and the respective peak profiles, area and width obtained are summarized in Table 7.5. In going from the larger molar ratio q=3, to the smaller molar ratio, q=2, it shows broadening of the main melting peak at T_m and a very small shift in its position. The split second peak on the other hand, occurs at a lower temperature (shifts from ~20 to 18 °C) and is also much broader. ~1°C shift in the pre transitional peak is also seen between the two mixtures. If the split peak,

Table 7.5: Peak fit parameters to DSC data on C14/C6=2 and 3 mixtures each of same lipid concentration 0.03 g/ml.

	Position	Area	Width	Peak fraction
C14/C6=2				
Peak 1	15.34	572.2 (9.47)	1.75(0.02)	0.06
Peak 2	18.12	2244.0(23.49)	4.91(0.04)	0.22
Peak 3	24.26	7507.0(44.77)	6.65(0.02)	0.73
C14/C6=3				
Peak 1	16.51	476.1 (18.76)	3.26(0.08)	0.07
Peak 2	20.13	1769.7(11.91)	2.26(0.01)	0.27
Peak 3	24.67	4264.2(41.6)	4.04(0.02)	0.66

(Peak 2) resulted from mixing of the long lipid into edges, then one would expect them to be present in patches of atleast 8-10 lipids [55], which is very unlikely, since for entropic reasons, one would expect them to be randomly mixed. Also, if they were to be present in the rims, as mixed monolayer with the short lipids, the order-disorder transition can be hardly expected in that case.
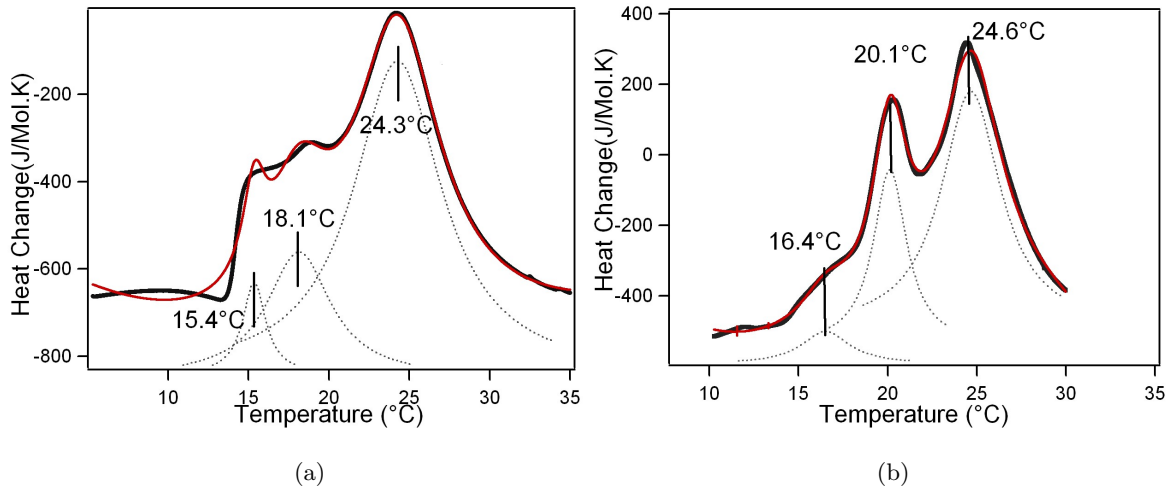
Figure 7.21: DSC scans of C14/C6, c=0.03 g/ml mixtures of different molar ratios (a) q=2.0 and (b) q=3.0, in the regular mixtures showing three deconvoluted peaks.

Next we consider a different possibility, as discussed before in Chapter 2. This is

based on the curvature of the boundary lipids, at the farthest edge or boundary of the core lipids. Such lipids, covered by a micelle forming rim, are 'different' from the lipids in the bulk and extend to a atleast a few mono layers. Boundary lipids have been implicated in many lipid-protein studies, starting from the seminal work of McConnell and coworkers in the early 80's [172], and play an important role in regulating the structure and function of proteins due to the energetics involved. In our mixed system, the short lipid species in the rim reduce the interfacial tension at the hydrocarbon-water interface, covering the hydrophobic tails of the outer layer lipids. These 'affected' outer monolayer plus a few layers can be collectively called 'boundary lipids', and represent those lipids affected by the hydrocarbon-water interface [27]. Increased disparity in packing in these lipids could be responsible for the presence of the second peak at a lower temperature. For such a boundary effect, the peak fraction would be expected to be proportional to the size of the perimeter. Indeed, from Table 7.5, the ratio of peak fractions (of Peak 2) for the two mixtures are $0.21/0.27 \sim 0.77$, while the ratio of their perimeters are $\sim 2\pi R_1/2\pi R_2 \approx 0.8$, where R_1 and R_2 are taken as 60 and 75 Å respectively (Chapter 5).

This effect is confirmed further by the presence of a single peak in the C14/C8 mixture at a temperature 4°C below the main T_m of C14, at $\sim$20°C , (see Fig. 7.2). In this mixture, whose cross-sectional dimension is $\sim$ 62 Å, all the C14 lipids are like the boundary lipids and their combined melting, possibly produces the sharp transition seen in the calorimetry data at $\sim$20°C . Presence of C8 lipids mixed into the C14 lipid core in these mixtures, seem to have negligible effect in broadening, likely with the cooperative melting from the large aggregate size overtaking any disordering effect. Any mixing in these mixtures could thus, not be resolved by this technique. The calorimetry data on both the mixtures, along with the scattering data, do however, indicate the role of interfacial changes in affecting the bulk property, the bending modulus in driving the structural changes. Further work is needed to understanding the interconnected role of interfacial changes in the boundary lipids and the bending modulus of the aggregate structure.

7.5.3 Implications for Membrane Protein studies

The work presented in this thesis did not include any membrane proteins, yet it warrants some comments on this topic given its relevance to membrane protein studies. Preliminary studies for this work, on inserting one such small protein, Gramicidin (which forms channels in lipid membranes) into the 'bicelle' mixtures using traditional recipes cited in the literature [20] were unsuccessful, possibly due to the mixing protocols used. Those initial attempts, led us to investigate the basics of the lipid mixtures presented in this study. The discussion in the previous two sections, sheds light on the phase behavior of the lipid mixtures, that will be relevant for any further work including proteins. Both scattering and calorimetry techniques combined, lead the way to understanding the structural changes at macroscopic and molecular level, that would be critical in any membrane protein application, crystallization or even simply peptide/protein insertion in mimetic mixtures. The interfacial properties of lipids affecting their phase behavior, the hydrophobic mismatch between the lipids and the surfactants, their spontaneous curvatures and bending rigidities, can all be tailored using the variety of naturally occurring lipids and surfactants. The small attempt in this work in understanding the phase behavior of lipid mixtures, can be seen as just the beginning of their applications to a whole range of different applications for understanding membrane proteins.

Chapter 8

Summary and Future Directions

The main goal of this thesis has been to examine the structure and transitions in phospholipid mixtures, of considerable interest to the membrane protein field for applications ranging from NMR based structure determination to their crystallization. This goal has been realized by use of scattering techniques to two parts of their phase diagram, at low and intermediate temperatures, defined by the melting transition temperature of the long lipids. The results of this work in three Chapters, 5-7 is summarized here along with some outstanding issues and future work.

The full power of the small angle scattering technique with neutrons, SANS, is used to investigate the discoidal 'bicelle' phase of a model mixture DMPC/DHPC (or C14/C6) at low temperatures in Chapter 5. Using a combination of analysis techniques, we characterized the aggregate sizes in mixtures of varying initial composition, molar ratio and the total lipid concentration. We have shown that it is essential to take into account the thermodynamics of the system to correctly determine aggregate sizes. SANS experiments with hydrogenated and deuterated lipids in contrast enhanced (CE) mixtures of the same lipid, give direct evidence of the segregated discoidal morphology. A quantitative model encompassing surfactant behavior and molecular parameters for the lipids, the 'modified

ideal bicelle model' is proposed in place of the 'ideal bicelle models' in the literature. The measured growth of the discoidal aggregates on dilution however, are less than that predicted by the fully segregated models. For the measured sizes to scale with molar ratio of the two lipids in the aggregate, allowance for a net mixing of the long lipid into the short lipid rim is found necessary and is confirmed by CE SANS.

Previously ignored and unaccounted for, we find that such a mixing behavior in the discoidal phase, with a net mixing of the two lipids in the rim and negligible mixing in the disc core can be explained by the energetics of the self-assembly, a balance of bending energy and edge energy in a continuum description first proposed by Fromherz. As a consequence of the same, limiting size of the discoids at ~120 Å and a 'bicelle to vesicle' transition for dilution induced growth beyond that limiting size is shown.

Molecular models in the literature for mixed lipid systems have mostly relied on ideal mixing for the entropy, the bending modulus and the spontaneous curvatures [159, 15, 162, 173, ?]. While explaining the phase behavior of two bilayer forming lipids with small hydrophobic mismatch, models accounting for non-ideally mixed systems with vastly different spontaneous curvatures are lacking. The results from the model mixture in this study, can be used to guide further theoretical investigation on mixtures with large differences in hydrophobic tail length and spontaneous curvatures. Also, to compliment the experimental results in this work and to guide further theoretical investigation, combined theoretical and experimental studies on understanding the non-ideality is critically needed.

Complimentary small angle scattering techniques, SANS and SAXS is used in Chapter 6 to study other phospholipid-detergent mixtures. 'Universality' of the segregated discoidal phase is observed in a range of different lipid and detergent mixtures, by systematically varying the rim species with C14 lipid in the core and by varying the core lipid with C6 in the rim. In the unique aggregate 'discoidal' assembly the individual curvatures are preserved so that the long species forms the core while the short phospholipid (or detergent) forms the curved rim with the disc thickness being the unperturbed bilayer thickness of the

long phospholipid. The main criteria required for the formation of the segregated discoidal aggregates is seen to be the presence of a phospholipid species with rigid tails and defined by well characterized melting temperature T_m, and the presence of a second component, another smaller micelle forming amphiphile to stabilize the edges. The modified ideal bicelle model is found to be a good quantitative description for the dilution induced growth in all the mixtures independent of the lipid and detergent species. Further using evidence from contrast enhancing SANS technique, we show that partial mixing of the long species in the rim scales inversely with the aggregate size. Increased mixing in the rim leading to smaller aggregate sizes, is seen to be the effect of decreasing hydrophobic mismatch between the tails of the two components lipids. When the size of the smaller lipid species is increased, in DMPC/DOPC(C14/C8) mixtures the morphology changes from discoidal to elongated tablet like aggregates, while the segregation persists as evident from CE SANS data.

In applying the modified bicelle model to quantify the dilution induced growth of the discoidal aggregates in both Chapter 5-6, the role of molecular parameters of the lipids is critical. While high resolution structure of one component bilayer forming lipids and several micelle forming industrial detergents have been extensively studied in the literature, corresponding data on biologically relevant, micelle forming lipids as also many mild detergents used in membrane protein research are few [43, 42]. Combined SANS and SAXS study on their structure will be very useful for extending the lipid-mixtures in this study to other combinations.

Finally, in Chapter 7, to understand the complex morphologies in C14/C6 mixtures at higher temperature as well as the elongated aggregate morphology in C14/C8 mixtures at lower temperature, we extended our scattering study, accompanied by calorimetry measurements to a range of temperatures encompassing both the pre T_m and T_m of the long lipid, C14. Elongated structures frequently seen in many mixed lipid-surfactant systems and proposed as cylindrical with circular cross-section with the two lipids mixed in the cylinder body cannot describe our data. Both CE-SANS and SAXS along with calorimetry

results, corroborate the bilayer characteristic and evidence of segregation even in the elongated morphology persists. An elongated tablet with a rectangular cross-section, consisting of long tail lipid core with edges of short lipid is the best description of such aggregates. In contrast to prior literature, where uniform core-shell cylinder models have been used to analyze scattering data from such elongated aggregates, we develop a non-uniform core-shell parallelepiped model to fit the scattering data in the segregated case. Based on the growth behavior from such a model, and theoretical work by Bergstrom and coworkers, we propose that softening of the bending modulus of the long lipid leads to one -dimensional growth. In that respect, chain melting and increased mixing of smaller species in to the core lipid, due to decreasing chain length difference in C14/C8 and chain-melting in C14/C6 mixtures result in lowering of the bending modulus and preferential growth in one dimension. Calorimetry data further point to the influence of boundary layer lipids resulting in splitting of the main melting peak. The effect of a boundary layer is seen in the temperature shift of the split of the melting peak in C14/C6 mixtures and the occurrence of a sharp peak in the C14/C8 mixtures at the same position, highlighting their predominant role in the elongated aggregate morphologies. Further understanding of the boundary layer lipids in defining the edge tension and leading to the observed elongated morphology is needed.

The observations in Chapters 6-7, on the universality of the segregated phase at low temperature as also in the overall phase behavior scaled to the melting temperature, opens up more questions for future work on the science aspect of this work. Does the universality extend to mixtures of other ionic and non-ionic industrial double tail bilayer and micelle forming amphiphiles? How critical is the role of the zwitterionic headgroup in the overall assembly? Also, since above the melting temperature, both melting and mixing of the two species occur simultaneously, decoupling the two effects on the line tension is needed for a better understanding.

The tablet model introduced in Chapter 7, to account for 1-dimensional growth of aggregates with increasing temperature also raises questions for future work. If the

low temperature tablets are equivalent to small discoids, then while dilution leads to their two dimensional growth, increasing temperature results in elongation and one-dimensional growth. What drives the preferential one or two dimensional growth? While some possible solutions from Fromherz's analysis for the two dimensional growth at low temperature and Bergstrom's tablet model for the intermediate temperature growth have been invoked, a detailed model accounting for the non-ideal mixing factor is needed.

While this work started with the goal of understanding membrane protein crystallization conditions, only the first and foremost important step of understanding the lipid templates has been realized in this work. So, on the application side, the next step in this study would be inserting small membrane proteins, and a step by step analysis of the crystallization process. Complimentary small angle scattering studies as demonstrated in this work, can be expected to lead to detailed insights into effect of different crystallization agents. Time resolved, stop-flow, scattering experiments with addition of different species, could be the possible first test measurements.

The work presented here, highlights the role of the molecular properties manifested as macromolecular parameters, the bending rigidity and the line tension of the long lipids and the strength of the short lipids (or detergents) in stabilizing the edges of the aggregates observed. Segregation of two lipids is an effect that can be seen easily when the long tail lipid is in its frozen gel phase, some segregation persists even in the melted state, possibly due to the vast difference in the intrinsic curvatures of the two species. We also explored the role of the appropriate combination of long and short lipids for particular applications in membrane protein crystallization or in NMR studies of structure and interactions between membranes and proteins. The choice of the lipid mixture can be based on the temperature, the hydrophobic mismatch and the detergent strength needed for a particular application. An understanding of the underlying morphology of mixed systems, such as this study is expected to lead to a better understanding of membrane protein interaction with complex native membranes.

Appendix A

Radius of Gyration - Details

To obtain the net dimension of a discoidal aggregate with curved edges, we use the radius of gyration (R_g) obtained from SANS data. In this section, we derive the actual dimension for disks with ellipsoidal or hemispherical rims (schematic shown in Fig.A.1) from R_g of the composite disc.

For an object with a center of symmetry, the radius of gyration about the center of mass is given as

$$R_g^2 = (1/V) \int_V r^2 d^3r \qquad (A.1)$$

The parametric equation of the surface that will generate a hemispherical or ellipsoidal rim is (Note: use of R instead of R_c for ease of notation)

$$z = r \cos\theta$$

$$x = (R + r\sin\theta)\cos\varphi$$

$$y = (R + r\sin\theta)\sin\varphi$$

where θ is the angle measured from the z-axis and ϕ lies in the plane of the disk, so that $(0 \leq r \leq a)$, $(0 \leq \theta \leq \pi)$ and $(0 \leq \phi \leq 2\pi)$
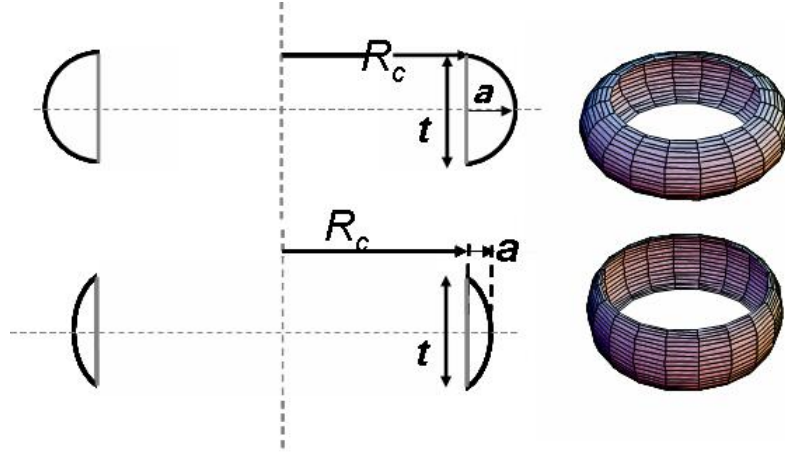
Figure A.1: Schematic of hemispherical and ellipsoidal rims on edges of core of radius R_c. The thickness of the disk is t and the radius of curvature $t/2 = a$ for a hemispherical rim and $t/2 \neq a$ for ellipsoidal rim.

In the above equations, when the coefficient in the z-term is changed to $t/2 \neq r$, we have the equation for an ellipsoid rim. Thus in Fig.A.1 we have

Hemispherical rim: t/2=a, while for an **Ellipsoidal rim: t/2≠a**

For calculating the integral in equation (A.1), we need the volumes of the rim, which can be calculated as follows-

A.1 Volumes of curved rims

Using Pappus's Centroid theorem

[see for e.g, http://mathworld.wolfram.com/PappussCentroidTheorem.html]

$V = (2\pi) \times$ Area of rotating surface$\times$ distance from rotation axis

So, that the volume of the ellipsoidal or hemispherical rims are given as

$$V = 2\pi \times (\pi a t/2)/2 \times [R + 4a/3\pi]$$

Since the center of mass of an ellipse of semi-minor axis a and semi-major axis $t/2$ is $4a/3\pi$. If the rotating surface was sphere (for a hemispherical rim), $(\pi at/2)/2 \rightarrow \pi a^2/2$ when $a = t/2$

$$
\begin{aligned}
V_{rim} &= 2\pi \left(\frac{\pi at/2}{2}\right) \left[R + \frac{4a}{3\pi}\right]\Big|_{Ellipsoidal} \rightarrow 2\pi \left(\frac{\pi a^2}{2}\right) \left[R + \frac{4a}{3\pi}\right]\Big|_{Hemispherical} \\
&= \tfrac{1}{2}\pi^2 rt \left(R + \frac{4a}{3\pi}\right)\Big|_{Ellipsoidal} \rightarrow 2\pi^2 a^2 \left[R + \frac{4a}{3\pi}\right]\Big|_{Hemispherical}
\end{aligned} \tag{A.2}
$$

Volumes of rims using Integrals in Parametric Coordinates

The volumes of the rim can also be obtained by integrating the Jacobian computed from the parametric equations, which is given by the following for a hemispherical rim

$$
J = \left|\frac{\partial(x,y,z)}{\partial(\theta,\phi,r)}\right| = \begin{vmatrix} \frac{\partial x}{\partial \theta} & \frac{\partial y}{\partial \phi} & \frac{\partial z}{\partial r} \\ \frac{\partial x}{\partial \theta} & \frac{\partial y}{\partial \phi} & \frac{\partial z}{\partial r} \\ \frac{\partial x}{\partial \theta} & \frac{\partial y}{\partial \phi} & \frac{\partial z}{\partial r} \end{vmatrix}
$$

$$
= r(R + r \sin\theta)
$$

So that volume of the rim can be calculated as

$$
\begin{aligned}
V_{rim} &= \int_0^{2\pi} \int_0^{\pi} \int_0^a r(R + r\sin\theta)\, dr\, d\theta\, d\phi \\
&= 2\pi \int_0^a \left(r\,(R\theta - r\cos\theta)\big|_0^{\pi}\right) dr \\
&= 2\pi \int_0^a \left(\pi r R + 2r^2\right) dr \\
&= 2\pi \left(\frac{\pi r^2 R}{2} + \frac{2r^3}{3}\right)\Big|_0^a = \frac{4\pi a^3}{3} + \pi^2 a^2 R
\end{aligned}
$$

This can be written in the more familiar form $2\pi(R + 4a/3\pi)(\pi a^2/2)$ to give the volume of a hemispherical rim V_{HS}

$$
V_{HS} = \pi^2 a^2 (R + 4a/3\pi)) \tag{A.3}
$$

In the limits R→0, V→volume of a sphere of radius $a = 4\pi a^3/3$

While for an ellipsoid, the Jacobian is given by

$$J = \left| \frac{\partial(x,y,z)}{\partial(\theta,\phi,r)} \right| = \frac{t}{2}(R + r\sin\theta)\sin^2\theta$$

Just as for the hemispherical case, the volume can be calculated as

$$
\begin{aligned}
V_{rim} &= \int_0^{2\pi} \int_0^{\pi} \int_0^{a} (t/2)(R + r\sin\theta)\sin^2\theta\, dr\, d\theta\, d\phi \\
&= 2\pi \int_0^{\pi} (t/2)\sin^2\theta \left(Ra + \frac{a^2}{2}\sin\theta \right) d\theta \\
&= \pi t \int_0^{a} \left(aR\sin^2\theta + \frac{a^2}{2}\sin^3\theta \right) dr \\
&= \pi at \left(\frac{\pi R}{2} + \frac{2a}{3} \right) \Big| \rightarrow 2\pi(R + 4a/3\pi)\frac{(\pi at/2)}{2}
\end{aligned}
$$

When R→0, V→volume of the prolate ellipsoid (of semiaxis a and t/2)≡(4π $a^2.t/2$)/3 so that for a=t/2(equal axes), we have prolate ellipsoid → sphere V→ $(4\pi/3)(t/2)^3$ which is ≡ Volume of sphere (of radius=t/2)

Thus, for the ellipsoidal rim V_{rim} from here on will be used as

$$V_{EL} = \pi^2 at(R/2 + 2a/3\pi) \tag{A.4}$$

A.2 Rg: Disk with Hemispherical rim

The distance r^2 of any point (x,y,z) on a hemispherical rim, in the parametric form will be given as

$$
\begin{aligned}
r^2 &= (x^2 + y^2 + z^2) = (R + r\sin\theta)^2 + r^2\cos^2\theta \\
&= R^2 + r^2 + 2Rr\sin\theta
\end{aligned}
$$

So that the integral in Eqn.A.1 is written as

$$
\begin{aligned}
R_g^2 &= \frac{1}{V} \int_V (R^2 + r^2 + 2Rr\sin\theta)r(R + r\sin\theta)\, dr\, d\theta\, d\phi \\
&= \int_{r=0}^{r=a} \int_{\theta=0}^{\theta=0} 2\pi(R^2 + r^2 + 2Rr\sin\theta)r(R + r\sin\theta)\, dr\, d\theta
\end{aligned}
$$

211

The integral inside (besides the factor of 2π) can be rewritten as

$$
\begin{aligned}
I &= \int_{\theta}\int_{r} (R^2 + r^2)rR + r^2\sin\theta(R^2 + r^2) + 2Rr^2(R\sin\theta + r\sin^2\theta)\, dr\, d\theta \\
&= \int_{r} (R^2 + r^2)rR\theta + r^2(R^2 + r^2)(-\cos\theta) + 2R^2r^2(-\cos\theta) + 2Rr^3\frac{1}{2}(\theta - \cos\theta\sin\theta)\, |_0^\pi\, dr \\
&= \int_{r} (R^2 + r^2)rR\pi + 2r^2(R^2 + r^2) + 4R^2r^2 + 2Rr^3\frac{\pi}{2}\, dr \\
&= \int_0^a \pi R^3 r + 2\pi r^3 R + 6R^2 r^2 + 2r^4\, dr \\
&= \frac{\pi R^3 a^2}{2} + \frac{2\pi a^4 R}{4} + \frac{6R^2 a^3}{3} + \frac{2a^5}{5}
\end{aligned}
$$

This gives

$$
\begin{aligned}
R_g^2 &= \frac{2\pi}{\pi a^2(\pi R + 4a/3)}\left(\frac{\pi R^3 a^2}{2} + \frac{\pi a^4 R}{2} + \frac{2\pi R^2 a^3}{1} + \frac{2a^5}{5}\right) \\
&= \frac{1}{(\pi R + 4a/3)}\left(\pi R^3 + \pi a^2 R + 4R^2 a + \frac{4\pi a^3}{5}\right)
\end{aligned}
$$

In terms of thickness $t = 2a$, the Radius of gyration of the hemispherical rim can be rewritten as-

$$
R_g^2 = \frac{1}{(\pi R + 2t/3)}\left(\frac{t^3}{10} + \frac{\pi R t^2}{4} + 2tR^2 + \pi R^3\right) \tag{A.5}
$$

In the limit R→0 and t=2a, $R_g^2 \to \frac{3}{5}R^2$: for a sphere of radius R

Finally, Radius of gyration of a discoid which consists of

(1) rim as derived above; of Mass m_1, Volume V_1 (derived in Eqn.A.3)

(2) central core also of radius R_c and thickness t: Mass (m_2), Volume (V_2)

can be obtained as the weighted average of the two respective radii's as:

$$
R_g^2|\, bicelle = \frac{m_1 R_{g_1}^2 + m_2 R_{g_2}^2}{m1 + m2} = \frac{V_1 R_{g_1}^2 + V_2 R_{g_2}^2}{V_1 + V_2} \tag{A.6}
$$

where $R_{g_2}^2 = R^2/2 + t^2/12$ for core of radius R_c and $V_2 = \pi R_c^2 t$.

In general, the densities of the the core and rim regions may not be equal, so that the volume equivalence may not be absolutely true.

A.3   Rg: Disk with Ellipsoidal rim

The distance r^2 of any point (x,y,z) on an ellipsoidal rim, in the parametric form will be given as

$$r^2 = (x^2 + y^2 + z^2) = (R + r\sin\theta)^2 + t^2\cos^2\theta/4$$

So that the integral in equation is written as

$$
\begin{aligned}
R_g^2 &= \frac{1}{V}\int_V \left((R + r\sin\theta)^2 + \frac{t^2}{4}\cos^2\theta\right)(t/2)(R + r\sin\theta)\sin^2\theta \, dr \, d\theta d\phi \\
&= \int_{r=0}^{r=a}\int_{\theta=0}^{\theta=0} 2\pi(t/2)\left((R + r\sin\theta)^3 + \frac{t^2}{4}\cos^2\theta(R + r\sin\theta)\right)\sin^2\theta_d r d\theta
\end{aligned}
$$

The integral inside (besides the factor of 2π) can be rewritten as

$$\int_\theta\int_r \left((R + r\sin\theta)^3\sin^2\theta + \frac{t^2}{4}\cos^2\theta\sin^2\theta(R + r\sin\theta)\right) dr \, d\theta$$

In the above integral, we can make use of the following results

$$
\begin{aligned}
\int(a + b\sin x)^3\sin^2 x \, dx &= \frac{b^3}{80}\cos 5x + \frac{3}{32}a\sin 4x.b^2 - \frac{b}{8}(18a^2 + 5b^2)\cos x \\
&+ \frac{b}{48}(12a^2 + 5b^2)\cos 3x + \frac{a}{8}(4a^2 + 9b^2)x - \frac{a}{4}(a^2 + 3b^2)\sin 2x \\
\int(a + b\sin x)\sin^2 x\cos^2 x \, dx &= \frac{ax}{8} - \frac{b\cos x}{8} - \frac{b\cos 3x}{48} + \frac{b\cos 5x}{80} - \frac{a\sin 4x}{32}
\end{aligned}
$$

where the limits of integration are again from $(0, \pi)$. Thus the integrals over θ give-

$$
\begin{aligned}
&\left[\frac{r^3}{40} + \frac{r}{4}(18R^2 + 5r^2) - \frac{r}{24}(12R^2 + 5r^2) + \frac{\pi R}{8}(4R^2 + 9r^2)\right] \\
&\qquad\qquad + \frac{t^2}{4}\left[\frac{\pi R}{8} + r(\frac{2}{8} + \frac{2}{24} - \frac{2}{80})\right] \\
&= \frac{16}{15}r^3 + \frac{9\pi}{8}Rr^2 + 4rR^2 + \frac{\pi R^3}{2} + \frac{\pi Rt^2}{32} + \frac{t^2 r}{15}
\end{aligned}
$$

213

and finally, R_g is obtained as

$$\begin{aligned} R_g^2 &= \frac{1}{V}\int_r \left(\frac{16}{15}r^3 + \frac{9\pi}{8}Rr^2 + 4rR^2 + \frac{\pi R^3}{2} + \frac{\pi Rt^2}{32} + \frac{t^2 r}{15}\right)2\pi(t/2)\,dr \\ &= \frac{\pi t}{V}\left(\frac{4a^4}{15} + \frac{t^2 a^2}{30} + \frac{3\pi Ra^3}{8} + 2R^2 a^2 + \frac{\pi R}{2}(R^2 + \frac{t^2}{16})a\right) \end{aligned}$$

which can be rewritten in this final form

$$R_g^2 = \frac{1}{\pi a(R/2 + 2a/3\pi)}\left(\frac{4a^4}{15} + \frac{t^2 a^2}{30} + \frac{3\pi Ra^3}{8} + 2R^2 a^2 + \frac{\pi R}{2}(R^2 + \frac{t^2}{16})a\right) \qquad \text{(A.7)}$$

In the limit R→0

$$R_g^2 \rightarrow \left(\frac{1}{2a^2/3}\right)(\frac{4a^2}{15} + \frac{t^2 a^2}{30}) \equiv \frac{1}{5}(2a^2 + t^2/4)$$

for a prolate ellipsoid of semi-axis a and $t/2$.

Again, the Rg of the whole bicelle disc can be obtained as the weighted average of the core and ellipsoidal rim, like Eqn.A.6

Figure A.2 compares the net dimension $R_c + r$ of discoidal aggregate of thickness 50Åand curvature $a = 25$Åfor a hemispherical rim and $a = 11$Åfor ellipsoidal rim with a disk of rectangular edge of the same dimension. With the small difference, ≈2-3Åbetween the different edges, the simpler rectangular edge is used in Chapters 5 and 6.
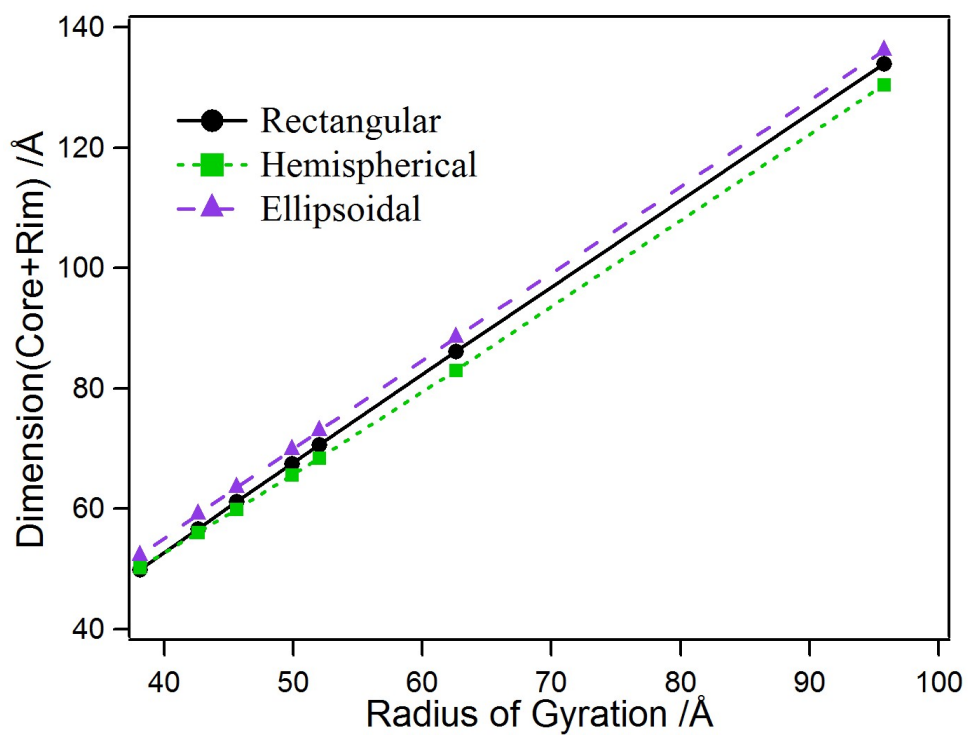
Figure A.2: Comparison of the net dimensions (core+ rim) of discoidal aggregates with rectangular, hemispherical and ellipsoidal edges obtained from R_g of the composite disc.

Appendix B

Form Factors for Composite Discs/Cylinders

The form factor for scattering from an object of some shape is given as

$$P(Q) = <|A(Q)|^2> \text{ where } A(Q) = \frac{1}{V} \int_V e^{iQ.r} \tag{B.1}$$

The integral over V implies that the phase factor has to be summed over the whole object and the angular brackets $<>$ implies average over all possible orientations of the object. In the following sections, a derivation of form factors for composite disc/cylinder like objects, with simple geometrical shapes and non-homogeneous variation of Scattering length densities(SLD) is presented. These models are of importance in Chapters 5 and 6, where *non uniform SLD variation* in the shells of disks (caps vs rims) has been used.

B.1 Scattering from Cylindrical/Disk-like objects

Disk-like or cylindrical objects lack spherical symmetry. So every orientation of the cylinder is different and will give different contributions to the phase factor. So once
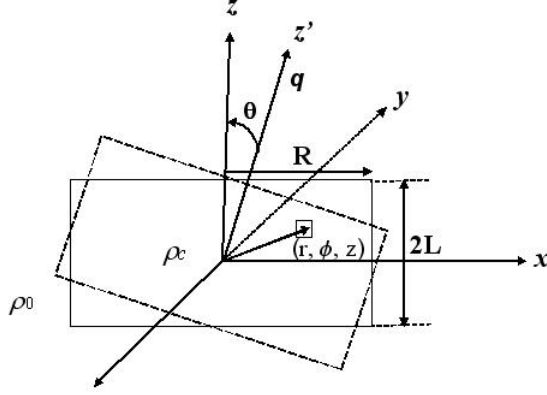
Figure B.1: Orientation of coordinates in a cylindrical (disk-like) object with respect to scattering vector Q.

the integral over the whole volume is done in some fixed orientation, a sum over all possible orientations of the cylinder has to be done as the last step to obtain the average in equation (1) as-

$$P_{cyl}(\mathbf{Q}) = < |\mathbf{A}(\mathbf{Q})|^2 > = \int |\mathbf{A}(\mathbf{Q}, \theta)|^2 \sin \theta \, \mathbf{d}\theta \qquad (B.2)$$

We first obtain the integral of the phase factor for a cylindrical disk, of thickness 2L, radius R and volume $V = \pi R^2 2L$ that is oriented at an angle θ from the z-axis as follows: Assume $\mathbf{Q}$ is oriented parallel to the z'-axis in the cylinder's original coordinate axis (x',y',z'). Then this coordinate system is rotated by an angle θ to obtain the new axes (x,y,z). Any point on the cylinder given is transformed by this rotation as: $\mathbf{r} = \mathbf{R}(\theta) \times \mathbf{r}'$

where $R(\theta)$ is the rotation transformation around y-axis given as

$$R(\theta) = \begin{pmatrix} \cos \theta & 0 & -\sin \theta \\ 0 & 1 & 0 \\ \sin \theta & 0 & \cos \theta \end{pmatrix}$$

For doing the integration with the phase factor, we need only the z-component of

217

the transformed coordinates, given by

$$z = x' \sin \theta + z' \cos \theta = r \cos \phi \sin \theta + z \cos \theta$$

$$\mathbf{Q.r} = Qr \cos \phi \sin \theta + Qz \cos \theta$$

Thus the form factor in this orientation is obtained as

$$A(Q) = \frac{1}{V} \int_r \int_\phi \int_z e^{(iQr \cos \phi \sin \theta + iQz \cos \theta)} r \, dr \, d\phi \, dz \qquad (B.3)$$

We can easily do seperation of variables in the above integral and write

$$A(Q) = \frac{1}{V} \int_r \int_\phi e^{(iQr \cos \phi \sin \theta)} r \, dr \, d\phi \int_z e^{(iQz \cos \theta)} \, dz \qquad (B.4)$$

For the two integrals, we can make use of the following relation for Bessel functions and exponential functions (text by Arfken pg. 675)

$$J_0(x) = \frac{1}{2\pi} \int_0^{2\pi} e^{ix \sin \theta} \, d\theta = \frac{1}{2\pi} \int_0^{2\pi} e^{ix \cos \theta} \, d\theta$$

$$\text{and } \int_{-L}^{L} e^{(iQz \cos \theta)} \, dz = \frac{e^{iq \cos \theta}}{iq \cos \theta}\Big|_{-L}^{L}$$

$$= \frac{2 \sin(qL \cos \theta)}{Q \cos \theta}$$

so that equation (6) can be written as

$$A(Q) = \frac{2\pi}{V} \int_r J_0(iQr \sin \theta) r \, dr \int_z e^{(iQz \cos \theta)} \, dz \qquad (B.5)$$

By using the relation between $J_0(x)$ and $J_1(x)$ given by

$$\int_x J_0(ax) \, dx = \frac{x J_1(ax)}{a}$$

we obtain

$$A(Q) = \frac{2\pi}{\pi R^2 2L} \frac{R J_1(QR \sin \theta)}{Q \sin \theta} \frac{2 \sin(qL \cos \theta)}{Q \cos \theta}$$

218

The above expression simplifies to give the widely used form factor for the cylinder as

$$P_{cyl}(Q) = <|A(Q)|^2> = \int \left(\frac{J_1(QR\sin\theta)}{QR\sin\theta} \frac{2\sin(qL\cos\theta)}{qL\cos\theta} \right)^2 \sin\theta \, d\theta \qquad \text{(B.6)}$$

B.2 Scattering from Core-shell discs

For the core-shell geometry of cylinders/disks, we will also need to sum over shells, which may have varying scattering length densities and thicknesses, when doing the integrals. From here on, we use the term 'discs' which are more relevant to the work in this thesis, but in essence the same ideas are applicable to elongated cylinders as well.

To include varying SLD's, we incorporate the contrast factor $(\rho(r) - \rho_0)$ inside the integral in Eqn. B.1 as

$$A(Q) = \frac{1}{V} \int_V (\rho(r) - \rho_0) e^{iq.r} \qquad \text{(B.7)}$$

where $\rho(r)$ is the variable SLD in the object and ρ_0 is the SLD of the solvent. Thus, for a homogeneous particles of unifrom SLD ρ_p immersed in a solvent ρ_0 we just have an extra term in the front $(\rho_p - \rho_0)^2$ in Eqn. B.6.

Consider now a core-shell discoidal object of length 2L, radius R and shell thickness t (Note: the notation here is different from that used in the text). The SLD for this model is given below and will be referred to as **CSCPr** Model for elsewhere.

$$\rho(r) = \begin{cases} \rho_c & \text{for } 0 \leq r \leq R; \; -L \leq z \leq L \\ \rho_s & \text{for } R \leq r \leq R+t; \; -(L+t) \leq z \leq -L \text{and } L \leq z \leq L+t \end{cases}$$

Taking the above SLD's into account, integration over the volume, Eqn.B-7 be-
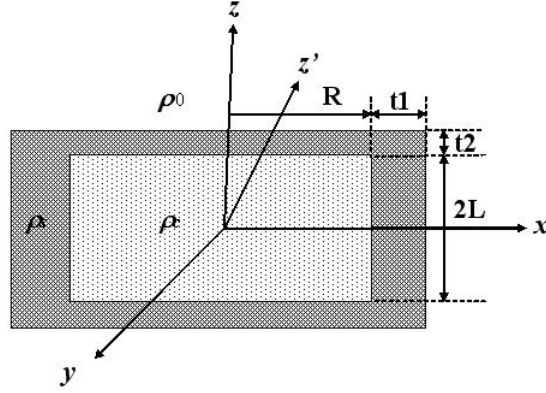
Figure B.2: Orientation of coordinates in core-shell cylindrical/disk-like (CSCPr Model) object with respect to Q.

comes

$$
\begin{aligned}
A(Q) &= \frac{2\pi}{V} \int_0^{R+t} \int_{-(L+t)}^{L+t} (\rho(r) - \rho_0) J_0(iQr\sin\theta) e^{iQz\cos\theta} r\, dr\, dz \\
&= \frac{2\pi}{V} \left((\rho_c - \rho_0) \int_0^R \int_{-L}^L I + (\rho_s - \rho_0) \int_0^R (\int_{-(L+t)}^{-L} + \int_L^{L+t}) I \right. \\
&\quad + \left. (\rho_s - \rho_0) \int_R^{R+t} \int_{-(L+t)}^{L+t} I \right)
\end{aligned}
$$

where the integrand I stands for $J_0(QR\sin\theta) e^{iQz\cos\theta} r\, dr\, dz$.

The first integral is seen to be the result derived in Eqn. (6) for a homogeneous particle of SLD ρ_c, while for the 2nd term, the integral in z results in

$$
\begin{aligned}
(\int_{-(L+t)}^{-L} + \int_L^{L+t}) e^{(iQz\cos\theta)}\, dz &= \frac{1}{iq\cos\theta} \left(e^{-iqL\cos\theta} - e^{-iq(L+t)\cos\theta} + e^{iq(L+t)\cos\theta} - e^{iqL\cos\theta} \right) \\
&= \frac{2\sin(Q(L+t)\cos\theta)}{Q\cos\theta} - \frac{2\sin(qL\cos\theta)}{Q\cos\theta}
\end{aligned}
$$

220

Thus A(Q) can be written as

$$
\begin{aligned}
A(Q) \;=\; &\frac{2\pi}{V}\left[(\rho_c-\rho_0)\frac{RJ_1(QR\sin\theta)}{Q\sin\theta}\frac{2\sin(Q\cos\theta)}{Q\cos\theta}\right.\\
&+(\rho_s-\rho_0)\left(\frac{(R+t)J_1(Q(R+t)\sin\theta)}{Q\sin\theta}-\frac{RJ_1(QR\sin\theta)}{Q\sin\theta}\right)\frac{2\sin(Q(L+t)\cos\theta)}{Q\cos\theta}\\
&\left.+\,(\rho_s-\rho_0)\frac{RJ_1(QR\sin\theta)}{Q\sin\theta}\left(\frac{2\sin(Q(L+t)\cos\theta)}{Q\cos\theta}-\frac{2\sin(qL\cos\theta)}{Q\cos\theta}\right)\right]
\end{aligned}
$$

which simplifies to give

$$
\begin{aligned}
=\;&\frac{2\pi}{V}\left[(\rho_c-\rho_s)\frac{RJ_1(QR\sin\theta)}{Q\sin\theta}\frac{2\sin(qL\cos\theta)}{Q\cos\theta}\right.\\
&\left.+\,(\rho_s-\rho_0)\frac{(R+t)J_1(Q(R+t)\sin\theta)}{Q\sin\theta}\frac{2\sin(Q(L+t)\cos\theta)}{Q\cos\theta}\right]
\end{aligned}
$$

Then by introducing the inner/outer (core/core+shell) volumes as $V_{in}=\pi R^2 2L$ and $V_o=\pi(R+t)^2 2(L+t)$ in the above result, we get

$$
\begin{aligned}
A_{cshl}(Q) \;=\; &\frac{1}{V_o}\left[(\rho_c-\rho_s)V_{in}\frac{J_1(QR\sin\theta)}{QR\sin\theta}\frac{2\sin(qL\cos\theta)}{qL\cos\theta}\right.\\
&\left.+\,(\rho_s-\rho_0)V_o\frac{J_1(Q(R+t)\sin\theta)}{Q(R+t)\sin\theta}\frac{2\sin(Q(L+t)\cos\theta)}{Q(L+t)\cos\theta}\right]
\end{aligned}
\tag{B.8}
$$

So that the form factor for this core-shell cylinder is

$$
P_{cshl}(Q)=<|A_{cshl}(Q)|^2>=\int\left\langle|A(Q)|^2\right\rangle\sin\theta\,d\theta
\tag{B.9}
$$

The way these integrals are calculated by seperation of variables, we can see that the above result can be easily generalised to core-shell cylinder with different thicknesses on the rim and head. So that, if instead of a uniform thickness t, and outer dimensions $R+t$ and $2(L+t)$, we now have $R+t1$ and $2(L+t2)$ as the outer dimensions, then A_{cshl} will be given by

$$
\begin{aligned}
A_{cshl}(Q) \;=\; &\frac{1}{V_o}\left[(\rho_c-\rho_s)V_{in}\frac{J_1(QR\sin\theta)}{QR\sin\theta}\frac{2\sin(qL\cos\theta)}{qL\cos\theta}\right.\\
&\left.+\,(\rho_s-\rho_0)V_o\frac{J_1(Q(R+t1)\sin\theta)}{Q(R+t1)\sin\theta}\frac{2\sin(Q(L+t2)\cos\theta)}{Q(L+t2)\cos\theta}\right]
\end{aligned}
\tag{B.10}
$$

B.3 Inhomogeneous Core-shell disks

Now we consider core-shell cylinders with different SLD's in the rim and caps. Let us first consider the following variation, referred to as **PCSm1 Model**

$$
\rho(r) = \begin{cases} \rho_c & \text{for } 0 \leq r \leq R \ ; \ -L \leq z \leq L \\ \rho_h & \text{for } 0 \leq r \leq R + t1; -(L + t2) \leq z \leq -L \text{ and } L \leq z \leq (L + t2) \\ \rho_r & \text{for } R \leq r \leq R + t1; -L \leq z \leq L \end{cases}
$$

Figure B.3: Orientation of coordinates in the core-shell cylindrical/disc (PCSm1 Model) with respect to Q.

where ρ_c, ρ_r and ρ_h stand for the SLD's of the core, rim and the head respectively.

The integrals can now be written as

$$
\begin{aligned}
A(Q) &= \frac{2\pi}{V}\int_0^{R+t1}\int_{-(L+t2)}^{L+t2}(\rho(r)-\rho_0)J_0(QR\sin\theta)e^{iQz\cos\theta}r\,dr\,dz \\
&= \frac{2\pi}{V}\left((\rho_c-\rho_0)\int_0^{R}\int_{-L}^{L}I + (\rho_h-\rho_0)\int_0^{R+t1}(\int_{-(L+t2)}^{-L}+\int_L^{L+t2}I) + (\rho_r-\rho_0)\int_R^{R+t1}\int_{-L}^{L}I\right) \\
&= \frac{2\pi}{V}\left[(\rho_c-\rho_0)R\frac{J_1(QR\sin\theta)}{Q\sin\theta}\frac{2\sin(qL\cos\theta)}{Q\cos\theta}\right. \\
&+\ (\rho_r-\rho_0)\left(\frac{(R+t1)J_1(Q(R+t1)\sin\theta)}{Q\sin\theta}-\frac{RJ_1(QR\sin\theta)}{Q\sin\theta}\right)\frac{2\sin(qL\cos\theta)}{Q\cos\theta} \\
&+\ \left.(\rho_h-\rho_0)\frac{(R+t1)J_1(Q(R+t1)\sin\theta)}{Q\sin\theta}\left(\frac{2\sin(Q(L+t2)\cos\theta)}{Q\cos\theta}-\frac{2\sin(qL\cos\theta)}{Q\cos\theta}\right)\right]
\end{aligned}
$$

This can be simplified to give the form factor. In the above equation, V stands for the volume of the whole object, which is $\pi(R+t1)^2 2(L+t2)$. Again introducing the inner, outer and 'included' volumes as $V_{in}=\pi R^2 2L$, $V_o=\pi(R+t1)^2 2(L+t2)$ and $V_{ic}=\pi(R+t1)^2 2L$, we get

$$
\begin{aligned}
A(Q) &= \frac{1}{V_o}\left[(\rho_c-\rho_r)V_{in}\frac{J_1(QR\sin\theta)}{QR\sin\theta}\frac{2\sin(qL\cos\theta)}{qL\cos\theta}\right. \\
&+(\rho_r-\rho_h)V_{ic}\frac{J_1(Q(R+t1)\sin\theta)}{Q(R+t1)\sin\theta}\frac{2\sin(qL\cos\theta)}{qL\cos\theta} \\
&+\left.(\rho_h-\rho_0)V_o\frac{J_1(Q(R+t1)\sin\theta)}{Q(R+t1)\sin\theta}\frac{2\sin(Q(L+t2)\cos\theta)}{Q(L+t2)\cos\theta}\right] \quad\text{(B.11)}
\end{aligned}
$$

When $\rho_r=\rho_h$ we can easily see that we recover eqn. (12).

Similarly for the alternate variation of SLD where $\rho(r)$ is given as (referred to as **PCSm2 Model**)

$$
\rho(r)=\begin{cases}
\rho_c & \text{for } 0\leq r\leq R;\ -L\leq z\leq L \\
\rho_h & \text{for } 0\leq r\leq R;\ -(L+t2)\leq z\leq -L\text{and } L\leq z\leq (L+t2) \\
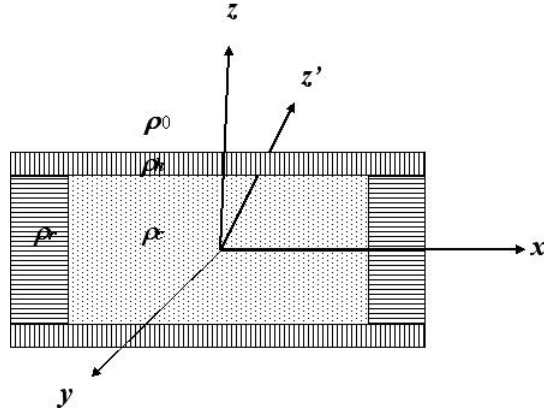\rho_r & \text{for } R\leq r\leq R+t1;\ -(L+t2)\leq z\leq (L+t2)
\end{cases}
$$

Figure B.4: Orientation of coordinates in the core-shell cylindrical/dis (PCSm2 Model) with respect to Q.

In this case, $A(Q)$ can be obtained by breaking the integrals as

$$
\begin{aligned}
A(Q) &= \frac{2\pi}{V} \int_0^{R+t1} \int_{-(L+t2)}^{L+t2} (\rho(r) - \rho_0) J_0(QR\sin\theta) e^{iQz\cos\theta} r \, dr \, dz \\
&= \frac{2\pi}{V} \left((\rho_c - \rho_0) \int_0^R \int_{-L}^{L} + (\rho_h - \rho_0) \int_0^R (\int_{-(L+t2)}^{-L} + \int_L^{L+t2}) + (\rho_r - \rho_0) \int_R^{R+t1} \int_{-(L+t2)}^{L+t2} \right) I \\
&= \frac{2\pi}{V} \left[(\rho_c - \rho_0) R \frac{J_1(QR\sin\theta)}{Q\sin\theta} \frac{2\sin(qL\cos\theta)}{Q\cos\theta} \right. \\
&\quad + (\rho_h - \rho_0) \frac{RJ_1(QR\sin\theta)}{Q\sin\theta} \left(\frac{2\sin(Q(L+t2)\cos\theta)}{Q\cos\theta} - \frac{2\sin(qL\cos\theta)}{Q\cos\theta} \right) \\
&\quad \left. + (\rho_r - \rho_0) \left(\frac{(R+t1)J_1(Q(R+t1)\sin\theta)}{Q\sin\theta} - \frac{RJ_1(QR\sin\theta)}{Q\sin\theta} \right) \frac{2\sin(Q(L+t2)\cos\theta)}{Q\cos\theta} \right]
\end{aligned}
$$

On simplification, by defining the volumes with $V_{ic} = \pi R^2(L+t2)$ and V_{in} and V_o as before

224

$$A(Q) = \frac{1}{V_o}\left[(\rho_c - \rho_h)V_{in}\frac{J_1(QR\sin\theta)}{QR\sin\theta}\frac{2\sin(qL\cos\theta)}{qL\cos\theta}\right.$$
$$+ (\rho_h - \rho_r)V_{ic}\frac{J_1(QR\sin\theta)}{QR\sin\theta}\frac{2\sin(Q(L+t2)\cos\theta)}{Q(L+t2)\cos\theta}$$
$$\left. + (\rho_r - \rho_0)V_o\frac{J_1(Q(R+t1)\sin\theta)}{Q(R+t1)\sin\theta}\frac{2\sin(Q(L+t2)\cos\theta)}{Q(L+t2)\cos\theta}\right] \tag{B.12}$$

Again, when $\rho_r = \rho_h$ we see that we recover eqn. (12).

Finally, consider the following variation of SLD (referred to as **PCSm3 Model**)

$$\rho(r) = \begin{cases} \rho_c & \text{for } 0 \le r \le R; \ -L \le z \le L \\ \rho_h & \text{for } 0 \le r \le R; \ -(L+t2) \le z \le -L \text{and } L \le z \le (L+t2) \\ \rho_r & \text{for } R \le r \le R+t1; \ -L \le z \le L \end{cases}$$
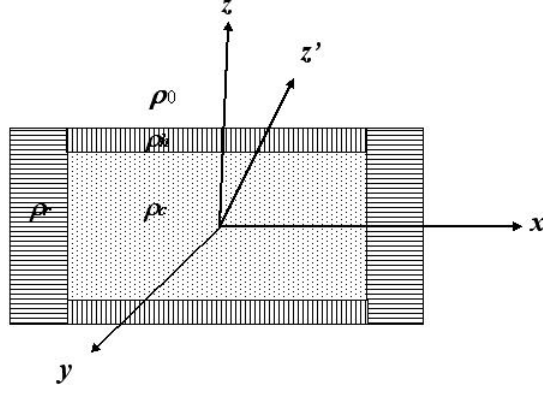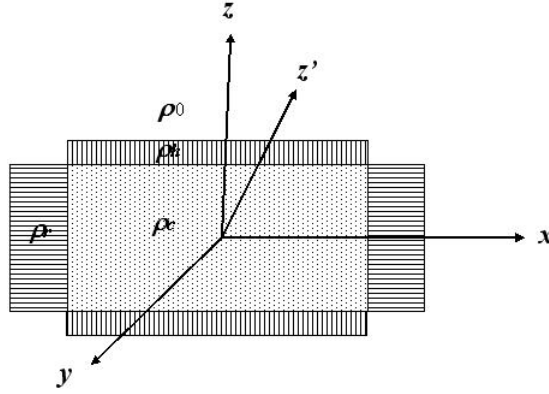

Figure B.5: Orientation of coordinates in the core-shell cylndrical/disc (PCSm3 Model) with respect to Q.

In this case, we can break up the integrals into

$$
\begin{aligned}
A(Q) &= \left((\rho_c - \rho_0) \int_0^R \int_{-L}^{L} + (\rho_h - \rho_0) \int_0^R (\int_{-(L+t2)}^{-L} + \int_{L}^{L+t2}) + (\rho_r - \rho_0) \int_R^{R+t1} \int_{-L}^{L} \right) I \\
&= \frac{2\pi}{V} \left[(\rho_c - \rho_0) R \frac{J_1(QR\sin\theta)}{Q\sin\theta} \frac{2\sin(qL\cos\theta)}{Q\cos\theta} \right. \\
&\quad + (\rho_h - \rho_0) \frac{RJ_1(QR\sin\theta)}{Q\sin\theta} \left(\frac{2\sin(Q(L+t2)\cos\theta)}{Q\cos\theta} - \frac{2\sin(qL\cos\theta)}{Q\cos\theta} \right) \\
&\quad \left. + (\rho_r - \rho_0) \left(\frac{(R+t1)J_1(Q(R+t1)\sin\theta)}{Q\sin\theta} - \frac{RJ_1(QR\sin\theta)}{Q\sin\theta} \right) \frac{2\sin(qL\cos\theta)}{Q\cos\theta} \right]
\end{aligned}
$$

By denoting $V_1 = \pi R^2 (L + t2)$ and $V_2 = \pi(R + t1)^2 L$ and on simplification, the above expression gives the following relation for A(Q)-

$$
\begin{aligned}
A(Q) &= \frac{1}{V_o} \left[(\rho_c - \rho_h - \rho_r + \rho_o) V_{in} \frac{J_1(QR\sin\theta)}{QR\sin\theta} \frac{2\sin(qL\cos\theta)}{qL\cos\theta} \right. \\
&\quad + (\rho_h - \rho_o) V_1 \frac{J_1(QR\sin\theta)}{QR\sin\theta} \frac{2\sin(Q(L+t2)\cos\theta)}{Q(L+t2)\cos\theta} \\
&\quad \left. + (\rho_r - \rho_0) V_2 \frac{J_1(Q(R+t1)\sin\theta)}{Q(R+t1)\sin\theta} \frac{2\sin(qL\cos\theta)}{qL\cos\theta} \right]
\end{aligned}
\qquad \text{(B.13)}
$$

Fig. B.6 compares formfactors from two of the models developed in this section to two of the available models on the NCNR webpage (at http://www.ncnr.nist.gov/programs/sans/). From this figure, it is clear that the corner effects in models PCSm2 and PCSm3 do not affect the form factor significantly in the regular contrast case (see chapter 5). While in the contrast enhanced case in Fig.B.7, CSCpr shows some difference at low Q as opposed to PCSm2 and PCSm3. The cypr model cannot capture the shell effect at all in this case.

226

Legend: ywave_cypr, ywave_CSCpr, ywave_PCSm2, ywave_PCSm3

Point	parameters_cypr	coef_cypr
0	scale	0.01
1	radius (A)	110
2	length (A)	30
3	polydispersity of Radius	0.1
4	SLD diff (A^-2)	6e-06
5	incoh. bkg (cm^-1)	0.006

Point	parameters_CSCpr	coef_CSCpr
0	scale	0.01
1	mean CORE radius (A)	100
2	radial polydispersity (sigma)	0.1
3	CORE length (A)	30
4	radial shell thickness (A)	10
5	face shell thickness (A)	0
6	SLD core (A^-2)	-4e-07
7	SLD shell (A^-2)	2e-06
8	SLD solvent (A^-2)	6.3e-06
9	incoh. bkg (cm^-1)	0.006

Point	parameters_PCSm2	coef_PCSm2	parameters_PCSm3	coef_PCSm3
0	scale	0.01	scale	0.01
1	mean CORE radius (A)	100	mean CORE radius (A)	100
2	radial polydispersity (sigma)	0.1	radial polydispersity (sigma)	0.1
3	CORE length (A)	30	CORE length (A)	30
4	radial shell thickness (A)	10	radial shell thickness (A)	10
5	face shell thickness (A)	0	face shell thickness (A)	0
6	SLD core (A^-2)	-4e-07	SLD core (A^-2)	-4e-07
7	SLD head (A^-2)	2e-06	SLD head (A^-2)	2e-06
8	SLD rim(A^-2)	2e-06	SLD rim(A^-2)	2e-06
9	SLD solvent (A^-2)	6.3e-06	SLD solvent (A^-2)	6.3e-06
0	incoh. bkg (cm^-1)	0.006	incoh. bkg (cm^-1)	0.006

Figure B.6: Model comparison 1 with regular contrast (see chapter 6): Form factors showing equality of the PCSm2 and PCSm3 models in this work to cypr and CSCpr models available in the SANS analysis package. Model with shell of uniform SLD and thickness (CSCpr) is equivalent to models with non uniform shell

Point	parameters_cypr	coef_cypr
0	scale	0.01
1	radius (A)	110
2	length (A)	40
3	polydispersity of Radius	0.1
4	SLD diff (A^-2)	1e-06
5	incoh. bkg (cm^-1)	0.06

Point	parameters_CSCpr	coef_CSCpr
0	scale	0.01
1	mean CORE radius (A)	100
2	radial polydispersity (sigma)	0.1
3	CORE length (A)	40
4	radial shell thickness (A)	10
5	face shell thickness (A)	0
6	SLD core (A^-2)	7.5e-06
7	SLD shell (A^-2)	3.5e-06
8	SLD solvent (A^-2)	6.3e-06
9	incoh. bkg (cm^-1)	0.06

Point	parameters_PCSm2	coef_PCSm2	parameters_PCSm3	coef_PCSm3
0	scale	0.01	scale	0.01
1	mean CORE radius (A)	100	mean CORE radius (A)	100
2	radial polydispersity (sigma)	0.1	radial polydispersity (sigma)	0.1
3	CORE length (A)	40	CORE length (A)	40
4	radial shell thickness (A)	10	radial shell thickness (A)	10
5	face shell thickness (A)	0	face shell thickness (A)	0
6	SLD core (A^-2)	7.5e-06	SLD core (A^-2)	7.5e-06
7	SLD head (A^-2)	5e-06	SLD head (A^-2)	5e-06
8	SLD rim (A^-2)	2e-06	SLD rim(A^-2)	2e-06
9	SLD solvent (A^-2)	6.3e-06	SLD solvent (A^-2)	6.3e-06
10	incoh. bkg (cm^-1)	0.06	incoh. bkg (cm^-1)	0.06

Figure B.7: Model comparison 2 in the contrast enhanced case: Non uniform shells with PCSm2 and PCSm3 models are not equivalent to the CSCpr model. While the cypr model cannot capture the difference at all.

B.4 Cylinder with Hemispherical rim
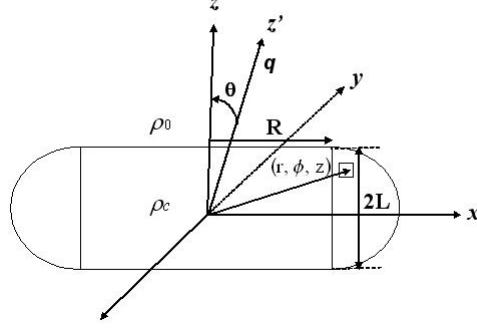
Now consider the case of a disk with hemispherical rim, unlike the vertical rims so far. Scattering from this object will essentially come from the regular disk in the center and the solid hemi-torus wrapping around the disk. As any point on the rim is specified by the following parametric equation

$$
\begin{aligned}
x &= (R + r\sin\alpha)\cos\phi \\
y &= (R + r\sin\alpha)\sin\phi \\
z &= r\cos\alpha
\end{aligned}
$$

where $0 \leq r \leq L$ $0 \leq \alpha \leq \pi$ and $0 \leq \phi \leq 2\pi$

and α is related to z and r as $\alpha = \cos^{-1}(z/r)$

Again, like for the simple cylinder considered before, for rotation by an angle θ, the z-coordinate for any point on the rim transforms as

$$
\begin{aligned}
z &= x'\sin\theta + z'\cos\theta \\
&= (R + r\sin\alpha)\cos\phi\sin\theta + r\cos\alpha\cos\theta \\
&= (R + r\sqrt{(1 - z^2/r^2)})\cos\phi\sin\theta + z\cos\theta
\end{aligned}
$$

229

Thus, the phase factor is: $iq \cdot r = iq \left[R + \sqrt{(1 - z^2/r^2)} \cos\phi \sin\theta + z \cos\theta \right]$ and

$$
\begin{aligned}
A(Q) &= \int_V e^{iq\left[R + \sqrt{(1-z^2/r^2)} \cos\phi \sin\theta + z \cos\theta \right]} r \, dr \, d\phi \, dz \\
&= \int_{-L}^{L} \int_0^L e^{iQz\cos\theta} 2\pi J_0[Q(R + \sqrt{(r^2 - z^2)}) \sin\theta] r \, dr \, dz \qquad \text{(B.14)}
\end{aligned}
$$

This equation is solved using Mathematica and leads to a nasty solution!

Appendix C

ParallelPiped FormFactor-Details

C.1 Homogeneous ParallelPiped FormFactor(FF)

Imagine a parallelpiped with edges $C > B > A$ aligned roughly with C(length) along z, B(width) along y and A(thickness) along x directions. Scattering vector Q vector is in some arbitrary direction at angle α from z-axis and β from y axis. Then it can be written in terms of unit vectors as

$$\vec{Q} = |Q|(\sin\beta\sin\alpha\hat{x} + \cos\beta\sin\alpha\hat{y} + \cos\alpha\hat{z}) \tag{C.1}$$

The phase factor $e^{i\vec{Q}\cdot\vec{r}}$ will be given as

$$i\vec{Q}\cdot\vec{r} = iQ(\sin\beta\sin\alpha x + \cos\beta\sin\alpha y + \cos\alpha z) \tag{C.2}$$

This gives the scattering term as

$$\int_V e^{i\vec{Q}\cdot\vec{r}} = \int_{-C/2}^{C/2}\int_{-B/2}^{B/2}\int_{-A/2}^{A/2} e^{iQ(\sin\beta\sin\alpha x + \cos\beta\sin\alpha y + \cos\alpha z)}\,dx\,dy\,dz \tag{C.3}$$

$$= I(A,B,C) \qquad \text{where} \tag{C.4}$$

$$I(A,B,C) = \frac{\sin(QA/2\sin\alpha\sin\beta)}{QA/2\sin\alpha\sin\beta}\frac{\sin(QB/2\sin\alpha\cos\beta)}{QB/2\sin\alpha\cos\beta}\frac{\sin(QC/2\cos\alpha)}{QC/2\cos\alpha} \times ABC \tag{C.5}$$

To obtain the Form factor of parallelpiped, two orientational averages have to be done over the angles α and β. Above term is written in terms of the reduced lengths given by

$$a \equiv \frac{A}{B}; \qquad b \equiv \frac{B}{B} = 1; \qquad c \equiv \frac{C}{B};$$

$$
\begin{aligned}
F_{(A,B,C)}(Q) \\
&= \int_0^{\pi/2} \int_0^{\pi/2} \left(I_{(A,B,C)}(Q)\right)^2 \sin\alpha \, d\alpha \, d\beta \\
&= \int_0^{\pi/2} \int_0^{\pi/2} \left(\frac{\sin(QA/2 \sin\alpha \sin\beta)}{QA/2 \sin\alpha \cos\beta} \frac{\sin(QB/2 \sin\alpha \cos\beta)}{QB/2 \sin\alpha \cos\beta}\right)^2 \left[\frac{\sin(QC/2 \cos\alpha)}{QC/2 \cos\alpha}\right]^2 \\
&\times \quad \sin\alpha \, d\alpha \, d\beta
\end{aligned}
\tag{C.6}
$$

This is written in terms of variables $\mu = QB$, $\cos\alpha = \sigma$ and $\beta = (\pi/2)u$ and the function $S(x) = \sin x/x$ as

$$F_{a,b,c}(Q) = \int_0^1 \int_0^1 \left\{S[\mu a/2 \sqrt{1-\sigma^2} \sin(\pi/2u)] S[\mu b/2 \sqrt{1-\sigma^2} \cos(\pi/2u)]\right\}^2 du \, [S(\mu c\sigma/2)]^2 \, d\sigma \tag{C.7}$$

Notes:

1. The integrals need to be done only from $(0,\pi/2)$ due to rectangular symmetry (check if factor of 2 off or not for inner integral..unlike cylinder FF, where integral over $d\phi \equiv \beta = 2\pi$, we DO NOT have the cylindrical symmetry here, and need a double integral over $d\beta$).

To obtain the FF on an absolute scale, the above equation is multiplied by

$$(\pi/2) \times (Scale/Volume) \times (\delta\rho)^2 10^8$$

where $\delta\rho = \rho_p - \rho_0$ is the contrast term between the parallelpiped and solvent of SLDs ρ_p and ρ_0 respectively.

2. Eqn.(3) is equivalent to the expression given in SANS Analysis package when the integrals are written in terms of $\sigma \equiv \cos\alpha$; $\mu = QB$ and u

3. The factor $(\pi/2)$ factor is needed to get correct limits of the PP formfactor with that of sherical/ellipsoidal shapes.

C.2 CoreShell-ParallelPiped FF
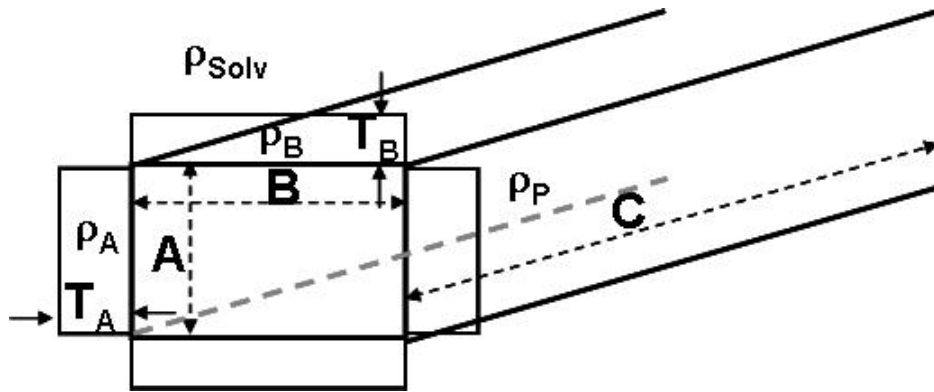
Figure C.1: A schematic of the coreshell PPiped model, showing the rims on sides A and B of thickness T_A and T_B respectively.

For a core-shell structure Parallelpiped, of edge lengths $(A+2T_A, B+2T_B, C+2T_C)$ (the rims of lengths T_A, T_B and T_C extend out on each face), and of SLDs (ρ_a, ρ_b, ρ_c) and ρ_p in the core, the phase factor becomes

$$\int_V e^{i\vec{Q}\cdot\vec{r}} = \int_{-(C/2+T_C)}^{C/2+T_C} \int_{-(B/2+T_B)}^{B/2+T_B} \int_{-(A/2+T_A)}^{A/2+T_A} e^{iQ\cdot r}\, dx\, dy\, dz$$

$$= I(A,B,C)$$

$$+ \left(\int_{-(A/2+T_A)}^{-A/2} + \int_{A/2}^{(A/2+T_A)} \right) \int_{-B/2}^{B} \int_{-C/2}^{C}$$

$$+ \int_{-A/2}^{A/2} \left(\int_{-(B/2+T_B)}^{-B/2} + \int_{(B/2)}^{B/2+T_B} \right) \int_{-C/2}^{C}$$

$$+ \int_{-A/2}^{A/2} \int_{-B/2}^{B/2} \left(\int_{-(C/2+T_C)}^{-C/2} + \int_{(C/2)}^{C/2+T_C} \right)$$

For each edge, this gives an extra term besides the core term as

$$I(A + 2T_A, B, C) =$$

$$\left(\frac{\sin(Q(A+2T_A)/2 \sin\alpha \sin\beta)}{Q(A+2T_A)/2 \sin\alpha \sin\beta} - \frac{\sin(QA/2 \sin\alpha \sin\beta)}{QA/2 \sin\alpha \sin\beta} \right) \frac{\sin(QB/2 \sin\alpha \cos\beta)}{QB/2 \sin\alpha \cos\beta} \frac{\sin(QC/2 \cos\alpha)}{QC/2 \cos\alpha}$$
$$\times (\rho_a - \rho_0)(V1 \equiv 2T_A BC)$$

$$I(A, B + 2T_B, C) =$$

$$\frac{\sin(QA/2 \sin\alpha \sin\beta)}{QA/2 \sin\alpha \sin\beta} \left(\frac{\sin(Q(B+2T_B)/2 \sin\alpha \cos\beta)}{Q(B+2T_B) \sin\alpha \cos\beta} - \frac{\sin(QB/2 \sin\alpha \cos\beta)}{QB/2 \sin\alpha \cos\beta} \right) \frac{\sin(QC/2 \cos\alpha)}{QC/2 \cos\alpha}$$
$$\times (\rho_b - \rho_0)(V2 \equiv A2T_B C)$$

$I(A, B, C + 2T_C)$ is similarly

$$\frac{\sin(QA/2 \sin\alpha \sin\beta)}{QA/2 \sin\alpha \sin\beta} \frac{\sin(QB/2 \sin\alpha \cos\beta)}{QB/2 \sin\alpha \cos\beta} \left(\frac{\sin(Q(C+2T_C)/2 \cos\alpha)}{Q(C+2T_C)/2 \cos\alpha} - \frac{\sin(QC/2 \cos\alpha)}{QC/2 \cos\alpha} \right)$$
$$\times (\rho_c - \rho_0)(V3 \equiv AB2T_C)$$

which can be written in terms of reduced lengths

$$a + t_a \equiv \frac{A + 2T_A}{B};$$
$$b + t_b \equiv \frac{B + 2T_B}{B};$$
$$c + t_c \equiv \frac{C + 2T_B}{B}$$

This gives the form factor as the sum of inner core term plus extra terms for each edge with the correct SLD term variation and volumes as

$$
\begin{aligned}
F_{(a+t_a,b+t_b,c+t_c)}(Q) \;=\; & \frac{1}{V_{ot}} \int_0^{\pi/2} \int_0^{\pi/2} \{ (\rho_p - \rho_0) I(a,b,c) ABC \\
& + \; (\rho_a - \rho_0)[I(a+t_a,b,c) - I(a,b,c)] 2T_A BC \\
& + \; (\rho_b - \rho_0)[I(a,b+t_b,c) - I(a,b,c)] A 2T_B C \\
& + \; (\rho_c - \rho_0)[I(a,b,c+t_c) - I(a,b,c)] AB 2T_C \}^2 \sin\alpha \, d\alpha \, d\beta
\end{aligned}
$$

(C.8)

where V_{ot} is the total volume of the parallelpiped, and is equal to

$$V_{ot} = ABC + 2T_A BC + A 2T_B C + AB 2T_C$$

The CshlPP formfactor is written in Igor to go with the SANS Analysis Package.
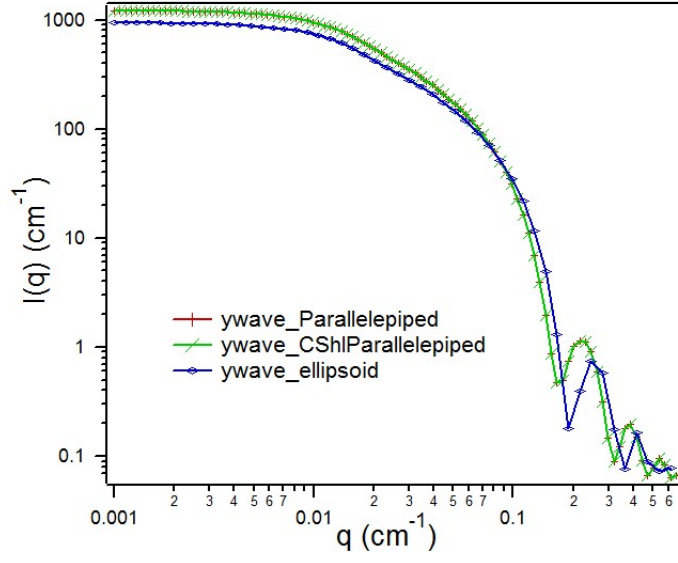
(a)
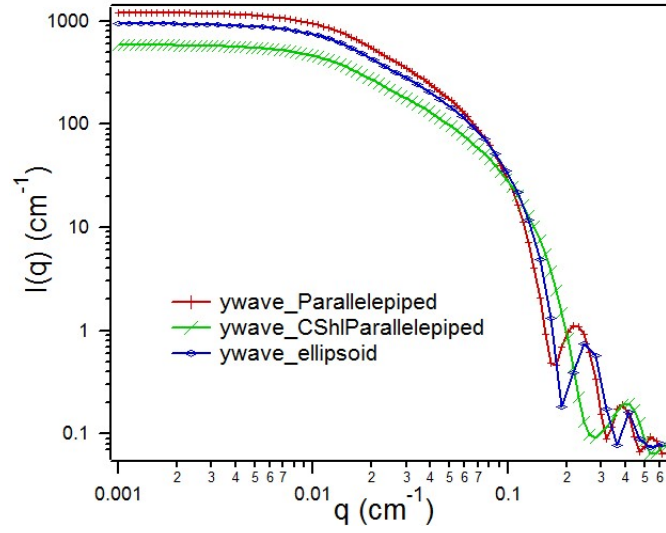
(b)

Figure C.2: (a)The coreshellPPiped model compared with the regular PP and a cylinder with ellispoidal cross-section. Rims of core-shellPPiped model have been made equal to zero. Dimensions of PP edges A, B and C are 40, 40 and 300Årespectively, chosen to compare with cylinder of radius 20Åand length 300Å. (b) Effect of rims: In core-shellPPiped model, rims A and B are 5Åeach and edges A and B are 35Åeach.

Bibliography

[1] J.S. Pedersen. Analysis of small-angle scattering data from colloids and polymer solutions: modeling and least-squares fitting. *Advances in Colloid and Interface Science*, 70:171–210, 1997.

[2] H. Lodish, A. Berk, P. Matsudaira, P. Kaiser, M. Krieger, M. Scott, S.L Zipursky, and J. Darnell. *Molecular Cell Biology, 5e.* John Wiley and Sons: New York, 2004.

[3] Nature Insight: Membrane Biology. Editorial and other contributed articles. *Nature*, 438(7068):577–621, 2005.

[4] P.L Felgner. *Scientific American*, 276:102–106, 1997.

[5] W Helfrich. Elastic properties of lipid bilayers: Theory and possible experiments. *Z. Naturoforch.*, 28c:510–515, 1973.

[6] S.J Singer and G.L. Nicolson. The fluid mosaic model of the structure of cell membranes. *Science*, 175:720–731, 1972.

[7] R. Lipowsky. The conformation of membranes. *Nature*, 349:475–481, 1991.

[8] D. Marsh. Elastic curvature constants of lipid monolyers. *Chemistry and Physics of Lipids*, 144:146–159, 2006.

[9] R. Lipowsky and E. Sackmann. *Structure and Dynamics of Membranes.* Elsevier: Amsterdam, 1995.

[10] R. Parthasarathy and J.T. Groves. Curvature and spatial organization in biological membranes. *Soft Matter*, 3(1):24–33, 2007.

[11] J. F. Nagle and S. Tristram-Nagle. Structure of lipid bilayers. *Biochimica Et Biophysica Acta-Biomembranes*, 1469:159–195, 2000.

[12] J. F. Nagle and S. Tristram-Nagle. Lipid bilayer structure. *Current Opinions in Structural Biology*, 10:474–480, 2000.

[13] S. A. Safran and F.C. MacKintosh. Phase separation and curvature of bilayer membranes. *Physical Review E*, 47, 1993.

[14] F. M. Menger, , and J.S Keiper. Chemistry and physics of giant vesicles as biomembrane models. *Curr. Opin. Chem. Biol.*, 2:726–732, 1998.

[15] W. M. Gelbart and A. Ben-Shaul. The "new" science of "complex fluids. *Journal of physical chemistry*, 100:13169–13189, 1996.

[16] S.H. White. The progress of membrane protein structure determination, 2004. http://blanco.biomol.uci.edu/Membrane Proteins xtal.html.

[17] C. Ostermeier and H. Michel. Crytsallization of memrane proteins. *Current Opinion in Structural Biology*, 7:697–701, 1997.

[18] A. Arora and L.K. Tamm. Biophysical approaches to membrane protein structure determination. *Current Opinion in Structural Biology*, 11:540–547, 2001.

[19] N. Tjandra and A. Bax. Direct measurement of distances and angles in biomolecules by nmr in a dilute liquid crystalline medium. *Science*, 278(5340):1111–1114, 1997.

[20] I. Marcotte and M. Auger. Bicelles as model membranes for solid- and solution-state nmr studies of membrane peptides and proteins. *Concepts in Magnetic Resonance Part A*, 24A(1):17–37, 2005.

[21] P. Nollert, J. Navarro, and E.M. Landau. Crystallization of membrane proteins in cubo. *Methods Enzymol*, 343, 2002.

[22] J. Katsaras, T. A. Harroun, J. Pencer, and M. P. Nieh. 'bicellar' lipid mixtures as used in biochemical and biophysical studies. *Naturwissenschaften*, 92(8):355–366, 2005.

[23] S. Faham and J. Bowie. Bicelle crystallization: A new method for crystallizing membrane proteins yields a monomeric bacteriorhodopsin structure. *J Mol Biol*, 316:1–6, 2002.

[24] S. Faham, G. L. Boulting, E. A. Massey, S. Yohannan, D. Yang, and J. U. Bowie. Crystallization of bacteriorhodopsin from bicelle formulations at room temperature. *Protein Science*, 14(3):836–840, 2005.

[25] J. N. Israelachvili, D.J Mitchell, , and B.W. Ninham. *J. Chem. Soc. Faraday Trans. II*, 72:1525–1568, 1976.

[26] J. N. Israelachvili, S. Marcelja, and R. Horn. Physical prnciples of membrane organization. *Q Rev Biophys*, 13:121–200, 1980.

[27] J. Israelachvilli. *Intermolecular and Surface forces*. Academic Press, 1992.

[28] C. Tanford. *The Hydrophobic Effect: Formation of Micelles and Biological membranes*. John Wiley and Sons: New York, 1980.

[29] S.A. Safran. *Statistical Thermodynamics of Surfaces, Interfaces, and Membranes*. Westview Press: Boulder, CO, 2003.

[30] S.W Hyde, S. Andersson, K. Larsson, Z. Blum, T. Landh, S. Lidin, and B. Ninham. *The Language of Shape.* Elsevier Science: Amsterdam, 1997.

[31] S. Puvvada and D. Blankschtein. Thermodynamic description of micellization, phase behavior, and phase separation of aqueous solutions of surfactant mixtures. *J. Phys. Chem.*, 96:5567, 1992.

[32] A. Shiloach and D. Blankschtein. Prediction of critical micelle concentrations and synergism of binary surfactant mixtures containing zwitterionic surfactants. *Langmuir*, 13:3968–3981, 1997.

[33] R. Nagarajan and E. Ruckenstein. Theory of surfactant self-assembly: a predictive molecular thermodynamic approach. *Langmuir*, 7:2934–2969, 1981.

[34] D.M Small and B.M Craven. *The physical chemistry of lipids: from alkanes to phospholipids.* Plenum Press: Newyork, 1988.

[35] G. Cevc and D. Marsh. *Phospholipid Bilayers: Physical Principles and Models.* Wiley New York, 1987.

[36] T-L. Lin, S.-H Chen, Gabriel N.E, and Roberts M.F. Use of small-angle neutron scattering to determine the structure and interaction of dihexanoylphosphatidylcholine micelles. *J Am Chem Soc*, 108:3499–3501, 1986.

[37] T.-L. Lin, S.-H Chen, N.E Gabriel, and M.F Roberts. Small angle neutron scattering technique applied to the study of polydisperse rodlike diheptanoylphosphatidylcholine micelles. *J Phys Chem*, 91:406–413, 1991.

[38] S. Tristram-Nagle, Y. Liu, J. Legleiter, and J.F Nagle. Structure of gel phase dmpc determined by x-ray diffraction. *Biophysical Journal*, 83:3324–3335, 2002.

[39] N. Kucerka, Y. Liu, N. Chu, H. I. Petrache, S. Tristram-Nagle, and John F. Nagle. Structure of fully hydrated fluid phase dmpc and dlpc lipid bilayers using x-ray scattering from oriented multilamellar arrays and from unilamellar vesicles. *Biophysical Journal*, 88:2626–2637, 2005.

[40] J. F. Nagle, R. Zhang, S. Tristram-Nagle, W. Sun, H. Petrache, and R. M. Suter. X-ray structure determination of fully hydrated l_{alpha} phase dipalmitoylphosphatidylcholine bilayers. *Biophys. J.*, 70:1419–1431, 1996.

[41] W. J. Sun, S. Tristram-Nagle, R. M. Suter, and J. F. Nagle. Structure of gel phase saturated lecithin bilayers: Temperature and chain length dependence. *Biophysical Journal*, 71(2):885–891, 1996.

[42] M. le Maire, P. Champeil, and J. V. Moller. Interaction of membrane proteins and lipids with solubilizing detergents. *Biochim. Biophys. Acta*, 1508:86–111, 2000.

[43] J. Lipfert, L. Columbus, V.B. Chu, S.A. Lesley, and S. Doniach. Size and shape of detergent micelles determined by small-angle x-ray scattering. *J. Phys. Chem. B*, 111:312427 – 12438,, 2007.

[44] H.H. Paradies. Shape and size of a nonionic surfactant micelle. triton x-100 in aqueous solution. *The Journal of Physical Chemistry*, 84:599–607, 1980.

[45] A. Tardieu, V. Luzzati, and F.C. Reman. Structure and polymorphism of the hydrocarbon chains of lipids: A study of lecithin-water phases. *Journal of Molecular Biology*, 75:711–718, 1973.

[46] M.J Janiak, D.M Small, and G.G Shipley. Nature of the thermal pretransition of synthetic phospholipids: dimyristoyl-and dipalmitoyllecithin. *Biochemistry*, 15:4575, 1976.

[47] Ruthven N. A. H. Lewis, Nanette Mak, and Ronald N. McElhaney. A differential scanning calorimetric study of the thermotropic phase behavior of model membranes composed of phosphatidylcholines containing linear saturated fatty acyl chains. *Biochemistry*, 26(19):6118–6126, 1987. Journal.

[48] G. S. Smith, E. B. Sirota, C. R. Safinya, and N. A. Clark. Structure of the l_β phases in a hydrated phosphatidylcholine multimembrane. *Phys. Rev. Lett.*, 60:813–816, 1988.

[49] C. R. Safinya, E. B. Sirota, D. Roux, and G. S. Smith. Universality in interacting membranes: The effect of cosurfactants on the interfacial rigidity. *Phys. Rev. Lett.*, 62(10):1134–1137, 1989.

[50] V. A. Raghunathan and J. Katsaras. Structure of the $l_{c'}$ phase in a hydrated lipid multilamellar system. *Phys. Rev. Lett.*, 74(22):4456–4459, 1995.

[51] K. Sengupta, V. A. Raghunathan, and J. Katsaras. Structure of the ripple phase of phospholipid multibilayers. *Phys. Rev. E*, 68(3):031710, 2003.

[52] G. Pabst, H. Amenitsch, D. P. Kharakoz, P. Laggner, and M. Rappolt. Structure and fluctuations of phosphatidylcholines in the vicinity of the main phase transition. *Phys. Rev. E*, 70(2):021908, 2004.

[53] J.F Nagle. Theory of biomembrane phase transitions. *J. Chem. Phys.*, 58:252, 1973.

[54] H. Ebel, P. Grabitz, and T. Heimburg. Enthalpy and volume changes in lipid membranes.i. the proportionality of heat and volume changes in the lipid melting transition and its implication for the elastic constants. *Journal of Physical Chemistry B*, 105(30):7353–7360, 2001.

[55] J.F Nagle. Lipid bilayer phase transition: Dilatometry and theory. *Proc.Natl. Acad. Sci.*, 70:3443, 1973.

[56] J. F. Nagle and D. A. Wilkinson. Lecithin bilayers: Density measurements and molecular interactions. *Biophys. J.*, 23:159, 1978.

[57] M. C. Wiener, S. Tristram-Nagle, D. A. Wilkinson, L. E. Campbell, and J. F. Nagle. Specific volumes of lipids in fully hydrated bilayer dispersions. *Biochim. Biophys. Acta*, 938:135–142, 1988.

[58] Thomas Heimburg. Mechanical aspects of membrane thermodynamics: Estimation of the mechanical properties of lipid membranes close to the chain melting transition from calorimetry. *Biochimica et Biophysica Acta (BBA) - Biomembranes*, 1415:147–162, 1998.

[59] E. Evans and W. Rawicz. Entropy-driven tension and bending elasticity in condensed-fluid membranes. *Phys. Rev. Lett.*, 64:2094–2097, 1990.

[60] R. Dimova, B. Pouligny, and C. Dietrich. Pretransitional effects in dimyristoylphosphatidylcholine vesicle membranes: optical dynamometry study. *Biophys. J.*, 79:340–356, 2000.

[61] Chau-Hwang Lee, Wan-Chen Lin, and Jyhpyng Wang. All-optical measurements of the bending rigidity of lipid-vesicle membranes across structural phase transitions. *Phys. Rev. E*, 64:020901, 2001.

[62] S.A. Safran, P.A Pincus, D.A. Andelman, and F.C. MacKintosh. Stability and phase behavior of mixed surfactant vesicles. *Physical Review A*, 43, 1991.

[63] Julia S. Higgins and Henry C. Benoit. *Polymers and Neutron Scattering.* Oxford University Press, UK, 1997.

[64] N.J Chang and E.W Kaler. The structure of sodium dodecyl sulfate micelles in solutions of water and deuterium oxide. *The Journal of Physical Chemistry*, 89:2997, 1985.

[65] H. Matsuki, H. Okuno, F. Sakano, M. Kusube, and S. Kaneshina. Effect of deuterium oxide on the thermodynamic quantities associated with phase transitions of phosphatidylcholine bilayer membranes. *Biochimica Et Biophysica Acta-Biomembranes*, 1712(1):92–100, 2005.

[66] W. Knoll, J. Haas, H. B. Stuhrmann, H.-H. Fúldner, H. Vogel, and E. Sackmann. Small-angle neutron scattering of aqueous dispersions of lipids and lipid mixtures. a contrast variation study. *Journal of Applied Crystallography*, 14:191–202, 1981.

[67] Hiromi Nagano, Tadashi Nakanishi, Haruhiko Yao, and Kenji Ema. Effect of vesicle size on the heat capacity anomaly at the gel to liquid-crystalline phase transition in unilamellar vesicles of dimyristoylphosphatidylcholine. *Phys. Rev. E*, 52(4):4244–4250, Oct 1995.

[68] K. Uchida, H. Yao, and K. Ema. Effect of chain length on the heat-capacity anomaly at the gel to liquid-crystalline phase transition in unilamellar vesicles of phosphatidylcholines. *Physical Review E*, 56(1):661–666, 1997. Jul Effect of chain length on the heat-capacity anomaly at the gel to liquid-crystalline phase transition in unilamellar vesicles of phosphatidylcholines ISI:A1997XM37700019 Part B.

[69] P. Brocca, L. Cantu, M. Corti, E. Del Favero, S. Motta, and M.C. Nodari. Curved single-bilayers in the region of the anomalous swelling: Effect of curvature and chain

length. *Colloids and Surfaces A: Physicochemical and Engineering Aspects*, 291:63–68, 2006.

[70] R.J.M. Tausk, J.van Esch, J. Karmiggelt, G. Voordouw, and J.T. Overbeek. Physical chemical studies of short-chain lecithin homlogues. i. influence of the chain length of the fatty acid ester and of the electrolytes on the critical micelle concentration. *Biophysical Chemistry*, 1:175–183, 1974.

[71] R.J.M. Tausk, J.Van Esch, J. Karmiggelt, and J.T. Voordouw, Overbeek. Physical chemical studies of short-chain lecithin homlogues ii: Micellar weights of dihexanoyl- and diheptanouyl lecithin. *Biophysical Chemistry*, 1:184–203, 1974.

[72] R.J.M. Tausk, C. Oudshoorn, and J.T. Overbeek. Physical chemical studies of short-chain lecithin homlogues iii: Phase seperation and light scattering studies on aqueous dioctanoyllecithin solutions. *Biophysical Chemistry*, 1:184–203, 1974.

[73] Jorg H. Kleinschmidt and Lukas K. Tamm. Structural transitions in short-chain lipid assemblies studied by 31p-nmr spectroscopy. *Biophys. J.*, 83:994–1003, 2002.

[74] L. van Dam, G. Karlsson, and K. Edwards. Direct observation and characterization of dmpc/dhpc aggregates under conditions relevant for biological solution nmr. *Biochimica Et Biophysica Acta-Biomembranes*, 1664(2):241–256, 2004.

[75] N. Funasaki, R. Ueshiba, S. Hada, and S. Neya. Chromatographic study on stepwise aggregation patterns of zwitterionic derivatives of cholic acid -. *J. Chem. Soc. Faraday Trans.,*, 89:4355 – 4362, 1993.

[76] N. Funasaki, M. Fukuba, T. Hattori, S. andd T Ishikawa, and S. Neya. Micelle formation of bile salts and zwitterionic derivative as studied by two-dimensional nmr spectroscop. *Chemistry and Physics of Lipids*, 142:43–57, 2006.

[77] F. Jr. Szoka and D. Papahadjopoulos. Comparative properties and methods of preparation of lipid vesicles (liposomes). *Annual Review of Biophysics and Bioengineering*, 9:467–508, 1980.

[78] E. J. Shimshick and H.M. McConnell. Lateral phase separation in phospholipid membranes. *Biochemistry.*, 12:2351–2360, 1973.

[79] K. Jrgensen and O.G. Mouritsen. Phase separation dynamics and lateral organization of two-component lipid membranes. *Biophys. J.*, 69:942–954, 1995.

[80] L. A. Bagatolli and E. Gratton. A correlation between lipid domain shape and binary phospholipid mixture composition in free standing bilayers: A two-photon fluorescence microscopy study. *Biophys. J.*, 79:434–447, 2000.

[81] J. Leng, S. U. Egelhaaf, and M. E. Cates. Kinetics of the micelle-to-vesicle transition: Aqueous lecithin-bile salt mixtures. *Biophysical Journal*, 85(3):1624–1646, 2003.

[82] P. W. M. Vandijck, A. J. Kaper, H. A. J. Oonk, and J. Degier. Miscibility properties of binary phosphatidylcholine mixtures - calorimetric study. *Biochimica Et Biophysica Acta*, 470(1):58–69, 1977.

[83] G. G. Chernik. Phase-equilibria in phospholipid water-systems. *Advances in Colloid and Interface Science*, 61:65–129, 1995.

[84] I. Marcotte, A. Belanger, and M. Auger. The orientation effect of gramicidin a on bicelles and eu3+-doped bicelles as studied by solid-state nmr and ft-ir spectroscopy. *Chemistry and Physics of Lipids*, 139(2):137–149, 2006.

[85] M. Ottiger and A. Bax. Characterization of magnetically oriented phospholipid micelles for measurement of dipolar couplings in macromolecules. *Journal of Biomolecular NMR*, 12(3):361–372, 1998.

[86] C. R. Sanders and J. H. Prestegard. Magnetically orientable bilayers containing small amounts of bile salt analogue, chapso. *Biophysical Journal*, 58:447–460, 1990.

[87] C. R. Sanders and J. P. Schwonek. Characterization of magnetically orientable bilayers in mixtures of dihexanoylphosphatidylcholine and dimyristoylphosphatidylcholine by solid-state nmr. *Biochemistry*, 31(37):8898–8905, 1992.

[88] G. Raffard, S. Steinbruckner, A. Arnold, J. H. Davis, and E. J. Dufourc. Temperature-composition diagram of dimyristoylphosphatidylcholine-dicaproylphosphatidylcholine bicelles, self-orienting in the magnetic field: A solid state h-2 and p-31 nmr study. *Langmuir*, 16(20):7655–7662, 2000.

[89] R. R. Vold and R. S. Prosser. Magnetically oriented phospholipid bilayered micelles for structural studies of polypeptides. does the ideal bicelle exist? *Journal of Magnetic Resonance Series B*, 113(3):267–271, 1996.

[90] E Boroske and W Helfrich. Magnetic anisotropy of egg lecithin membranes. *Biophys. J.*, 24:863–868, 1978.

[91] F. Scholz, E. Boroske, and W. Helfrich. Magnestic anisotropy of lecithin membranes. *Biophys. J*, 45:589–592, 1984.

[92] N. E. Gabriel and M. F. Roberts. Interaction of short-chain lecithin with long-chain phospholipids - characterization of vesicles that form spontaneously. *Biochemistry*, 25(10):2812–2821, 1986.

[93] N. E. Gabriel, N. V. Agman, and M. F. Roberts. Enzymatic-hydrolysis of short-chain lecithin long-chain phospholipid unilamellar vesicles - sensitivity of phospholipases to matrix phase state. *Biochemistry*, 26(23):7409–7418, 1987.

[94] N. E. Gabriel and M. F. Roberts. Short-chain lecithin long-chain phospholipid unilamellar vesicles - asymmetry, dynamics, and enzymatic-hydrolysis of the short-chain component. *Biochemistry*, 26:2432–2440, 1987.

[95] T.-L. Lin, C.-C. Liu, M.F Roberts, and S.-H Chen. Structure of mixed short-chain and long-chain lecithin aggregates studied by small angle neutron scattering. *J Phys Chem*, 95:6020–6027, 1991.

[96] B.J. Hare, J.H Prestegard, and D.M Engelman. Small angle x-ray scattering studies of magnetically oriented lipid bilayers. *Biophys.J.*, 69:1891–1896, 1995.

[97] R. R. Vold, R. S. Prosser, and A. J. Deese. Isotropic solutions of phospholipid bicelles: A new membrane mimetic for high-resolution nmr studies of polypeptides. *Journal of Biomolecular Nmr*, 9(3):329–335, 1997.

[98] J. Struppe and R. R. Vold. Dilute bicellar solutions for structural nmr work. *Journal of Magnetic Resonance*, 135(2):541–546, 1998.

[99] K. J. Glover, J. A. Whiles, G. H. Wu, N. J. Yu, R. Deems, J. O. Struppe, R. E. Stark, E. A. Komives, and R. R. Vold. Structural evaluation of phospholipid bicelles for solution-state studies of membrane-associated biomolecules. *Biophysical Journal*, 81(4):2163–2171, 2001.

[100] F.M. Marassi, A. Ramamoorthy, and Stanley J. Opella. Complete resolution of the solid-state nmr spectrum of a uniformly 15n-labeled membrane protein in phospholipid bilayers. *PNAS*, 94:8551–8556, 1997. Journal.

[101] M. P. Nieh, C. J. Glinka, S. Krueger, R. S. Prosser, and J. Katsaras. Sans study of the structural phases of magnetically alignable lanthanide-doped phospholipid mixtures. *Langmuir*, 17(9):2629–2638, 2001.

[102] M. Ottiger and A. Bax. Bicelle-based liquid crystals for nmr-measurement of dipolar couplings at acidic and basic ph values. *Journal of Biomolecular Nmr*, 13(2):187–191, 1999.

[103] J. J. Chou, J. L. Baber, and A. Bax. Characterization of phospholipid mixed micelles by translational diffusion. *Journal of Biomolecular Nmr*, 29(3):299–308, 2004.

[104] M. P. Nieh, C. J. Glinka, S. Krueger, R. S. Prosser, and J. Katsaras. Sans study on the effect of lanthanide ions and charged lipids on the morphology of phospholipid mixtures. *Biophysical Journal*, 82(5):2487–2498, 2002.

[105] M. P. Nieh, V. A. Raghunathan, C. J. Glinka, T. A. Harroun, G. Pabst, and J. Katsaras. Magnetically alignable phase of phospholipid 'bicelle' mixtures is a chiral nematic made up of wormlike micelles. *Langmuir*, 20(19):7893–7897, 2004.

[106] M. N. Triba, D. E. Warschawski, and P. F. Devaux. Reinvestigation by phosphorus nmr of lipid distribution in bicelles. *Biophysical Journal*, 88(3):1887–1901, 2005.

[107] B. A. Rowe and S. L. Neal. Fluorescence probe study of bicelle structure as a function of temperature: Developing a practical bicelle structure model, 2003.

[108] T. A. Harroun, M. Koslowsky, M. P. Nieh, C. F. de Lannoy, V. A. Raghunathan, and J. Katsaras. Comprehensive examination of mesophases formed by dmpc and dhpc mixtures. *Langmuir*, 21(12):5356–5361, 2005.

[109] D. Lichtenberg and Editor. *Detergents in biomembrane studies, Special Issue of Biochimica et Biophysica Acta (BBA) - Biomembranes*. Elsevier Journals, 2000.

[110] Rumiana Koynova and Boris Tenchov. Interactions of surfactants and fatty acids with lipids. *Current Opinion in Colloid and Interface Science*, 6:277–286, June 2001.

[111] A.S Sadaghiani, A. Khan, and B. Lindman. Liquid crystallinity of lecithin systems. ternary phase diagram of lecithin-water with triton x-100 and decanol. *J. Colloid Interf. Sci.*, 132:352–361, 1989.

[112] K. Edwards and M. Almgren. Solubilization of lecithin vesicles by c12e8. structural transitions and temperature effects. *J. Colloid Interf. Sci.*, 147:1–21, 1991.

[113] D. Otten, L. Lobbecke, and K. Beyer. Stages of the bilayer-micelle transition in the system phosphatidylcholine-c(12)e(8) as studied by deuterium-nmr and phosphorus-nmr, light-scattering, and calorimetry. *Biophysical Journal*, 68(2):584–597, 1995.

[114] P. R. Majhi and A. Blume. Temperature-induced micelle-vesicle transitions in dmpc-sds and dmpc-dtab mixtures studied by calorimetry and dynamic light scattering. *Journal of Physical Chemistry B*, 106(41):10753–10763, 2002.

[115] M. Ollivon, O. Eidelman, R. Blumenthal, and A. Walter. Micelle vesicle transition of egg phosphatidylcholine and octyl glucoside. *Biochemistry*, 27(5):1695–1703, 1988.

[116] P. K. Vinson, Y. Talmon, and A. Walter. Vesicle-micelle transition of phosphatidylcholine and octyl glucoside elucidated by cryo-transmission electron-microscopy. *Biophysical Journal*, 56(4):669–681, 1989.

[117] A.I. Polozova, G.E. Dubachev, T.N. Simonova, and Barsukov. L.I. Temperature-induced micellar-lamellar transformation in binary mixtures of saturated phosphatidylcholines with sodium cholate. *FEBS Letters*, 358:17–22, 1995.

[118] C. Q. Sun, Y. Sano, H. Kashiwagi, and M. Ueno. Characterization of aggregate structures of phospholipid in the process of vesicle solubilization with sodium cholate using laser light scattering method. *Colloid and Polymer Science*, 280(10):900–907, 2002.

[119] K. Edwards, M. Almgren, J. Bellare, and W. Brown. Effects of triton x-100 on sonicated lecithin vesicles. *Langmuir*, 5(2):473–478, 1989.

[120] N. A. Mazer, G. B. Benedek, and M. C. Carey. Quasi-elastic light-scattering-studies of aqueous biliary lipid systems - mixed micelle formation in bile-salt lecithin solutions. *Biochemistry*, 19(4):601–615, 1980.

[121] P. Schurtenberger, N. Mazer, and W. Kanzig. Micelle to vesicle transition in aqueous solutions of bile salt and lecithin. *J. Phys. Chem*, 89:1042–1049, 1985.

[122] R.P Jr. Hjelm, P. Thiyagarajan, and H. Alkan-Onyuksel. Organization of phosphatidylcholine and bile salt in rodlike mixed micelles. *Journal of Physical Chemistry*, 96:8653–8661, 1992.

[123] J. S. Pedersen, S. U. Egelhaaf, and P. Schurtenberger. Formation of polymerlike mixed micelles and vesicles in lecithin-bile salt solutions: A small-angle neutron-scattering study. *Journal of Physical Chemistry*, 99(4):1299–1305, 1995.

[124] L. Arleth, R Bauer, L.H Ogendal, S.U Egelhaaf, P. Schurtenberger, and J.K Pedersen. Growth behavior of mixed wormlike micelles: a small-angle scattering study of the lecithin-bile salt system. *Langmuir*, 19, 2003.

[125] Alexey Goltsov and Leonid Barsukov. Synergetics of the membrane self-assembly: A micelle-to-vesicle transition. *Journal of Biological Physics*, 26,:27–41, 2000.

[126] O. Kratky, H. Leopold, and H. Stabinger. Determination of density of liquids and gases to an accuracy of 1 /millionth g/cu cm with a sample volume of only 0.6 cu cm. *Z. Angew. Phys. (West Berlin)*, 27:273–277, 1969.

[127] D. Orthaber, A. Bergmann, and O. Glatter. Saxs experiments on absolute scale with kratky systems using water as a secondary standard. *Journal of Applied Crystallography*, 33(2):218–225, Apr 2000.

[128] D. A. Wilkinson and J. F. Nagle. Specific heats of lipid dispersions in single phase regions. *Biochim. Biophys. Acta*, 688:107, 1982.

[129] B. Hammouda. *The SANS Toolbox*. Wiley, Newyork, 2007.

[130] S. Seifert, R.E. Winans, D.M. Tiede, and P. Thiyagarajan. Design and performance of a ASAXS instrument at the Advanced Photon Source. *Journal of Applied Crystallography*, 33:782–784, 2000.

[131] J. Fitter, T. Gutberlet, and J.(Eds.) Katsaras. *Neutron Scattering in Biology: Techniques And Applications*. Springer, 2006.

[132] A. Guinier and G. Fournet. *Small-angle Scattering of X-rays*. John Wiley and Sons, Inc. (London), 1955.

[133] O. Guinier and O. Kratky. *Small-angle X-ray Scattering*. Academic Press, 1982.

[134] D. I. Svergun, L. A. Feigin, and B. M. Schedrin. Small-angle scattering: direct structure analysis. *Acta Crystallographica Section A*, 38(6):827–835, Nov 1982.

[135] Dmitri I. Svergun. Small-angle scattering studies of macromolecular solutions. *Journal of Applied Crystallography*, 40(s1):s10–s17, Apr 2007.

[136] S. R. Kline. Reduction and analysis of sans and usans data using igor pro. *J Appl. Cryst.*, 39(6), 2006.

[137] B.E. Warren. *X-ray Diffraction*. Courier Dover Publications, 1990.

[138] A. Arnold, T. Labrot, R. Oda, and E. J. Dufourc. Cation modulation of bicelle size and magnetic alignment as revealed by solid-state nmr and electron microscopy. *Biophys. J*, 83:2667–2680, 2002.

[139] M. N. Triba, P. F. Devaux, and D. E. Warschawski. Effects of lipid chain length and unsaturation on bicelles stability. a phosphorus nmr study. *Biophysical Journal*, 91(4):1357–1367, 2006.

[140] L. van Dam, G. Karlsson, and K. Edwards. Morphology of magnetically aligning dmpc/dhpc aggregates-perforated sheets, not disks. *Langmuir*, 22(7):3280–3285, 2006.

[141] J. R. Bian and M. F. Roberts. Phase-separation in short-chain lecithin gel-state long-chain lecithin aggregates. *Biochemistry*, 29(34):7928–7935, 1990.

[142] P. C. Mason, B. D. Gaulin, R. M. Epand, and J. Katsaras. Critical swelling in single phospholipid bilayers. *Phys. Rev. E*, 61(5):5634–5639, May 2000.

[143] Magnus Bergstrom. Thermodynamics of anisotropic surfactant micelles. i. the influence of curvature free energy on the micellar size and shape. *The Journal of Chemical Physics*, 113(13):5559–5568 and 5569–5571, 2000.

[144] Magnus Bergstrom. Bending energetics of tablet-shaped micelles: A novel approach to rationalize micellar systems. *ChemPhysChem*, 8(3):462–472, 2007.

[145] J. Pencer, T. Mills, V. Anghel, S. Krueger, R.M Epand, and J. Katsaras. Detection of submicron-sized raft-like domains in membranes by small-angle neutron scattering. *The European Physical Journal E - Soft Matter*, 18:447–458, 2005.

[146] P. Balgavy, M. Dubnickova, N. Kucerka, M. A. Kiselev, S. P. Yaradaikin, and D. Uhrikova. Bilayer thickness and lipid interface area in unilamellar extruded 1,2-diacylphosphatidylcholine liposomes: a small-angle neutron scattering study. *Biochim Biophys Acta.*, 1512(1):40–52, 2001. Journal.

[147] Curtis W. Meuse, Susan Krueger, Charles F. Majkrzak, Joseph A. Dura, Joseph Fu, Jason T. Connor, and Anne L. Plant. Hybrid bilayer membranes in air and water: Infrared spectroscopy and neutron reflectivity studies, March 1, 1998 1998.

[148] Michael Kotlarchyk and Sow-Hsin. Chen. Analysis of small angle neutron scattering spectra from polydisperse interacting colloids. *J. Chem. Phys.*, 79(5):2461–2469, 1983.

[149] Michael Kotlarchyk, Richard B. Stephens, and John S. Huang. Study of schultz distribution to model polydispersity of microemulsion droplets. *J. Phys. Chem*, 92(6):1533–1538, 1988.

[150] J. H. CLINT. Micellization of mixed nonionic surface active agents. *Faraday Transaction*, 1974.

[151] G. G. Warr, F. Grleser, and T. W. Healy. Composition of mixed micelles of polydisperse nonionic surfactants. *J. Phys. Chem*, 87:1220–1223, 1983.

[152] Shiloach. A and D. Blankschtein. Predicting micellar properties of binary surfactant mixtures. *Langmuir*, 14, 1998.

[153] Th. Zemb, M. Dubois, and B. Gulik-Krzywicki. Self-assembly of flat nanodiscs in salt-free catanionic surfactant solutions. *Science*, 283:816–819, 1999.

[154] J. de Joannis, F. Y. Jiang, and J. T. Kindt. Coarse-grained model simulations of mixed-lipid systems: Composition and line tension of a stabilized bilayer edge. *Langmuir*, 22(3):998–1005, 2006.

[155] P. Fromherz. Lipid-vesicle structure - size control by edge-active agents. *Chemical Physics Letters*, 94(3):259–266, 1983.

[156] M. M. Kozlov, D. Lichtenberg, and D. Andelman. Shape of phospholipid/surfactant mixed micelles: Cylinders or disks? theoretical analysis. *Journal of Physical Chemistry B*, 101(33):6600–6606, 1997. Journal.

[157] D. Andelman, M. M. Kozlov, and W. Helfrich. Phase transitions between vesicles and micelles driven by competing curvatures. *Europhys. Lett.*, 25:231, 1994.

[158] S. Leikin, M. M. Kozlov, N. L. Fuller, and R. P. Rand. Measured effects of diacylglycerol on structural and elastic properties of phospholipid membranes. *Biophys. J.*, 71:2623, 1996.

[159] I. Szleifer, D. Kramer, A. Ben-Shaul, D. Roux, and W. M. Gelbart. Curvature elasticity of pure and mixed surfactant films. *Phys. Rev. Lett.*, 60:1966, 1988.

[160] M. Dubois, T. Zemb, and coworkers. Shape control through molecular segregation in giant surfactant aggregates. *Proc. of Nat. Acad. of Sci*, 101:15082–15087, 2004.

[161] P. Fromherz, C. Rocker, and D. Ruppel. From discoid micelles to spherical vesicles. the concept of edge activity. *Faraday Discussions of the Chemical Society*, 94(3):259–266, 1986.

[162] S. May and A. Ben-Shaul. Spontaneous curvature and thermodynamic stability of mixed amphiphilic layers. *Journal of chemical physics*, 103:3839–3848, 1995.

[163] D. I. Svergun, A. V. Semenyuk, and L. A. Feigin. Small-angle-scattering-data treatment by the regularization method. *Acta Crystallographica Section A*, 44(3):244–250, May 1988.

[164] D. I. Svergun. A direct indirect method of small-angle scattering data treatment. *Journal of Applied Crystallography*, 26(2):258–267, Apr 1993.

[165] S. S. Funari, B. Nuscher, G. Rapp, and K. Beyer. Detergent-phospholipid mixed micelles with a crystalline phospholipid core. *Proceedings of the National Academy of Sciences of the United States of America*, 98(16):8938–8943, 2001.

[166] B. Madler, H. Binder, and G. Klose. Compound formation in mixed phospholipid membranes induced by a nonionic surfactant of the oligo-alkyl ether type: A comparitive dsc and ftir study. *J. of Colloid and Interface Science*, 202:124–138, 1998.

[167] D. I. Svergun. Determination of the regularization parameter in indirect-transform methods using perceptual criteria. *Journal of Applied Crystallography*, 25(4):495–503, Aug 1992.

[168] M. Bergstrom and J.S. Pedersen. A small-angle neutron scattering (sans) study of tablet-shaped and ribbonlike micelles formed from mixtures of an anionic and a cationic surfactant. *Journal of Physical Chemistry B*, 103(40):8502–8513, 1999.

[169] M. Bergstrom, J.S. Pedersen, P. Schurtenberger, and S.U. Egelhaaf. Small-angle neutron scattering (sans) study of vesicles and lamellar sheets formed from mixtures of an anionic and a cationic surfactant. *Journal of Physical Chemistry B*, 103(45):9888–9897, 1999.

[170] M. Bergstrom and J.S. Pedersen. A small-angle neutron scattering study of surfactant aggregates formed in aqueous mixtures of sodium dodecyl sulfate and didodecyldimethylammonium bromide. *Journal of Physical Chemistry B*, 104(17):4155–4163, 2000.

[171] M. F. Schneider, D. Marsh, W. Jahn, B. Kloesgen, and T. Heimburg. Network formation of lipid membranes: Triggering structural transitions by chain melting. *Proceedings of the National Academy of Sciences*, 96:14312–14317, 1999.

[172] J.C Owicki and H.M. McConnell. Theory of protein-lipid and protein-protein interactions in bilayer membranes. *Proceedings of the National Academy of Sciences of the United States of America*, 76:4750–4754, 1979.

[173] V. Schram, H. N. Lin, and T. E. Thompson. Topology of gel-phase domains and lipid mixing properties in phase- separated two-component phosphatidylcholine bilayers. *Biophys. J.*, 71:1811–1822, 1996. Journal.

Vita

Divya Singh was born in Sasaram[1], India, to a scientist father and a teacher mother. Growing up in university campuses around India, both science and philosophy had a strong influence in her formative years. In 2000, she graduated from the Indian Institute of Technology, Kanpur with a BS-MS (Integrated) Physics degree. During this time, she spent a few wonderful summers at national laboratories, getting introduced to research, with a strong desire to pursue the same. In 2001, she joined the Physics department at Johns Hopkins University under the mentorship of Prof. Bob Leheny. Drawn to biological physics, she dabbled in a few different projects with research advisors in different divisions in the university, before joining Dr's. Paul Butler and Lionel Porcar at the the NIST Center for Neutron Research. Since attending the Summer school in Scattering techniques in 2004 at NIST, she worked a series of scattering experiments at the same facility, which form her dissertation. Upon graduation, she will continue to apply her training in modeling and experimentation with the Resolution Enhancement Technology group of Intel Corp. in Portland, Oregon.

---

[1]a small historic town in the state of Bihar